Generalized Differential Quadrature Finite Element Method applied to Advanced Structural Mechanics

PhD Thesis in
"Structural Engineering and Hydraulics"
XXV Cycle

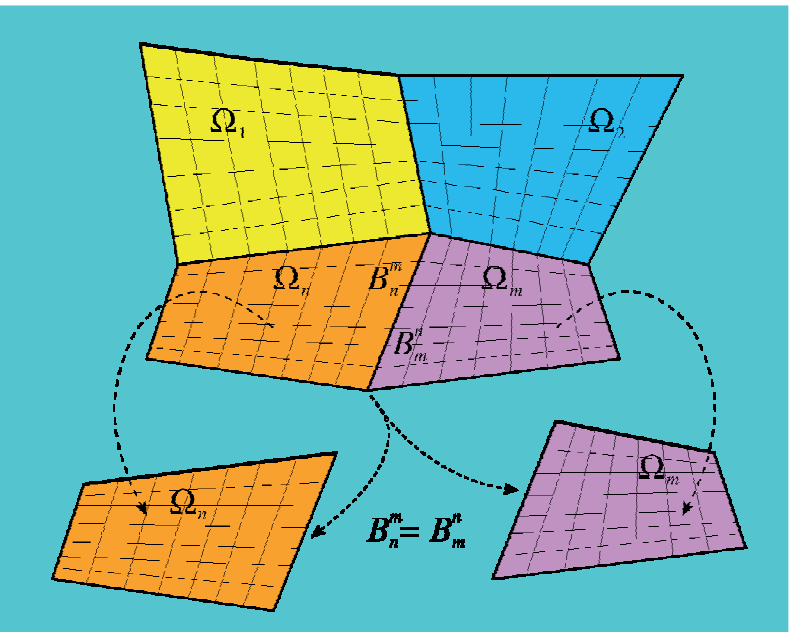

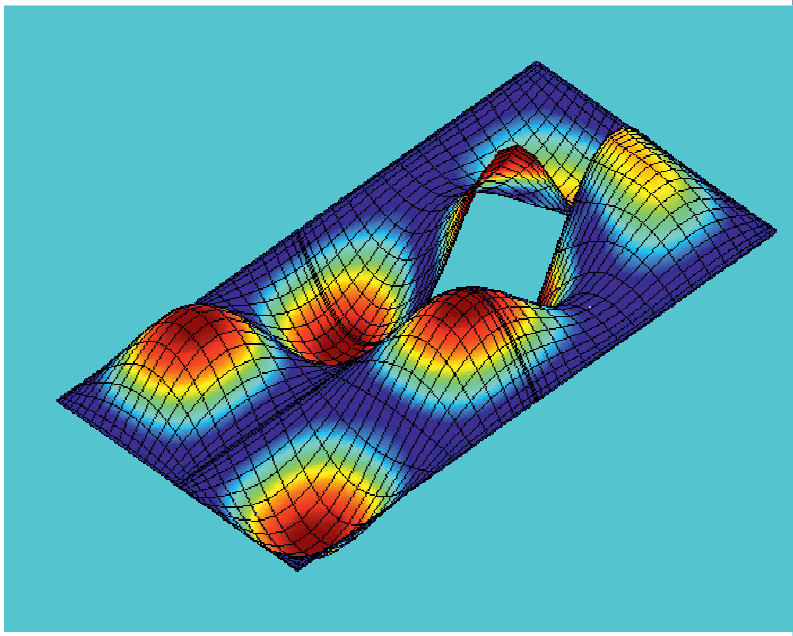

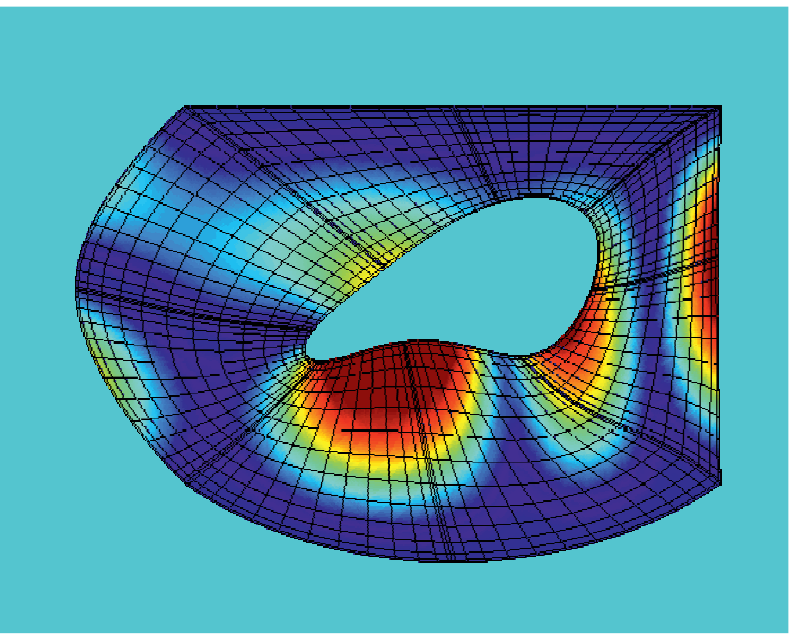

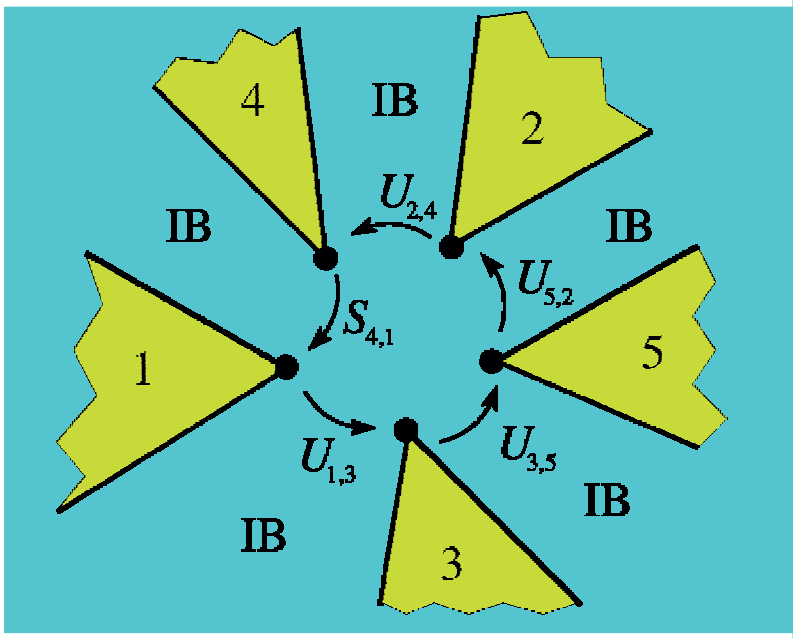

PhD Candidate
Nicholas Fantuzzi

Advisor: Prof. Erasmo Viola
Co-Advisor: Ass. Prof. Francesco Tornabene

University of Bologna

University of Bologna

PhD Thesis in
Structural Engineering and Hydraulics
Cicle XXV

Generalized Differential Quadrature Finite Element Method applied to Advanced Structural Mechanics

PhD Candidate:
Nicholas Fantuzzi

Advisor:
Prof. Erasmo Viola

PhD coordinator:
Prof. Erasmo Viola

Co-Advisor:
Ass. Prof. Francesco Tornabene

April 10, 2013

Universitá di Bologna

Tesi di Dottorato di Ricerca in
Ingegneria Strutturale ed Idraulica

XXV Ciclo

Settore Scientifico-Disciplinare ICAR/08

Settore Concorsuale 08/B2

Generalized Differential Quadrature Finite Element Method applied to Advanced Structural Mechanics

Candidato:
Nicholas Fantuzzi

Relatore:
Prof. Erasmo Viola

Coordinatore:
Prof. Erasmo Viola

Correlatore:
Ing. Francesco Tornabene

April 10, 2013

To Ilaria for her support, encouragement,
and constant love.

A Ilaria che mi ha sostenuto, incoraggiato e
costantemente amato.

Abstract

Over the years the Differential Quadrature (DQ) method has distinguished because of its high accuracy, straightforward implementation and general application to a variety of problems. There has been an increase in this topic by several researchers who experienced significant development in the last years.

DQ is essentially a generalization of the popular Gaussian Quadrature (GQ) used for numerical integration functions. GQ approximates a finite integral as a weighted sum of integrand values at selected points in a problem domain whereas DQ approximate the derivatives of a smooth function at a point as a weighted sum of function values at selected nodes. A direct application of this elegant methodology is to solve ordinary and partial differential equations. Furthermore in recent years the DQ formulation has been generalized in the weighting coefficients computations to let the approach to be more flexible and accurate. As a result it has been indicated as Generalized Differential Quadrature (GDQ) method.

However the applicability of GDQ in its original form is still limited. It has been proven to fail for problems with strong material discontinuities as well as problems involving singularities and irregularities. On the other hand the very well-known Finite Element (FE) method could overcome these issues because it subdivides the computational domain into a certain number of elements in which the solution is calculated. Recently, some researchers have been studying a numerical technique which could use the advantages of the GDQ method and the advantages of FE method. This methodology has got different names among each research group, it will be indicated here as Generalized Differential Quadrature Finite Element Method (GDQFEM).

The purpose of this PhD Thesis is to introduce the limitations of the direct GDQ method and more importantly the implementation technique of the GDQFEM. Moreover, in order to show the accuracy, stability and flexibility of the current methodology some numerical examples are shown. The examples are related to the mechanics of civil and mechanical engineering structures such as membranes, state plane structures and flat plates. The static and dynamic behaviour of these structures are proposed in the following chapters. Numerical comparisons with literature and FE analyses are reported and very good agreement is observed in all the computations.

Sommario

Negli ultimi anni il metodo di Quadratura Differenziale (DQ) si è distinto per la sua elevata accuratezza, semplicità di implementazione e applicazione a svariati problemi matematici. Recentemente, molti ricercatori hanno utilizzato sempre più frequentemente questa tecnicha per la risoluzione di problemi di meccanica delle strutture.

Il metodo DQ è essenzialmente una generalizzazione della Quadratura Gaussiana (GQ) utilizzata per l'integrazione numerica delle funzioni. Il metodo GQ approssima un integrale finito come una somma dei valori della funzione integranda in certi punti particolari del dominio, mentre la tecnica DQ approssima le derivate di una funzione regolare in un punto, come somma pesata di valori della funzione nei punti del dominio. Una diretta applicazione di questa metodologia si trova nella risoluzione di sistemi di equazioni alle derivate parziali e totali. La formulazione DQ classica è stata generalizzata per quanto riguarda il calcolo dei coefficienti di ponderazione, e ciò ha permesso di avere un calcolo dei coefficienti più flessibile ed accurato. Infatti, in letteratura viene indicato come metodo Generalizzato di Quadratura Differenziale (GDQ).

Tuttavia l'applicabilità della tecnica GDQ nella sua forma originaria rimane comunque limitata. Il metodo non può essere applicato in presenza di discontinuità del materiale come anche in problemi che riguardano le singolarità e la forma generica. D'altro canto, il ben noto metodo agli Elementi Finiti (FE) può andare oltre questi aspetti poiché suddivide il dominio computazionale in un certo numero di elementi in cui viene calcolata la soluzione. Recentemente, molti ricercatori si sono occupati di una tecnica numerica in grado di unire i vantaggi del metodo GDQ e del metodo FE. In letteratura, questa tecnica viene indicata in svariati modi a seconda del gruppo di ricerca che se ne è occupato, anche se in tutti i casi la tecnica ha sempre lo scopo di andare oltre i limiti della tecnica DQ standard. In questa tesi, tale tecnica, viene indicata come Metodo agli Elementi Finiti basato sulla Quadratura Differenziale Generalizzata (GDQFEM).

L'obiettivo di questa tesi è quindi quello di introdurre le limitazioni del metodo diretto GDQ e di mostrate le tecniche di implementazione del metodo GDQFEM. Inoltre per mostrare l'accuratezza, la stabilità e la flessibilità del GDQFEM vengono proposti alcuni esempi numerici (e.g. membrane, stati piani e piastre piane) relativi alla meccanica delle strutture sia in ambito civile che meccanico. Per ogni esempio si riporta: il comportamento statico e dinamico e le correlazioni numeriche tra i risultati pubblicati in letteratura, le soluzioni ottenute con analisi FE e quelli proposti. Tutte le correlazioni numeriche hanno evidenziato un ottimo accordo.

Acknowledgements

I am most grateful to the members of my research group, Prof. Erasmo Viola and Ass. Prof. Francesco Tornabene for their time, encouragement, and expertise throughout this research project. Special thanks to my co-advisor, for his exquisite attention to detail and for his demand for excellence. He was instrumental in the great success of this research, because he has always given me new ideas to improve it.

There are people in everyone's lives who make success both possible and rewarding. I appreciate the way in which my mother and father gave me their support. I will always be grateful to them even though at times it was really difficult.

A special thanks to Ilaria who always steadfastly supported and encouraged me all these years together.

Ringraziamenti

Sono molto grato ai membri del mio gruppo di ricerca, il Prof. Erasmo Viola e Ass. Prof. Francesco Tornabene, per il loro tempo, incoraggiamento, e la competenza in questo progetto di ricerca. Un ringraziamento speciale al mio correlatore, per la sua attenzione ai dettagli e per la sua richiesta di eccellenza. Parte del successo di questa ricerca la devo a lui, poiché è stato in grado di darmi sempre nuove idee per migliorarla.

Ci sono persone nella vita di tutti che non solo la rendono possibile ma anche gratificante. Apprezzo il modo in cui mia madre e mio padre mi hanno dato il loro sostegno. Sarò sempre grato a loro, anche se a volte è stato davvero difficile.

Un ringraziamento speciale a Ilaria che mi ha sempre sostenuto con fermezza e mi ha incoraggiato in tutti questi anni insieme.

Contents

List of Figures

List of Tables

Chapter 1

Generalized Differential Quadrature Finite Element Method

Sommario

Gran parte dei problemi ingegneristici sono governati da sistemi di equazioni alle derivate parziali (PDEs) con opportune condizioni al contorno. In generale, risulta molto complesso ottenere una soluzione in forma chiusa di questi sistemi differenziali. D'altro canto però, la soluzione di un PDE è necessaria per fini pratici.

Nella maggior parte dei casi, la soluzione approssimata è presentata con valori della funzione incognita in alcuni punti discreti del dominio (punti della griglia o della maglia). Le relazioni tra le derivate nel sistema di equazioni alle derivate parziali e i valori della funzione nei punti della griglia prende il nome di tecnica di discretizzazione.

Nel presente capitolo si presenta un'efficiente tecnica di discretizzazione per ottenere soluzioni numeriche accurate utilizzando un piccolo numero di punti di griglia. Questa tecnica è stato introdotto da Bellman *et al.* [7, 8] negli anni 70. In particolare Bellman introdusse il metodo di Quadratura Differenziale (DQ), secondo il quale una derivata parziale di una certa funzione, rispetto ad una coordinata direzionale, può essere espressa come una somma lineare pesata dei valori che la funzione assume in certi punti (detti punti di griglia) moltiplicati per dei coefficienti di ponderazione. Tale metodo fu successivamente generalizzato da Shu [9] permettendo una definizione ricorsiva dei coefficienti di ponderazione per il calcolo delle derivate di ordine superiore al primo. Tale tecnica prende il nome di metodo Generalizzato di Quadratura Differenziale (GDQ).

Risulta dunque possibile risolvere un qualsivoglia sistema differenziale discretizzando le derivate di tale sistema e ottenendo così un sistema algebrico di equazioni. È quindi possibile risolvere le equazioni fondamentali delle strutture direttamente in forma forte senza indebolire il sistema, come avviene invece per il metodo ad Elementi Finiti (FE).

Sicuramente un punto di forza del metodo GDQ è l'elevata accuratezza e stabilità, ma purtroppo non può essere applicato in casi in cui la geometria sia distorta o vi siano discontinuità geometriche o del materiale. Nella seconda parte di questo capitolo quindi si introduce una tecnica numerica avanzata che ha come base il metodo GDQ e ne generalizza i concetti per essere applicato in quei casi in cui il GDQ classico non può essere applicato. Tale tecnica viene qui indicata come Metodo agli Elementi Finiti basato sulla Quadratura Differenziale Generalizzata (GDQFEM) poiché è possibile far uso dei punti di forza del metodo GDQ e del metodo FE. Riassumendo, il metodo GDQFEM [11] inizial-

mente discretizza il dominio reale in una serie di sottodomini a seconda delle discontinuità presenti nel modello. Si applica una trasformazione conforme per passare da un dominio distorto ad uno regolare (così come avviene negli elementi finiti). Infine, si applica la tecnica GDQ sul dominio di forma regolare. L'assemblaggio tra gli elementi della suddivisione avviene tramite la scrittura di condizioni di compatilbità tra i bordi degli elementi e condizioni di equilibrio nei punti di spigolo degli elementi stessi.

1.1 Introduction

Most engineering problems are governed by a set of partial differential equations (PDEs) with proper boundary conditions. In general it is very difficult to obtain a closed form of a given differential problem. On the other hand, the solution of a PDE is always demanded due to practical interests.

In most cases, the approximate solution is represented by functional values at certain discrete points (grid points or mesh points). The connection between the derivatives in a partial differential equation system and the functional values at the grid points is the discretization technique.

Nowadays, several numerical discretization techniques are available. Among them the Finite Difference (FD), Finite Element (FE), and Finite Volume (FV) methods fall under the category of low order methods, whereas spectral and pseudo-spectral methods are considered global methods. The FD is based on the Taylor series expansion or the polynomial approximation. whereas the FE method is based on the variational principal or the principal of weighted residuals. The FV method applies the physical conservation law directly to a finite cell. The spectral method may be viewed as an extreme development of the class of discretization schemes known as the methods of weighted residuals. There is a close relationship between FE and spectral methods in the sense that both methods use a set of base functions and weighting functions. The choice of the base function is one of the features that distinguishes the spectral method from the FE method.

Most numerical simulations of engineering problems can be carried out by the low order FD, FE and FV methods using a large number of grid points. In some practical applications, however, the numerical solutions of PDEs are required at only a few specific points in the physical domain. In order to achieve an acceptable degree of accuracy, low order methods still require the use of a large number of grid points to obtain accurate solutions at these specified points. It seems that to avoid the drawbacks of low order methods the solution accuracy can be improved by using high order and global methods. In general, high order methods have a high order of truncation error. Thus, to achieve the same order of accuracy, the mesh spacing used by high order methods can be much larger than that used by lower order methods. As a consequence, high order methods are capable of yielding accurate numerical solutions using a very few amount of grid points. The spectral method is the natural choice for this purpose. At present, application of spectra methods demand substantial mathematical knowledge of the theory.

In seeking an efficient discretization technique to obtain accurate numerical solutions using a considerably small number of grid points, Bellman *et al.* [7, 8] introduced the method of differential quadrature (DQ), where a partial derivative of a function with respect to a coordinate direction is expressed as a linear weighted sum of all the functional values at all mesh points along that direction. The DQ method was initiated from the idea of integral quadrature. The key to DQ is to determine the weighting coefficients for the discretization of a derivative of any order. Bellman et al. [7, 8] suggested two methods to the determine the weighting coefficients of the first order derivative. The first method solves an algebraic equation system. The second uses a simple algebraic formulation, but with the coordinates of the grid points chosen as the roots of the shifted Legendre polynomial.

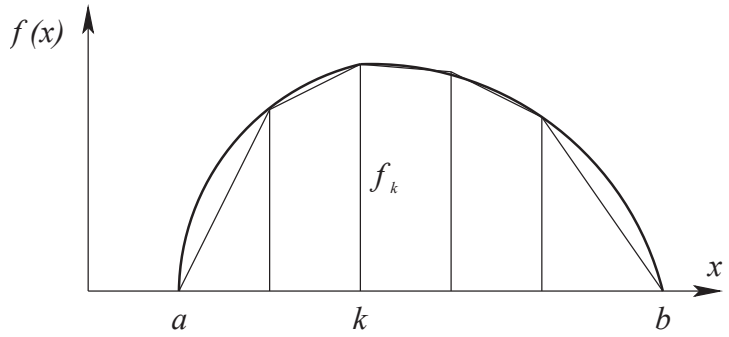

Figure 1.1: Integral of a generic function $f(x)$ over a closed interval $[a, b]$.

1.2 Integral quadrature

The differential quadrature (DQ) method was presented by Bellman and his associates in the early 1970's. It is a numerical discretization technique for the approximation of derivatives. The DQ method was initiated from the idea of conventional integral quadrature. In fact one problem which arises frequently in structural mechanics and in many other engineering problems is the evaluation of the integral

$$\int_a^b f(x)dx \tag{1.1}$$

over a finite and closed interval $[a, b]$. If F is a function such that $dF/dx = f$, then the value of the given integral is $F(b) - F(a)$. Unfortunately, in practical problems, it is extremely difficult, and most of the times impossible, to obtain an explicit expression for F. The values of f, perhaps, can be known at a discrete set of points and in this situation, a numerical approach is essential.

As it is very well known from literature that the integral (1.1) represents the area under the given curve $f(x)$ as shown in Figure 1.1. Since evaluating the integral is equivalent to the approximation of the area. Using this basic principle, many numerical method techniques were developed. In general, the integral (1.1) can be approximated by

$$\int_a^b f(x)dx = w_1 f_1 + w_2 f_2 + \cdots + w_n f_n = \sum_{k=1}^{n} w_k f_k \tag{1.2}$$

where $w_1, w_2, \ldots, w_n$ are the weighting coefficients, $f_1, f_2, \ldots, f_n$ are the functional values at the discrete points $a = x_1, x_2, \ldots, x_n = b$. Equation (1.2) is called the integral quadrature, which uses all the functional values in the whole integral domain to approximate an integral over a finite interval.

In general, the discrete points are selected so as to give a uniform distribution, e.g. $x_i = x_{i-1} + h$, $i = 2, 3, \ldots, n$, where h is called the step size. All the conventional quadrature rules can be written in the form of (1.2).

1.3 Differential Quadrature

As shown in Figure 1.2 a one dimensional problem is considered. It is assumed that a function $f(x)$ is sufficiently smooth over the whole domain. The given function must not have any singularity and it should be derivable over the domain.

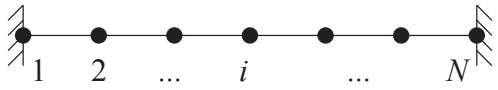

Figure 1.2: A one dimensional problem discretization.

Following the idea of integral quadrature (1.2), Bellman et al. [8] suggested that the first order derivative of the function $f(x)$ with respect to x at a grid point x_i, is approximated by a linear sum of all the functional values in the whole domain, that is

$$f_x(x_i) = \left.\frac{df}{dx}\right|_{x_i} = \sum_{j=1}^{N} a_{ij} f(x_j), \quad \text{for } i = 1, 2, \ldots, N \tag{1.3}$$

where a_{ij} represent the weighting coefficients, and N is the number of grid points in the whole domain. The differential quadrature is represented by (1.3). It should be noted that the weighting coefficients a_{ij} are different at different locations of x_i. The main procedure in DQ approximation is to determine the weighting coefficients a_{ij}. In [9, 10, 41] the determination of the weighting coefficients are presented in detail from the analysis of a linear vector space and the analysis of function approximation. For the sake of completeness only the main formulae are given in the following.

1.3.1 First order weighting coefficients

In this section, same details will be shown for the determination of the weighting coefficients in the DQ approximation when the solution of a partial differential equation (PDE) is approximated by a polynomial of high degree. For the sake of simplicity, since the DQ approximation is related to the polynomial approximation to the solution of a PDE, this methodology is termed polynomial based differential quadrature (PDQ) method.

Consider a one dimensional problem over a closed interval $[a, b]$. It is supposed that there are N grid points with the coordinates $a = x_1 x_2, \ldots, x_N = b$. Bellman et al. [8] assumed that a function $f(x)$ is sufficiently smooth over the interval $[a, b]$ so that its first order derivative $f^{(1)}(x)$ at any grid point can be approximated by the following formulation

$$f_x^{(1)}(x) = \sum_{j=1}^{N} a_{ij} f(x_j), \quad \text{for } i = i, 2, \ldots, N \tag{1.4}$$

where $f(x_j)$ representes the functional values at a grid point x_j, $f_x^{(1)}(x_i)$ indicates the first order derivative of $f(x)$ at x_i, and a_{ij} is the weighting coefficient of the first order derivative. It is shown in [9, 10, 41] that $f_x^{(1)}(x)$ is a linear operator. The determination of the weighting coefficients a_{ij} of (1.4) is a key procedure in the DQ approximation. Once the weighting coefficients are determined, the derivatives in the governing differential equation and the functional values at the mesh points are related by (1.4). In other words, with the weighting coefficients, one can easily use the functional values to compute the derivatives.

Bellman's approaches

Bellman et al. [8] proposed two approaches to compute the weighting coefficients a_{ij} (1.4). The two approaches are based on the use of two different test functions.

In his first approach the test functions are chosen as

$$g_k(x) = x^k, \quad \text{for } k = 0, 1, \ldots, N-1 \tag{1.5}$$

Obviously, (1.5) gives N test functions. For the weighting coefficients a_{ij} in (1.4) i and j are taken from 1 to N. Thus, the total number of weighting coefficients is $N \times N$. In order to obtain these weighting coefficients, the N test functions should be applied at N grid points x_1, x_2, ..., x_N. As a consequence, the following $N \times N$ algebraic equations for a_{ij} are obtained.

$$\begin{cases} \sum_{j=1}^{N} a_{ij} = 0 \\ \sum_{j=1}^{N} a_{ij} x_j = 1 \qquad\qquad \text{for } i = 1, 2, \ldots, N \\ \sum_{j=1}^{N} a_{ij} x_j^k = k x_i^{k-1}, \quad \text{for } k = 2, 3, \ldots, N-1 \end{cases} \tag{1.6}$$

Equation (1.6) has a unique solution because its matrix is of Vandermonde form. Unfortunately, when N is large, the matrix is ill-conditioned and its inversion is difficult. In the practical application of this approach, N is usually chosen to be less than 13.

In the Bellman's second approach, that is similar to the first one, nevertheless it has different test functions

$$g_k(x) = \frac{L_N(x)}{(x - x_k) L_N^{(1)}(x_k)}, \quad \text{for } k = 1, 2, \ldots, N \tag{1.7}$$

where $L_N(x)$ is the Legendre polynomial of degree N and $L_N^{(1)}(x)$ is the first order derivative of $L_N(x)$. By choosing x_k to be the roots of the shifted Legendre polynomial and applying (1.7) at N grid points x_1, x_2, ..., x_N, Bellman et al.[8] obtained a simple algebraic formulation to compute a_{ij}.

$$\begin{aligned} a_{ij} &= \frac{L_N^{(1)}(x_i)}{(x_i - x_j) L_N^{(1)}(x_j)}, \quad \text{for } j \neq i \\ a_{ii} &= \frac{1 - 2x_i}{2x_i(x_i - 1)} \end{aligned} \tag{1.8}$$

Using (1.8), the computation of the weighting coefficients is a simple task, nevertheless this approach is not flexible as the first approach because the coordinates of the grid points in this approach can not be chosen arbitrarily. They should have chosen as the roots of the Legendre polynomial of degree N instead. As a result (1.8) reflects only a special case. Due to the inflexibility associated with the second approach in selecting the grid points, the first approach is usually adopted in practical applications.

Quan and Chang's approach

In order to improve Bellman's approaches in computeing the weighting coefficients, many attempts have been made by a lot of researchers. One of the most useful approaches is the one introduced by Quan and Chang [18, 19]. They used the following Lagrange interpolation polynomials as test functions

$$g_k(x) = \frac{M(x)}{(x - x_k) M^{(1)}(x_k)}, \quad \text{for } k = 1, 2, \ldots, N \tag{1.9}$$

where

$$\begin{aligned} M(x) &= (x - x_1)(x - x_2)\dots(x - x_N) \\ M^{(1)}(x_i) &= \prod_{k=1, k\neq i}^{N} (x_i - x_k) \end{aligned} \tag{1.10}$$

Subsequently, by applying (1.9) at N grid points, they obtained the following algebraic formulations to compute the weighting coefficients a_{ij}

$$\begin{aligned} a_{ij} &= \frac{1}{x_j - x_i} \prod_{k=1, k\neq i}^{N} \frac{x_i - x_k}{x_j - x_k}, \quad \text{for } j \neq i \\ a_{ii} &= \sum_{k=1, k\neq i}^{N} \frac{1}{x_i - x_k} \end{aligned} \tag{1.11}$$

When (1.11) are used, there is no restriction on the choice of the grid points.

Shu's general approach

Shu's general approach was inspired by Bellman's approaches. It covers all the approaches, including Quan and Chang's approach.

It is shown in [9, 10, 41] that the solution of a PDE can be accurately approximated by a polynomial of high degree. It is supposed that the degree of the approximated polynomial is $N - 1$.

$$f(x) = \sum_{k=1}^{N} c_k x^{k-1} \tag{1.12}$$

where c_k is a constant. This approximate polynomial constitutes an N dimensional linear vector space V_N with the operation of vector addition and scalar multiplication. Many sets of base vectors in the linear vector space V_N exist. In the current case, the vector is actually the polynomial. As a result the base vectors are also called the base polynomials. For the sake of generality, two sets of base polynomials have been used. The Lagrange interpolation polynomials are taken as the first set of base polynomials

$$\begin{aligned} r_k(x) &= \frac{M(x)}{(x - x_k)M^{(1)}(x_k)}, \quad \text{for } k = 1, 2, \dots, N \\ M(x) &= N(x, x_k)(x - x_k), \quad \text{for } k = 1, 2, \dots, N \end{aligned} \tag{1.13}$$

with $N(x_i, x_j) = M^{(1)}(x_i)\delta_{ij}$, where δ_{ij} is the Kronecker operator. Using the second of (1.13), the first of (1.13) can be simplified to

$$r_k(x) = \frac{N(x, x_k)}{M^{(1)(x_k)}}, \quad \text{for } k = 1, 2, \dots, N \tag{1.14}$$

so the coefficients with the given base polynomial are

$$a_{ij} = \frac{N^{(1)(x_i,x_j)}}{M^{(1)}(x_j)} \tag{1.15}$$

In (1.15), $M^{(1)}(x_j)$ can be computed from the second of (1.10). To evaluate $N^{(1)}(x_i, x_j)$ the first of (1.13) have to be differentiate with respect to x so the following recurrence formulation is obtained

$$\begin{aligned} &M^{(m)}(x) = N^{(m)}(x, x_k)(x - x_k) + mN^{(m-1)}(x, x_k) \\ &\text{for } m = 1, 2, \ldots, N-1 \quad k = 1, 2, \ldots, N \end{aligned} \tag{1.16}$$

where $M^{(m)}(x)$ and $N^{(m)}(x, x_k)$ indicate the m-th order derivative of $M(x)$ and $N(x, x_k)$. From (1.16) the expressions of $N(x_i, x_j)$ can be obtained

$$\begin{aligned} N^{(1)}(x_i, x_j) &= \frac{M^{(1)}(x_i)}{x_i - x_j}, \quad \text{for } i \neq j \\ N^{(1)}(x_i, x_j) &= \frac{M^{(2)}(x_i)}{2} \end{aligned} \tag{1.17}$$

Substituting (1.17) into (1.15) the weighting coefficients are obtained

$$\begin{aligned} a_{ij} &= \frac{M^{(1)}(x_i)}{(x_i - x_j)M^{(1)}(x_j)}, \quad \text{for } \ i \neq j \\ a_{ii} &= \frac{M^{(2)}(x_i)}{2M^{(1)}(x_i)} \end{aligned} \tag{1.18}$$

It is observed from (1.18) that if x_i is given, it is easy to compute $M^{(1)}(x_i)$ from (1.10) and as a consequence a_{ij} for $i \neq j$. However, the calculation of a_{ii} is based on the computation of the second order derivative $M^{(2)}(x_i)$ which is not an easy task. This difficulty can be eliminated by using the second set of base polynomials. According to the property of a linear vector space, if one set of base polynomials matches a linear operator, so does another set of base polynomials. As a result, the equation system for the determination of a_{ij} derived from the Lagrange interpolation polynomials should be equivalent to that derived from another set of base polynomials $x^{k-1}, k = 1, 2, \ldots, N$. Thus a_{ij} satisfies the following equation which is obtained by the base polynomial x^{k-1} when $k = 1$

$$\sum_{j=1}^{N} a_{ij} = 0 \quad \text{or} \quad a_{ii} = -\sum_{j=1, j\neq i}^{N} a_{ij} \tag{1.19}$$

The first of (1.18) and (1.19) are the two formulations to compute the weighting coefficients a_{ij}. It is noted that in the development of these two formulations, two sets of base polynomials were used in the linear polynomial vector space V_N.

1.3.2 Higher order weighting coefficients

For the discretization of the second order derivative a similar approximation is introduced

$$f_x^{(2)}(x_i) = \sum_{j=1}^{N} b_{ij} f(x_j), \quad \text{for } i = 1, 2, \ldots, N \tag{1.20}$$

where $f_x^{(2)}(x_i)$ is the second order derivative of $f(x)$ at x_i, b_{ij} are the weighting coefficients of the second order derivative. It is clear that (1.20) is a linear operator and it has got the same form of (1.4).

Quan and Chang's approach

In this approach Quan and Chang used the Lagrange interpolation polynomials as the test functions and then derived

$$\begin{aligned} b_{ij} &= \frac{2}{x_j - x_i} \left(\prod_{k=1, k\neq i,j}^{N} \frac{x_i - x_k}{x_j - x_k} \right) \left(\sum_{l=1, l\neq i,j}^{N} \frac{1}{x_i - x_l} \right), \quad \text{for } i \neq j \\ b_{ii} &= 2 \sum_{k=1, k\neq i}^{N-1} \left(\frac{1}{x_i - x_k} \sum_{l=k+1, l\neq i}^{N} \frac{1}{x_i - x_l} \right) \end{aligned} \tag{1.21}$$

Shu's general approach

Following the same idea of the first order derivative, Shu's general approach is based on polynomial approximation and linear vector space analysis. Two sets of base polynomials are used obtaining

$$b_{ij} = \frac{N^{(2)}(x_i, x_j)}{M^{(1)}(x_j)} \tag{1.22}$$

On the other hand from (1.16) it is obtained

$$\begin{aligned} N^{(2)}(x_i, x_j) &= \frac{M^{(2)}(x_i) - 2N^{(1)}(x_i, x_j)}{x_i - x_j}, \quad \text{for } i \neq j \\ N^{(2)}(x_i, x_i) &= \frac{M^{(3)}(x_i)}{3} \end{aligned} \tag{1.23}$$

Substituting (1.23) into (1.22) yields

$$\begin{aligned} b_{ij} &= \frac{M^{(2)}(x_i) - 2N^{(1)}(x_i, x_j)}{(x_i - x_j) M^{(1)}(x_j)}, \quad \text{for } i \neq j \\ b_{ii} &= \frac{M^{(3)}(x_i)}{3M^{(1)}(x_i)} \end{aligned} \tag{1.24}$$

Finally by substituting the first order weighting coefficients (1.18) into (1.24) the final form of the second order weighting coefficients is obtained

$$b_{ij} = 2a_{ij} \left(a_{ii} - \frac{1}{x_i - x_j} \right), \quad \text{for } i \neq j \tag{1.25}$$

While the computation of the weighting coefficients when $i \neq j$ is easy, on the contrary that is not same when $i = j$, because it involves the third order derivative of $M^{(3)}(x_i)$ which can not be computed easily (1.24). This difficulty can be eliminated by employing the properties of a linear vector space. Similar to the analysis for the case of the first order derivative, the equation system for b_{ij} is derived from the Lagrange interpolation polynomials (a set of base polynomials) is equivalent to that derived from another set of base polynomials x^{k-1}, $k = 1, 2, \ldots, N$. Thus b_{ij} should be also satisfy the following formulation derived from the base polynomial x^{k-1} when $k = 1$

$$\sum_{j=1}^{N} b_{ij} = 0 \quad \text{or} \quad b_{ii} = -\sum_{j=1, j\neq i}^{N} b_{ij} \tag{1.26}$$

For the application of Shu's approach, b_{ij} is firstly computed when $i \neq j$. Subsequently b_{ii} is calculated.

1.3.3 Higher order recurrence formulation

For the discretization of higher order derivatives, the following two linear operators are applied

$$\begin{aligned} f_x^{(m-1)}(x_i) &= \sum_{j=1}^{N} w_{ij}^{(m-1)} f(x_j) \\ f_x^{(m)}(x_i) &= \sum_{j=1}^{N} w_{ij}^{(m)} f(x_j) \\ \text{for } i &= 1, 2, \ldots, N \quad m = 2, 3, , \ldots, N-1 \end{aligned} \tag{1.27}$$

where $f_x^{(m-1)}(x_i)$, $f_x^{(m)}(x_i)$ indicate the $(m-1)$-th and the m-th order derivatives of $f(x)$ with respect to x at x_i. The weighting coefficients related to $f_x^{(m-1)}(x_i)$, $f_x^{(m)}(x_i)$ are w_{ij}^{m-1}, w_{ij}^{m}. Two sets of base polynomials will also be used to derive explicit formulations for $w_{ij}^{(m)}$. The first set of base polynomials is given by (1.14), so substituting that relationship into (1.27) gives

$$\begin{aligned} w_{ij}^{(m-1)} &= \frac{N^{(m-1)}(x_i, x_j)}{M^{(1)}(x_j)} \\ w_{ij}^{(m)} &= \frac{N^{(m)}(x_i, x_j)}{M^{(1)}(x_j)} \end{aligned} \tag{1.28}$$

by rewriting the first of (1.28)

$$N^{(m-1)}(x_i, x_j) = w_{ij}^{(m-1)} M^{(1)}(x_j) \tag{1.29}$$

which is valid for any i and j. From the recurrence formulation (1.16) can be obtained

$$
\begin{aligned}
N^{(m-1)}(x_i, x_j) &= \frac{M^{(m)}(x_i)}{m} \\
N^{(m)}(x_i, x_j) &= \frac{M^{(m)}(x_i) - mN^{(m-1)}(x_i, x_j)}{x_i - x_j}, \quad \text{for } i \neq j \\
N^{(m)}(x_i, x_i) &= \frac{M^{(m+1)}(x_i)}{m+1}
\end{aligned}
\tag{1.30}
$$

Substituting the first of (1.30) into the second of (1.30) leads to

$$
N^{(m)}(x_i, x_j) = \frac{m\left(N^{(m-1)}(x_i, x_i) - N^{(m-1)}(x_i, x_j)\right)}{x_i - x_j}, \quad \text{for } i \neq j \tag{1.31}
$$

which can be further simplified by using (1.29)

$$
N^{(m)}(x_i, x_j) = \frac{m\left(w_{ii}^{(m-1)} N^{(1)}(x_i) - w_{ij}^{(m-1)} N^{(1)}(x_j)\right)}{x_i - x_j}, \quad \text{for } i \neq j \tag{1.32}
$$

Substituting (1.32) into the second of (1.28) and using the recurrence formulation of the first order (1.18) a recurrence formulation is obtained as follows

$$
\begin{aligned}
&w_{ij}^{(m)} = m\left(a_{ij} w_{ii}^{(m-1)} - \frac{w_{ij}^{(m-1)}}{x_i - x_j}\right) \\
&\text{for } i, j = 1, 2, \ldots, N \quad m = 2, 3, \ldots, N-1
\end{aligned}
\tag{1.33}
$$

where a_{ij} is the weighting coefficient of the first order derivative described above. The formulation for $w_{ii}^{(m)}$ can be obtained by substituting the third of (1.30) into the second of (1.28), which gives

$$
\begin{aligned}
&w_{ii}^{(m)} = \frac{M^{(m+1)}(x_i)}{(m+1)M^{(1)}(x_i)} \\
&\text{for } i, j = 1, 2, \ldots, N \quad m = 2, 3, \ldots, N-1
\end{aligned}
\tag{1.34}
$$

Unfortunately this relationship does not give an east expression to evaluate the weighting coefficients $w_{ii}^{(m)}$. Again this difficulty is overcome by the properties of a linear vector space, as it has been done in the previous sections.

$$
\sum_{j=1}^{N} w_{ij}^{(m)} = 0 \quad \text{or} \quad w_{ii}^{(m)} = -\sum_{j=1, j\neq i}^{N} w_{ij}^{(m)} \tag{1.35}
$$

1.4 Multi dimensional case

In the most of practical engineering problems the physical domain under study is two or three dimensional. Thus, it is necessary to extend the DQ approximation from the one dimensional case to the multi dimensional one. In the following section the extension

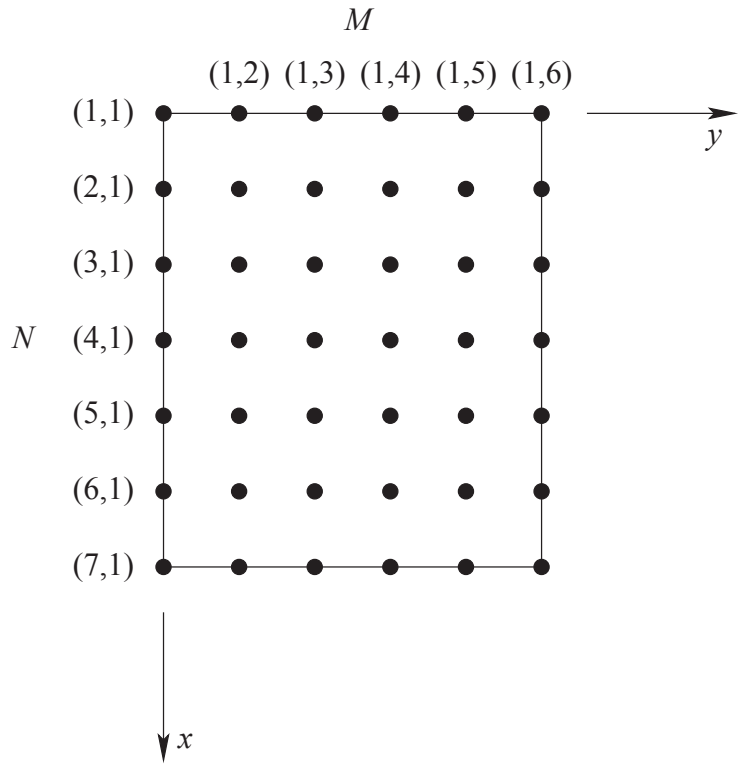

Figure 1.3: Mesh distribution sample on a regular domain.

from the one to the two dimensional case is reported. For the three dimensional problems other works can be used as a reference [10, 41].

The DQ approximation is based on polynomial approximations. Since these kind of functions differ if the domains are regular or irregular the extension of DQ approximation would be quite different in these two cases.

As shown by Shu [20], the one dimensional PDQ formulation can be directly extended to the multi dimensional case if the discretization domain is regular. The regular domain could be a rectangle or other regular shapes such as a circle. Here, for simplicity, a rectangular domain is considered. Consider a two dimensional function $f(x, y)$ defined on a rectangular domain, as shown in Figure 1.3. In the case presented in figure N and M grid points have been chosen along x and y, respectively. In Figure 1.3 $N = 7$ and $M = 6$, so it is not necessary that the two coordinates are discretized with the same amount of points. Hence in a DQ application there can be $N \neq M$.

It has been shown in the previous sections that the DQ derivative of a given function in a fixed point can be written as a function of all the other points in the given domain. In a two dimensional problem two kinds of derivatives can be used. A derivative along a direction line (x or y) and the mixed derivative in which both x and y appear.

In Figure 1.4 a general order derivative along x is graphically presented. The point at which the derivative is calculated is indicated by a cross $f(x_i, y_j)$ and the solid line rectangle represents all the points involved in the computation. When the derivative along x of the function $f(x, y)$ have to be evaluated at the point (x_i, y_j) it is clear that the resultant polynomial expression varies only with the first index i.

On the other hand (see Figure 1.5) the evaluation of a general order derivative along y involves only the index j. In Figure 1.5 the crossed point $f(x_i, y_j)$ reveals where the

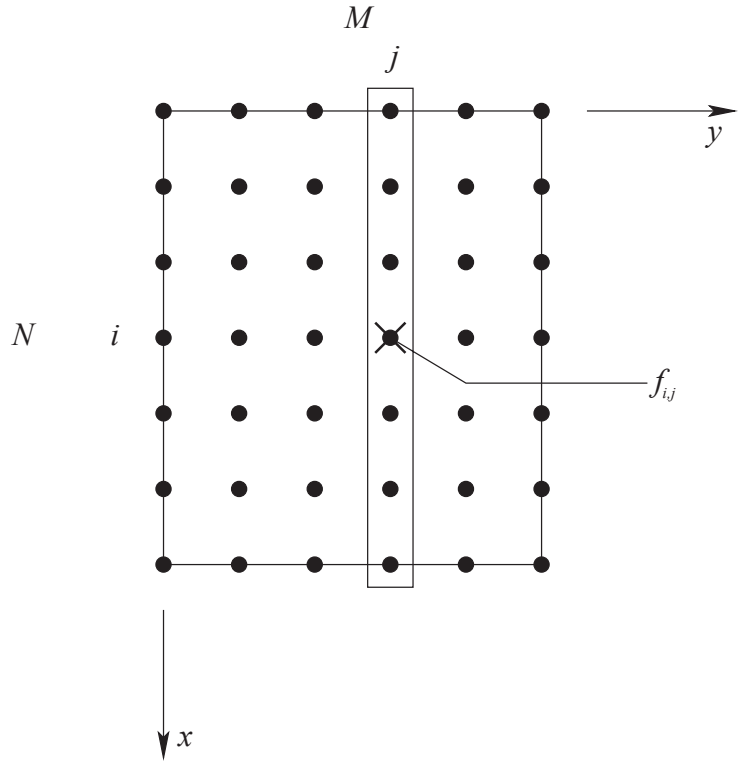

Figure 1.4: Graphical meaning of the derivative along x.

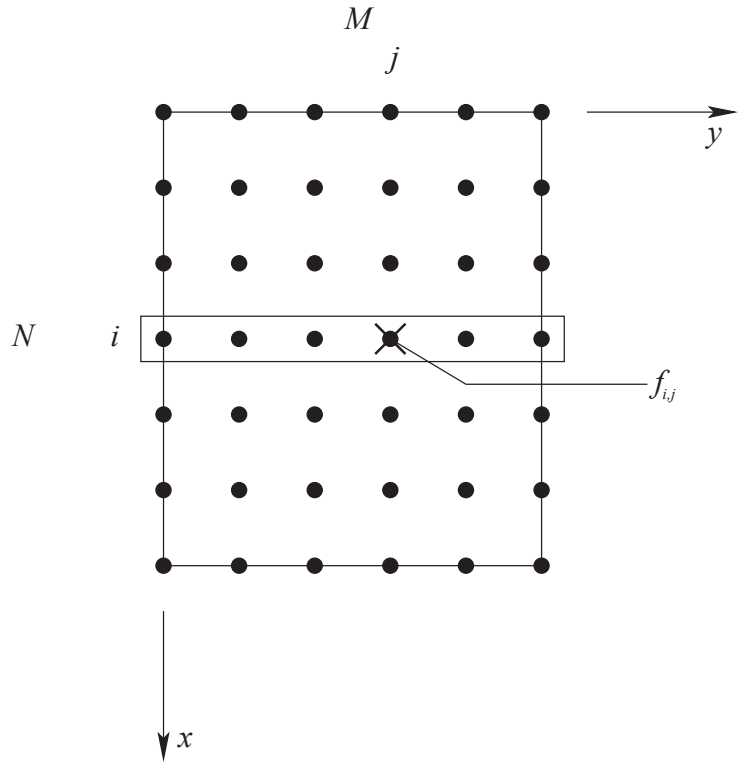

Figure 1.5: Graphical meaning of the derivative along y.

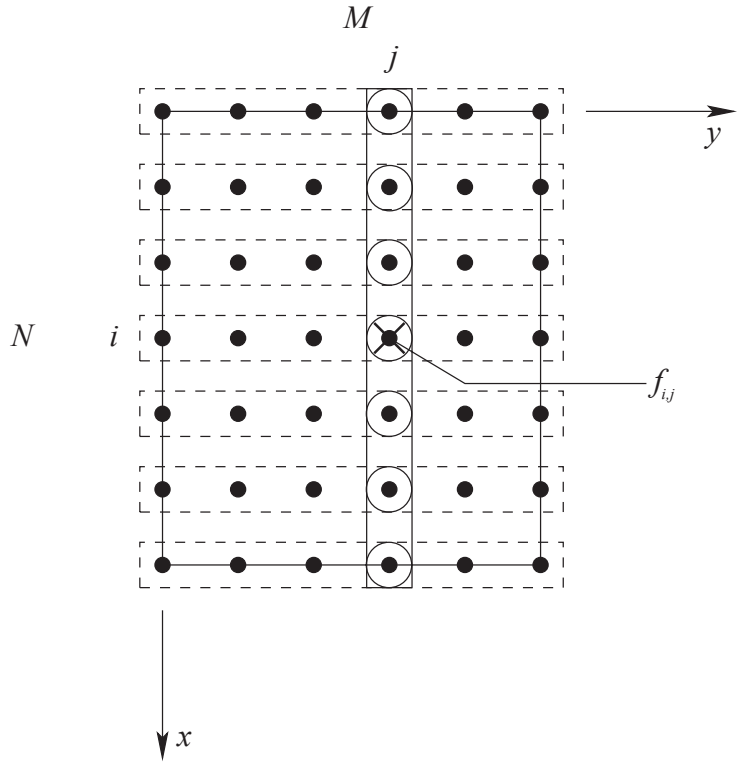

Figure 1.6: Graphical meaning of the mixed derivative.

derivative is calculated and the solid line rectangle represents the points involved in the numerical computation.

Finally when a mixed derivative has to be evaluated the computation involves all the points of the domain. In fact first the derivative takes all the points along one direction (solid rectangular line) and the second derivative needs the other points in the second direction (dashed rectangular lines) for every point of the previous derivative (empty circle points). Following the graphical rules presented in Figures 1.4-1.6 the mathematical expressions of the derivatives along a direction are

$$\begin{aligned} f_x^{(1)}(x_i, y_j) &= \left.\frac{\partial f(x,y)}{\partial x}\right|_{\substack{x=x_i \\ y=y_j}} = \sum_{k=1}^{N} a_{ik} f(x_k, y_j), \quad \text{for } i = 1, 2, \ldots, N \\ f_y^{(1)}(x_i, y_j) &= \left.\frac{\partial f(x,y)}{\partial y}\right|_{\substack{x=x_i \\ y=y_j}} = \sum_{l=1}^{M} \bar{a}_{jl} f(x_i, y_l), \quad \text{for } j = 1, 2, \ldots, M \end{aligned} \tag{1.36}$$

where a_{ik} and $\bar{a}_{jl}$ are the first order weighting coefficient along x and y respectively. It is noted that for a general order derivative the equations can be be written using Shu's notation.

$$
\begin{aligned}
f_x^{(n)}(x_i, y_j) = \left.\frac{\partial^{(n)} f(x,y)}{\partial x^n}\right|_{\substack{x=x_i \\ y=y_j}} &= \sum_{k=1}^{N} w_{ik}^{(n)} f(x_k, y_j) \\
\text{for } i = 1, 2, \ldots, N \;\; n = 1, 2, \ldots, N-1 & \\
f_y^{(m)}(x_i, y_j) = \left.\frac{\partial^{(m)} f(x,y)}{\partial y^m}\right|_{\substack{x=x_i \\ y=y_j}} &= \sum_{l=1}^{M} \bar{w}_{jl}^{(m)} f(x_i, y_l) \\
\text{for } j = 1, 2, \ldots, M \;\; m = 1, 2, \ldots, M-1 &
\end{aligned}
\tag{1.37}
$$

where $w_{ik}^{(n)}$ and $\bar{w}_{jl}^{(m)}$ are the weighting coefficients of order n and m along x and y respectively. Furthermore following the same rule of (1.37) the mixed derivative can be written as follows

$$
\begin{aligned}
f_{xy}^{(n+m)}(x_i, y_j) = \left.\frac{\partial^{(n+m)} f(x,y)}{\partial x^n \partial y^m}\right|_{\substack{x=x_i \\ y=y_j}} &= \sum_{k=1}^{N} w_{ik}^{(n)} \left(\sum_{l=1}^{M} \bar{w}_{jl}^{(m)} f(x_k, y_l) \right) \\
\text{for } i = 1, 2, \ldots, N \;\; j = 1, 2, \ldots, M & \\
\text{for } n = 1, 2, \ldots, N-1 \;\; m = 1, 2, \ldots, M-1 &
\end{aligned}
\tag{1.38}
$$

where $w_{ik}^{(n)}$ and $\bar{w}_{jl}^{(m)}$ have the same meaning of (1.37).

1.4.1 Multi dimensional weighting coefficient matrices

When a one dimensional problem is considered the derivatives that belong to the problem can be written using DQ as the previous sections have shown. The resultant algebraic system of linear equations has got a $N \times N$ dimension, if N is the total number of grid point which have been used to discretize the physical domain (see the next section for further details about grid point distributions).

When a multi dimensional case is considered, using (1.37), (1.38) can result to be not computationally handy. Thus new weighting coefficients matrix form can be defined instead. Starting off Figure 1.7, the main step between the one and two dimensional case is the disposition of the functional values that are written in (1.37), (1.38). For the one dimensional case it is obvious that the functional values vector goes from $f(x_1)$ to $f(x_N)$. However in the two dimensional case the sorting of the functional values can not be defined uniquely. All the numerical results that will be shown in the following chapters for several two dimensional cases, the functional values are stored as depicted in Figure 1.7.

The generic grid point $f(x_i, y_j)$ structure starts from the first column $j = 1$ and $1 \leq i \leq N$ to the last column $j = M$ and $1 \leq i \leq N$. As a result following these rules the (1.37), (1.38) can be rewritten as

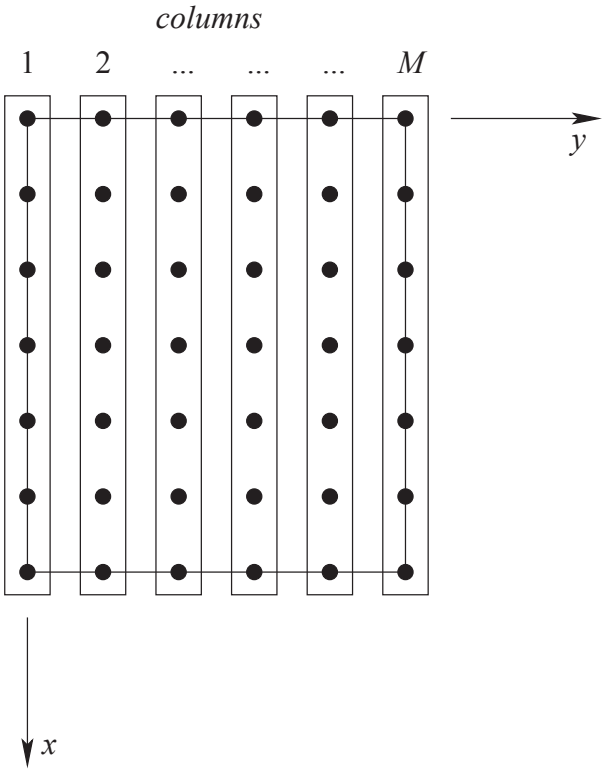

Figure 1.7: Functional values in a two dimensional problem.

$$
\begin{aligned}
\left.\frac{\partial^{(n)} f(x,y)}{\partial x^n}\right|_{\substack{x=x_i \\ y=y_j}} &= \sum_{k=1}^{N} w_{i,k}^{(n)} f(x_k, y_j) = \\
&= w_{i,1}^{(n)} f(x_1, y_j) + w_{i,2}^{(n)} f(x_2, y_j) + \cdots + w_{i,N}^{(n)} f(x_N, y_j) \\
\left.\frac{\partial^{(m)} f(x,y)}{\partial y^m}\right|_{\substack{x=x_i \\ y=y_j}} &= \sum_{l=1}^{M} \bar{w}_{j,l}^{(m)} f(x_i, y_l) = \\
&= \bar{w}_{j,1}^{(m)} f(x_i, y_1) + \bar{w}_{j,2}^{(m)} f(x_i, y_2) + \cdots + \bar{w}_{j,M}^{(m)} f(x_i, y_M) \\
\left.\frac{\partial^{(n+m)} f(x,y)}{\partial x^n \partial y^m}\right|_{\substack{x=x_i \\ y=y_j}} &= \sum_{k=1}^{N} w_{i,k}^{(n)} \left(\sum_{l=1}^{M} \bar{w}_{j,l}^{(m)} f(x_k, y_l) \right) = \\
&= w_{i,1}^{(n)} \left(\bar{w}_{j,1}^{(m)} f(x_1, y_1) + \bar{w}_{j,2}^{(m)} f(x_1, y_2) + \cdots + \bar{w}_{j,M}^{(m)} f(x_1, y_M) \right) + \\
&+ w_{i,2}^{(n)} \left(\bar{w}_{j,1}^{(m)} f(x_2, y_1) + \bar{w}_{j,2}^{(m)} f(x_2, y_2) + \cdots + \bar{w}_{j,M}^{(m)} f(x_2, y_M) \right) + \\
&+ \cdots + \\
&+ w_{i,N}^{(n)} \left(\bar{w}_{j,1}^{(m)} f(x_N, y_1) + \bar{w}_{j,2}^{(m)} f(x_N, y_2) + \cdots + w_{j,M}^{(m)} f(x_N, y_M) \right)
\end{aligned}
\tag{1.39}
$$

So the derivative respect to x is a function of each point along the same column of the point (x_i, y_j) chosen. On the contrary the derivative respect to y is a function of each point along the same row of the point (x_i, y_j) chosen. Finally the mixed derivative is a

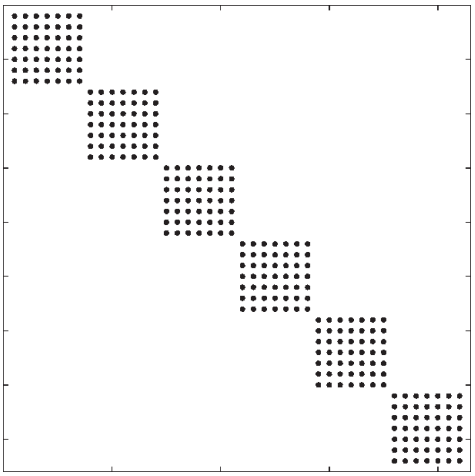

Figure 1.8: Extended matrix derivative along x direction.

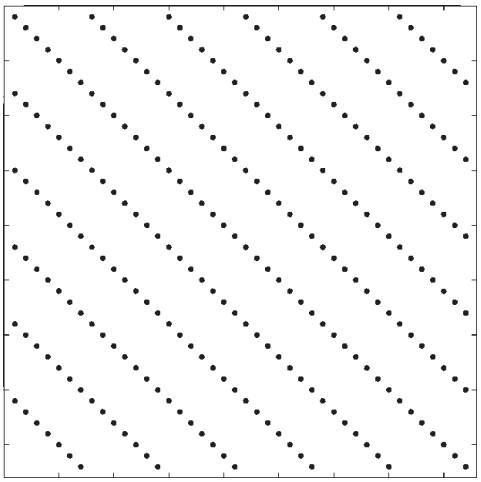

Figure 1.9: Extended matrix derivative along y direction.

function of all the domain points, because for each weighting coefficient $w_{ij}^{(n)}$ there are all the columns multiplied by the coefficients $\bar{w}_{ij}^{(m)}$.

The extended polynomial expressions (1.39) simplify all the algebraic and numerical expressions of the code. Each expression of (1.39) represent a $N\,M \times N\,M$ matrix, because the total number of grid points in a two dimensional problem has got $N\,M$ points. These matrices are general when the functional values order is defined and they are valid for any derivation order. They differ from each other for the inner algebraic structure.

The matrix representing the derivative along x for the whole computational grid is termed $\boldsymbol{\mathcal{W}}_x^{(n)}$, which has got $\mathbf{w}^{(n)}$ matrix on the main diagonal repeated M times as graphically presented in Figure 1.8. In fact each $\mathbf{w}^{(n)}$ matrix depicted in Figure 1.8 has got $N \times N$ dimension. In the particular grid point choice of Figure 1.3 where $N = 7$ and $M = 6$, $\boldsymbol{\mathcal{W}}_x^{(n)}$ is made of six blocks ($M = 6$) of 7×7 $\mathbf{w}^{(n)}$ matrices.

In Figure 1.9 the derivative along y is presented and the matrix is termed $\boldsymbol{\mathcal{W}}_y^{(m)}$ which has got $\bar{\mathbf{w}}^{(m)}$ linearised and put next to each other. In particular each column of $\bar{\mathbf{w}}^{(m)}$ matrix is taken separately. Every column vector is transposed and each component is outdistanced of N spaces in the $\boldsymbol{\mathcal{W}}_y^{(m)}$ matrix line. In other words for the case reported

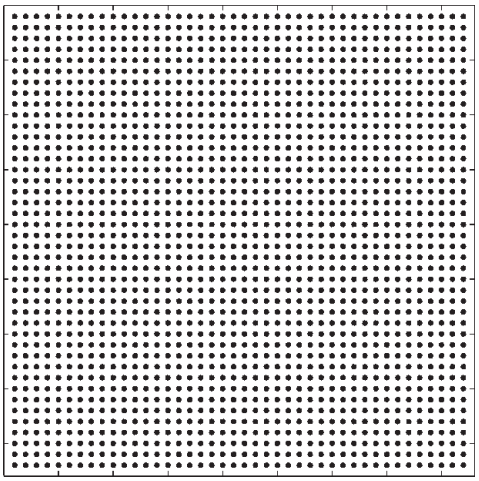

Figure 1.10: Extended matrix for the mixed derivative.

in Figure 1.3, the first line of $\boldsymbol{\mathcal{W}}_y^{(m)}$, see Figure 1.9, has got six bullets ($M = 6$) shifted of seven columns among them. Furthermore the following lines shifts of one column right every row down. So the resultant extended matrix $\boldsymbol{\mathcal{W}}_y^{(m)}$ is graphically represented by a series of diagonal bullets.

In the end the mixed derivative is depicted in Figure 1.10 and, as reported by (1.38), it gets all the grid points of the computational domain. The extended mixed derivative matrix is full, and generally it does not have any zero element whereas $\boldsymbol{\mathcal{W}}_x^{(n)}$ and $\boldsymbol{\mathcal{W}}_y^{(m)}$ have a lot of zero elements. The extended mixed derivative matrix is indicated by $\boldsymbol{\mathcal{W}}_{xy}^{(n+m)}$

1.5 Typical grid point distributions

In the previous sections the main DQ development has been shown. It is noted that (1.37), (1.38) are valid if and only if a discretization procedure is preformed (other than the weighting coefficient computation). The grid point distribution is a fundamental choice of the technique. In fact stability and accuracy strongly depend on the discretization [9, 10, 41]. For the sake of simplicity a one dimensional problem is considered in the following. Starting off a linear domain it can be divided following a equally spaced or a not equally spaced grid (not uniform). It is more often preferred a not uniform grid, due to the fact that DQ gives more accurate results respect to the one with a uniform grid.

A type of discretization must be chosen as roots of an orthogonal polynomial, which can be taken as base vectors of the polynomial vector space. The Jacobi polynomial, defined in a closed interval are used in the DQ method. A not uniform discretization can be chosen as roots of Chebyshev polynomial of the first kind, or the second kind or of the Legendre polynomial. Thus all these kinds of discretization belong to the orthogonal polynomial category.

The most used grid distribution in literature is the Chebyshev-Gauss-Lobatto. In this kind of discretization the location of the nodal points is defined with a cosine function (not uniform discretization). However it will be shown in this PhD Thesis that the roots of the Legendre polynomial gives the best results for the method developed in this study. Another not uniform discretization is given by the quadratic grid point distribution. It should be also noted that the uniform discretization leads to not accurate and not stable

numerical results, due to the ill conditioned weighting coefficient matrices when N and M increase.

If N are the number of points along the one dimensional domain under study. For the sake of generality the domain is considered dimensionless $a \leq x \leq b \rightarrow 0 \leq \xi \leq 1$, when $\xi = (x-a)/L$ and $L = b - a$ that is the length of the closed interval $[a, b]$.

- **Uniform grid distribution**

$$\xi_k = \frac{k-1}{N-1}, \quad k = 1, 2, \ldots, N \tag{1.40}$$

- **Chebyshev-Gauss-Lobatto grid distribution**

$$\xi_k = \frac{1}{2}\left(1 - \cos\left(\frac{k-1}{N-1}\pi\right)\right), \quad k = 1, 2, \ldots, N \tag{1.41}$$

- **Quadratic discretization**

$$\begin{cases} \xi_k = 2\left(\dfrac{k-1}{N-1}\right)^2, & k = 1, 2, \ldots, \frac{N+1}{2} \\ \xi_k = -2\left(\dfrac{k-1}{N-1}\right)^2 + 4\left(\dfrac{k-1}{N-1}\right) - 1, & k = \frac{N+1}{2} + 1, \ldots, N-1, N \end{cases} \tag{1.42}$$

- **Roots of the Chebyshev polynomial of the first kind**

$$\xi_k = \frac{r_k - r_1}{r_N - r_1}, \;\; r_k = \cos\left(\frac{2k-1}{2N}\pi\right), \;\; k = 1, 2, \ldots, N \tag{1.43}$$

- **Roots of the Chebyshev polynomial of the second kind**

$$\xi_k = \frac{r_k - r_1}{r_N - r_1}, \;\; r_k = \cos\left(\frac{k}{N+1}\pi\right), \;\; k = 1, 2, \ldots, N \tag{1.44}$$

- **Roots of the Legendre polynomial**

$$\xi_k = \frac{r_k - r_1}{r_N - r_1}, \;\; r_k = \left(1 - \frac{1}{8N^2} + \frac{1}{8N^3}\right)\cos\left(\frac{4k-1}{4N+2}\pi\right), \;\; k = 1, 2, \ldots, N \tag{1.45}$$

It should be noted that the last three discretizations use the roots of some orthogonal polynomial as reference points in the grid.

All these distributions can be used in the multi dimensional case, even though they have been defined for a one dimensional problem. In addition to the previous discretizations it is possible to define other grids in which the points are more or less refined as a function of a parameter. This technique is called stretching formulation. It is possible to relocate the grid points of a standard grid as follows

$$\zeta_k = (1-\alpha)\left(3\xi_k^2 - 2\xi_k^3\right) + \alpha\xi_k, \quad k = 1, 2, \ldots, N \tag{1.46}$$

where α is the stretching parameter. It is noted that for $\alpha = 1 \Rightarrow \zeta_k = \xi_k$. When $\alpha < 0$ some nodal values can go beyond the initial closed interval $[a, b]$. In order to avoid this inconvenience, the grid points near the domain boundaries must satisfy the following relations

$$\zeta_k < 0, \quad \zeta_{k+1} > 0, \quad k = 1, 2, \ldots, \frac{N+1}{2} \tag{1.47}$$

and they are redefined as

$$\zeta_k = \beta\zeta_{k+1}, \quad \zeta_{N-k+1} = 1 - \zeta_k \tag{1.48}$$

where β is a positive constant that must verify the condition: $\zeta_k - \zeta_{k-1} < \zeta_{k+1} - \zeta_k$. Frequently $\beta = 0.1$. Applying this kind of discretization it is possible to arbitrary refine ($\alpha < 1$) or clear ($\alpha > 1$) the grid points of any boundary mesh.

1.6 Solution techniques

In most applications of the DQ method to engineering problems, which are governed by time-dependent partial differential equations (PDEs), the spatial derivatives are discretized by the DQ method whereas the time derivatives are discretized by low order finite difference schemes. For the general case a time dependent PDE is considered as follows

$$\ell(u(\mathbf{x}, t)) + q(\mathbf{x}, t) = \frac{\partial^2 u(\mathbf{x}, t)}{\partial t^2} \tag{1.49}$$

where $\ell(u)$ is a differential operator containing all the spatial derivatives and q is a given function. The configuration variable u depends on space $\mathbf{x}$ and time t. The problem (1.49) should be specified with proper initial and boundary conditions for the solution. By using DQ method to discretize the spatial derivatives in the differential operator $\ell(u)$ and applying the (1.49) at all interior grid points, a set of ordinary differential equations (ODEs) is obtained

$$\mathcal{L}\mathbf{U} + \mathbf{Q} = \frac{d^2\mathbf{U}}{dt^2} \tag{1.50}$$

where $\mathbf{U}$ is a vector representing a set of unknown functional values at all the interior points, $\mathcal{L}$ is a matrix resulting from the DQ discretization and $\mathbf{Q}$ is a known vector arising from the function q and the given initial and boundary conditions.

In this PhD Thesis static and dynamic engineering problems are solved. It must be underlined that the dynamic process investigated here is related to free vibrations only. As a result the dynamic equilibrium equations of a system is transformed into a linear eigenvalue problem through the variable separation process

$$u(\mathbf{x}, t) = U(\mathbf{x})e^{i\lambda t} \tag{1.51}$$

substituting (1.51) into (1.49), considering $q = 0$ a linear eigenvalue problem is obtained

$$\ell(U(\mathbf{x})) + \lambda^2 U(\mathbf{x}) = 0 \tag{1.52}$$

after the discretization of (1.52) the eigenvalues λ^2 and the eigenvectors U of the problem can be found, in a discrete form (1.52) becomes

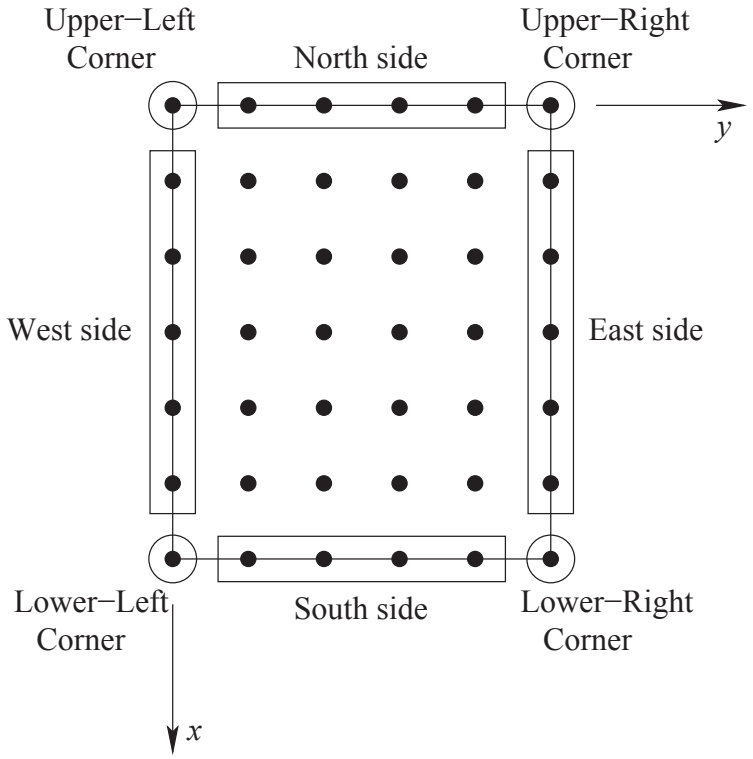

Figure 1.11: Boundary points of a rectangular DQ discretized domain.

$$\mathcal{L}\mathbf{U} + \lambda^2\mathbf{U} = \mathbf{0} \tag{1.53}$$

On the contrary when a static analysis is performed the configuration variable does not depend on time $u(\mathbf{x}, t) = u(\mathbf{x})$ and the (1.49) becomes

$$\ell(u(\mathbf{x})) + q(\mathbf{x}) = 0 \tag{1.54}$$

that in discrete form becomes

$$\mathcal{L}\mathbf{U} + \mathbf{Q} = 0 \tag{1.55}$$

The linear algebraic systems (1.53) and (1.55), obtained by using DQ rule, can not be solved directly because the boundary conditions have not been introduced yet.

1.6.1 Boundary condition implementation

A proper implementation of the boundary conditions is very important for accurate and stable numerical solution of ODEs (1.53), (1.55). It has been widely shown in literature that the DQ discretization of the boundary conditions leads to accurate and stable results [9, 10, 41]. According to mathematics, in any PDE at least two kinds of boundary conditions exist: the Dirichlet condition and the Neumann condition. The first is a condition on the configuration variable, $u(\bar{\mathbf{x}}, t) = c_1$, and the second one is a condition on the derivative of the configuration variable $u'(\bar{\mathbf{x}}, t) = c_2$. In the previous cases c_1 and c_2 are two arbitrary constants and $\bar{\mathbf{x}}$ represents the coordinates of the domain boundary. It is underlined that in all the problems developed in this PhD Thesis the number of boundary

conditions are always equal to the number of degrees of freedom per point, so there is no need of implementing any mixed condition (the same conditions that have to be used in the Euler-Bernoulli beam and in the Kirchhoff-Love plate for example) which would lead to a complex implementation of the technique [9, 10, 41].

In Figure 1.11 the boundary points for a rectangular discretized DQ domain is presented. Since either Dirichlet or Neumann boundary conditions can be implemented four sides and four corners should be considered. Considering the plane reference system x-y the four sides can be named as the four cardinal directions: west and east edges for the sides of normal y and north and south for the sides of normal x. It is compulsory to separate the corner points from the sides because they have separate boundary conditions depending on the boundary conditions of the neighbouring sides. In fact the Upper-Left corner (UL corner) conditions depend on the Dirichlet and Neumann conditions of the west and north side, the Upper-Right corner (UR corner) conditions depend on the north and east sides, the Lower-Right corner (LL corner) conditions depend on the west and south sides, finally the Lower-Right corner (LR corner) conditions depend on the east and south conditions.

It can be noticed from Figure 1.11 that if a DQ discretized domain is composed of $N\,M$ grid points: there are $(N-2)(M-2)$ domain points and $2N+2(M-2)$ boundary points (sides plus corners). It will be shown in the next section that when more complex problems are studied the boundary conditions play a fundamental role for the solution of the algebraic system.

1.6.2 Solving the discretized problems

Since the discretized systems of equations obtained via DQ method (1.55), (1.53) after the imposition of the boundary conditions are linear, the linear algebra rules can be applied as follows. In structural mechanics the linear algebraic operator $\mathcal{L}$ used in (1.55), (1.53) is called stiffness matrix and it is generally indicated $\mathbf{K}_t$, which is the stiffness matrix of the whole system. In particular

$$\mathbf{K}_t = \begin{bmatrix} \mathbf{K}_{bb} & \mathbf{K}_{bd} \\ \mathbf{K}_{db} & \mathbf{K}_{dd} \end{bmatrix} \tag{1.56}$$

where all the boundary conditions are written in the first couple of matrices $\mathbf{K}_{bb}$ and $\mathbf{K}_{bd}$, whereas the domain equations are written in $\mathbf{K}_{db}$ and $\mathbf{K}_{dd}$. As a result the static solution (1.55) of a generic structural model can be found as

$$\begin{bmatrix} \mathbf{K}_{bb} & \mathbf{K}_{bd} \\ \mathbf{K}_{db} & \mathbf{K}_{dd} \end{bmatrix} \begin{bmatrix} \mathbf{U}_b \\ \mathbf{U}_d \end{bmatrix} + \begin{bmatrix} \mathbf{Q}_b \\ \mathbf{Q}_d \end{bmatrix} = \begin{bmatrix} \mathbf{0} \\ \mathbf{0} \end{bmatrix} \tag{1.57}$$

where $\mathbf{U}_b$, $\mathbf{U}_d$ are the displacements on the boundary and domain points respectively, and $\mathbf{Q}_b$, $\mathbf{Q}_d$ are the external forces, the first represent the reaction forces of the boundaries and the second stands for the external loads. Thus with reference to the algebraic structure (1.57) the static condensation of the variables can be performed in order to improve the numerical performance. From the first set of equations the boundary displacements can be found as a function of the domain displacements

$$\mathbf{U}_b = -\mathbf{K}_{bb}^{-1}\mathbf{K}_{bd}\mathbf{U}_d - \mathbf{K}_{bb}^{-1}\mathbf{Q}_b \tag{1.58}$$

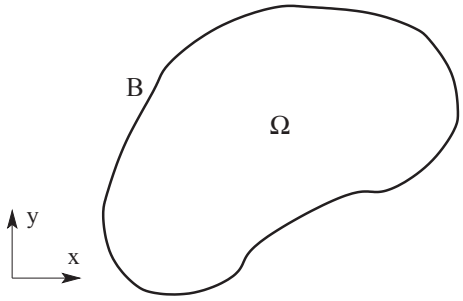

Figure 1.12: Generic plane domain of boundary B and internal domain Ω.

Substituting (1.58) into the second set of equations of (1.57) the solution system can be written

$$\left(\mathbf{K}_{dd} - \mathbf{K}_{db}\mathbf{K}_{bb}^{-1}\mathbf{K}_{bd}\right)\mathbf{U}_d = \mathbf{K}_{db}\mathbf{K}_{bb}^{-1}\mathbf{Q}_b - \mathbf{Q}_d \tag{1.59}$$

Once the linear algebraic system (1.59) in terms of domain displacements, the boundary displacements can be found using (1.58) where now $\mathbf{U}_d$ is not an unknown vector any more.

Analogously for the dynamic case (1.53) the condensation can be applied to the eigenvalue problem also. However the external load vector is considered null, $\mathbf{Q} = \mathbf{0}$. As it is very well known by linear algebra an eigenvalue problem can be solved by

$$\left(\mathbf{K}_t + \lambda^2\mathbf{M}\right)\mathbf{U} = \mathbf{0} \tag{1.60}$$

where $\mathbf{M}$ is the mass matrix of a structural system, λ^2 are the eigenvalues and $\mathbf{U}$ represent the eigenvectors of the problem under study. In structural mechanics the mass matrix $\mathbf{M}$ represent the inertia forces of a mechanical system, nevertheless the boundary of the physical domain do not attend into the equation of motion so

$$\begin{bmatrix}\mathbf{K}_{bb} & \mathbf{K}_{bd}\\ \mathbf{K}_{db} & \mathbf{K}_{dd}\end{bmatrix}\begin{bmatrix}\mathbf{U}_b\\ \mathbf{U}_d\end{bmatrix} + \lambda^2\begin{bmatrix}\mathbf{0} & \mathbf{0}\\ \mathbf{0} & \mathbf{M}_{dd}\end{bmatrix}\begin{bmatrix}\mathbf{U}_b\\ \mathbf{U}_d\end{bmatrix} = \begin{bmatrix}\mathbf{0}\\ \mathbf{0}\end{bmatrix} \tag{1.61}$$

The static condensation can be performed in (1.61) by using (1.58), imposing $\mathbf{Q} = \mathbf{0}$. The linear eigenvalue problem becomes

$$\left(\mathbf{K}_{dd} - \mathbf{K}_{db}\mathbf{K}_{bb}^{-1}\mathbf{K}_{bd} + \lambda^2\mathbf{M}_{dd}\right)\mathbf{U}_d = \mathbf{0} \tag{1.62}$$

1.7 Multi-domain differential quadrature

In the previous sections the applications of the DQ method for solving simple domains have been described. The DQ method discretizes the derivatives along a straight line. Thus, it requires the computational domain to be regular so that the physical boundary could be a mesh line. If the physical boundary is generally curved, the DQ method can not be directly applied. There are two basic approaches to overcome this difficulty. The first is called the multi-domain DQ approach, in which the whole domain is decomposed into several regular sub-domains and the DQ discretization is applied locally upon each sub-domain. The other follows the coordinate transformation approach. In the latter, the irregular physical domain in the Cartesian coordinate system is transformed into a regular

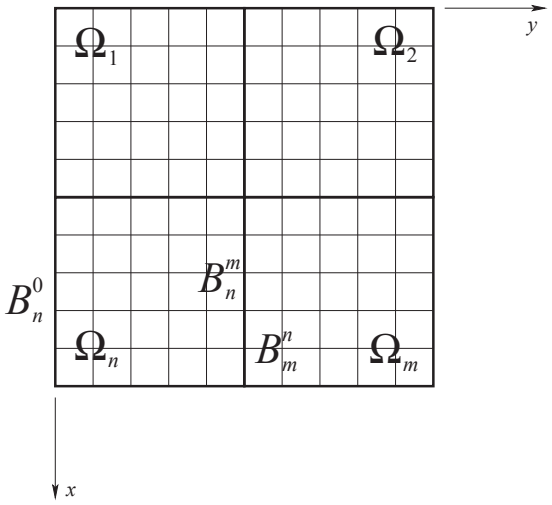

Figure 1.13: Generic multi-domain decomposition using regular elements.

domain. So it becomes similar to the very well-known Finite Element FE method. The big difference between the DQ applied to irregular domains and the FE method is that the equations are solved in their strong form and the connections between the elements are imposed with the inter-element compatibility conditions. In this section the multi-domain technique is firstly explained and than the irregular multi-domain method will be shown in the following section.

1.7.1 General aspects of the technique

The domain decomposition technique was firstly introduced by Shu [20] to simulate incompressible flows past a backward facing step and a square step. In the past decades many authors [11, 22–25, 28, 30–35] apply this technique to several problems. All over the years researchers have been used different definitions to name this advanced DQ technique: multi-domain technique, quadrature element method, etc. In this PhD Thesis are all used as synonyms but the main term is Generalized Differential Quadrature Finite Element Method (GDQFEM). The technique is called 'Generalized' because it is based on the DQ rule of Shu [9], who was the first to define a general formulation of the weighting coefficients definition. Moreover the 'Finite Element' is introduced because, as it will be shown in the following chapters, the implemented code make one do a general shape computational domain to solve several engineering problems, without defining a priori any geometric limit to the element shapes, like the standard FE methodology.

Considering a generic physical domain, Figure 1.12, of a general shape that can be represented by Ω with a continuous boundary B. The multi-domain technique firstly decomposes the domain Ω into several sub-domains Ω_n, $n = 1, 2, n_e$, where n_e is the total number of sub-domains, as presented in Figure 1.13. For the sake of simplicity, the sub-domains can be called elements also, by analogy with the FE method. Over each sub-domain Ω_n a local discretization is performed and a local DQ technique is applied in the same manner as the application of DQ in a single domain problem. It is underlined that every sub-domain is disjoint to each other, that is $\Omega_n \cap \Omega_m = \emptyset$ if $n \neq m$, where $\emptyset$ is the empty set. It is also noted that $\Omega = \Omega_1 \cup \Omega_2 \cup \Omega_{n_e}$. The decomposition of the domain into several sub-domains should follow the general guidelines that the physical constants

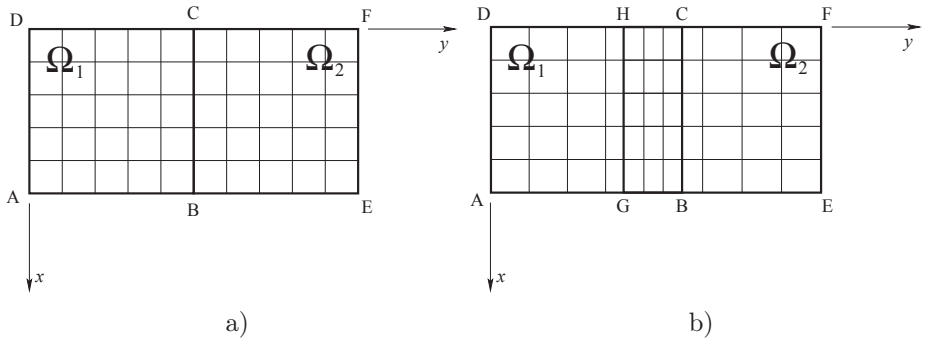

Figure 1.14: The two kinds of interface topology: a) patched, b) overlapped.

in each sub-domain such as material constants, density and thickness are kept constant.

The information exchange between neighbouring sub-domains is conducted through the interface. The solutions for the interior grid points are independent for each sub-domain. Globally, the information exchange between sub-domains is required. This can be achieved across the interface boundaries of the sub-domains. Since any complex geometry can be transformed into a rectangular domain or combination of rectangular sub-domains, a rectangular domain is chosen for demonstration without loss of generality. Basically, there are two kinds of interface topology: patched and overlapped. The second one considers two sub-domains that have an overlapping area which is needed to exchange information between the two elements, in fact the boundary points of one element should be related to the interior points of the second element. Considering Figure 1.14b the sub-domain ABCD is overlapped with sub-domain GEFH. It is noted that the right boundary of the subdomain Ω_1, BC, is in the interior of sub-domain Ω_2, and the left boundary of sub-domain Ω_2, GH, is in the interior of sub-domain Ω_1. On the other hand, the patched interface topology that is applied also in this PhD Thesis is based on the enforcing of the continuity conditions between the two given elements. For the patched interface, the governing equation is not applied along the interface. Instead, the continuity condition is enforced. The common approach is to let the function and its normal derivative be continuous across the interface. In other words, the function is considered as $\mathcal{C}^1$ continuous across the interface. In detail two different kinds of boundary conditions are indicated B_n^0 and B_n^m in Figure 1.13. The first condition is an external boundary condition. The second one is related to the inter-element boundary condition, that in this case is treated as a patched interface.

A generic interface (Figure 1.13) of each sub-domain has got two types of boundaries: an external boundary condition B_n^0 and a connectivity boundary condition B_n^m (interface), which is the boundary between element n and m, for $n \neq m$. It should be noted that B_n^m and B_m^n are two different compatibility conditions. A compatibility condition must have a kinematic relation (on the displacements) and a static one (on the stresses), so two boundary relations are needed in order to connect the two sub-domains properly. In other words if the kinematic relations are written on the edge B_n^m, the corresponding static relations must be written on the B_m^n edge. In fact the information exchange between neighbouring sub-domains is conducted through the interfaces. Whereas the boundary conditions on B_n^0 can be treated in the same way as in the single domain GDQ approach. On the generic interface B_n^m care must be taken to properly treat boundary conditions. The boundary conditions on the interfaces, called compatibility conditions, are imposed within two rela-

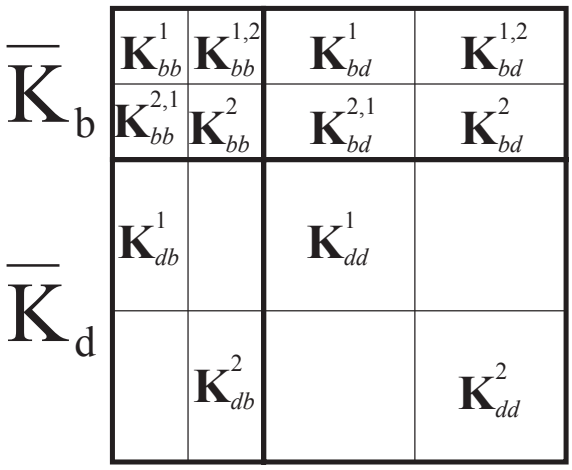

Figure 1.15: Total stiffness matrix multi-domain structure.

tions. In the first one, the displacements calculated from the two neighbouring domains are set equal $U_n = U_m$, where U is one of the generalized displacements of the model. In the second set of equations, the tension at the interfaces are set equal $S_n = S_m$, where S is one of the generalized stress components taken by the external boundary condition of the mathematical mode.

The main idea of the multi-domain GDQ technique is to assembly a system like the algebraic one (1.56), following the physical approach for each sub-domain. For instance let us consider a rectangular plate composed of two sub-domains. As shown in Figure 1.14a the two neighbouring sub-domains are overlapped by one grid points line, along the line BC. It is noted that the right boundary of the sub-domain Ω_1 is connected to the left boundary of the sub-domain Ω_2. Therefore, the first condition B_1^2 is written as a kinematic condition between the two boundaries and the second one B_2^1 is written as a static condition on that edge. Whereas in each sub-domain the governing equations are discretized at all interior points and they are completely independent. Following the structure of equation (1.56) a total stiffness system is written for the multi-domain approach. It is clear that the global system must be in the same form

$$\mathbf{K}_t = \begin{bmatrix} \bar{\mathbf{K}}_{bb} & \bar{\mathbf{K}}_{bd} \\ \bar{\mathbf{K}}_{db} & \bar{\mathbf{K}}_{dd} \end{bmatrix} \tag{1.63}$$

where each stiffness matrix $\bar{\mathbf{K}}$ is composed as a function of the two sub-domains in different manners. The external and internal (compatibility) equations are written in $\bar{\mathbf{K}}_{bb}$ and $\bar{\mathbf{K}}_{bd}$, whereas the internal domain equations are written in $\bar{\mathbf{K}}_{db}$ and $\bar{\mathbf{K}}_{dd}$. Starting off Figure 1.15 the matrix structure will be explained below. It is clear that the domain relations are independent between the elements, in fact $\bar{\mathbf{K}}_{db}$ and $\bar{\mathbf{K}}_{dd}$ fill only the diagonal areas of the total stiffness matrix and they have zeros out of the main diagonal, because the internal points of each element are not related to the neighbouring elements. On the contrary the bounded part contains not only external boundary conditions $\mathbf{K}_b^n$ and $\mathbf{K}_b^m$ but connectivity relations $\mathbf{K}_b^{n,m}$ and $\mathbf{K}_b^{m,n}$ as well. The $\bar{\mathbf{M}}_{dd}$ do not change respect to the single domain case because the inertia terms lead to the domain points only. This is in agreement with what it has been proposed in (1.63). This will also be validated by numerical examples given in the following.

It must be underlined that if the sub-domain boundaries are not parallel to the exter-

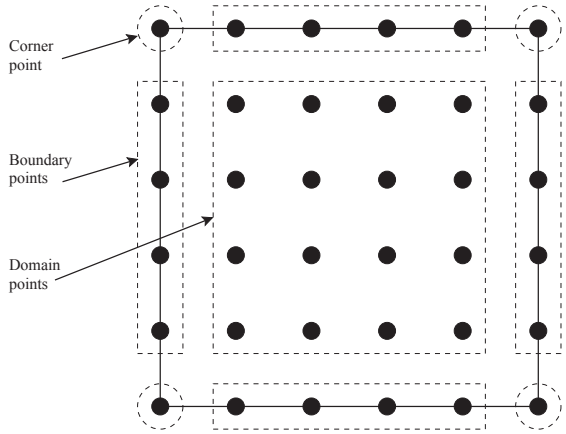

Figure 1.16: Differential quadrature finite element topology.

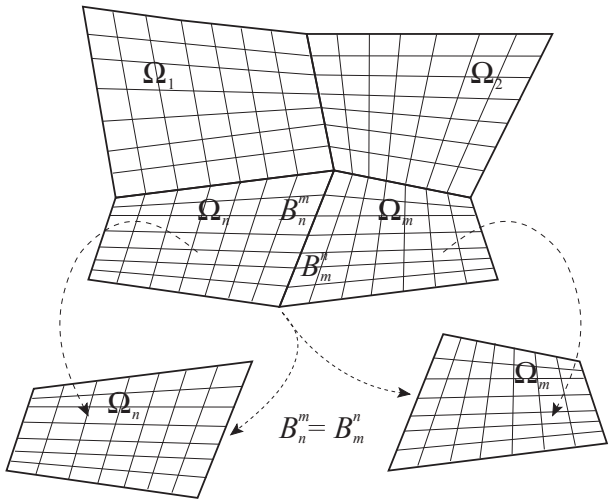

Figure 1.17: Computational domain decomposition for an arbitrarily shaped problem.

nal reference system, irregular sub-domain decomposition is needed, nevertheless further details will be given in the following.

For the sake of completeness in Figure 1.16 a sample domain DQ finite element is represented. Obviously the generic element follows the same computational scheme depicted in Figure 1.11 which has been used in standard DQ technique. The general element is composed of three different groups of points: the domain points used for the fundamental equations implementation, the boundary points along the element sides are used for the imposition of boundary conditions, external and internal (compatibility conditions), finally the corner points that must follow some special rules. The main issue of the Generalized Differential Quadrature Finite Element Method (GDQFEM) are the implementation of the boundary conditions and in particular of the inter-element conditions. However the numerical implementation of the GDQFEM concerning the boundary conditions will be explained in the following.

1.7.2 Mapping technique for irregular domains

When the domain subdivision is made by only regular (e.g. rectangular) elements, the boundaries of each sub-domain are parallel to the external Cartesian system (Figure 1.13). It follows that local GDQ scheme can be applied directly to each sub-domain in the same manner as the single domain. In a multi-domain DQ approach applied to arbitrarily shaped structures the computational domain is divided into a certain number of sub-domains, as depicted in Figure 1.17, according to the problem geometry [11, 36]. In this case coordinate transformation is needed to map the irregular domains into a square computational domain in the natural coordinates. The same technique is applied in classic FE analysis. The all set of differential equations: fundamental equation, boundary conditions and compatibility conditions are transformed into the natural coordinate system. Consequently all the computations are performed in the rectangular computational domain, as reported in Figure 1.16. Furthermore applying this methodology it is possible to consider several inhomogeneities, such as irregular boundaries, different materials and mixed boundary conditions in the problem under study.

Coordinate transformation is used to transform the irregular sub-domains in the Cartesian x-y plane to a square computational domain in the natural coordinate ξ-η by using the following equations

$$x = x(\xi, \eta), \qquad y = y(\xi, \eta) \tag{1.64}$$

In literature the (1.64) is very well known as mapping technique. In fact the same method is used in the FE method to map any finite element. All the spacial derivatives of the configuration variables of the problem have to be mapped to the new coordinate system ξ-η (computational domain). Since DQ method solves directly the strong form of any engineering problem the configuration variable for all the cases under study in this PhD Thesis are the structure displacements.

The first order derivatives of an arbitrary function defined in the Cartesian x-y plane with respect to x and y, are given by

$$\begin{aligned} \frac{\partial}{\partial x} &= \frac{\partial}{\partial \xi}\frac{\partial \xi}{\partial x} + \frac{\partial}{\partial \eta}\frac{\partial \eta}{\partial x} = \frac{\partial}{\partial \xi}\xi_x + \frac{\partial}{\partial \eta}\eta_x \\ \frac{\partial}{\partial y} &= \frac{\partial}{\partial \xi}\frac{\partial \xi}{\partial y} + \frac{\partial}{\partial \eta}\frac{\partial \eta}{\partial y} = \frac{\partial}{\partial \xi}\xi_y + \frac{\partial}{\partial \eta}\eta_y \end{aligned} \tag{1.65}$$

where ξ_x, η_x, ξ_y, η_y are the first order derivatives of ξ and η with respect to x and y respectively.

The second order derivatives of a function can be derived from (1.65) as

$$\begin{aligned} \frac{\partial^2}{\partial x^2} &= \frac{\partial}{\partial x}\frac{\partial}{\partial x} = \xi_x^2\frac{\partial^2}{\partial \xi^2} + \eta_x^2\frac{\partial^2}{\partial \eta^2} + 2\xi_x\eta_x\frac{\partial^2}{\partial \xi \partial \eta} + \xi_{xx}\frac{\partial}{\partial \xi} + \eta_{xx}\frac{\partial}{\partial \eta} \\ \frac{\partial^2}{\partial y^2} &= \frac{\partial}{\partial y}\frac{\partial}{\partial y} = \xi_y^2\frac{\partial^2}{\partial \xi^2} + \eta_y^2\frac{\partial^2}{\partial \eta^2} + 2\xi_y\eta_y\frac{\partial^2}{\partial \xi \partial \eta} + \xi_{yy}\frac{\partial}{\partial \xi} + \eta_{yy}\frac{\partial}{\partial \eta} \\ \frac{\partial^2}{\partial x \partial y} &= \frac{\partial}{\partial x}\frac{\partial}{\partial y} = \xi_x\xi_y\frac{\partial^2}{\partial \xi^2} + \eta_x\eta_y\frac{\partial^2}{\partial \eta^2} + (\xi_x\eta_y + \xi_y\eta_x)\frac{\partial^2}{\partial \xi \partial \eta} + \xi_{xy}\frac{\partial}{\partial \xi} + \eta_{xy}\frac{\partial}{\partial \eta} \end{aligned} \tag{1.66}$$

The mapping of a sub-domain from the initial configuration to the current configuration is performed using an approximate deformation map. The deformation gradient

$\mathbf{F}_n$ is used to perform the mapping technique upon a generic sub-domain Ω_n [11]. It is noted that the mapping procedure is the discrete version of the continuum mechanical description of the motion of a body. The deformation gradient is related to the Jacobian matrix which can be obtained directly from (1.65).

$$\begin{bmatrix} \frac{\partial}{\partial x} \\ \frac{\partial}{\partial y} \end{bmatrix} = \begin{bmatrix} \xi_x & \eta_x \\ \xi_y & \eta_y \end{bmatrix} \begin{bmatrix} \frac{\partial}{\partial \xi} \\ \frac{\partial}{\partial \eta} \end{bmatrix} = \mathbf{J}^{-1} \begin{bmatrix} \frac{\partial}{\partial \xi} \\ \frac{\partial}{\partial \eta} \end{bmatrix} \tag{1.67}$$

The above 2×2 matrix denoted by $\mathbf{J}^{-1}$ is the inverse of Jacobian matrix of the transformation $\mathbf{J}$ defined as

$$\mathbf{J} = \begin{bmatrix} x_\xi & y_\xi \\ x_\eta & y_\eta \end{bmatrix} \tag{1.68}$$

From (1.68) it is possible to obtain the inverse matrix of Jacobian as

$$\mathbf{J}^{-1} = \frac{1}{\det \mathbf{J}} \begin{bmatrix} y_\eta & -y_\xi \\ -x_\eta & x_\xi \end{bmatrix}, \qquad \det \mathbf{J} = x_\xi y_\eta - x_\eta y_\xi \tag{1.69}$$

where $\det \mathbf{J}$ is the determinant of the Jacobian.

Comparing the inverse matrix of Jacobian in (1.69) with that in (1.67), the following relationships are obtained

$$\begin{aligned} \xi_x &= \frac{y_\eta}{\det \mathbf{J}}, & \xi_y &= -\frac{x_\eta}{\det \mathbf{J}} \\ \eta_x &= -\frac{y_\xi}{\det \mathbf{J}}, & \eta_y &= \frac{x_\xi}{\det \mathbf{J}} \end{aligned} \tag{1.70}$$

The substitution of (1.70) into (1.65) yields

$$\begin{aligned} \frac{\partial}{\partial x} &= \frac{1}{\det \mathbf{J}} \left(y_\eta \frac{\partial}{\partial \xi} - y_\xi \frac{\partial}{\partial \eta} \right) \\ \frac{\partial}{\partial y} &= \frac{1}{\det \mathbf{J}} \left(-x_\eta \frac{\partial}{\partial \xi} + x_\xi \frac{\partial}{\partial \eta} \right) \end{aligned} \tag{1.71}$$

Then, the second order derivatives of ξ with respect to x and y can be expressed as

$$\begin{aligned} \frac{\partial^2 \xi}{\partial x^2} &= \frac{\partial}{\partial x} \left(\frac{\partial \xi}{\partial x} \right) = \frac{\partial}{\partial x}(\xi_x) = \frac{1}{\det \mathbf{J}} \left(y_\eta \frac{\partial}{\partial \xi} - y_\xi \frac{\partial}{\partial \eta} \right) \left(\frac{y_\eta}{\det \mathbf{J}} \right) = \\ &= \frac{1}{\det \mathbf{J}^2} \left(y_\eta y_{\xi\eta} - \frac{y_\eta^2}{\det \mathbf{J}} \det \mathbf{J}_\xi - y_\xi y_{\eta\eta} + \frac{y_\xi y_\eta}{\det \mathbf{J}} \det \mathbf{J}_\eta \right) \\ \frac{\partial^2 \xi}{\partial y^2} &= \frac{\partial}{\partial y} \left(\frac{\partial \xi}{\partial y} \right) = \frac{\partial}{\partial y}(\xi_y) = \frac{1}{\det \mathbf{J}} \left(-x_\eta \frac{\partial}{\partial \xi} + x_\xi \frac{\partial}{\partial \eta} \right) \left(\frac{-x_\eta}{\det \mathbf{J}} \right) = \\ &= \frac{1}{\det \mathbf{J}^2} \left(x_\eta x_{\xi\eta} - \frac{x_\eta^2}{\det \mathbf{J}} \det \mathbf{J}_\xi - x_\xi x_{\eta\eta} + \frac{x_\xi x_\eta}{\det \mathbf{J}} \det \mathbf{J}_\eta \right) \end{aligned} \tag{1.72}$$

In a similar manner, the second order derivatives of η with respect to x and y can also be obtained

$$\begin{aligned}
\frac{\partial^2\eta}{\partial x^2} &= \frac{\partial}{\partial x}\left(\frac{\partial\eta}{\partial x}\right) = \frac{\partial}{\partial x}(\eta_x) = \frac{1}{\det\mathbf{J}}\left(y_\eta\frac{\partial}{\partial\xi} - y_\xi\frac{\partial}{\partial\eta}\right)\left(\frac{-y_\xi}{\det\mathbf{J}}\right) = \\
&= \frac{1}{\det\mathbf{J}^2}\left(-y_\eta y_{\xi\xi} + \frac{y_\eta y_\xi}{\det\mathbf{J}}\det\mathbf{J}_\xi + y_\xi y_{\xi\eta} - \frac{y_\xi^2}{\det\mathbf{J}}\det\mathbf{J}_\eta\right) \\
\frac{\partial^2\eta}{\partial y^2} &= \frac{\partial}{\partial y}\left(\frac{\partial\eta}{\partial y}\right) = \frac{\partial}{\partial y}(\eta_y) = \frac{1}{\det\mathbf{J}}\left(-x_\eta\frac{\partial}{\partial\xi} + x_\xi\frac{\partial}{\partial\eta}\right)\left(\frac{x_\xi}{\det\mathbf{J}}\right) = \\
&= \frac{1}{\det\mathbf{J}^2}\left(-x_\eta x_{\xi\xi} + \frac{x_\eta x_\xi}{\det\mathbf{J}}\det\mathbf{J}_\xi + x_\xi x_{\xi\eta} - \frac{x_\xi^2}{\det\mathbf{J}}\det\mathbf{J}_\eta\right)
\end{aligned} \tag{1.73}$$

where $\det\mathbf{J}_\xi$ and $\det\mathbf{J}_\eta$ are the first order derivatives of the determinant of Jacobian with respect to ξ and η, respectively. Differentiation of $\det\mathbf{J}$ in (1.69) leads to

$$\begin{aligned}
\det\mathbf{J}_\xi &= x_\xi y_{\xi\eta} - y_\xi x_{\xi\eta} + y_\eta x_{\xi\xi} - x_\eta y_{\xi\xi} \\
\det\mathbf{J}_\eta &= -x_\eta y_{\xi\eta} + y_\eta x_{\xi\eta} - y_\xi x_{\eta\eta} + x_\xi y_{\eta\eta}
\end{aligned} \tag{1.74}$$

and finally the mixed derivatives of ξ and η with respect to x and y are given by

$$\begin{aligned}
\frac{\partial^2\xi}{\partial x\partial y} &= \frac{1}{\det\mathbf{J}^2}\left(-y_\eta x_{\xi\eta} + \frac{y_\eta x_\eta}{\det\mathbf{J}}\det\mathbf{J}_\xi + y_\xi x_{\eta\eta} - \frac{y_\xi x_\eta}{\det\mathbf{J}}\det\mathbf{J}_\eta\right) \\
\frac{\partial^2\eta}{\partial x\partial y} &= \frac{1}{\det\mathbf{J}^2}\left(-y_\xi x_{\xi\eta} - \frac{y_\eta x_\xi}{\det\mathbf{J}}\det\mathbf{J}_\xi + y_\eta x_{\xi\xi} + \frac{y_\xi x_\xi}{\det\mathbf{J}}\det\mathbf{J}_\eta\right)
\end{aligned} \tag{1.75}$$

The above formulation of coordinate transformation is general, so various shape functions for coordinate transformation can be used. Herein, an 8-nodes and a 12-nodes serendipity element has been presented and depicted in Figure 1.18. It is worth noted that linear shapes can not be used because GDQ method is an high order method, therefore when the second derivative is applied the shape function becomes null.

Quadratic serendipity element

The mapping of quadratic serendipity domain (see Figure 1.18a-b) in the Cartesian x-y plane to an 8-node square computational domain in the natural coordinates ξ-η, $|\xi,\eta| \leq 1$ can be achieved by using the following relationships

$$\begin{aligned}
x &= \sum_{i=1}^{8}\mathcal{N}_i(\xi,\eta)x_i \\
y &= \sum_{i=1}^{8}\mathcal{N}_i(\xi,\eta)y_i
\end{aligned} \tag{1.76}$$

where x_i and y_i are the coordinates of the i-th boundary node in x-y plane, $\mathcal{N}_i(\xi,\eta)$ are the quadratic serendipity shape functions defined as

$$\mathcal{N}_i = \frac{1}{4}(1+\xi\xi_i)(1+\eta\eta_i)(\xi\xi_i+\eta\eta_i-1), \qquad i=1,2,3,4 \tag{1.77}$$

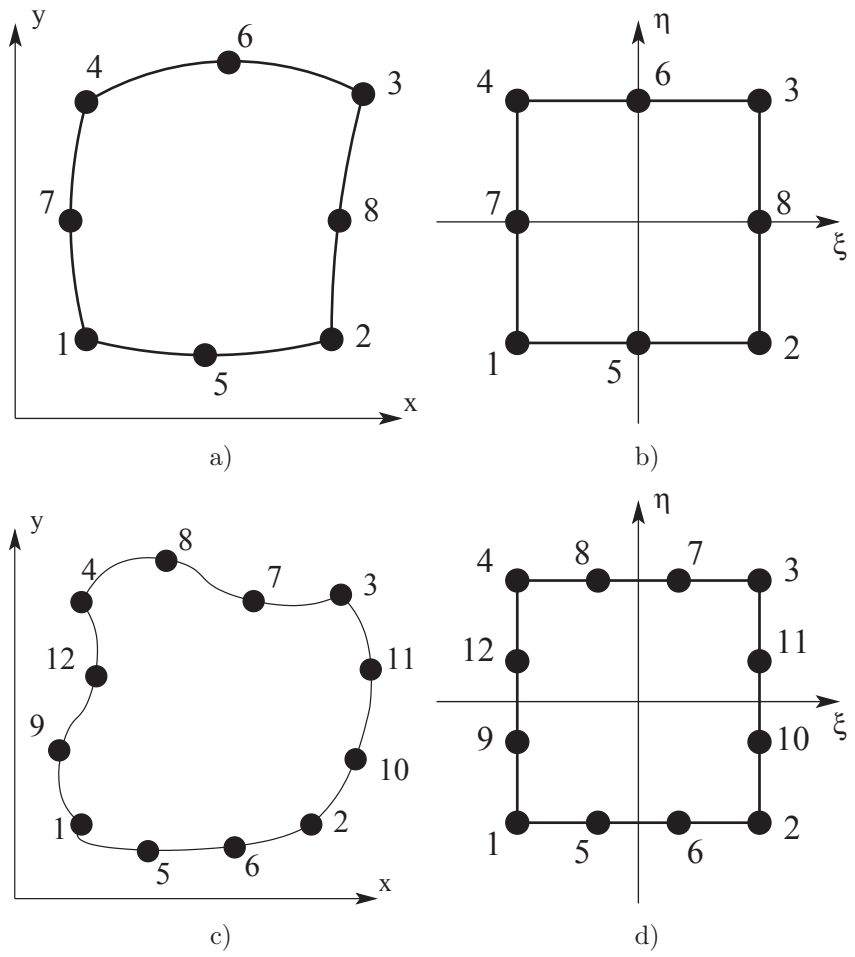

Figure 1.18: Mapping of a quadrilateral 8-nodes serendipity element: a) physical domain, b) computational domain. Mapping of a cubic 12-nodes serendipity element: c) physical domain, d) computational domain.

$$\mathcal{N}_i = \frac{1}{2}(1-\xi^2)(1+\eta\eta_i), \qquad i = 5,6 \tag{1.78}$$

$$\mathcal{N}_i = \frac{1}{2}(1-\eta^2)(1+\xi\xi_i), \qquad i = 7,8 \tag{1.79}$$

where ξ_i and η_i are the coordinates of the node i in the ξ-η plane. All of these shape functions possess the delta function property, i.e., the shape functions are equal to unity at the i-th point and zero at all the other points. The first order derivatives of the physical coordinates with respect to the natural coordinates are calculated as

$$\begin{aligned} x_\xi &= \sum_{i=1}^{4}\frac{1}{4}\xi_i(1+\eta\eta_i)(2\xi\xi_i+\eta\eta_i)x_i + \sum_{i=5}^{6}-\xi(1+\eta\eta_i)x_i + \sum_{i=7}^{8}\frac{1}{2}\xi_i(1-\eta^2)x_i \\ x_\eta &= \sum_{i=1}^{4}\frac{1}{4}\eta_i(1+\xi\xi_i)(\xi\xi_i+2\eta\eta_i)x_i + \sum_{i=5}^{6}\frac{1}{2}\eta_i(1-\xi^2)x_i + \sum_{i=7}^{8}-\eta(1+\xi\xi_i)x_i \end{aligned} \tag{1.80}$$

$$\begin{aligned} y_\xi &= \sum_{i=1}^{4}\frac{1}{4}\xi_i(1+\eta\eta_i)(2\xi\xi_i+\eta\eta_i)y_i + \sum_{i=5}^{6}-\xi(1+\eta\eta_i)y_i + \sum_{i=7}^{8}\frac{1}{2}\xi_i(1-\eta^2)y_i \\ y_\eta &= \sum_{i=1}^{4}\frac{1}{4}\eta_i(1+\xi\xi_i)(\xi\xi_i+2\eta\eta_i)y_i + \sum_{i=5}^{6}\frac{1}{2}\eta_i(1-\xi^2)y_i + \sum_{i=7}^{8}-\eta(1+\xi\xi_i)y_i \end{aligned} \tag{1.81}$$

And the second order derivative are given by

$$\begin{aligned} x_{\xi\xi} &= \frac{1}{2}\sum_{i=1}^{4}\xi_i^2(1+\eta\eta_i)x_i - \sum_{i=5}^{6}(1+\eta\eta_i)x_i \\ x_{\eta\eta} &= \frac{1}{2}\sum_{i=1}^{4}\eta_i^2(1+\xi\xi_i)x_i - \sum_{i=7}^{8}(1+\xi\xi_i)x_i \end{aligned} \tag{1.82}$$

$$\begin{aligned} y_{\xi\xi} &= \frac{1}{2}\sum_{i=1}^{4}\xi_i^2(1+\eta\eta_i)y_i - \sum_{i=5}^{6}(1+\eta\eta_i)y_i \\ y_{\eta\eta} &= \frac{1}{2}\sum_{i=1}^{4}\eta_i^2(1+\xi\xi_i)y_i - \sum_{i=7}^{8}(1+\xi\xi_i)y_i \end{aligned} \tag{1.83}$$

Finally mixed derivatives are

$$\begin{aligned} x_{\xi\eta} &= \sum_{i=1}^{4}\frac{1}{4}\xi_i\eta_i(2\xi\xi_i+2\eta\eta_i+1)x_i + \sum_{i=5}^{6}-\xi\eta_i x_i + \sum_{i=7}^{8}-\eta\xi_i x_i \\ y_{\xi\eta} &= \sum_{i=1}^{4}\frac{1}{4}\xi_i\eta_i(2\xi\xi_i+2\eta\eta_i+1)y_i + \sum_{i=5}^{6}-\xi\eta_i y_i + \sum_{i=7}^{8}-\eta\xi_i y_i \end{aligned} \tag{1.84}$$

Cubic serendipity element

A curvilinear quadrilateral domain with curve boundaries (see Figure 1.18c-d) in the physical coordinate x-y. Each side of the domain can be approximated by a cubic function. The irregular domain can be mapped into a square domain $|\xi, \eta| \leq 1$ by use of the following serendipity shape functions

$$\begin{aligned} x &= \sum_{i=1}^{12} \mathcal{N}_i(\xi, \eta) x_i \\ y &= \sum_{i=1}^{12} \mathcal{N}_i(\xi, \eta) y_i \end{aligned} \tag{1.85}$$

where $\mathcal{N}_i(\xi, \eta)$ is the cubic serendipity shape function defined by

$$\mathcal{N}_i(\xi, \eta) = \frac{1}{32}(1 + \xi_i\xi)(1 + \eta_i\eta)(9(\xi^2 + \eta^2) - 10), \qquad i = 1, 2, 3, 4 \tag{1.86}$$

$$\mathcal{N}_i(\xi, \eta) = \frac{9}{32}(1 - \xi^2)(1 + \eta_i\eta)(1 + 9\xi_i\xi), \qquad i = 5, 6, 7, 8 \tag{1.87}$$

$$\mathcal{N}_i(\xi, \eta) = \frac{9}{32}(1 + \xi_i\xi)(1 - \eta^2)(1 + 9\eta_i\eta), \qquad i = 9, 10, 11, 12 \tag{1.88}$$

where ξ_i and η_i are the coordinates of the node i in the ξ-η plane. All of these shape functions possess the delta function property, i.e., the shape functions are equal to unity at the i-th point and zero at all the other points. The first order derivative of the physical coordinate with respect to the natural coordinate are derived as

$$\begin{aligned} x_\xi = &\sum_{i=1}^{4} \frac{1}{32}(1 + \eta_i\eta)(\xi_i(9\xi^2 + 9\eta^2 - 10) + 18\xi(1 + \xi_i\xi))x_i + \\ &+ \sum_{i=5}^{8} \frac{9}{32}(1 + \eta_i\eta)(-2\xi(1 + 9\xi_i\xi) + 9\xi_i(1 - \xi^2))x_i + \sum_{i=9}^{12} \frac{9}{32}(1 - \eta^2)(1 + 9\eta_i\eta)\xi_i x_i \\ x_\eta = &\sum_{i=1}^{4} \frac{1}{32}(1 + \xi_i\xi)(\eta_i(9\xi^2 + 9\eta^2 - 10) + 18\eta(1 + \eta_i\eta))x_i + \\ &+ \sum_{i=5}^{8} \frac{9}{32}(1 - \xi^2)(1 + 9\xi_i\xi)\eta_i x_i + \sum_{i=9}^{12} \frac{9}{32}(1 + \xi_i\xi)(-2\eta(1 + 9\eta_i\eta) + 9\eta_i(1 - \eta^2))x_i \end{aligned} \tag{1.89}$$

$$
\begin{aligned}
y_\xi &= \sum_{i=1}^{4} \frac{1}{32}(1+\eta_i\eta)(\xi_i(9\xi^2+9\eta^2-10)+18\xi(1+\xi_i\xi))y_i + \\
&+ \sum_{i=5}^{8} \frac{9}{32}(1+\eta_i\eta)(-2\xi(1+9\xi_i\xi)+9\xi_i(1-\xi^2))y_i + \sum_{i=9}^{12} \frac{9}{32}(1-\eta^2)(1+9\eta_i\eta)\xi_i y_i \\
y_\eta &= \sum_{i=1}^{4} \frac{1}{32}(1+\xi_i\xi)(\eta_i(9\xi^2+9\eta^2-10)+18\eta(1+\eta_i\eta))y_i + \\
&+ \sum_{i=5}^{8} \frac{9}{32}(1-\xi^2)(1+9\xi_i\xi)\eta_i y_i + \sum_{i=9}^{12} \frac{9}{32}(1+\xi_i\xi)(-2\eta(1+9\eta_i\eta)+9\eta_i(1-\eta^2))y_i
\end{aligned}
\tag{1.90}
$$

and the second order derivatives are obtained as follows

$$
\begin{aligned}
x_{\xi\xi} &= \sum_{i=1}^{4} \frac{1}{32}(1+\eta_i\eta)(18+54\xi_i\xi)x_i + \sum_{i=5}^{8} \frac{9}{32}(1+\eta_i\eta)(-2-54\xi_i\xi)x_i \\
x_{\eta\eta} &= \sum_{i=1}^{4} \frac{1}{32}(1+\xi_i\xi)(18+54\eta_i\eta)x_i + \sum_{i=9}^{12} \frac{9}{32}(1+\xi_i\xi)(-2-54\eta_i\eta)x_i
\end{aligned}
\tag{1.91}
$$

$$
\begin{aligned}
y_{\xi\xi} &= \sum_{i=1}^{4} \frac{1}{32}(1+\eta_i\eta)(18+54\xi_i\xi)y_i + \sum_{i=5}^{8} \frac{9}{32}(1+\eta_i\eta)(-2-54\xi_i\xi)y_i \\
y_{\eta\eta} &= \sum_{i=1}^{4} \frac{1}{32}(1+\xi_i\xi)(18+54\eta_i\eta)y_i + \sum_{i=9}^{12} \frac{9}{32}(1+\xi_i\xi)(-2-54\eta_i\eta)y_i
\end{aligned}
\tag{1.92}
$$

$$
\begin{aligned}
x_{\xi\eta} &= \sum_{i=1}^{4} \frac{1}{32}(18\xi_i\eta+27\xi_i\eta_i(\xi^2+\eta^2)-10\xi_i\eta_i+18\xi\eta_i)x_i + \\
&+ \sum_{i=5}^{8} \frac{9}{32}\eta_i(-2\xi-27\xi_i\xi^2+9\xi_i)x_i + \sum_{i=9}^{12} \frac{9}{32}\xi_i(-2\eta+9\eta_i-27\eta^2\eta_i)x_i \\
y_{\xi\eta} &= \sum_{i=1}^{4} \frac{1}{32}(18\xi_i\eta+27\xi_i\eta_i(\xi^2+\eta^2)-10\xi_i\eta_i+18\xi\eta_i)y_i + \\
&+ \sum_{i=5}^{8} \frac{9}{32}\eta_i(-2\xi-27\xi_i\xi^2+9\xi_i)y_i + \sum_{i=9}^{12} \frac{9}{32}\xi_i(-2\eta+9\eta_i-27\eta^2\eta_i)y_i
\end{aligned}
\tag{1.93}
$$

1.7.3 Inter-element compatibility conditions

As far as the GDQFEM numerical implementation is concerned a specific procedure must be followed in order to solve the algebraic problem for arbitrarily shaped structures. As it has been already explained the physical domain must be divided into several sub-domains. The best accuracy can be yield by increasing the number of elements and fixing

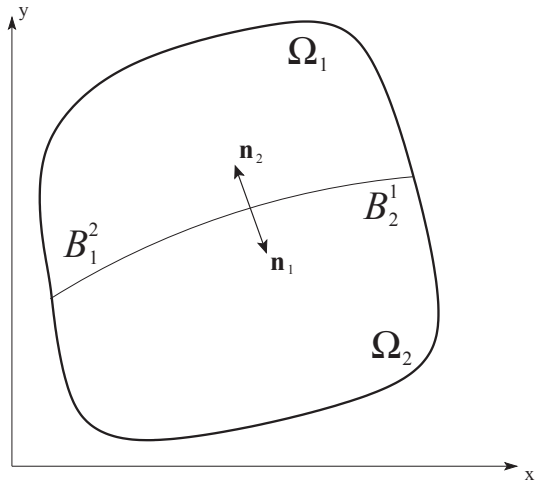

Figure 1.19: Generic representation of the normal vector **n** between two elements.

a certain number of grid points, or keeping the same amount of elements and increasing the number of nodes per element. However in order to solve an algebraic discretized system of equations some boundary conditions are needed. In all the PDEs presented in this PhD Thesis the number of equations is equal to the number of unknown paramters. So a single grid point line is enough, as reported in Figure 1.16, to impose all the boundary conditions necessary to solve the differential problem.

In general the boundary conditions of a quadrature element can be classified as two kinds: internal boundary conditions (IB) and external boundary conditions (EB). As far as the external boundary conditions are concerned the discussion can be moved to the single domain DQ method widely known in literature [39–61]. The compatibility conditions between two adjacent elements require that at each node of the internal boundary displacements and the derivative of the given displacements are equal [22], [11].

Taking the simplest example reported in Figure 1.18a which consider a mesh of two elements. The kinematic and natural transition conditions over the inter-element boundary of two adjacent elements n and m (as reported in Figures 1.13, 1.17) are the continuities of the displacements and the equilibrium conditions written as

$$U^{(1)} = U^{(2)} \quad \text{and} \quad S^{(1)} = S^{(2)} \qquad \text{on } B \tag{1.94}$$

where U stands for one of the generalized displacements of the model and S is one of the stress components of the model, which has to be written for a general outward normal if the sub-domain has been divided using an irregular shape. These relationships (1.94) have to be referred to the normal vector **n** of the current sub-domain. It is worth noting that the outward unit normal vectors $\mathbf{n}_1$ and $\mathbf{n}_2$ at a point upon the interface B are different from each other as depicted in Figure 1.19.

The direction cosines of the outward unit normal vector **n** on the element boundary are necessary for defining the discrete natural transition conditions and the natural boundary conditions. Several techniques can be used to calculate the direction cosines of the outward unit normal vector **n** at a node on the element boundary. The mapping technique used for generating the mesh and the grid in conjunction with the tangent operation and the transformation operation of the first-order Cartesian tensor are adopted [11, 36]. In constructing the secant approximation, the positions of the two consecutive nodes are used

to construct the unit secant vectors at the two end nodes of an element side, whereas the locations of three consecutive nodes are used to construct the unit secant vector at interior nodes.

Direction cosines of the outward unit normal vector on the element boundary are necessary for the natural transition conditions and the Neumann boundary conditions. Let $\mathbf{n} = (n_x, n_y)$, where n_x, n_y are the cosines of the angles between the normal direction $\mathbf{n}$ and the axes x and y, in other words they are the normal vector components. The expression for the two direction cosines on the four sides of a quadrilateral sub-domain can be given as follows

$$n_x = \frac{\xi}{\sqrt{x_\eta^2 + y_\eta^2}} y_\eta, \quad n_y = -\frac{\xi}{\sqrt{x_\eta^2 + y_\eta^2}} x_\eta, \qquad \text{for} \quad \xi = \pm 1 \tag{1.95}$$

The expression above is valid for the edges parallel to ξ axis, and the following is used for the edges parallel to η axis

$$n_x = -\frac{\eta}{\sqrt{x_\xi^2 + y_\xi^2}} y_\xi, \quad n_y = \frac{\eta}{\sqrt{x_\xi^2 + y_\xi^2}} x_\xi, \qquad \text{for} \quad \eta = \pm 1 \tag{1.96}$$

It should be noted that ξ and η correspond to x and y when the domain has got all the edges parallel to the external Cartesian system (see Figure 1.13). Obviously, the displacement compatibility, the first of (1.94), can be applied into the natural coordinate directly without coordinate transformation. In fact they do not have any derivative.

The static conditions, the second of (1.94), should be mapped into the computational domain, instead, as a function of x and y because the membrane inter-element tension is related to the derivatives $\partial/\partial x$ and $\partial/\partial y$ of the direction cosines, n_x and n_y, of the given outward normal on the current boundary. The formal mathematical development of these conditions depend on the PDEs that are used to describe the problem under study. In general the first step is the decomposition of the stress components written in Cartesian coordinates x-y along the normal and tangential direction of the current edge. Then the coordinate transformation (1.70) must be applied so the decomposed stress can be written in natural coordinates ξ-η. An easy logic scheme is reported by

$$S(x, y) \rightarrow S_{\mathbf{n}}(x, y) \rightarrow S_{\mathbf{n}}(\xi, \eta) \tag{1.97}$$

where the generic stress $S(x, y)$ in Cartesian coordinates, is firstly decomposed $S_{\mathbf{n}}(x, y)$ upon two orthogonal directions of the current side of normal $\mathbf{n}$, nevertheless it remains in Cartesian coordinates. Finally the coordinate transformation is applied and $S_{\mathbf{n}}(\xi, \eta)$ is the final stress boundary component that is needed for the boundary condition implementation.

1.7.4 Corner type compatibility condition

The inter-element compatibility conditions, presented above, are valid when the conditions are written between two opposite sides as it is well depicted in Figure 1.17. One of the technical details encountered in quadrature element analysis is the establishment of equations at the corners of a generic quadrilateral element [22, 28, 36, 37].

Considering a system of PDEs composed of f_μ equations. It is noted that the number of equations μ is considered equal to the number of degrees of freedom of the mathematical model under study. Thus μ equations are set up at each node of a given element.

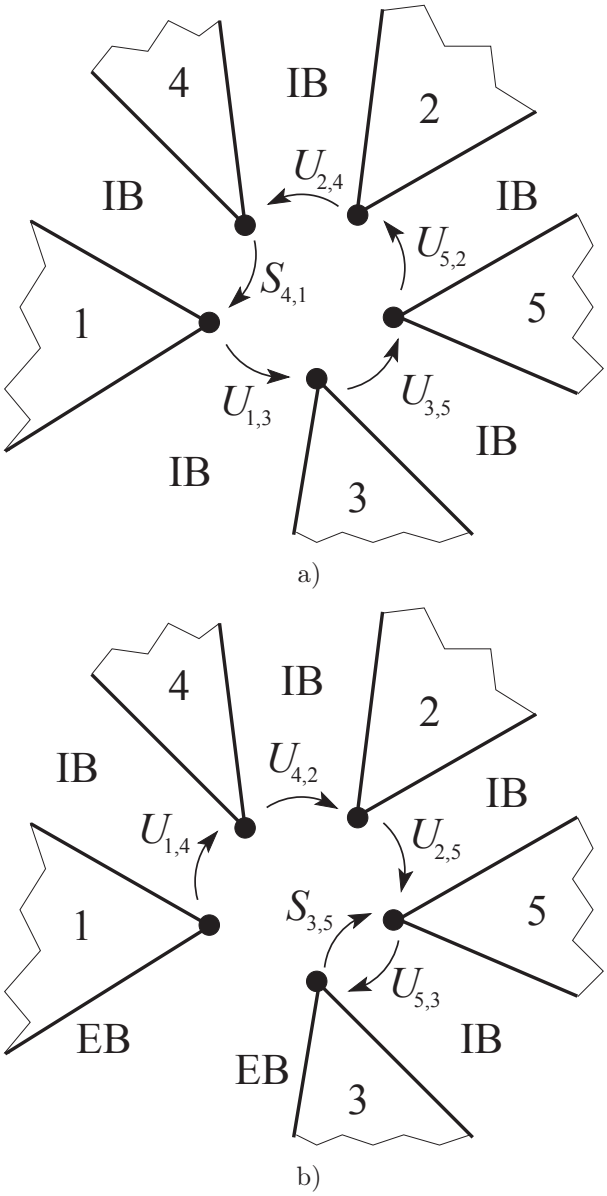

Figure 1.20: a) Internal corner compatibility condition implementation work out. b) boundary corner compatibility implementation work out.

Since a kinematic and a static compatibility condition must be written at each connected element boundary, the same should have been done at element corners. When any domain decomposition/subdivision is performed during a numerical analysis, either by FEM or GDQFEM, there are some configurations for an element corner which are reported in Figure 1.20 [22, 28, 36, 37]. It is supposed to have a mesh as in Figures 1.20, where only one corner per element is represented. The numbers represent the element enumeration of the current mesh. In general the element enumeration does not follow the boundary condition implementation.

For a corner, as depicted in Figure 1.20a, both kinematic and static compatibility conditions must be prescribed. It has been discovered by the author that it is sufficient to write a static condition between two corners and a kinematic one among the others. In fact, the numerical code imposes the kinematic conditions at first until it reaches the final corner in which it enjoins the static one. For example taking Figure 1.20a as a reference in the current corner five elements concur at the displayed node. At first the code has to find out the correct sequence of elements which belong to the current node, e.g. in Figure 1.20a the sequence is 1, 3, 5, 2, 4. Hence following the given sequence the algorithm imposes the kinematic conditions $U_{i,j}$, which are written in the node i respect to the node j till the end of the sequence in which the static condition is enjoined. It must be underlined that the kinematic condition $U_{i,j}$ stands for the first of the (1.94) $U_i = U_j$.

In the other configuration reported in 1.20b, there are two different boundary conditions the external and the internal one. This is generally the most complicated one. In fact the boundary conditions enforcement depend on the physical toughness of the condition itself. In other words if structural mechanics is taken as an example the clamped edge condition is stronger than a compatibility condition that is more robust than the free edge condition. Besides the free condition is weaker than a continuity condition that is weaker than the fixed edge condition. So the corner implementation work out strongly depend on which kind of boundary conditions are the EBs. Because if they are clamped the corner owned by that element should be fixed at first and than the continuity condition can be written. If the external boundary if free the corner should follow the previous computational rule, valid for the interior corner. In conclusion in Figure 1.20b the case of free EBs is graphically presented. The continuity condition is enforced between the elements owned by the corner following the same rule of the interior node, in which firstly all the kinematic conditions are imposed and a static condition is written in the end. Moreover, it has been found out by the author that it is forbidden to enforce a condition between two nodes that are on two opposite sides of the external boundaries in fact there is no connection between them.

It should be added that, in the FE analysis the corners are the mesh nodes, so there is one node at which several elements belong to, nevertheless in the GDQFEM there are as many nodes as many elements concur at that point. So in the case presented in Figures 1.20 there are five nodes which are owned by five different elements, so at least five equations have to be written in order to solve the system. This condition leads to another aspect. When a solution is found by FE method, the stresses are no longer continuous between the elements, whereas in a GDQFEM implementation either the displacements and the internal stresses are continuous through the entire mesh.

Chapter 2

Arbitrarily Shaped Membranes with Inclusions

Sommario

In questo capitolo viene risolto il problema delle vibrazioni libere di membrane sottili. Questo problema è stato considerato da vari autori in letteratura [13, 62–69, 76–85] sia per membrane di forma generica che in materiale composito.

In letteratura, si possono trovare numerosi articoli relativi alla soluzione esatta di membrane di forma semplice come quella rettangolare o circolare. Tuttavia, per membrane di forma complessa la soluzione è possibile soltanto in forma numerica. Kang ed il suo gruppo di ricerca hanno presentato un rapporto completo sul problema delle vibrazioni libere delle membrane di varia forma [77–81, 85], risolvendo i problemi attraverso membrane connesse in modo semplice o multi-connesse. Allo stesso tempo Wu *et al.* [84] hanno applicato le *local radial basis function-based on differential quadrature* per lo studio di membrane di forma generica.

In generale la tecnica numerica che si utilizza per risolvere i sistemi strutturali deve essere stabile [93–95]. Rispetto all'ormai consolidato metodo agli Elementi Finiti (FE), la tecnica GDQ porta risultati molto accurati utilizzando un numero di punti esiguo. Questa caratteristica di elevata accuratezza è stata ampiamente presentata e dimostrata in letteratura [39–61, 96–105]. Tuttavia, sorgono alcune difficoltà quando si vogliono trattare problemi elastici con discontinuità o sconnessioni, per esempio, in strutture di forma generica come membrane, piastre oppure nei casi in cui vi siano inclusioni di materiale e/o la presenza di fessurazioni interne.

In questo capitolo, sono risolte con l'innovativa tecnica GDQFEM le stesse strutture analizzate in letteratura [13, 62–69, 76–85] (come ad esempio le membrane di forma qualunque e composte da più materiali) e sono proposti nuovi casi studio per possibili sviluppi futuri. Si vuole far rilevare che, nella prima parte dei risultati numerici sono proposte varie analisi di stabilità e accuratezza della tecnica con riferimento alla soluzione esatta per la membrana rettangolare.

2.1 Introduction

In this chapter the problem of solving the free vibration of membranes is considered in the following. Free vibration analysis of membrane has been solved by several authors in the past decades, as reported in [62]. The problem of a composite plate of various shapes has been deeply studied by Bhadra [63]. Buchanan et al. [64] and Buchanan [65] used Ritz and finite element method for vibration analysis of circular and elliptic membranes with variable density. The differential quadrature method was applied for frequency analysis of rectangular and circular membranes by Laura et al. [66, 67]. Moreover, the method of discrete singular convolution has been used recently for the vibration analysis of curvilinear membranes by Civalek et al. [62] who deeply studies skew and rhombic membrane also [68]. Ersoy *et al.* [69] have used the method of singular convolution on rectangular membranes with variable density.

Because of its relationship to the wave equation, the Helmholtz equation arises in problems in such areas of mathematical physics as the study of acoustics. In fact, some important studies concerning the Helmholtz equation and the waveguide problem have been studied by several authors [70–72]. Shu et al. [73–75] have used the differential quadrature technique and the multi-domain differential quadrature for solving the Helmholtz equation, too. The vibration of arbitrarily shaped membranes has been discussed by using the general methods which include the following: finite difference, point matching, Rayleigh-Ritz method, Galerkin method, finite element and boundary element method. These general methods are applied for solving the vibration of membranes of general shape [13, 76–85]. Furthermore, it is well-known that there is an analogy between membrane vibrations and plate vibrations. In fact, the eigenfrequencies of a simply supported polygonal plate are the squares of the eigenvalues of a membrane under constant tension with identical geometry and fixed edges, and their eigenfunctions are identical [14, 86–92]. This analogy has greatly evoked researchers' interest in vibration analysis of membranes, because solutions for polygonal membranes can be converted into those of polygonal simply supported plates.

For a membrane of simple geometry such as rectangular and circular membranes there are several exact solutions available in literature. However, for a membrane of a complex geometry only numerical solutions are possible. There is a complete presentation of the membrane vibration problem by Kang *et al.* in literature [77–81, 85], who have been solved the problem in several manners for simply and multi-connected membranes. Wu et al. [84] have applied the local radial basis function-based on differential quadrature to the study of arbitrarily shaped membranes.

In general the dynamic benchmarks for a structural system need to be very accurate in order to find out the stability and accuracy of the numerical technique [93–95].

Differential Quadrature was introduced by Bellman in the early 1970s as a simple and rapid method for solving linear and non linear differential equations. It is essentially a global collocation method that approximates the derivatives at a point by use of a weighted sum of function values at a group of nodal points. In his book Shu [9] developed the Generalized Differential Quadrature which leads to a more simple and straightforward implementation of this method to partial differential system of equations with well-known boundary conditions. Compared to the widely-used Finite Element Method (FEM), the GDQ method yields very accurate results by using very small number of nodal points. The character of high accuracy has been widely presented in some articles presented in

literature [39–61, 96–105]. However, there arise difficulties when GDQ is applied to elastic problems where discontinuities or disconnections are present, for example, in arbitrarily shaped structures such as membranes and plates or in the case of material inclusions and presence of internal cracks.

In this PhD Thesis a Generalized Differential Quadrature Finite Element Method has been applied to the study of arbitrarily shaped membranes. This technique is named also multi-domain differential quadrature [11, 22, 26–29, 35, 38, 75, 105, 127–135]. The aim of this technique is to subdivide the computational domain into several sub-domains or elements in which the quadrature rule [9] can be applied. The GDQFEM is an extension of the classic GDQ technique introduced by Shu [9]. The multi-domain method can be applied directly to regular sub-domains, of rectangular shape, nevertheless if the elements have a general shape the coordinate transformation must be implemented [11, 27, 29]. Subsequently, the mapping technique is used to transform both the governing differential or partial differential equations and the differential or partial differential type transition conditions of two adjacent sub-domains and the boundary conditions defined on the physical sub-domain into the regular master element in the parent space, called computational space.

The Generalized Differential Quadrature GDQ technique has been introduced to discretize all the equations defined by the natural coordinates in the master element. For the sake of clarity, the GDQFEM has been firstly applied to rectangular domains, in order to focus on the assembly technique when a regular domain is given. Secondly, the irregular multi-domain is introduced by using mapping technique also.

The present method is valid only if the solution function, the applied load and the material properties are continuous over the domain, in fact GDQ is not applicable if the elastic structure under consideration is made of different materials, not uniform external loadings and mixed boundary conditions over the same edge. In all these cases the stress components, at the interface of the discontinuity, lead to a finite jump of their value. According to mathematics, a finite discontinuity can not be described by a continuous function. Since GDQ is an high-order numerical technique (because it solves the strong form of the fundamental system) compatibility conditions must be applied at the discontinuity to obtain an accurate solution, nevertheless it remains of high-order elsewhere.

A GDQFEM is formulated in this paper to solve free vibration of arbitrarily shaped membranes in presence of discontinuities of any kind, e.g. material discontinuity or irregular geometry. By putting the boundary of each sub-domain on the corresponding interfaces, discontinuity is imposed with kinematic and static compatibility conditions at the interface. Pursuing the following multi-domain differential quadrature technique a generic engineering or scientific problem can be converted into a computer algorithm. The convergence of the solution can be usually achieved by either increasing the number of elements or nodes per element. In fact it has been shown by many papers that the GDQ convergence rate is excellent [39–61, 96–105].

The final numerical implementation of the global algebraic system obtained by this technique is simply and straightforward, because it follows the elements connectivity rule such as in FEM.

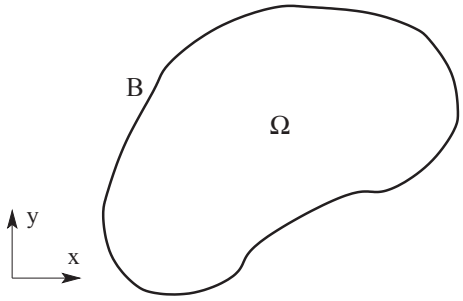

Figure 2.1: Arbitrarily shaped membrane with continuous boundary B and uniform domain Ω.

2.2 Equation of motion

Consider the transverse motion of an elastic membrane extended in two dimensions. The membrane equilibrium position lies in the x-y plane. Since the membrane has negligible bending stiffness. It is assumed that constant tension forces are applied uniformly to the membrane edges in all directions. Consider a uniform membrane of arbitrary shape (Figure 2.1), the equation of motion for the free flexural vibrations of a membrane is written as

$$T\left(\frac{\partial^2 w}{\partial x^2}+\frac{\partial^2 w}{\partial y^2}\right)=\rho h\frac{\partial^2 w}{\partial t^2} \tag{2.1}$$

where T is the uniform tension per unit length, ρ is the mass per unit area, h is the membrane thickness and w is the configuration variable or in other words the transverse deflection of the membrane. It is assumed that in the equilibrium position the membrane lies entirely on one plane under uniform tension T per unit length and it does not have any deflections at its edges. On the other hand the equation of motion for the free flexural vibration of a thin plate (Kirchhoff-Love plate theory) is written as

$$D\nabla^4 w+\rho_s\frac{\partial^2 w}{\partial t^2}=0 \tag{2.2}$$

ρ_s is the surface density and D is the flexural rigidity expressed as $D=Eh^3/12(1-\nu^2)$ in terms of Young's modulus E, Poisson's ratio ν and the plate thickness h.

The governing equation of motion of the membrane (2.1) and the one for the thin plate (2.2) can be both solved by using the method of variable separation. It is possible to seek solutions that are harmonic in time and whose frequency is $f=\omega/2\pi$. The flexural displacement w can be written as follows

$$w(x,y,t)=W(x,y)e^{i\omega t} \tag{2.3}$$

where the vibration spatial amplitude value W fulfil the fundamental equation (2.1). Hence, substituting (2.3) into (2.2) it leads

$$\nabla^4 W+\Lambda^4 W=0 \tag{2.4}$$

where $\nabla^4=\frac{\partial^4}{\partial x^4}+2\frac{\partial^4}{\partial x^2\partial y^2}+\frac{\partial^4}{\partial y^4}$, $\Lambda=(\rho_s\omega^2/D)^{1/4}$. In which Λ is called frequency parameter, which is a function of the actual frequency f [Hz]. Since an analogy exists between the vibration of polygonal plates with simply supported boundary conditions and

a similarly shaped membrane with fixed edges [14, 85–91], equation (2.4) can be reduced to the membrane equation, that is the same problem obtained starting from (2.1)

$$\nabla^2 W + \Lambda^2 W = 0 \tag{2.5}$$

where $\nabla^2 = \frac{\partial^2}{\partial x^2} + \frac{\partial^2}{\partial y^2}$. If the i-th eigenvalue Λ_i is obtained by solving equation (2.5), the i-th thin plate natural frequency may be calculated

$$f_i = \frac{\Lambda_i^2}{2\pi}\sqrt{\frac{D}{\rho_s}} \tag{2.6}$$

as reported in [85].

It should be noted that $c = \sqrt{T/\rho h}$ is the speed of sound. The frequencies of a vibrating membrane represent the sound produced by a membrane with the corresponding modal shape. The natural frequency $f = \omega/2\pi$ can be determined by solving the standard eigenvalue problem (2.5). In the following, the problem (2.5) will be solved for several structures and the numerical results will be compared to the analytical solutions, valid for a rectangular and circular membrane only, and some numerical solutions found in literature.

In order to solve the eigenvalue problem the boundary conditions must be applied to the membrane sides. Since the membrane is not having deflections at its sides the unique boundary condition is the clamped one

$$W = 0 \quad \text{on the boundary edge } B \tag{2.7}$$

It must be underlined that no free edge boundary condition is acceptable in this kind of theory.

2.3 Boundary conditions

The free vibration of elastic membrane problems described by (2.1) and (2.7) can be discretized by the GDQ method following the rules introduced in the first chapter. Once the dynamic system is written in a discretized form, the boundary conditions and the inter-element boundary conditions must be defined (see section 1.7.3). For the membrane case the S, introduced in (1.94) that each element exchanges with the neighbouring elements is the uniform tension T, which has to be written for a general outward normal. In other words, the static condition, for the membrane case, is actually a derivative of the generalized displacement W.

In this work the lowest number of elements within the highest number of grid points per element has been considered, because it can be noted from the numerical results that this solution gives the most accurate results. In fact increasing the number of elements the final matrix illness grows rapidly, due to the not symmetric element stiffness matrix.

The stress equations (1.94) are function of x and y. In fact, the membrane inter-element uniform tension T is related to the derivatives $\partial/\partial x$ and $\partial/\partial y$ of the direction cosines, n_x and n_y, of the given outward normal. In other words the directional derivative on each element side must be calculated and it can be written for the membrane case as

$$\frac{\partial W}{\partial n} = (n_x - n_y)^2 \frac{\partial W}{\partial x} + (n_x + n_y)^2 \frac{\partial W}{\partial y} \tag{2.8}$$

It is noted that if the current element is regular (rectangular sub-domain) the relation (2.8) coincides with the directional derivative ($\nabla W = \frac{\partial W}{\partial x} + \frac{\partial W}{\partial y}$) of a scalar function for any element edge.

When an irregular sub-domain is considered the coordinate transformation (1.70) must be applied, so the generalized directional derivative (2.8) becomes

$$\frac{\partial W}{\partial n} = \left((n_x - n_y)^2 \xi_{,x} + (n_x + n_y)^2 \xi_{,y}\right) \frac{\partial W}{\partial \xi} + \left((n_x - n_y)^2 \eta_{,x} + (n_x + n_y)^2 \eta_{,y}\right) \frac{\partial W}{\partial \eta} \quad (2.9)$$

As far as the corner type compatibility condition are concerned, all the necessary computational data have been reported in section 1.7.4. For the membrane case the external conditions are always stronger than the internal compatibility ones, because only the clamped case can be considered. As a result, a generic corner node is fixed and the kinematic conditions is written automatically by the code.

2.4 Numerical applications

In order to show the accuracy and stability of the current technique some numerical tests are performed comparing the GDQFEM solution to the exact solutions of rectangular and circular membranes. It should be noted beforehand that the solution for circular membranes is exact only mathematically, in fact in order to find the actual eigenvalues the zeros of the Bessel function of the first kind must be found. Moreover some other comparisons have been done by following the results of several authors in literature [62, 70, 77–79, 84, 85]. In conclusion, some new arbitrarily composite and homogeneous membranes have been proposed for further studies.

The GDQFEM is based on a grid point distribution upon each sub-domain. Consequently, a test on several grid distributions has been performed in order to use the one that has the highest performance for this technique. In the following all the used distributions are presented [41]. It should be noted that the following point distributions are defined in the interval $\bar{\xi} \in [0, 1]$. Since the computational element is defined between $-1 \leq \xi, \eta \leq 1$ a coordinate shifting must be done.

The first is the *Chebyshev grid distribution* which can be recursively defined from the second to the previous, before the last point, when the first and the last points are fixed.

$$\bar{\xi}_1 = 0, \quad \bar{\xi}_N = 1, \quad \bar{\xi}_k = \frac{1}{2}\left(1 - \cos\left(\frac{2k-3}{2(N-2)}\pi\right)\right), \quad k = 2, \ldots, N-1 \quad (2.10)$$

Then there is the *extended Chebyshev grid distribution* (roots of the Chebyshev polynomial of first kind), that is defined by the roots r_k.

$$\bar{\xi}_k = \frac{r_k - r_1}{r_N - r_1}, \quad r_k = \cos\left(\frac{2k-1}{2N}\pi\right), \quad k = 1, 2, \ldots, N \quad (2.11)$$

Analogously to the previous distribution the *extended Chebyshev grid distribution* (roots of the Chebyshev polynomial of second kind) can be written

$$\bar{\xi}_k = \frac{r_k - r_1}{r_N - r_1}, \quad r_k = \cos\left(\frac{k}{N+1}\pi\right), \quad k = 1, 2, \ldots, N \quad (2.12)$$

The most used grid point distribution for the single domain case is the *Chebyshev-Gauss-Lobatto grid distribution*

$$\bar{\xi}_k = \frac{1}{2}\left(1 - \cos\left(\frac{k-1}{N-1}\pi\right)\right), \quad k = 1, 2, \ldots, N \tag{2.13}$$

Finally, the *Legendre grid distribution* (roots of the Legendre polynomial of second kind) is written

$$\frac{d^{N-2}}{d\tau^{N-2}}\left(\tau^{N-2}\left(\tau - 1\right)^{N-2}\right) = 0 \rightarrow \bar{\xi}_k, \quad k = 1, 2, \ldots, N \tag{2.14}$$

It should be noted that in order to find the Legendre grid distribution (2.14) the roots of the differential equation reported in (2.14) must be found for a fixed N points.

Firstly, several accuracy tests have been performed on the rectangular membrane compared to the exact solution. Secondly, several case studies have been considered in order to compare the numerical solution obtained with GDQFEM to some reference solutions found in literature [62, 70, 77–79, 84, 85]. The results are presented in form of tables and figures in which the first eigenfrequencies are depicted. It should be noted that FEM solutions are presented in the following tables. These kinds of numerical results have been obtained by many authors in literature by using the analogy between the membrane fixed at all edges and the thin simply supported plate.

2.4.1 Rectangular membrane

In the first example the natural frequencies of a rectangular membrane are considered. The exact reference solution is obtained, as it is well-known from literature [92] by the following equation

$$\omega_{mn} = \pi\sqrt{\frac{T}{\rho h}}\sqrt{\left(\frac{m}{a}\right)^2 + \left(\frac{n}{b}\right)^2} \tag{2.15}$$

where m, n are the modal shapes indices, a, b are the two sides of the rectangular membrane, T is the membrane tension, ρ is the material density and h is the membrane thickness. In the following the rectangular membrane whose dimensions are $a = 1.2$ m by $b = 0.9$ m is considered. First of all in order to show which is the best discretization technique to apply to GDQFEM, a numerical test has been shown. The aim of the accuracy test is to demonstrate how fast is the trend for the first twenty frequencies of a rectangular membrane solved by GDQFEM and what is the maximum error for the case under study. In Figures 2.2a-2.2e the five grid distributions reported above are used to find the first twenty frequencies with the exact solution. The number of grid points N per element edge is on the horizontal abscissa and the orthogonal axis represents the relative error

$$\mathcal{E}_r = \left|\frac{\Lambda_{gdq} - \Lambda_{exact}}{\Lambda_{exact}}\right| \tag{2.16}$$

It is noted that the chosen grid which leads to obtain the first twenty frequencies within the less number of grid points is the Legendre grid distribution. In fact for $N = 25$ the first twenty frequencies are kept within a relative error less than $\mathcal{E}_r < 10^{-14}$. In

addition another important aspect is that the accuracy is stable when the minimum error is reached.

In Figure 2.2f a summary of all the distributions is presented. The resulting eigenfrequencies Λ_{gdq} normalized with respect to the exact solution are plotted versus the mode number m by the total number of degrees of freedom (dofs) N_{tot} [93, 94]. To reproduce the spectra of Figure 2.2f, a grid of 51×51 points have been used so that $N_{tot} = 2601$ dofs. The total number of calculated modes, that is given by the dofs subtracted of the boundary conditions is $m_{tot} = 2401$. Each curve has been obtained within a fixed error tolerance $tol = 10^{-4}$. Almost, all the distributions have less than 25% of the modes accurate below the given tolerance, but above that the maximum error is almost 5% for the first 40% of the modes. This means that is not possible to obtain the 100% of accurate modes given a certain mesh. This numerical phenomenon explains why more points are needed to capture high frequencies. The symbol Pm reported in Figure 2.2f represents the percentage of the total number of accurate modes respect to the maximum m_{tot} computable. In must be underlined that if a less restricted tolerance is considered the maximum amount of accurate modes increases obviously.

Secondly, distortion effect on a two element mesh is presented in the following. In Figure 2.3a the parametric representation of the current mesh is presented. The dimension of the membrane are kept constant ($a = 1.2$ m, $b = 0.9$ m) and the parameter c varies from $c = 0.6$ m in which no distortion is applied to $c = 0$ m where the two elements degenerate into two triangles. In Figure 2.4 the discrete spectra for different grids are presented. The grid points number varies from $N = 11$ to $N = 41$. Figure 2.4 shows that increasing the distortion, so for $c = 0.6$ to $c = 0$, for all the considered grids the percentage of accurate frequencies, under the fixed tolerance $tol = 10^{-4}$, decreases. In fact the number of modes (and its percentage Pm) written in the legend of Figures 2.4a-d decreases when c increases.

The seven curves plotted in Figures 2.4a-d form a sheaf of lines that becomes thinner when the N increases. This is clear because it has been shown in 2.2, where the accuracy increases when the number of grid point increases, until it becomes stable. It is also noted that the maximum percentage is never above the 20% under the tolerance. So the GDQFEM (as any numerical method) can not capture the total number of modes related to a fixed number of degrees of freedom (dofs) nevertheless the maximum percentage is always below the 20% of the total number of the computable dofs m_{tot}.

The last numerical test is depicted in Figures 2.5-2.6. In Figure 2.6 the maximum percentage of accurate modal shapes Pm, under a fixed tolerance $tol = 10^{-4}$, is presented for several meshes (Figure 2.5). In Figure 2.5 all the meshes used for the numerical analysis of the rectangular membrane are graphically reported. The red digits represent the element number, whereas the black digits are the nodes used for in the coordinate transformation. In this case only 8 nodes elements have been used, because no curved boundaries are needed to map this geometry. In Figure 2.6a a Chebyshev-Gauss-Lobatto grid distribution has been used for solving the accuracy problem whereas in Figure 2.6b the Legendre grid distribution has been applied. Up to eleven different meshes have been used. Starting from the single element mesh to sixteen distorted element mesh. In the legend of Figure 2.6 the symbol n_e indicates the number of elements and with the acronym *sk* a skewed mesh is employed. It is clear that the percentage of accurate modes decreases if a skewed mesh and a high number of elements is considered. In fact for the single element mesh the $Pm > 20\%$ whereas for a mesh composed of sixteen elements, or almost

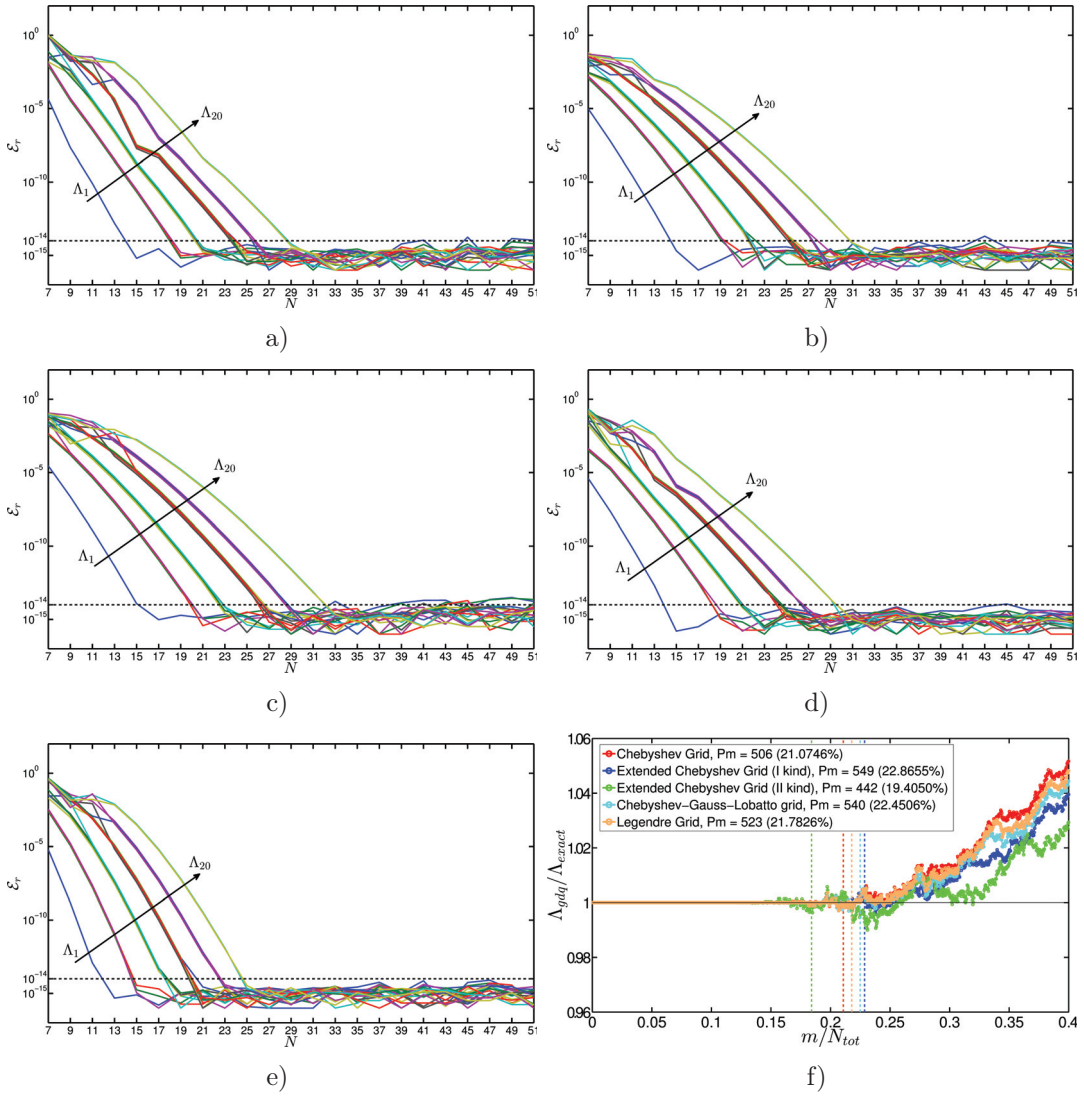

Figure 2.2: Accuracy test for a single element rectangular plate: a) Chebyshev grid, b) Extended Chebyshev grid (I kind), c) Extended Chebyshev grid (II kind), d) Chebyshev-Gauss-Lobatto grid, e) Legendre grid, f) Normalized discrete spectra.

all the skewed meshes, $Pm < 15\%$.

In Figure 2.7 the first nine modal shapes of the rectangular membrane are depicted. It should be noted that the pictures have been created by using a single element domain with a 41×41 grid distribution. The numerical solution obtained within several meshes and grid points numbers is compared to analytical solution and other numerical solutions found in literature [69, 77–79, 84, 85]. In Table 2.1 the first ten eigenfrequencies are reported for the rectangular membrane of sides $a = 1.2$ m and $b = 0.9$ m. The results are presented for three different meshes. Firstly one single element with $N = 41$ grid points is used which gives the same results as the single domain GDQ. Secondly four regular elements and twelve regular elements with $N = 21$ grid points are considered. It can be noted that the three cases under study gives the same results which are very accurate respect to the exact solution.

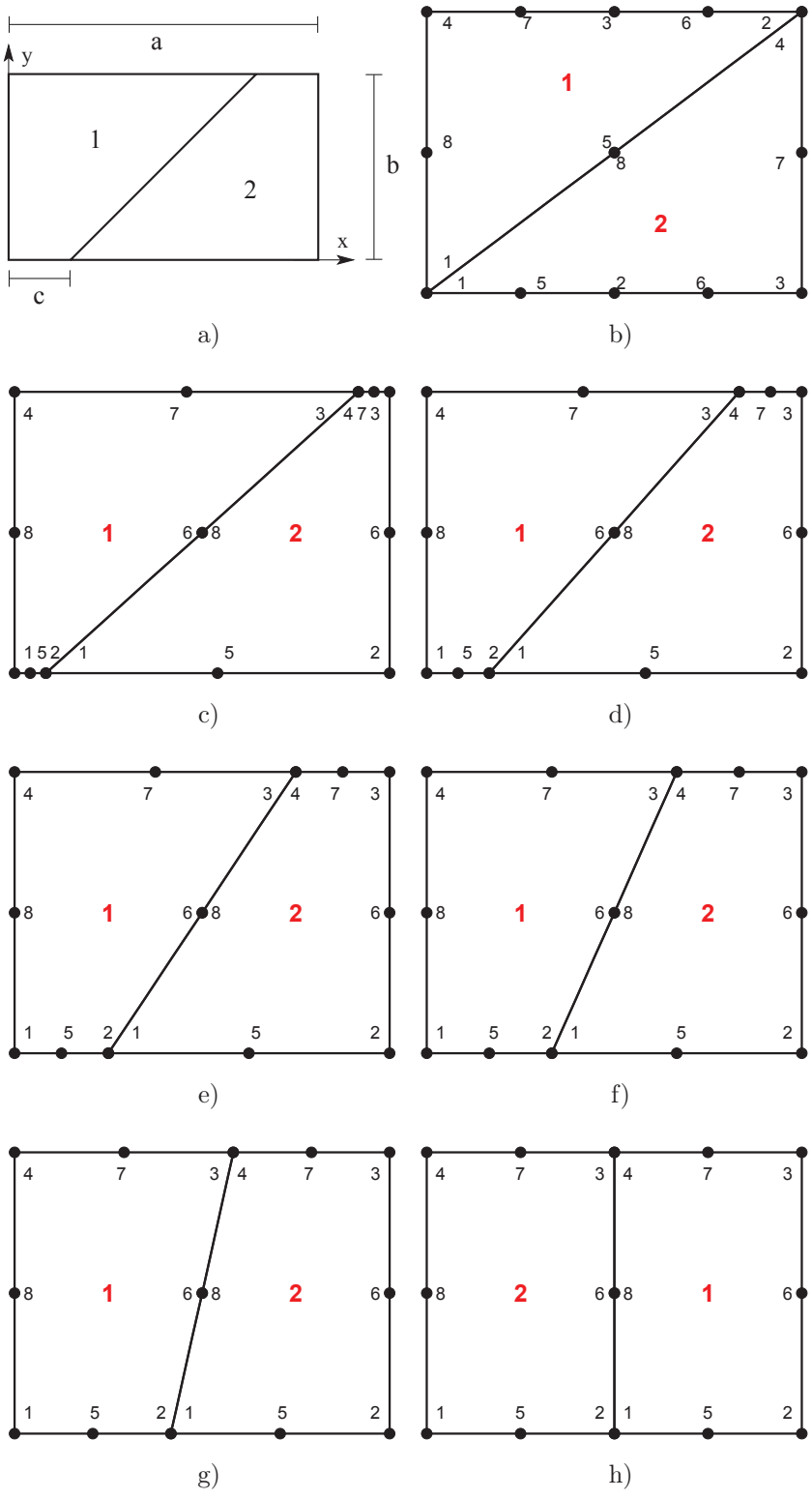

Figure 2.3: Distorted rectangular plate meshes: a) two element distorted mesh, where $0 \leq c \leq 0.6$, b) Distorted mesh with $c = 0$, c) Distorted mesh with $c = 0.1$, d) Distorted mesh with $c = 0.2$, e) Distorted mesh with $c = 0.3$, f) Distorted mesh with $c = 0.4$, g) Distorted mesh with $c = 0.5$, h) Distorted mesh with $c = 0.6$.

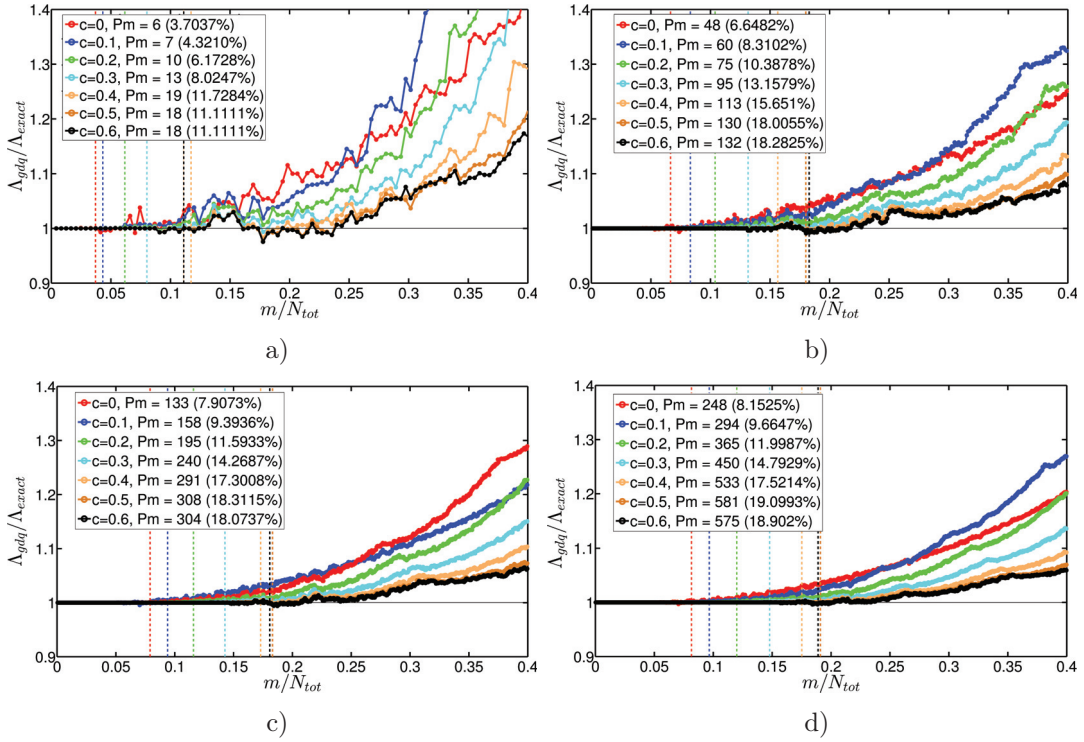

Figure 2.4: Normalized discrete spectra for a two distorted element rectangular plate: a) 11×11 grid, b) 21×21 grid, c) 31×31 grid, d) 41×41 grid.

Λ	Exact	Ref. [77]	FEM [77]	Ref. [78]	Ref. [79]	Ref. [84]	Ref. [85]	GDQFEM		
								$n_e = 1$ $N = 41$	$n_e = 4$ $N = 21$	$n_e = 12$ $N = 21$
1	4.36332	4.3633	4.3651	4.3633	4.363	4.3633	4.36	4.36332	4.36332	4.36332
2	6.29287	6.2929	6.3006	6.2929	6.293	6.2929	6.29	6.29287	6.29287	6.29287
3	7.45605	7.4560	7.4669	7.4560	7.456	7.4561	7.45	7.45605	7.45605	7.45605
4	8.59475	8.5948	8.6213	8.5945	8.596	8.5948	8.59	8.59475	8.59475	8.59475
5	8.72665	8.7266	8.7407	8.7266	8.726	8.7267	8.73	8.72665	8.72665	8.72665
6	10.50827	10.5083	10.5370	10.5135	10.50	10.5083	10.51	10.50827	10.50827	10.50827
7	10.79427	10.7943	10.8313	10.7871	10.79	10.7941	-	10.79427	10.79427	10.79427
8	11.03843	11.0389	11.1029	11.0385	11.05	11.0384	-	11.03843	11.03843	11.03843
9	11.70802	-	-	-	11.70	-	-	11.70802	11.70802	11.70802
10	12.58575	-	-	-	-	-	-	12.58575	12.58575	12.58575

Table 2.1: First ten eigenfrequencies of a rectangular membrane with $a = 1.2$ m and $b = 0.9$ m.

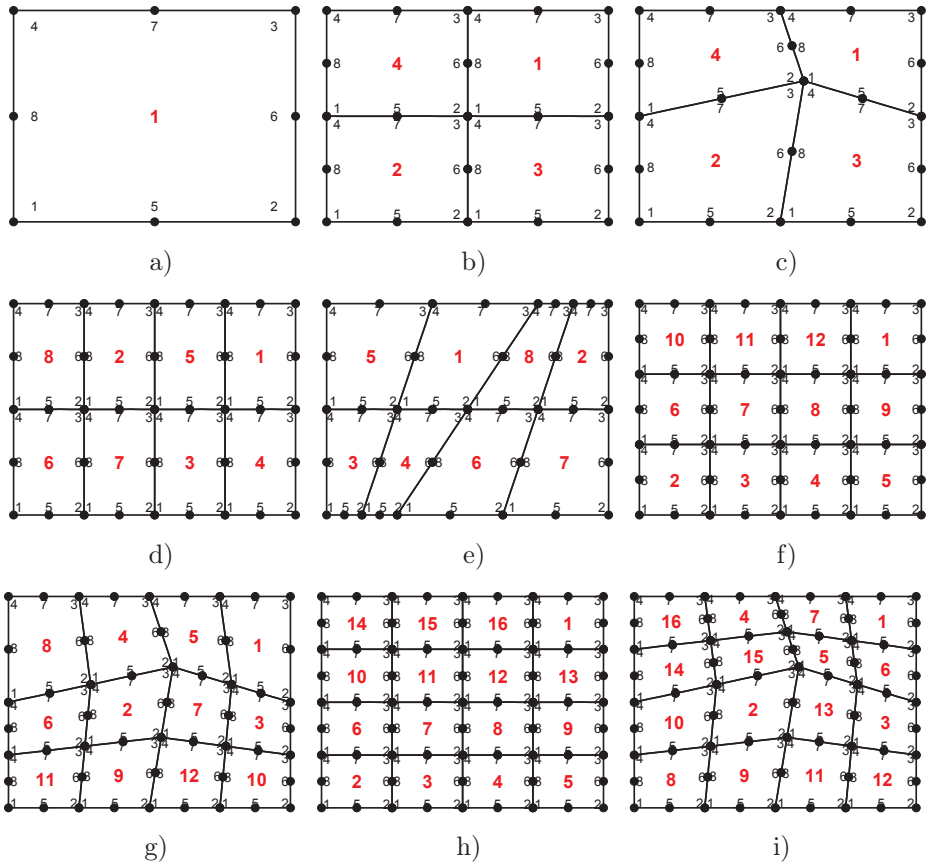

Figure 2.5: GDQFEM meshes for a rectangular membrane: a) single element, b) four elements, c) four skewed elements, d) eight elements, e) eight skewed elements, f) twelve elements, g) twelve skewed elements, h) sixteen elements, i) sixteen skewed elements.

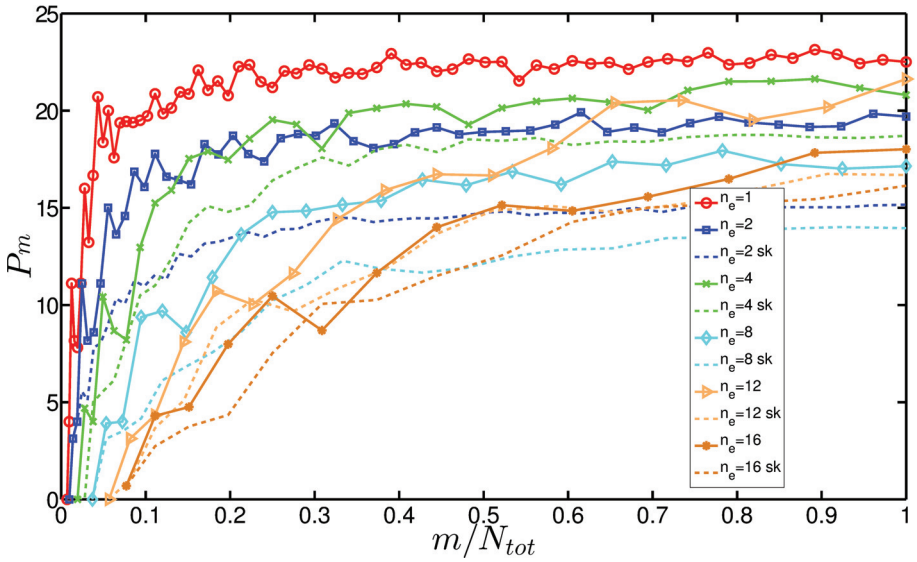

a)

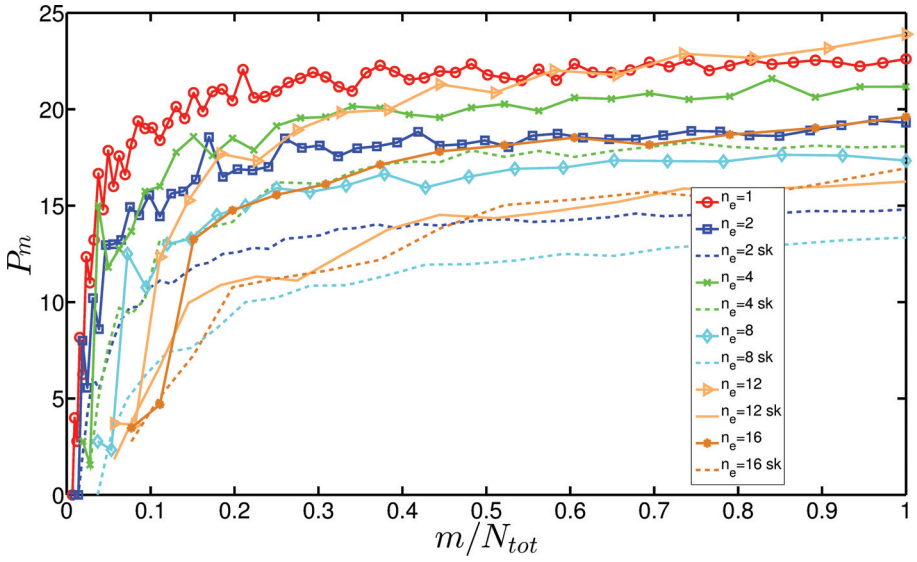

b)

Figure 2.6: Modal shape percentages for rectangular membrane: a) Chebyshev-Gauss-Lobatto grid distribution, b) Legendre grid distribution.

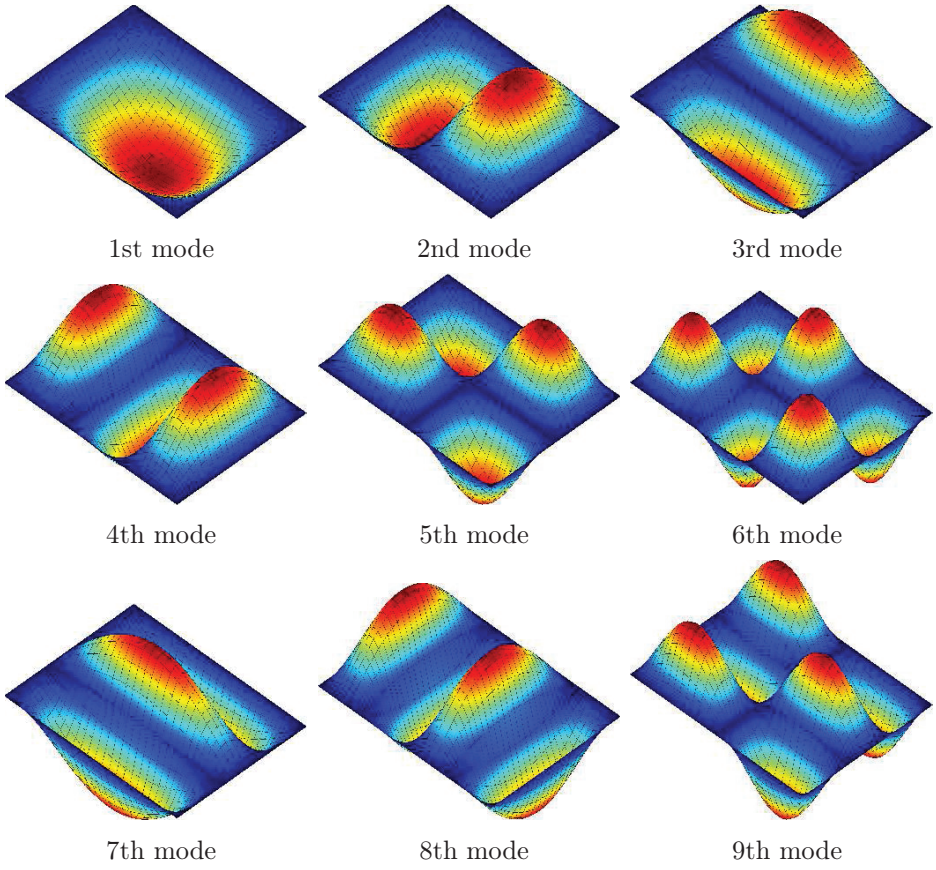

Figure 2.7: First 9 mode shapes for the rectangular membrane.

2.4.2 Circular membrane

Considering a clamped circular membrane with thickness h, radius R and mass density ρ is subjected to a uniform radial force per unit length T acting on its edge. The natural frequencies of vibration are identified by two integers (m, n) that characterize the mode shape. The index $m = 1, 2, 3, \ldots$ correspond to the number of circumferential lines, with r =constant, on the membrane that have zero displacement, whereas $n = 1, 2, 3, \ldots$ corresponds to the number of diametrical lines, with θ = constant, that have zero displacement. The natural frequencies of vibration are obtained by solving the differential equation of the membrane (2.1) written in polar coordinates

$$T\left(\frac{\partial^2 w}{\partial r^2} + \frac{1}{r}\frac{\partial w}{\partial r} + \frac{1}{r^2}\frac{\partial^2 w}{\partial \theta^2}\right) = \rho h \frac{\partial^2 w}{\partial t^2} \tag{2.17}$$

The general solution to this equation, which can be found by separation of variables [63], [14], is

$$w(r,\theta) = (AJ_n(k_{mn}r)\sin(n\theta + \theta_0) + BY_n(k_{mn}r)\sin(n\theta + \theta_1))\cos(\omega_{mn}t + \phi) \tag{2.18}$$

where $k_{mn} = \sqrt{\rho h/T}$, A, B, θ_0, θ_1, ϕ are arbitrary constants, and J_n, Y_n are Bessel functions of the first and the second kind, with order n, respectively. The solution must satisfy $w(\theta) = w(2\pi + \theta)$, which is only possible if n is an integer. Moreover the Bessel function of the second kind is infinite at $r = 0$, this implies $B = 0$. The transverse displacement must satisfy the boundary conditions $w = 0$ on the edge of the membrane, which leads to the condition

$$J_n(\omega_{mn}R\sqrt{\rho h/T}) = 0 \tag{2.19}$$

In conclusion, the problem of finding the natural frequencies of a circular membrane is transferred to find the zeros of the Bessel function of the first kind J_n.

Table 2.2 shows the first ten eigenfrequencies of a circular membrane of unit radius $R = 1$ m obtained by using GDQFEM with a single element (with 8 and 12 nodes), a four element mesh and a twelve element mesh all compared to some results found in literature [77], [79], [84]. It is noted how more accurate is a 12 node element respect to the 8 node one. This happens because the boundary of the circular membrane is not straight so more points are needed in order to apply the mapping technique accurately.

Figure 2.8 represents the four different meshes reported in Table 2.2. Figure 2.8a is a single element with 8 nodes, Figure 2.8b is a single element with 12 nodes, which has a mapping accuracy better than the previous one as demonstrated in Table 2.2. In Figure 2.8c, d are depicted a four element and a twelve element mesh, respectively. In conclusion the first fifteen modal shapes of the circular membrane are graphically presented in Figure 2.9, that have been generated by a single 12 node element with 41×41 grid.

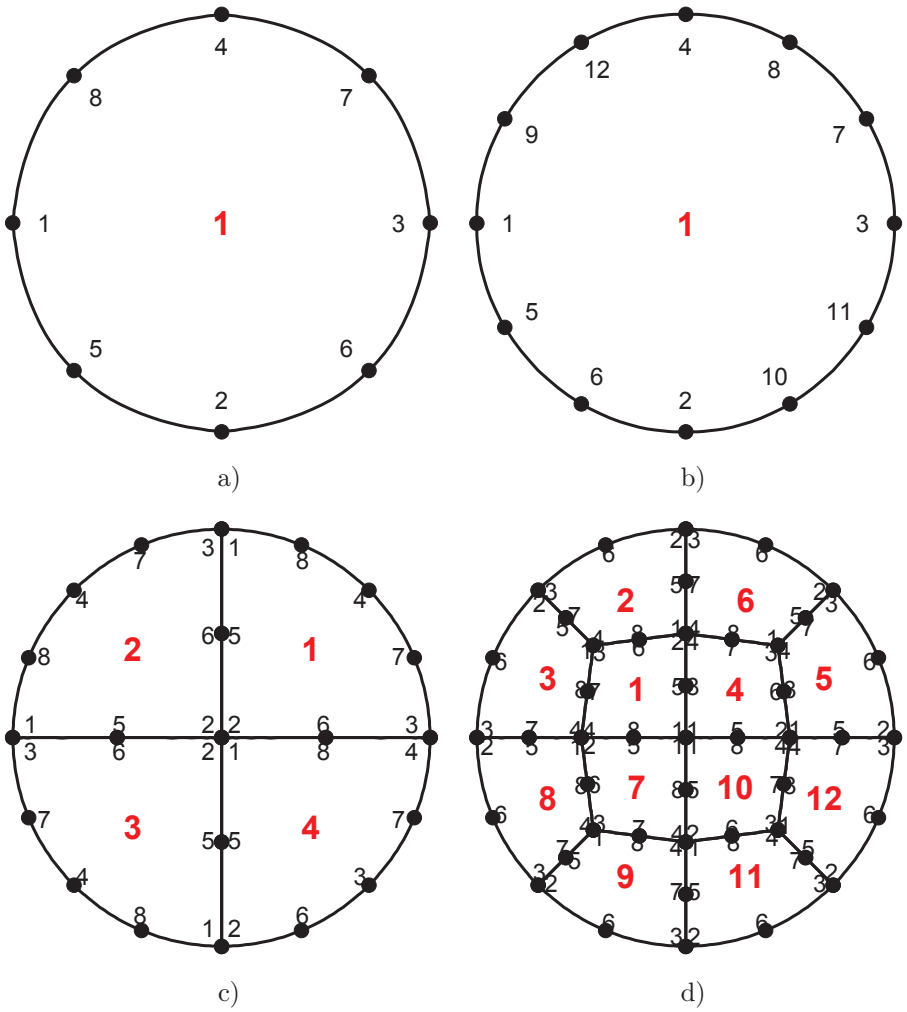

Figure 2.8: GDQFEM meshes for circular membrane: a) single element (8 nodes), b) single element (12 nodes), c) four elements, d) twelve elements.

Λ	Exact	Ref. [77]	FEM [77]	Ref. [79]	Ref. [84]	GDQFEM			
						$n_e = 1$ $N = 41$ (8 nodes)	$n_e = 1$ $N = 41$ (12 nodes)	$n_e = 4$ $N = 21$ (8 nodes)	$n_e = 12$ $N = 21$ (8 nodes)
1	2.4048	2.4048	2.4166	2.405	2.4047	2.41939	2.40301	2.40576	2.40576
2	3.8317	3.8317	3.8513	3.832	3.8316	3.85488	3.82881	3.83320	3.83320
3	5.1356	5.1356	5.1744	5.136	5.1356	5.15778	5.12694	5.13763	5.13763
4	5.5201	5.5201	5.5515	5.520	5.5202	5.55333	5.51588	5.52223	5.52223
5	6.3802	6.3802	6.4610	6.380	6.3802	6.41845	6.37528	6.38265	6.38265
6	7.0156	7.0156	7.0592	7.016	7.0158	7.05795	7.01029	7.01832	7.01832
7	7.5883	7.5876	7.7445	7.588	7.5884	7.62043	7.58610	7.59036	7.59224
8	8.4172	8.4172	8.4841	-	8.4174	8.45279	8.41863	8.42053	8.42053
9	8.6537	-	-	-	-	8.70591	8.64721	8.65710	8.65710
10	8.7715	-	-	-	-	8.82411	8.76481	8.77490	8.77490

Table 2.2: First ten eigenfrequencies of a circular membrane of radius $R = 1$ m.

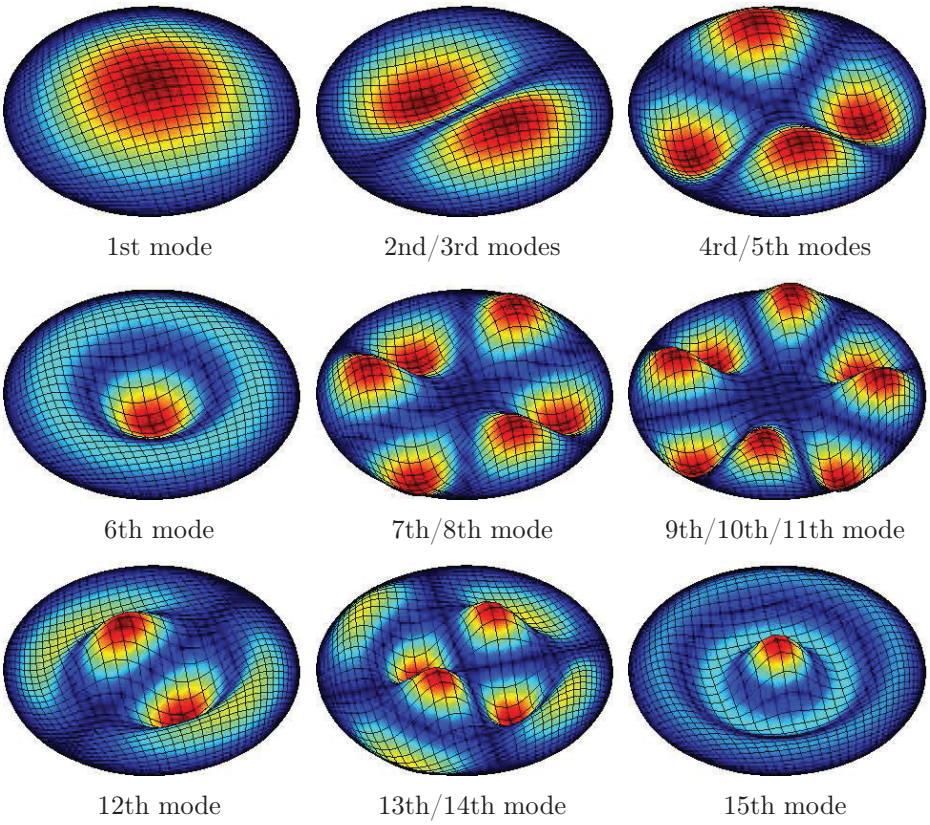

Figure 2.9: First 15 mode shapes for the circular membrane.

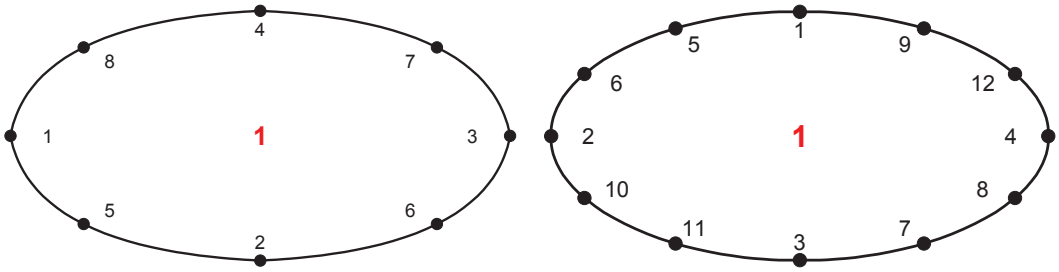

Figure 2.10: GDQFEM meshes of an elliptic membrane with $a/b = 2$: a) single element (8 nodes), b) single element (12 nodes).

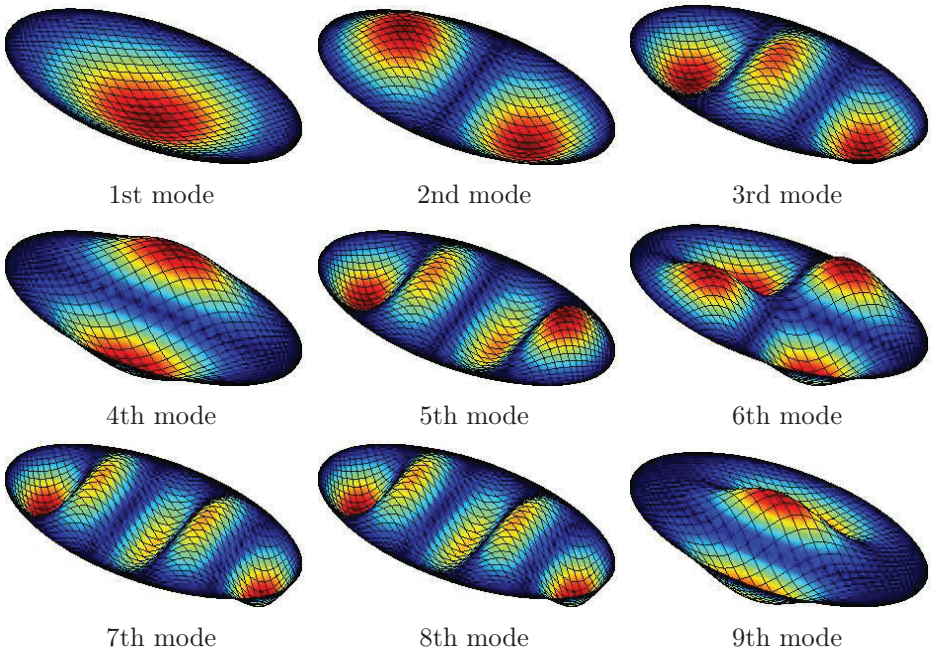

Figure 2.11: First 9 mode shapes for an elliptic membrane with $a/b = 2$.

2.4.3 Elliptic membrane

An elliptic membrane is considered in the following. Its major and minor axes are $2a$ and $2b$ respectively, as a result the major and minor semi-axes are a and b. Four different ellipses within three different a/b ratios are considered, $a/b = 1.5, 2, 2.5, 3$. It is noted that for $a/b = 1$ the ellipse becomes a circle. So increasing the ratio a/b the geometry tends to be every step more distorted. In Figure 2.10 a single element mesh with 12 and 8 nodes are depicted. It is more clear in this case respect to the previous one that the 12 nodes element is more suitable for solving the problem because the 8 nodes element is not sufficient for mapping the elliptical curve. In fact from Table 2.3, where the first ten eigenfrequencies are reported, the solution given by the 8 nodes single element mesh do not agree with the literature [62] and the solutions obtained with other geometries. In conclusion, in Figure 2.11 the first nine modal shapes are depicted for a single element mesh with 12 nodes and $N = 41$ for a $a/b = 2$ semi-axes ratio.

Λ	$a/b = 1.5$				$a/b = 2$			
	Ref. [62]	GDQFEM			Ref. [62]	GDQFEM		
		$n_e = 1$ $N = 41$ (12 nodes)	$n_e = 1$ $N = 41$ (8 nodes)	$n_e = 12$ $N = 21$ (8 nodes)		$n_e = 1$ $N = 41$ (12 nodes)	$n_e = 1$ $N = 41$ (8 nodes)	$n_e = 12$ $N = 21$ (8 nodes)
1	2.041	2.04125	2.05179	2.03991	1.892	1.88664	1.90085	1.88931
2	-	2.91870	2.93087	2.91676	-	2.50476	2.51751	2.50603
3	-	3.54806	3.56927	3.54623	-	3.16637	3.18140	3.16812
4	-	3.83828	3.86340	3.84253	-	3.42067	3.45093	3.42725
5	-	4.35050	4.35941	4.33940	-	3.85438	3.88067	3.85857
6	-	4.78022	4.82423	4.79099	-	3.98824	4.01469	3.99180
7	-	5.10449	5.14018	5.10483	-	4.56093	4.59722	4.56743
8	-	5.18280	5.18731	5.17220	-	4.58702	4.60023	4.58714
9	-	5.73312	5.78934	5.74859	-	4.97991	5.02613	4.99065
10	-	5.89534	5.91463	5.88134	-	5.20583	5.22263	5.20636
Λ	$a/b = 2.5$				$a/b = 3$			
	Ref. [62]	GDQFEM			Ref. [62]	GDQFEM		
		$n_e = 1$ $N = 41$ (12 nodes)	$n_e = 1$ $N = 41$ (8 nodes)	$n_e = 12$ $N = 21$ (8 nodes)		$n_e = 1$ $N = 41$ (12 nodes)	$n_e = 1$ $N = 41$ (8 nodes)	$n_e = 12$ $N = 21$ (8 nodes)
1	1.814	1.80810	1.82256	1.81098	-	1.76060	1.77539	1.76368
2	-	2.28123	2.29320	2.28243	-	2.14296	2.15527	2.14436
3	-	2.78894	2.79902	2.78956	-	2.55231	2.56014	2.55249
4	-	3.31984	3.33741	3.32196	-	2.98059	2.99295	2.98156
5	-	3.35594	3.38672	3.36295	-	3.31540	3.34621	3.32264
6	-	3.79614	3.82656	3.80099	-	3.42486	3.44266	3.42679
7	-	3.86887	3.89416	3.87258	-	3.67487	3.70826	3.68072
8	-	4.26006	4.27587	4.26104	-	3.88112	3.90673	3.88483
9	-	4.43072	4.46537	4.43668	-	4.05295	4.07224	4.05491
10	-	4.73908	4.75322	4.73946	-	4.34719	4.38013	4.35257

Table 2.3: First ten eigenfrequencies of an elliptic membrane for three values of a/b.

Λ	Ref. [77]	FEM [77]	Ref. [79]	FEM [79]	Ref. [84]	GDQFEM			
						$n_e = 1$ $N = 41$ (8 nodes)	$n_e = 1$ $N = 41$ (12 nodes)	$n_e = 3$ $N = 21$ (8 nodes)	$n_e = 12$ $N = 21$ (8 nodes)
1	2.7097	2.7230	2.709	2.728	2.7106	2.71992	2.71063	2.71121	2.71121
2	4.2279	4.2598	4.225	4.270	4.2310	4.24701	4.23211	4.23294	4.23294
3	4.3579	4.3786	4.359	4.386	4.3579	4.37239	4.35778	4.35878	4.35878
4	5.5649	5.6336	5.559	5.656	5.5728	5.59987	5.56888	5.57401	5.57401
5	5.9336	5.9846	5.934	6.003	5.9339	5.94775	5.93730	5.93525	5.93525
6	6.1159	6.1641	6.114	6.181	6.1180	6.13819	6.11819	6.11931	6.11931
7	6.9974	7.1334	6.985	7.117	7.0134	7.05239	7.00729	7.01465	7.01465
8	7.1868	7.3002	7.186	7.340	7.1880	7.21106	7.18680	7.18967	7.18967
9	-	-	-	-	-	7.77899	7.76632	7.76426	7.76426
10	-	-	-	-	-	7.85995	7.83897	7.83837	7.83837

Table 2.4: First 10 eigenfrequencies of an arbitrarily shaped membrane.

2.4.4 Arbitrarily shaped membrane

The free vibration analysis is carried out for an arbitrarily shaped membrane. In this case an exact solution do not exist. The membrane geometry is composed of a half-circle of a unit radius $R = 1$, and a triangle of sides $L = \sqrt{2}$, this kind of shape has been widely used in literature [77, 79, 84] and it is depicted in Figure 2.12 for several GDQFEM meshes. Since previous authors have done a very good work in the past [77, 79, 84], for sake of conciseness not all the geometric details are graphically reported in this paper.

This kind of shape has two geometrical issues given by the circle and the triangle, because both of them are not well represented by a quadrilateral element. Although this problem has been solved by using one irregular element only, the results suit the eigenfrequencies given by literature. The first 10 eigenfrequencies Λ_i are presented in Table 2.4 for a single element mesh and two subdivided meshes or three and twelve elements. It is noted that all the results obtained by using GDQFEM are in good agreement with the proposed results by literature. It is underlined that the geometric mapping with the 12-nodes element works better that the 8-nodes one, because it can capture the geometric circle shape better, so the coordinate transformation is better accomplished. In fact the results obtained with a 12-nodes single element are similar to a mesh composed of 12 elements with 8 nodes. The first nine modal shapes for the current structure is graphically presented in Figure 2.13.

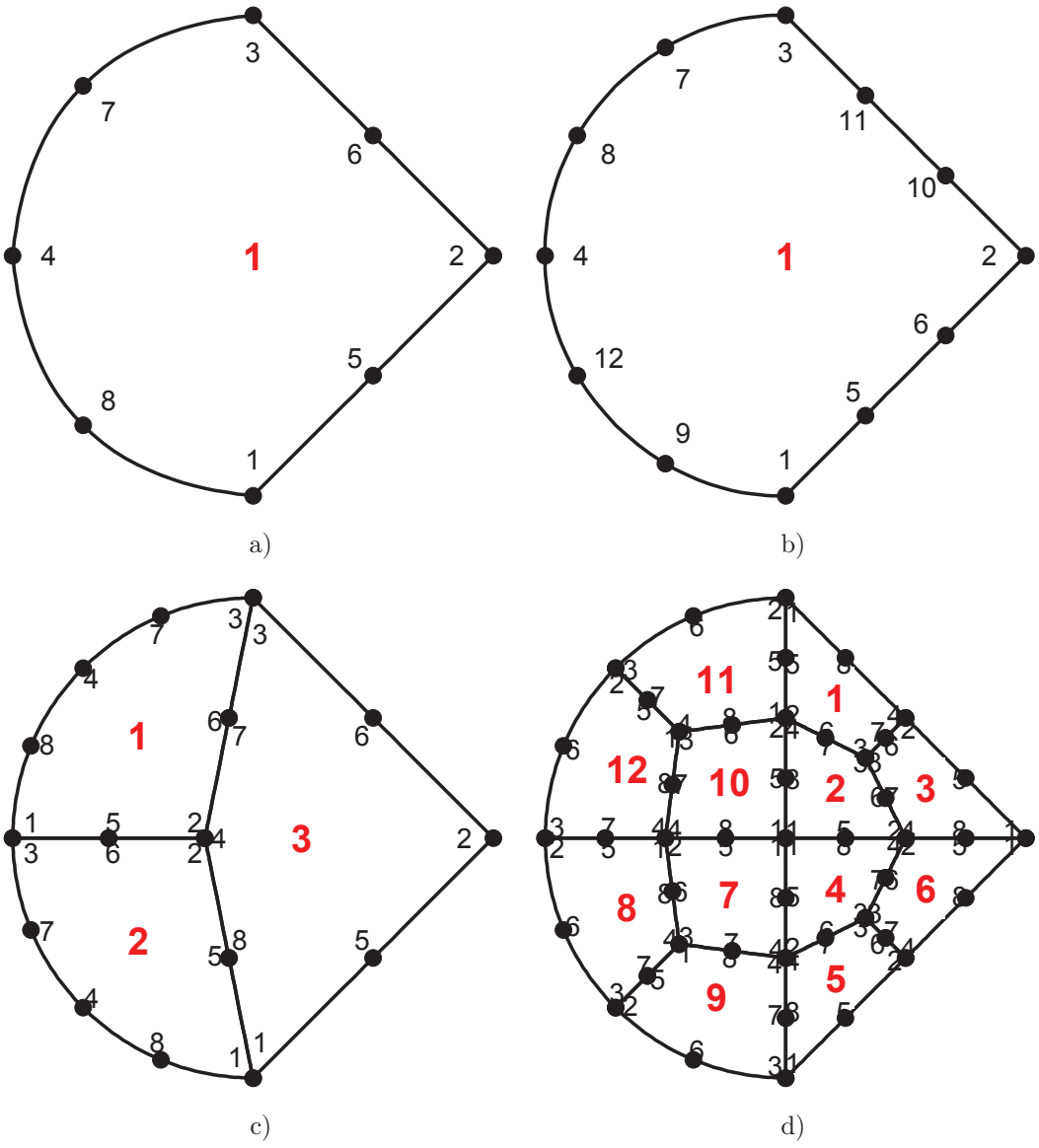

Figure 2.12: GDQFEM meshes for arbitrarily shaped membrane: a) Single element, b) Single element with 12 nodes, c) Three elements, d) Twelve elements.

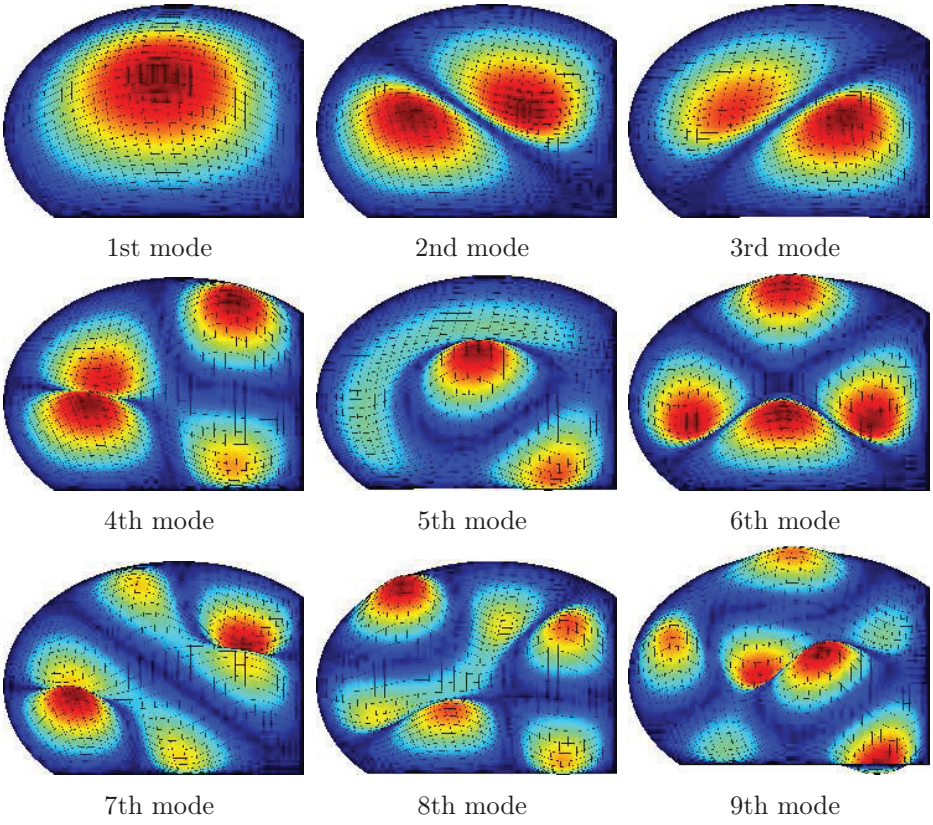

Figure 2.13: First 9 mode shapes for the arbitrarily shaped membrane.

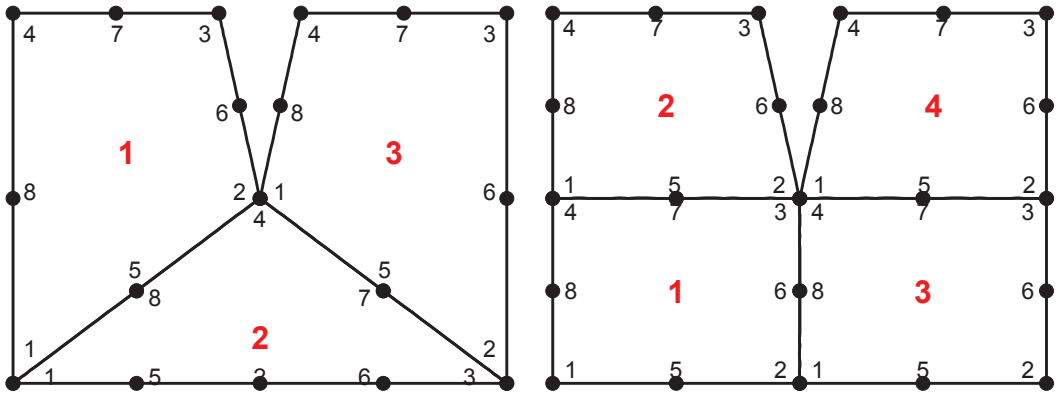

Figure 2.14: GDQFEM meshes for concave with high concavity membrane: a) Three elements, b) Four elements.

2.4.5 Concave membrane with high concavity

In order to obtain the eigenvalues of a concavely shaped membrane with high concavity, the GDQFEM is applied to rectangular membrane with a partially concave region, as shown in [78, 84, 85]. The concavity cuts a regular rectangle of $a = 1.2$ m and $b = 0.9$ at its half (for further details see what is reported in [78, 84, 85]). In Figure 2.14 two GDQFEM meshes are presented. Figure 2.14a presents a mesh with three elements in which one is a triangle (degenerate quadrilateral element) and in Figure 2.14b a four element more regular mesh is depicted. This kind of geometry has the main issue of being highly distorted so more than one element is needed to map it correctly. In Table 2.5 the first ten eigenfreqencies Λ_i are presented. It can be said that the first ten eigenvalues obtained by the present method are accurate compared with those obtained by literature [78, 84, 85]. It is underlined that a single-domain method can not be applied because the element shape must satisfy the Jacobian transformation, and in this case with high concavity the transformation matrix degenerates due to the geometric distortion. However a three element mesh (see Figure 2.14a) can be used even though one the elements degenerates into a triangle. Increasing the number of points upon each edge the results tend to the reference solutions, in fact it is clear from Table 2.5 that $N = 7$ is not sufficient to get the solution. Furthermore, the first nine modal shapes are depicted in Figure 2.15 for a four elements mesh.

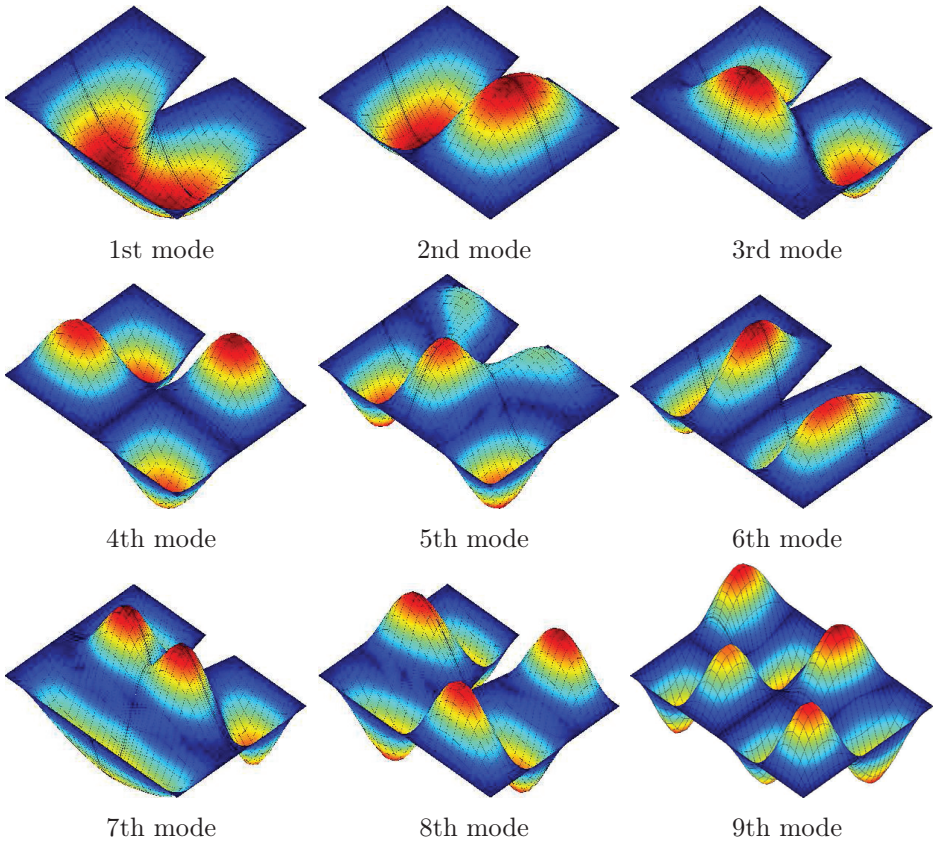

Figure 2.15: First 9 mode shapes for the highly concave shape membrane.

Λ	Ref. [78]	FEM [78]	Ref. [84]	Ref. [85]	FEM [85]	GDQFEM			
						$n_e = 3$ $N = 7$	$n_e = 3$ $N = 21$	$n_e = 4$ $N = 7$	$n_e = 4$ $N = 21$
1	5.79	5.71	5.7470	5.73	5.71	5.66509	5.69058	5.66305	5.69032
2	6.42	6.42	6.4186	6.43	6.42	6.41852	6.41887	6.41877	6.41887
3	8.15	8.17	8.1733	8.12	8.17	8.15453	8.15976	8.15322	8.15970
4	8.88	8.89	8.8845	8.89	8.89	8.88306	8.88430	8.88423	8.88430
5	9.92	9.87	9.8757	9.84	9.87	9.81900	9.83697	9.82108	9.83679
6	11.25	11.31	11.2627	11.27	11.31	11.35337	11.26363	11.29974	11.26363
7	11.55	11.46	11.4503	-	-	11.41094	11.41339	11.40127	11.41322
8	11.81	11.84	11.8172	-	-	11.86147	11.81728	11.81822	11.81728
9	-	-	-	-	-	12.50875	12.43991	12.46745	12.43990
10	-	-	-	-	-	13.15245	13.03749	13.07237	13.03749

Table 2.5: First ten eigenfrequencies of a concave membrane.

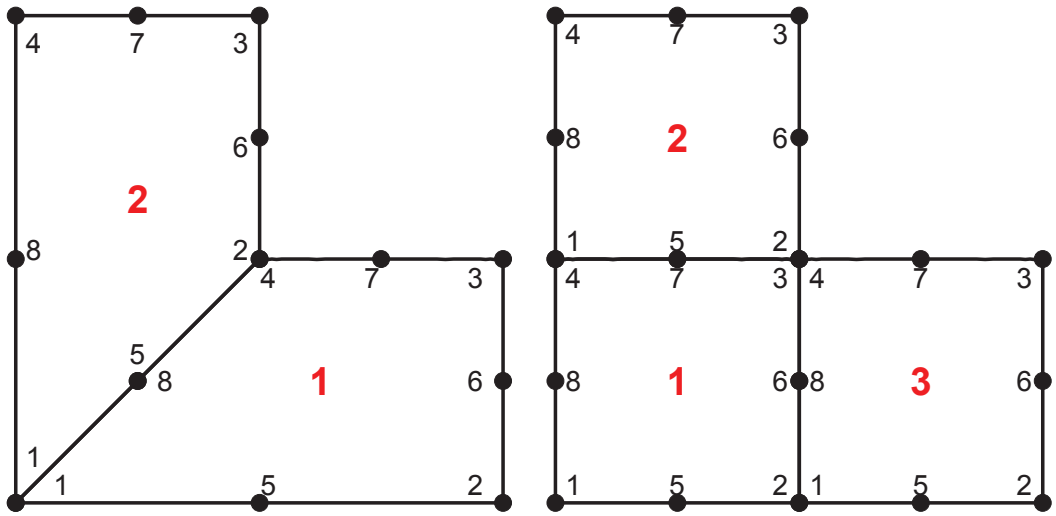

Figure 2.16: GDQFEM meshes for L-shaped membrane: a) Two elements, b) Three elements.

Λ	Ref. [78]	Ref. [78]	FEM [78]	Ref. [84]	Ref. [85]	FEM [85]	Ref. [86]	GDQFEM	
								$n_e = 2$ $N = 21$	$n_e = 3$ $N = 21$
1	3.16	3.14	3.11	3.1124	3.10	3.11	3.11	3.10478	3.10463
2	3.89	3.89	3.90	3.8982	3.93	3.90	3.9	3.89837	3.89837
3	4.44	4.44	4.45	4.4429	4.46	4.45	4.44	4.44288	4.44288
4	5.43	5.43	5.44	5.4334	5.45	5.44	5.44	5.43337	5.43337
5	5.72	5.70	5.67	5.6593	5.62	5.68	5.44	5.64912	5.64892
6	6.49	6.48	6.47	6.4469	6.47	6.47	5.83	6.44006	6.43993
7	6.68	6.69	6.73	6.7039	-	-	-	6.70436	6.70436
8	7.03	7.03	7.05	7.0249	-	-	-	7.02481	7.02481
9	-	-	-	-	-	-	-	7.02481	7.02481
10	-	-	-	-	-	-	-	7.53057	7.53045

Table 2.6: First ten eigenfrequencies of a L-shaped membrane.

2.4.6 L-shaped membrane

Figure 2.16 shows the GDQFEM discretized models for a L-shaped membrane with equal sides. The longest edge is $L = 2$ m and the shortest one $l = 1$ m. The total domain is divided into two (Figure 2.16a) or three (Figure 2.16b) sub-domains. No 12-node elements are needed in this case because there is no curved boundaries in this model. It is noted from Table 2.6 that the solution with two elements is enough to capture the first ten eigenvalues considering $N = 21$. The results are compared with some others found in literature [78, 84–86]. Moreover, the first nine modal shapes are presented in Figure 2.17 for a two element mesh.

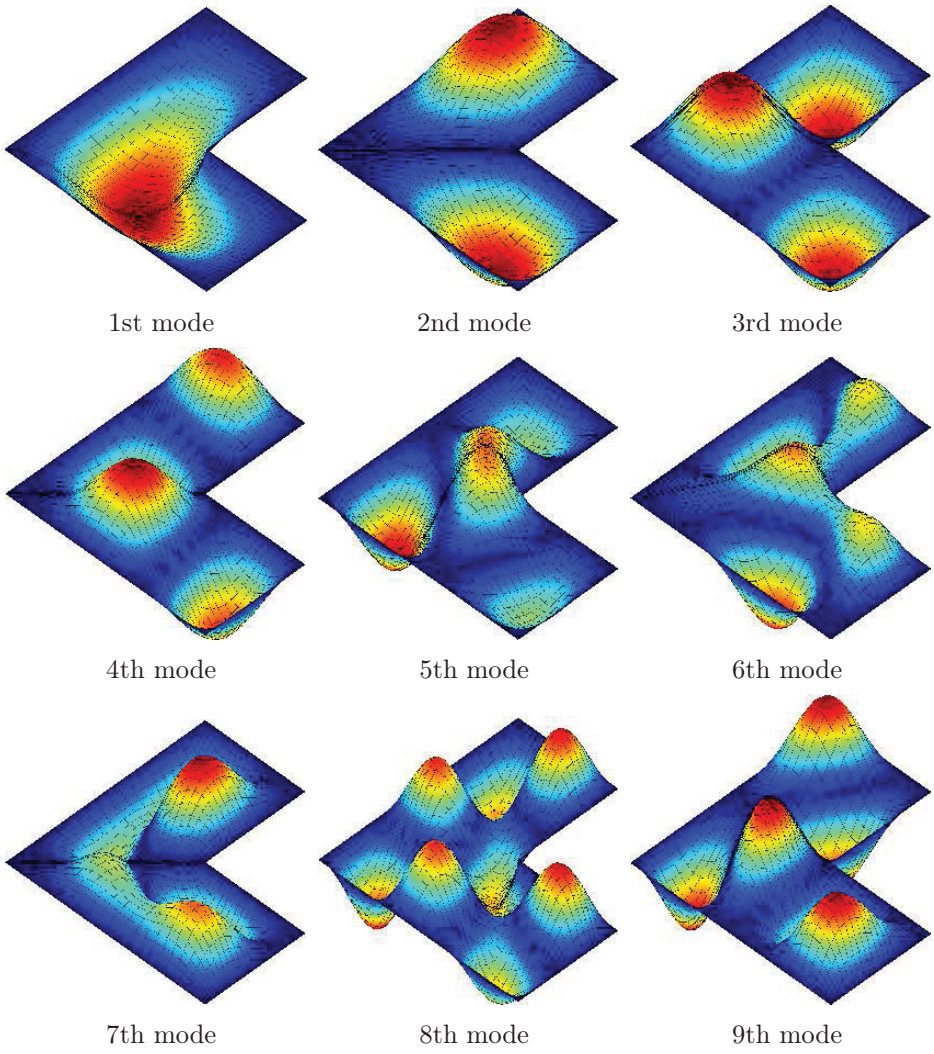

Figure 2.17: First 9 mode shapes for the L-shape membrane.

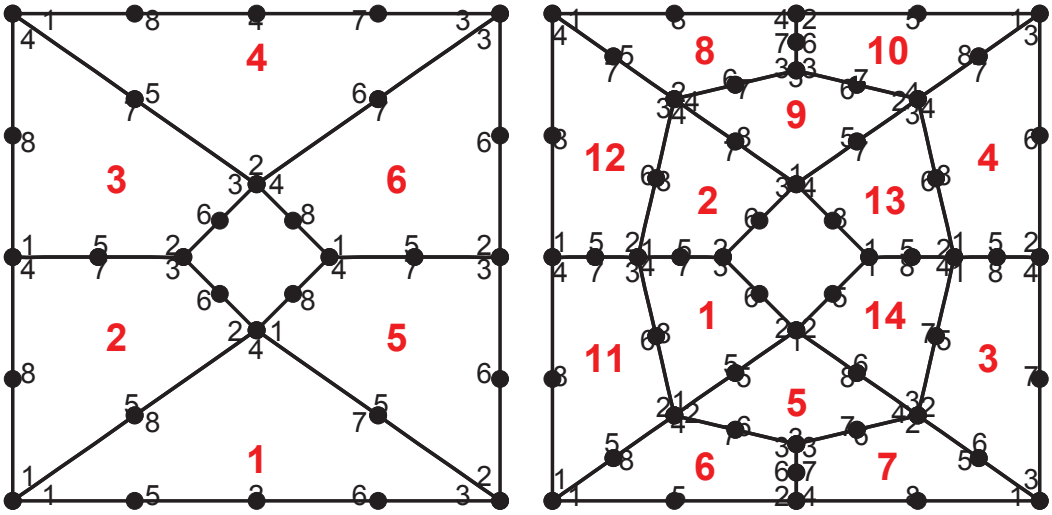

a) b)

Figure 2.18: GDQFEM meshes for square membrane with a rhombic hole: a) Six elements, b) Fourteen elements.

Λ	Ref. [78]	FEM [78]	Ref. [84]	GDQFEM					
				$n_e = 6$ $N = 7$	$n_e = 6$ $N = 15$	$n_e = 6$ $N = 21$	$n_e = 14$ $N = 7$	$n_e = 14$ $N = 15$	$n_e = 14$ $N = 21$
1	3.71	3.67	3.6731	3.63607	3.64121	3.64161	3.63739	3.64131	3.64164
2	4.00	3.99	3.9800	3.95333	3.96145	3.96201	3.95826	3.96197	3.96219
3	4.50	4.53	4.5084	4.50788	4.50948	4.50948	4.50942	4.50948	4.50948
4	5.27	5.19	5.1964	5.16035	5.16727	5.16764	5.16338	5.16736	5.16766
5	5.90	5.89	5.8615	5.84206	5.84782	5.84822	5.84567	5.84818	5.84834
6	6.48	6.51	6.4344	6.41746	6.40876	6.40909	6.40605	6.40885	6.40911
7	7.03	7.07	7.0287	7.03138	7.02895	7.02895	7.02867	7.02895	7.02895
8	7.12	7.24	7.1156	7.11596	7.10775	7.10805	7.10606	7.10803	7.10815
9	7.23	7.39	7.2455	7.34050	7.24790	7.24790	7.24746	7.24790	7.24790
10	7.77	7.73	7.7211	7.71306	7.70686	7.70706	7.70529	7.70692	7.70707

Table 2.7: First ten eigenfrequencies of a square membrane with a hole.

2.4.7 Square membrane with a rhombic hole

As shown in Figure 2.18 two discretized models can be used to find the eigenvalues of a square membrane with a rhombic hole [18,24]. The geometry is composed of a square of side $L = 2$ m with a centred rhombic hole of side $l = 0.5$ m. In Figure 2.18a a 6 element mesh is reported and it is the mesh with the lowest number of element possible for this geometry, then in Figure 2.18b a fourteen elements mesh is depicted. It should be noted that both the boundaries the external and the internal one are fixed in order to satisfy the membrane equation (2.1). Moreover, the six element mesh, used in the analysis, is composed of two triangular elements (quadrilateral degenerated elements) and four irregular quadrilateral elements. In spite of that, the numerical solutions are in very good agreement with the others found in literature [18,24] (see Table 2.7). In Table 2.7 the two presented meshes have been solved for different number of grid points $N = 7$, $N = 15$, $N = 21$. In addition, the first twelve modal shapes are represented in Figure 2.19.

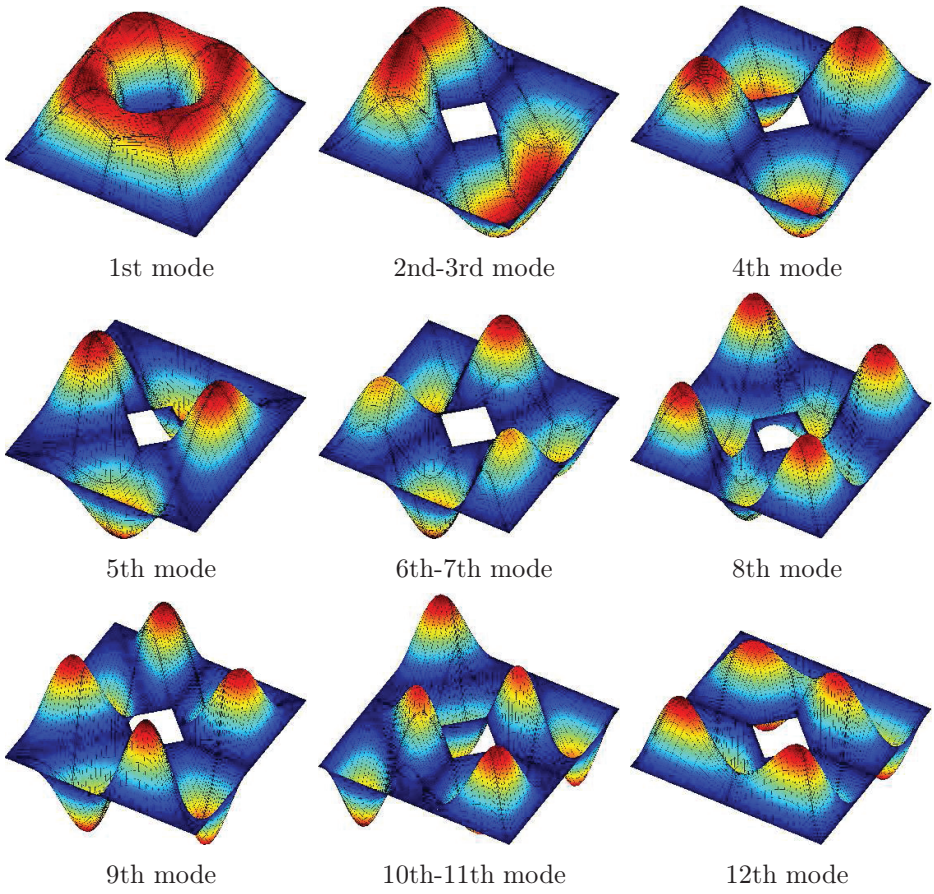

Figure 2.19: First 9 mode shapes for the L-shape membrane.

Λ	Ref. [81]	FEM [81]	GDQFEM						
			$n_e = 1$ $N = 7$	$n_e = 1$ $N = 15$	$n_e = 1$ $N = 21$	$n_e = 1$ $N = 41$	$n_e = 4$ $N = 7$	$n_e = 4$ $N = 15$	$n_e = 4$ $N = 21$
1	3.81	3.81	3.79961	3.79970	3.79970	3.79970	3.79968	3.79970	3.79970
2	5.28	5.29	5.28189	5.25530	5.25530	5.25530	5.25523	5.25530	5.25530
3	6.57	6.58	6.52742	6.56287	6.56287	6.56287	6.56282	6.56287	6.56287
4	7.06	7.07	6.85693	7.02835	7.02835	7.02835	7.02756	7.02835	7.02835
5	7.60	7.62	7.65102	7.57808	7.57808	7.57808	7.57907	7.57808	7.57808
6	8.73	8.75	8.77546	8.69734	8.69734	8.69734	8.71887	8.69734	8.69734
7	9.03	9.06	9.37736	8.98051	8.98052	8.98052	8.99064	8.98052	8.98052
8	9.73	9.78	10.00105	9.72533	9.72533	9.72533	9.72565	9.72533	9.72533
9	-	-	11.02739	10.08759	10.08759	10.08759	10.10097	10.08759	10.08759
10	-	-	13.26855	10.46275	10.46297	10.46297	10.51129	10.46297	10.46297

Table 2.8: First ten eigenfrequencies of a trapezoidal membrane (first type).

Λ	Ref. [85]	FEM [85]	GDQFEM						
			$n_e = 1$ $N = 41$	$n_e = 4$ $N = 21$	$n_e = 16$ $N = 21$	$n_e = 4$ $N = 7$ dist.	$n_e = 4$ $N = 21$ dist.	$n_e = 16$ $N = 7$ dist.	$n_e = 16$ $N = 21$ dist.
1	1.90	1.89	1.89725	1.89725	1.89725	1.89725	1.89725	1.89725	1.89725
2	2.88	2.88	2.88383	2.88383	2.88383	2.88381	2.88383	2.88383	2.88383
3	3.08	3.08	3.08253	3.08253	3.08253	3.08255	3.08253	3.08253	3.08253
4	3.80	3.79	3.80064	3.80064	3.80064	3.80188	3.80064	3.80063	3.80064
5	3.99	3.99	4.00871	4.00871	4.00871	4.01338	4.00871	4.00871	4.00871
6	4.36	4.35	4.35744	4.35744	4.35744	4.36605	4.35744	4.35742	4.35744
7	-	-	4.73760	4.73760	4.73760	4.74824	4.73760	4.73762	4.73760
8	-	-	4.99037	4.99037	4.99037	4.99489	4.99037	4.99037	4.99037
9	-	-	5.12632	5.12632	5.12632	5.14672	5.12632	5.12634	5.12632
10	-	-	5.62843	5.62843	5.62843	5.61886	5.62843	5.62852	5.62843

Table 2.9: First ten eigenfrequencies of a trapezoidal membrane (second type).

2.4.8 Trapezoidal membrane

A trapezoidal membrane is considered in the following. Two different reference geometries have been found in literature. One has been studied by Kang et al. [81] and another geometry was widely shown in the work by Kang et al. [85]. For more details about the two geometries it is suggested referring to [81, 85]. In Figure 2.20 all the used GDQFEM meshes are represented. Tables 2.8, 2.9 summarise the first ten eigenfrequencies for the two trapezoidal geometries compared to the same results found in literature. Several grid point numbers have been used $N = 7$, $N = 15$, $N = 21$ and for single element mesh $N = 41$. All the presented results are in good agreement with the same in literature. It should be noted that some distorted meshes have been applied in this study showing that there is good accordance for a distorted mesh too (see Table 2.9). Moreover, the first nine modal shapes are depicted in Figure 2.21.

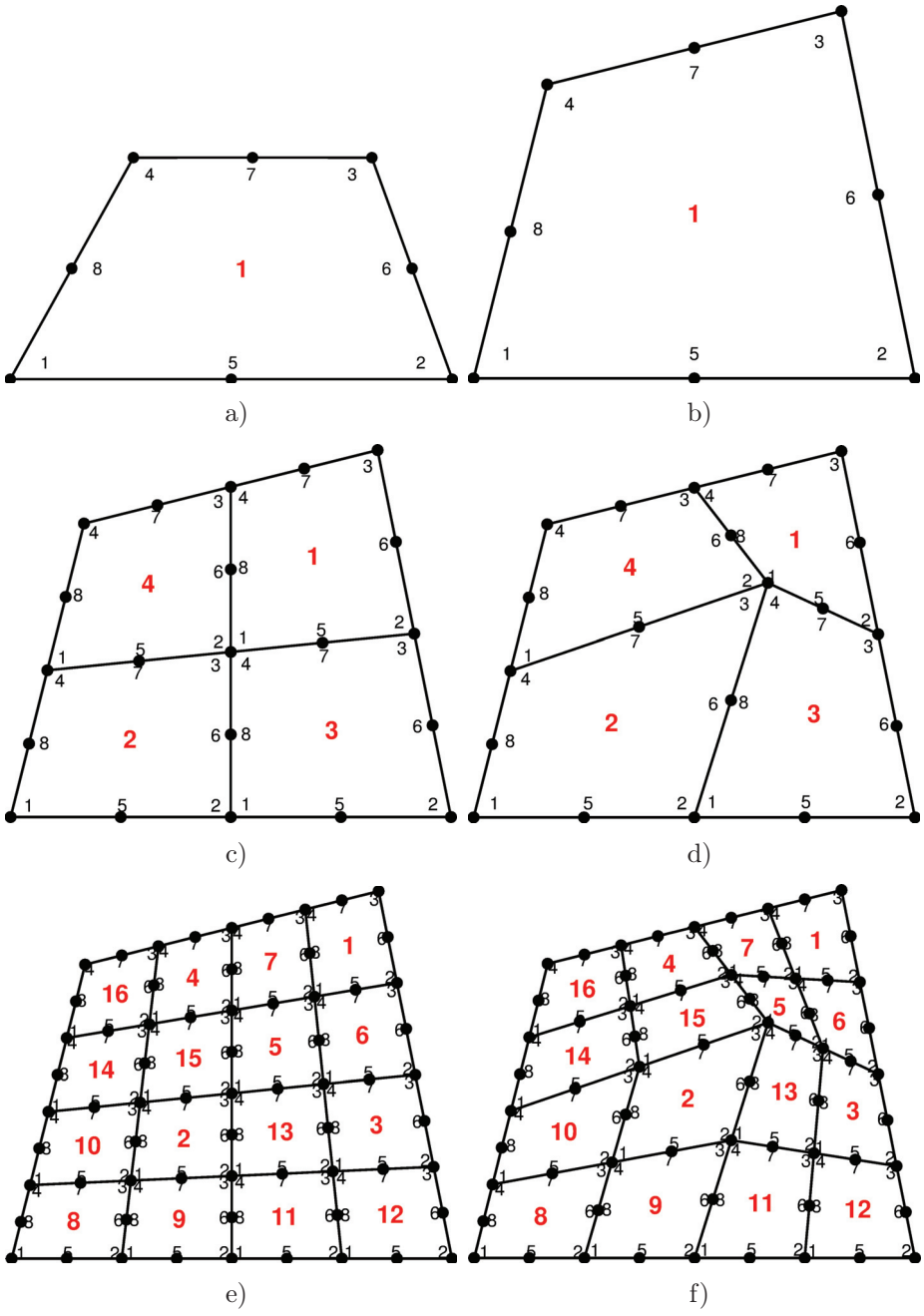

Figure 2.20: GDQFEM meshes for trapezoidal membrane: a) Single element (first type), b) Single element (second type), c) Four elements, d) Four elements distorted, e) Sixteen elements, f) Sixteen elements distorted.

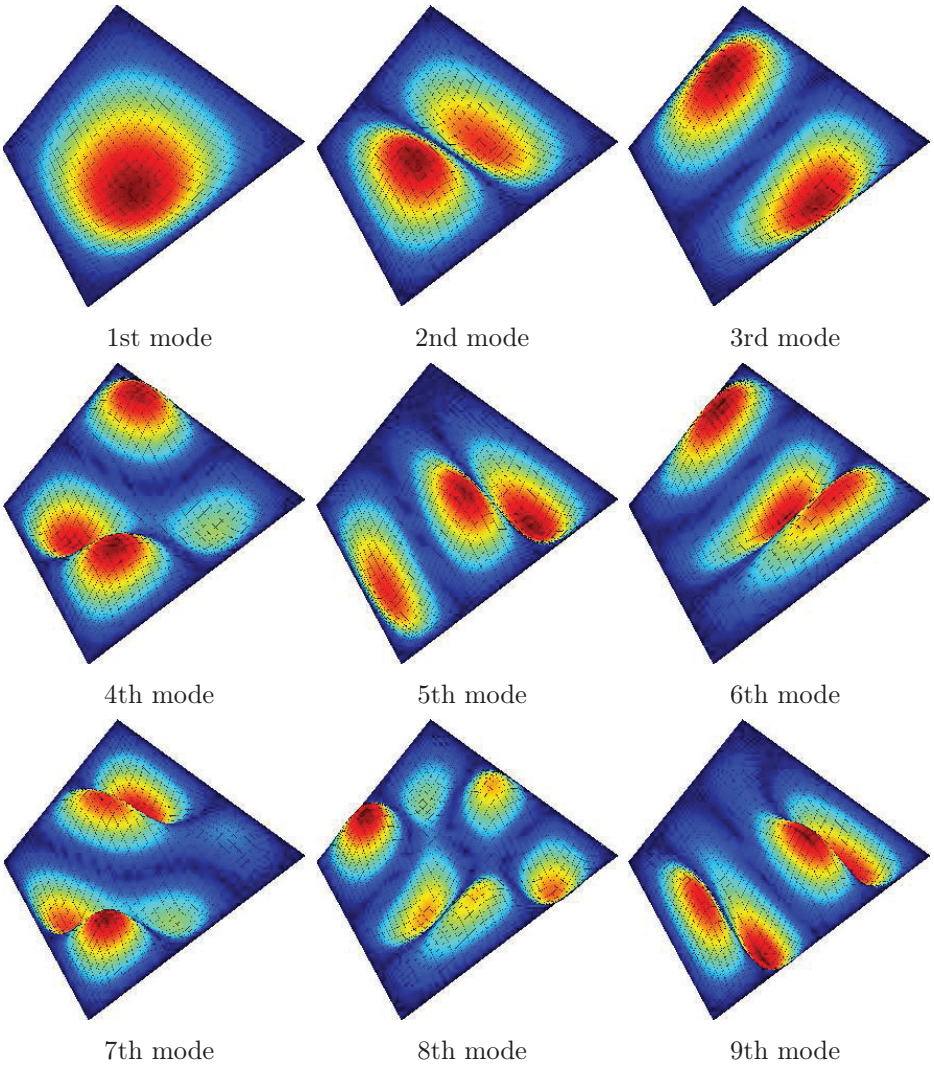

Figure 2.21: First 9 mode shapes for the trapezoidal membrane.

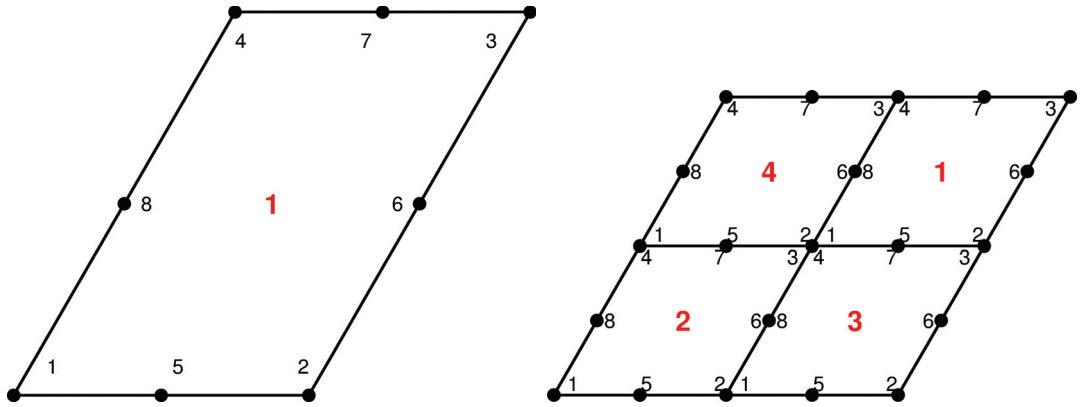

Figure 2.22: GDQFEM meshes for skewed or rhombic membrane for a skew angle of $\theta = \pi/3$: a) Single element, b) Four elements.

Λ	Ref. [68]	FEM [68]	GDQFEM						
			$n_e = 1$ $N = 15$	$n_e = 1$ $N = 21$	$n_e = 1$ $N = 41$	$n_e = 4$ $N = 15$	$n_e = 4$ $N = 21$	$n_e = 8$ $N = 15$	$n_e = 8$ $N = 21$
1	4.2611	4.2608	4.25686	4.25686	4.25686	4.25686	4.25686	4.25686	4.25686
2	5.7103	5.7049	5.69300	5.69299	5.69300	5.69300	5.69300	5.69300	5.69300
3	7.3568	7.3564	7.30990	7.30990	7.30990	7.30990	7.30990	7.30990	7.30990
4	7.6752	7.6741	7.61125	7.61125	7.61125	7.61125	7.61125	7.61125	7.61125
5	8.8156	8.8148	8.70857	8.70855	8.70857	8.70857	8.70857	8.70857	8.70857
6	9.0189	9.0162	8.86259	8.86259	8.86259	8.86259	8.86259	8.86259	8.86259
7	-	-	10.32732	10.32731	10.32732	10.32732	10.32732	10.32732	10.32732
8	-	-	10.34155	10.34155	10.34155	10.34155	10.34155	10.34155	10.34155
9	-	-	11.13091	11.13091	11.13091	11.13091	11.13091	11.13091	11.13091
10	-	-	11.64007	11.64007	11.64007	11.64007	11.64007	11.64007	11.64007

Table 2.10: First ten eigenfrequencies of a skew membrane $b/a = 3/2$ with $\theta = \pi/3$.

2.4.9 Skew or rhombic membrane

There has been an article by Civalek [68] which widely discussed the free vibration analysis of skew membranes. Hence, comparing the results obtained by [68] the GDQFEM is applied to several skew membranes. In Figure 2.22 two types of meshes are presented for a particular rhombic geometry. The skew or rhombic membrane has got two sides a and b of various length and a skew angle θ. In the following several ratios b/a and θ values are presented. In Table 2.10 is presented a rhombic membrane with the ratio $b/a = 3/2$ and $\theta = \pi/3$. Using one element is sufficient to capture the FEM solution with a negligible error. More refined meshes are presented too. A parametric study for a $b/a = 1$ skew membrane is presented in Table 2.11. The skew angle θ varies from $\theta = \pi/4$ to $\theta = 5\pi/12$. All the proposed results are in good accordance with the ones obtained by Civalek [68]. Another parametric study has been done in Table 2.12 for $b/a = 2$ and skew angle θ variable. Finally, varying b/a in Table 2.13 the results are presented for $\theta = \pi/3$. In conclusion, the first nine modal shapes are depicted in Figure 2.23 for a skew membrane of $b/a = 3/2$ and $\theta = \pi/3$.

	$\theta = \pi/4$				$\theta = \pi/3$			
		GDQFEM				GDQFEM		
Λ	Ref. [68]	$n_e = 1$ $N = 41$	$n_e = 4$ $N = 21$	$n_e = 8$ $N = 21$	Ref. [68]	$n_e = 1$ $N = 41$	$n_e = 4$ $N = 21$	$n_e = 8$ $N = 21$
1	5.9019	5.89528	5.89528	5.89528	4.9912	4.98993	4.98993	4.98993
2	8.1477	8.14171	8.14171	8.14171	7.2588	7.25530	7.25530	7.25530
3	10.0261	10.01317	10.01317	10.01317	8.4751	8.46840	8.46840	8.46840
4	10.3592	10.34676	10.34676	10.34676	9.1623	9.15593	9.15593	9.15593
5	11.8780	11.86690	11.86690	11.86690	11.0856	11.08264	11.08264	11.08264
6	-	12.97365	12.97365	12.97365	-	11.08268	11.08268	11.08268
7	-	13.60300	13.60300	13.60300	-	11.85141	11.85141	11.85141
8	-	14.77270	14.77269	14.77269	-	13.00895	13.00895	13.00895
9	-	14.98905	14.98905	14.98905	-	13.02982	13.02982	13.02982
10	-	15.39859	15.39859	15.39859	-	14.51061	14.51061	14.51061
	$\theta = 7\pi/18$				$\theta = 5\pi/12$			
		GDQFEM				GDQFEM		
Λ	Ref. [68]	$n_e = 1$ $N = 41$	$n_e = 4$ $N = 21$	$n_e = 8$ $N = 21$	Ref. [68]	$n_e = 1$ $N = 41$	$n_e = 4$ $N = 21$	$n_e = 8$ $N = 21$
1	4.6708	4.67779	4.67779	4.67779	4.5671	4.56809	4.56809	4.56809
2	7.0061	7.00860	7.00860	7.00860	6.9514	6.94262	6.94262	6.94262
3	7.7520	7.76083	7.76083	7.76083	7.4940	7.49040	7.49040	7.49040
4	8.9403	8.94571	8.94571	8.94571	8.8954	8.89012	8.89012	8.89012
5	10.4162	10.42871	10.42871	10.42871	10.2019	10.19774	10.19774	10.19774
6	-	10.82155	10.82155	10.82155	-	10.43476	10.43476	10.43476
7	-	10.96750	10.96750	10.96750	-	10.97543	10.97543	10.97543
8	-	12.29977	12.29977	12.29977	-	11.99422	11.99422	11.99422
9	-	12.95083	12.95083	12.95083	-	12.99845	12.99845	12.99845
10	-	13.70667	13.70667	13.70667	-	13.36409	13.36409	13.36409

Table 2.11: First ten eigenfrequencies of a skew membrane $b/a = 1$ for θ variable.

	$\theta = \pi/4$				$\theta = \pi/3$			
Λ	Ref. [68]	GDQFEM			Ref. [68]	GDQFEM		
		$n_e = 1$ $N = 41$	$n_e = 4$ $N = 21$	$n_e = 8$ $N = 21$		$n_e = 1$ $N = 41$	$n_e = 4$ $N = 21$	$n_e = 8$ $N = 21$
1	4.7903	4.77759	4.77759	4.77759	4.0046	3.98457	3.98457	3.98457
2	5.6728	5.64261	5.64261	5.64261	4.9288	4.88922	4.88922	4.88922
3	6.8153	6.77872	6.77872	6.77872	6.0811	6.06516	6.06516	6.06516
4	8.0096	7.96701	7.96701	7.96701	7.3029	7.25530	7.25530	7.25530
5	9.1403	9.03840	9.03840	9.03840	7.5362	7.52274	7.52274	7.52274
6	9.1719	9.09843	9.09843	9.09843	7.9846	7.94813	7.94813	7.94813
7	-	9.78725	9.78725	9.78725	-	8.65414	8.65414	8.65414
8	-	10.05661	10.05661	10.05661	-	8.83295	8.83295	8.83295
9	-	10.81602	10.81602	10.81602	-	9.87782	9.87782	9.87782
10	-	11.15829	11.15829	11.15829	-	9.94657	9.94657	9.94657
	$\theta = 7\pi/18$				$\theta = 5\pi/12$			
Λ	Ref. [68]	GDQFEM			Ref. [68]	GDQFEM		
		$n_e = 1$ $N = 41$	$n_e = 4$ $N = 21$	$n_e = 8$ $N = 21$		$n_e = 1$ $N = 41$	$n_e = 4$ $N = 21$	$n_e = 8$ $N = 21$
1	3.7116	3.70843	3.70843	3.70843	3.6447	3.62010	3.62010	3.62010
2	4.6329	4.62814	4.62814	4.62814	4.5802	4.54424	4.54424	4.54424
3	5.8359	5.82676	5.82676	5.82676	5.7857	5.75153	5.75153	5.75153
4	6.8602	6.85697	6.85697	6.85697	6.7240	6.68936	6.68936	6.68936
5	7.1648	7.15602	7.15602	7.15602	7.1081	7.08686	7.08686	7.08686
6	7.4413	7.42143	7.42143	7.42143	7.2495	7.24473	7.24473	7.24473
7	-	8.28620	8.28620	8.28620	-	8.09724	8.09724	8.09724
8	-	8.46712	8.46712	8.46712	-	8.43702	8.43702	8.43702
9	-	9.39081	9.39081	9.39081	-	9.18571	9.18571	9.18571
10	-	9.74868	9.74868	9.74868	-	9.75341	9.75341	9.75341

Table 2.12: First ten eigenfrequencies of a $b/a = 2$ skew membrane with variable θ.

	$b/a = 1$				$b/a = 1.5$			
		GDQFEM				GDQFEM		
Λ	Ref. [68]	$n_e = 1$ $N = 41$	$n_e = 4$ $N = 21$	$n_e = 8$ $N = 21$	Ref. [68]	$n_e = 1$ $N = 41$	$n_e = 4$ $N = 21$	$n_e = 8$ $N = 21$
1	4.9912	4.98993	4.98993	4.98993	4.2611	4.25686	4.25686	4.25686
2	7.2588	7.25530	7.25530	7.25530	5.7103	5.69300	5.69300	5.69300
3	8.4751	8.46840	8.46840	8.46840	7.3568	7.30990	7.30990	7.30990
4	9.1623	9.15593	9.15593	9.15593	7.6752	7.61125	7.61125	7.61125
5	11.0856	11.08264	11.08264	11.08264	8.8156	8.70857	8.70857	8.70857
6	-	11.08268	11.08268	11.08268	9.0189	8.86259	8.86259	8.86259
7	-	11.85141	11.85141	11.85141	-	10.32732	10.32732	10.32732
8	-	13.00895	13.00895	13.00895	-	10.34155	10.34155	10.34155
9	-	13.02982	13.02982	13.02982	-	11.13091	11.13091	11.13091
10	-	14.51061	14.51061	14.51061	-	11.64007	11.64007	11.64007
	$b/a = 2$				$b/a = 3$			
		GDQFEM				GDQFEM		
Λ	Ref. [68]	$n_e = 1$ $N = 41$	$n_e = 4$ $N = 21$	$n_e = 8$ $N = 21$	Ref. [68]	$n_e = 1$ $N = 41$	$n_e = 4$ $N = 21$	$n_e = 8$ $N = 21$
1	4.0046	3.98457	3.98457	3.98457	3.8006	3.68421	3.68421	3.68421
2	4.9288	4.88922	4.88922	4.88922	4.2403	4.15420	4.15420	4.15420
3	6.0811	6.06516	6.06516	6.06516	4.8999	4.83193	4.83193	4.83193
4	7.3029	7.25530	7.25530	7.25530	5.6425	5.63460	5.63460	5.63460
5	7.5362	7.52274	7.52274	7.52274	6.5117	6.49967	6.49967	6.49967
6	7.9846	7.94813	7.94813	7.94813	7.3310	7.10792	7.10792	7.10792
7	-	8.65414	8.65414	8.65414	-	7.37337	7.37337	7.37337
8	-	8.83295	8.83295	8.83295	-	7.38081	7.38081	7.38081
9	-	9.87782	9.87782	9.87782	-	7.84575	7.84575	7.84575
10	-	9.94657	9.94657	9.94657	-	8.14107	8.14107	8.14107

Table 2.13: First ten eigenfrequencies of a skew membrane with variable b/a and $\theta = \pi/3$.

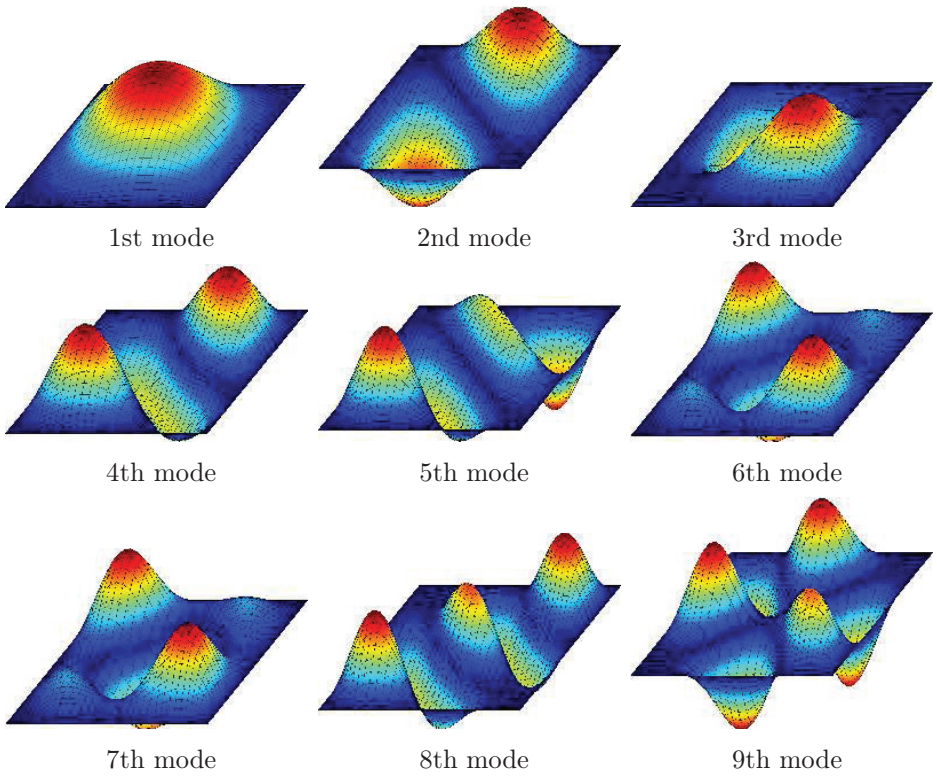

Figure 2.23: First 9 mode shapes for the skew membrane with $\theta = \pi/3$ and $b/a = 3/2$ membrane.

Λ	FEM [70]	BEM [70]	GDQFEM						
			$n_e = 4$ $N = 5$	$n_e = 4$ $N = 9$	$n_e = 4$ $N = 13$	$n_e = 4$ $N = 15$	$n_e = 4$ $N = 21$	$n_e = 4$ $N = 25$	$n_e = 4$ $N = 31$
1	2.03	2.06	2.05099	2.06135	2.06137	2.06137	2.06137	2.06137	2.06137
2	2.20	2.23	2.22236	2.23727	2.23729	2.23729	2.23729	2.23729	2.23729
3	2.20	2.23	2.22236	2.23727	2.23729	2.23729	2.23729	2.23729	2.23729
4	2.62	2.67	2.64238	2.67144	2.67145	2.67145	2.67145	2.67145	2.67145
5	2.62	2.67	2.67310	2.68062	2.68065	2.68066	2.68066	2.68066	2.68066
6	3.15	3.22	3.24398	3.23258	3.23261	3.23261	3.23261	3.23261	3.23261
7	3.15	3.22	3.24398	3.23258	3.23261	3.23261	3.23261	3.23261	3.23261
8	3.71	3.81	3.81578	3.81489	3.81505	3.81505	3.81506	3.81506	3.81506
9	3.71	3.81	4.15469	3.82889	3.82885	3.82885	3.82885	3.82885	3.82885
10	4.06	4.18	4.79012	4.18746	4.18744	4.18744	4.18744	4.18744	4.18744

Table 2.14: First ten eigenfrequencies of an annular membrane, $R_i = 0.5$ m, $R_e = 2$ m.

2.4.10 Multiply connected domain

In the work by Chen et al. [70] multiply connected domains for acoustic cavities have been studied within the Helmholtz equation. Since the fundamental equation has the same mathematical form of the free vibration of a membrane, the eigenvalues can be compared. However it is clear that they have different physical meaning. In Figure 2.24 the multi-connected membranes considered in this paper are graphically reported. The radius of the outer circle is $R = 2$ m and the inner circle radius is $r = 0.5$ m and the inner square has a side $l = 0.5$ m. In both the eccentric cases the inner circle and the square are shifted on the left of the same quantity of the inner main dimension ($l = r = 0.5$ m).

In table 2.14 the first ten eigenfrequencies are reported for an annular membrane, the GDQFEM results are compared with the numerical results obtained with FEM and Boundary Element Method (BEM) [70]. In Table 2.15 the first ten eigenfrequencies for an annular membrane which has an eccentric hole is considered and compared to several methodologies [13, 70, 95]. Another kind of geometry is considered in Table 2.16 in which a circular membrane with a square hole is taken into account. In conclusion a circular membrane with an eccentric square hole is numerically presented in Table 2.17. In all the results reported in this paper the less number of elements is used in this study in order to have the most accurate solution for this methodology. In addition, to see the rapid convergence of the GDQFEM sevaral grid point numbers are considered (see Tables 2.14-2.17). For further details about the modal shapes they can be found well depicted in [70], thus they are not reported in this PhD Thesis for the sake of conciseness.

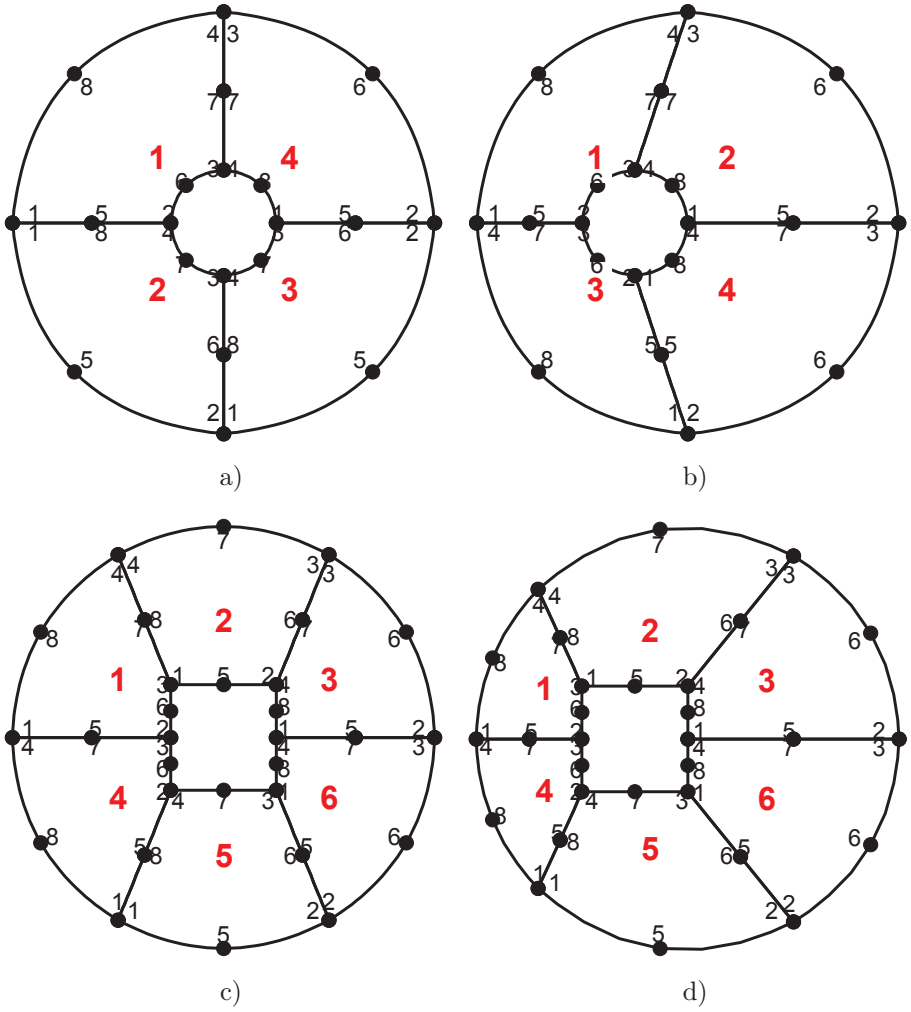

Figure 2.24: Multi connected membrane: a) Annular membrane, b) Annular eccentric membrane, c) Circular membrane with a square hole, d) Circular membrane with an eccentric square hole.

Λ	FEM [70]	Ref. [13]	Ref. [95]	Ref. [70]	GDQFEM				
					$n_e = 4$ $N = 5$	$n_e = 4$ $N = 11$	$n_e = 4$ $N = 15$	$n_e = 4$ $N = 21$	$n_e = 4$ $N = 31$
1	1.73	1.75	1.74	1.75	1.73339	1.74485	1.74485	1.74485	1.74485
2	2.13	2.14	2.14	2.14	2.13282	2.14429	2.14430	2.14430	2.14430
3	2.45	2.47	2.47	2.47	2.45323	2.47804	2.47805	2.47805	2.47806
4	2.76	2.78	2.78	2.78	2.79978	2.78287	2.78287	2.78287	2.78287
5	2.95	2.97	2.98	2.98	2.99047	2.98403	2.98404	2.98404	2.98404
6	3.30	3.33	3.33	3.33	3.40060	3.33627	3.33627	3.33627	3.33627
7	3.34	3.37	3.37	3.37	3.43506	3.38613	3.38615	3.38615	3.38615
8	3.36	3.38	3.39	3.39	4.04953	3.39119	3.39120	3.39120	3.39120
9	3.83	3.85	3.87	3.87	4.04953	3.87768	3.87768	3.87769	3.87769
10	3.84	3.87	3.87	3.87	4.20014	3.88442	3.88443	3.88444	3.88444

Table 2.15: First ten eigenfrequencies of an eccentric annular membrane, $R_i = 0.5$ m, $R_e = 2$ m.

Λ	FEM [70]	BEM [70]	GDQFEM						
			$n_e = 6$ $N = 5$	$n_e = 6$ $N = 9$	$n_e = 6$ $N = 13$	$n_e = 6$ $N = 15$	$n_e = 6$ $N = 21$	$n_e = 6$ $N = 25$	$n_e = 6$ $N = 31$
1	2.19	2.19	2.19737	2.19102	2.19006	2.18993	2.18977	2.18973	2.18970
2	2.33	2.33	2.33710	2.33926	2.33851	2.33841	2.33828	2.33824	2.33822
3	2.33	2.33	2.34089	2.33933	2.33852	2.33841	2.33828	2.33825	2.33823
4	2.67	2.69	2.66678	2.68510	2.68509	2.68509	2.68509	2.68509	2.68509
5	2.76	2.76	2.77300	2.77177	2.77079	2.77065	2.77049	2.77045	2.77042
6	3.22	3.24	3.24049	3.24535	3.24510	3.24507	3.24503	3.24502	3.24501
7	3.22	3.24	3.24971	3.24802	3.24774	3.24770	3.24765	3.24763	3.24763
8	3.76	3.81	3.81839	3.81111	3.81110	3.81110	3.81110	3.81110	3.81110
9	3.77	3.81	3.87910	3.81539	3.81523	3.81521	3.81518	3.81517	3.81517
10	4.32	4.40	4.43422	4.39112	4.39112	4.39112	4.39112	4.39112	4.39112

Table 2.16: First ten eigenfrequencies of a circular membrane with a square hole.

Λ	FEM [70]	BEM [70]	GDQFEM						
			$n_e = 6$ $N = 5$	$n_e = 6$ $N = 9$	$n_e = 6$ $N = 13$	$n_e = 6$ $N = 15$	$n_e = 6$ $N = 21$	$n_e = 6$ $N = 25$	$n_e = 6$ $N = 31$
1	1.81	1.81	1.81216	1.81274	1.81251	1.81249	1.81247	1.81247	1.81246
2	2.20	2.21	2.21769	2.21981	2.21949	2.21946	2.21943	2.21943	2.21942
3	2.50	2.53	2.52615	2.52954	2.52938	2.52936	2.52934	2.52933	2.52933
4	2.79	2.83	2.83281	2.83397	2.83388	2.83387	2.83385	2.83385	2.83384
5	3.07	3.10	3.12876	3.11083	3.11053	3.11050	3.11045	3.11043	3.11042
6	3.36	3.42	3.47473	3.43360	3.43330	3.43326	3.43321	3.43319	3.43318
7	3.40	3.47	3.52113	3.46600	3.46572	3.46569	3.46565	3.46564	3.46563
8	3.41	3.47	4.00575	3.48288	3.48258	3.48256	3.48254	3.48254	3.48253
9	3.79	3.90	4.05591	3.89608	3.89607	3.89607	3.89606	3.89606	3.89606
10	3.85	3.95	4.22877	3.96028	3.95996	3.95991	3.95986	3.95984	3.95983

Table 2.17: First ten eigenfrequencies of a circular membrane with an eccentric square hole.

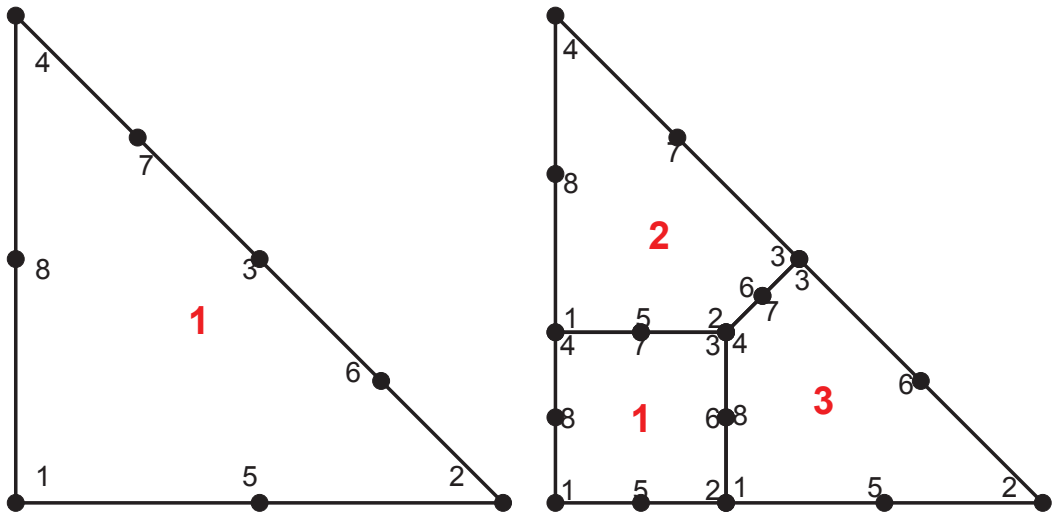

Figure 2.25: GDQFEM meshes for a triangular membrane: a) Single distorted element, b) Three quadrilateral elements.

2.4.11 Triangular membrane

In the next example a triangular membrane is considered (Figure 2.25). Since this kind of geometry is complex to model with only quadrilateral elements, its solution is proposed in this paper. The triangle is isosceles and right, with the two sides $a = b = 2$ m. The membrane is homogeneous but two different mesh are considered. The first is composed of a single triangular element (heavily distorted quadrilateral one), and the second one has three standard elements. In Table 2.18 the first ten eigenfrequencies of the two meshes are reported. Table 2.18 reports a convergence test for the two given meshes (Figure 2.25) from $N = 7$ to $N = 31$. It should be noted that the single element captures the solution like the three element mesh, with a small number of points per element. In addition the first nine modal shapes are graphically presented in Figure 2.26.

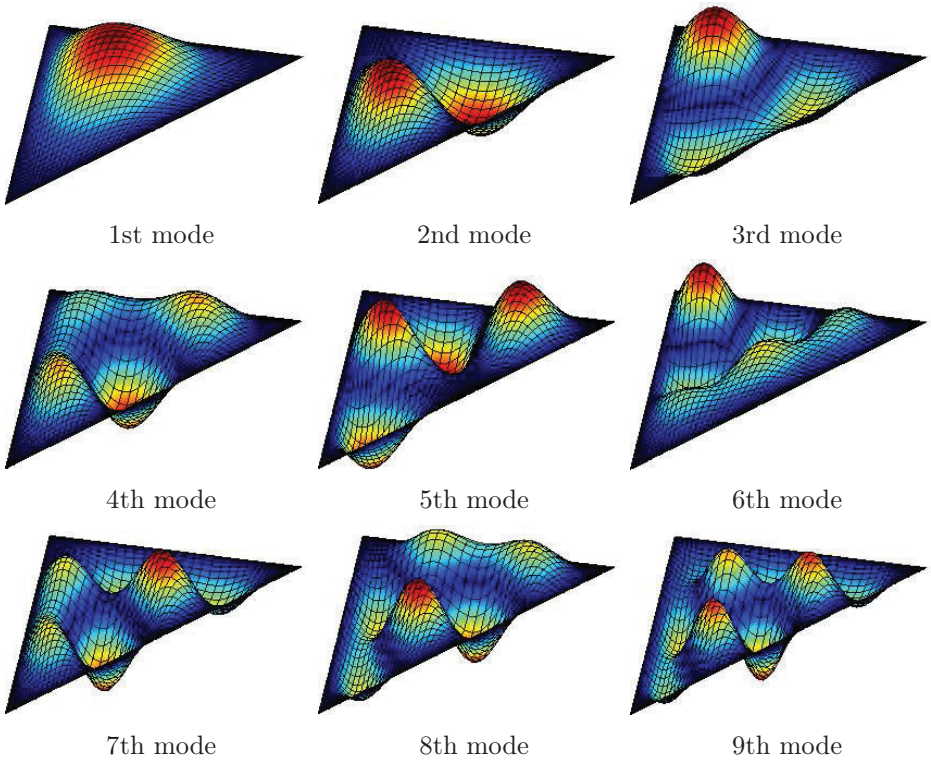

Figure 2.26: First 9 mode shapes for the triangular membrane with $a = b = 2$ m.

Λ	GDQFEM							
	$n_e = 1$ $N = 7$	$n_e = 1$ $N = 15$	$n_e = 1$ $N = 21$	$n_e = 1$ $N = 31$	$n_e = 3$ $N = 7$	$n_e = 3$ $N = 15$	$n_e = 3$ $N = 21$	$n_e = 3$ $N = 31$
1	3.51408	3.51241	3.51241	3.51241	3.51241	3.51241	3.51241	3.51241
2	4.96170	4.96729	4.96729	4.96729	4.96708	4.96729	4.96729	4.96729
3	5.64173	5.66359	5.66359	5.66359	5.66369	5.66359	5.66359	5.66359
4	6.47801	6.47656	6.47656	6.47656	6.47917	6.47656	6.47656	6.47656
5	7.32056	7.02481	7.02481	7.02481	7.03474	7.02481	7.02481	7.02481
6	7.94265	7.85398	7.85398	7.85398	7.85818	7.85398	7.85398	7.85398
7	8.99767	8.00952	8.00952	8.00952	8.05906	8.00952	8.00952	8.00952
8	10.72028	8.45899	8.45900	8.45900	8.52245	8.45900	8.45900	8.45900
9	11.91513	9.15923	9.15924	9.15924	9.24026	9.15924	9.15924	9.15924
10	12.24676	9.55482	9.55478	9.55478	9.57057	9.55478	9.55478	9.55478

Table 2.18: First ten eigenfrequencies of a homogeneous triangular membrane.

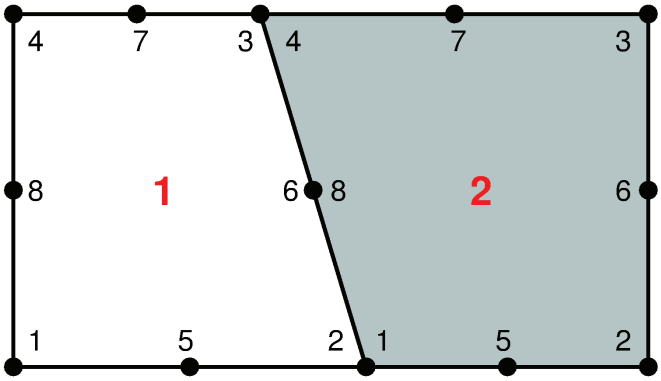

Figure 2.27: Not homogeneous rectangular membrane.

f	Ref. [82]	FEM [82]	GDQFEM						
			$n_e = 2$ $N = 7$	$n_e = 2$ $N = 9$	$n_e = 2$ $N = 11$	$n_e = 2$ $N = 15$	$n_e = 2$ $N = 21$	$n_e = 2$ $N = 31$	$n_e = 2$ $N = 41$
1	150.2	150.3	150.0465	150.0471	150.0471	150.0471	150.0471	150.0471	150.0471
2	215.2	215.5	214.9795	214.9755	214.9755	214.9755	214.9755	214.9755	214.9755
3	262.9	263.9	263.4968	262.6327	262.6284	262.6284	262.6284	262.6284	262.6284
4	271.6	272.3	271.6737	271.3645	271.3631	271.3631	271.3631	271.3631	271.3631
5	317.0	318.3	317.4088	316.6872	316.6862	316.6862	316.6862	316.6862	316.6862
6	342.1	343.8	341.0872	341.7805	341.7957	341.7958	341.7958	341.7958	341.7958
7	375.7	377.9	365.0773	375.1450	375.3420	375.3436	375.3436	375.3436	375.3436
8	380.2	383.0	378.4822	379.3738	379.7712	379.7751	379.7751	379.7751	379.7751
9	414.1	416.9	409.1291	413.4438	413.6652	413.6675	413.6675	413.6675	413.6675
10	418.1	421.0	411.9351	417.5918	417.9653	417.9693	417.9693	417.9693	417.9693

Table 2.19: First ten frequencies of a rectangular not homogeneous membrane.

2.4.12 Not homogeneous rectangular membrane

A composite rectangular membrane composed of two homogeneous regions, of which common boundary is oblique against the vertical axis, has been considered in the following. This problem was studied by Kang et al. [82] in their accurate work about transverse vibrations of composite rectangular membrane with oblique interface. In this paper only the not homogeneous example is considered. The dimensions of the membrane are $a = 1.8$ m, $b = 1.0$m and the coordinate of the points defining the oblique interface are $a_1 = 1.0$, $a_2 = 0.7$ m (see Kang et al. [82] for further details). In Figure 2.27 the membrane geometry is presented in which the grey area represents the second material. The values of the surface density are $\rho_{s1} = 1.293 \cdot 10^{-5}$ kg/m^2, $\rho_{s2} = 2\rho_{s1}$. It is noted that the defined densities are per surface area and not per unit volume, as a FEM program needs. Furthermore, the tension per unit length T is needed. Since the exact definition of T is not-existent in [82] it has been assumed to be $T = 1.5$ N. In conclusion, the results are summarised in Table 2.19 for the first ten frequencies for the given not-homogeneous membrane, and the GDQFEM are in perfect accordance with the solution proposed by Kang at el. [82] and the FEM solution. In conclusion, in Figure 2.28 the first nine modal shapes are presented for the case under study. Since a composite membrane has been considered the modal shapes are not symmetric due to the mechanical configuration of the membrane. Moreover, the first modes excites the part of the membrane that has a lower surface density due to the fact that is more flexible $\rho_{s1} < \rho_{s2}$.

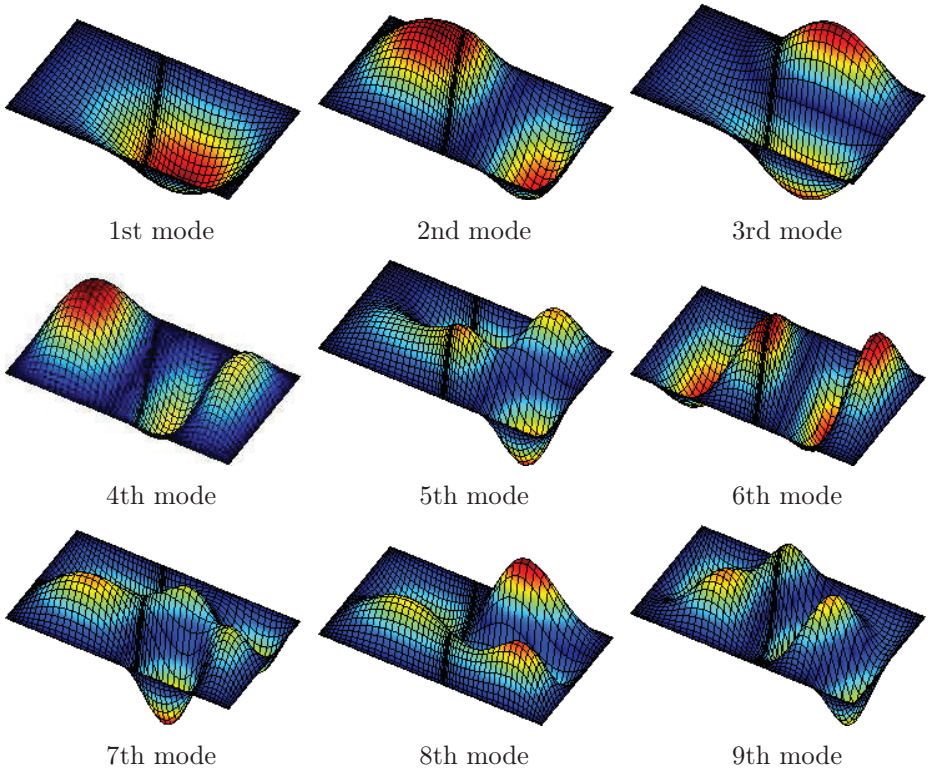

Figure 2.28: First 9 mode shapes for the not homogeneous rectangular membrane.

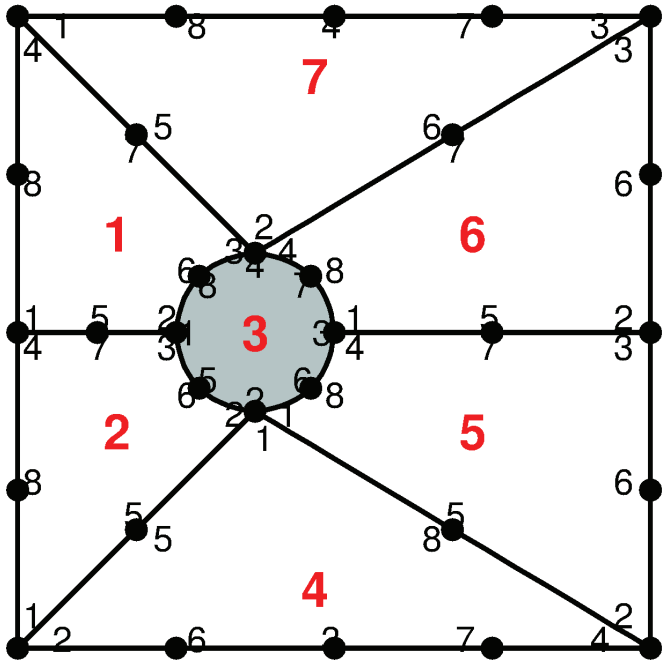

Figure 2.29: GDQFEM mesh for a multiply connected composite membrane.

2.4.13 Multiply connected not homogeneous membrane

Since the GDQFEM methodology and the implemented code has been tested with several reference solutions found in literature, some new results are proposed in this section. In particular a multiply connected membrane with different kind of materials will be solved. The membrane is a square one $a = b = 4$ m with a circular eccentric inclusion of radius $r_1 = 0.5$. The surface densities are $\rho_{s1} = 1.293 \cdot 10^{-5}$ kg/m^2 and $\rho_{s2} = \bar{\rho} \cdot \rho_{s1}$, where $\bar{\rho} \geq 0$.

At first a convergence analysis has been performed (Table 2.20) to see if increasing the number of points upon each domain the solution converges to a value. It should be noted that the convergence rate is very fast, just $N = 15$ is enough to get a stable solution. In Table 2.21 the first ten frequencies for several values of $\bar{\rho} = \rho_{s2}/\rho_{s1}$ are presented. It should be noted that when $\bar{\rho}$ increases, the inclusion increases its density until it is a couple of order of magnitude greater than the rest of the membrane. It is can be seen clearly from Figure 2.30 that there is a convergence to some values for the first ten frequencies presented here. This phenomenon has a physical explanation, due to the mass concentration of a free vibrating system. The first nine modal shapes for $\bar{\rho} = 100$ are depicted in Figure 2.31.

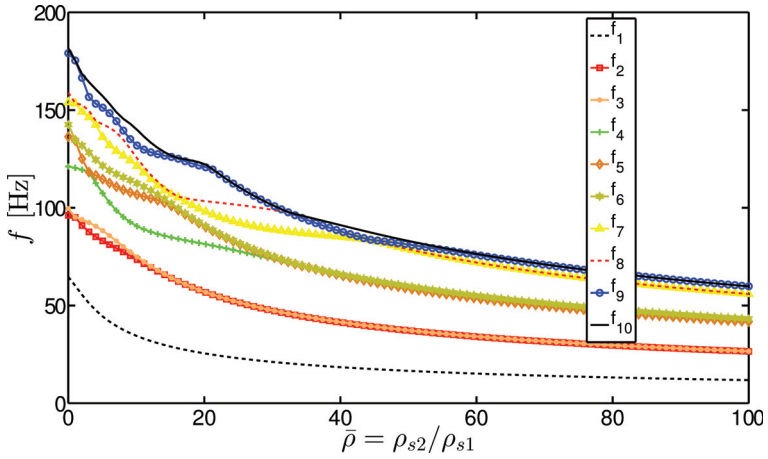

Figure 2.30: First ten frequencies as a function of the density ratio $\bar{\rho}$ between the two materials.

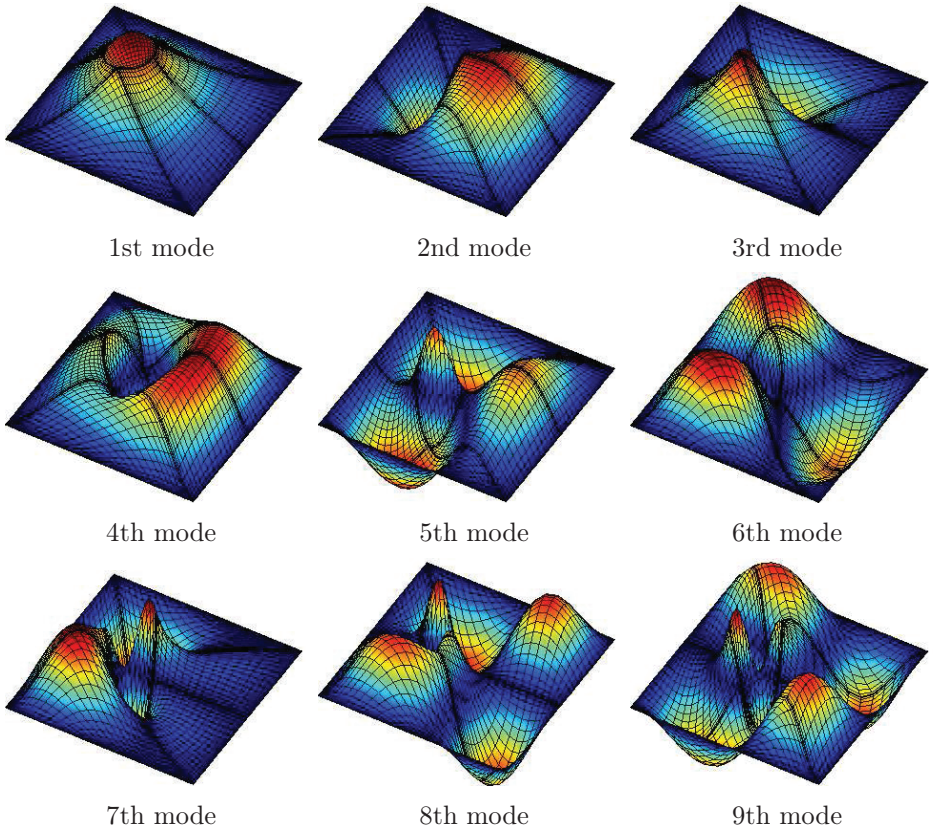

Figure 2.31: First 9 mode shapes for the multiply connected not homogeneous membrane for $\bar{\rho} = 100$.

f	GDQFEM								
	$N=5$	$N=7$	$N=9$	$N=11$	$N=13$	$N=15$	$N=17$	$N=19$	$N=21$
1	34.6484	34.5012	34.4997	34.5000	34.5001	34.5001	34.5001	34.5001	34.5001
2	74.0716	73.6562	73.6550	73.6547	73.6548	73.6548	73.6548	73.6548	73.6548
3	76.3162	75.1313	75.1127	75.1135	75.1137	75.1137	75.1137	75.1137	75.1137
4	91.8147	90.7731	90.7920	90.7915	90.7914	90.7915	90.7915	90.7915	90.7915
5	106.7880	106.8676	106.8550	106.8545	106.8545	106.8545	106.8545	106.8545	106.8545
6	112.8499	112.5921	112.6267	112.6273	112.6275	112.6275	112.6275	112.6275	112.6275
7	119.3370	121.5284	121.7230	121.7256	121.7249	121.7248	121.7248	121.7248	121.7248
8	130.0696	126.0597	125.8806	125.8816	125.8827	125.8828	125.8828	125.8828	125.8828
9	132.3283	131.7961	132.1487	132.1520	132.1514	132.1514	132.1514	132.1514	132.1514
10	143.3690	140.0522	140.2786	140.2823	140.2827	140.2828	140.2828	140.2828	140.2828

Table 2.20: Convergence of the first ten frequencies for a multiply connected not homogeneous membrane.

f	GDQFEM								
	$\bar{\rho}=0.01$	$\bar{\rho}=0.5$	$\bar{\rho}=1$	$\bar{\rho}=2$	$\bar{\rho}=5$	$\bar{\rho}=10$	$\bar{\rho}=20$	$\bar{\rho}=50$	$\bar{\rho}=100$
1	64.6370	62.5046	60.2104	55.5970	44.5712	34.5001	25.5146	16.5660	11.8151
2	96.1424	95.7029	95.2010	91.0617	83.1683	73.6548	56.9805	37.1871	26.5326
3	99.5594	97.4385	95.2010	94.0052	88.4188	75.1137	57.0158	37.2947	26.6118
4	121.1201	120.7970	120.4208	119.4922	107.6825	90.7915	81.4912	58.4954	41.5701
5	136.3449	135.5919	134.6345	125.3128	114.7667	106.8545	90.5362	58.7220	41.7268
6	142.6137	139.2744	134.6345	131.9958	121.6532	112.6275	90.9606	59.8642	43.1608
7	153.9685	153.7661	153.5070	149.2257	136.4922	121.7248	98.3322	78.7936	55.8694
8	158.9617	156.3680	153.5070	152.6544	142.8069	125.8828	103.4421	78.7962	55.8705
9	179.0877	177.7852	175.5420	166.8093	151.3406	132.1514	120.9102	81.1882	59.8125
10	181.5585	179.8294	175.5419	168.5625	157.2960	140.2828	122.3917	83.0111	59.8183

Table 2.21: First ten frequencies for a multiply connected not homogeneous membrane for $N=21$.

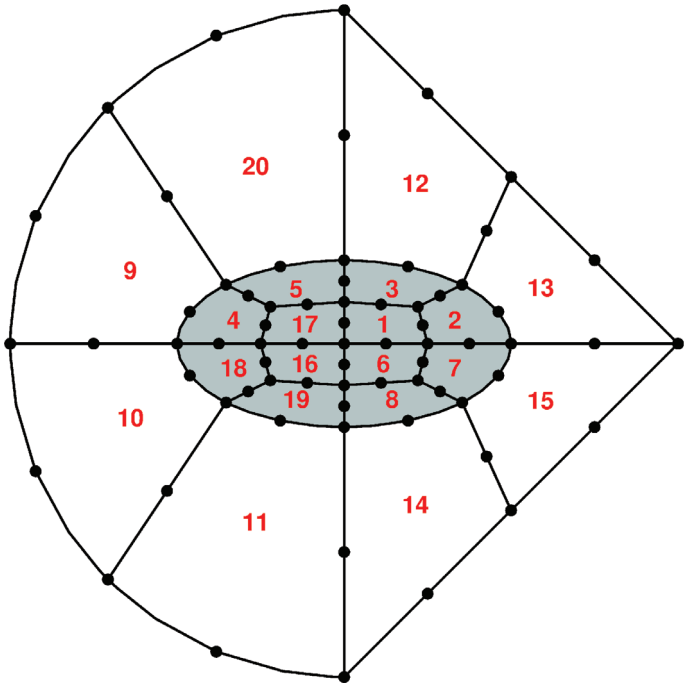

Figure 2.32: GDQFEM mesh for an arbitrarily shaped composite membrane with an elliptic inclusion.

2.4.14 Arbitrarily shaped composite membrane

An arbitrarily shaped composite membrane is considered in the following. The external boundaries follow the geometric shape of the arbitrarily shaped membrane studied by [78, 84, 85]. However, an internal elliptic inclusion has been inserted. The inclusion has $a = 0.5$ m and $b = 0.25$ m. The GDQFEM mesh is presented in Figure 2.32, for the sake of clarity the current mesh is reported without the node numbers per element.
The surface densities are $\rho_{s1} = 1.293 \cdot 10^{-5}$ kg/m^2 and $\rho_{s2} = \bar{\rho} \cdot \rho_{s1}$, where $\bar{\rho}$ is a number that defines how much the second density is greater or smaller than the first one. In this example $T = 1$ N has been considered and the thickness $h = 0.005$ m.

In Table 2.22 the first ten frequencies of the current model are presented as a function of the ratio between the two materials $\bar{\rho}$. It is noted that increasing the density coefficient $\bar{\rho}$ the resulting frequencies decrease due to the mass concentration. In other words, the system tends to be similar to a single degree of freedom because all the mass is concentrated at the membrane center. In conclusion the first nine modal shapes are depicted in Figure 2.33. It can be noted from the modal shapes that the center of the membrane has an higher density due to the concentration of the vibrating motions, especially in the higher modes.

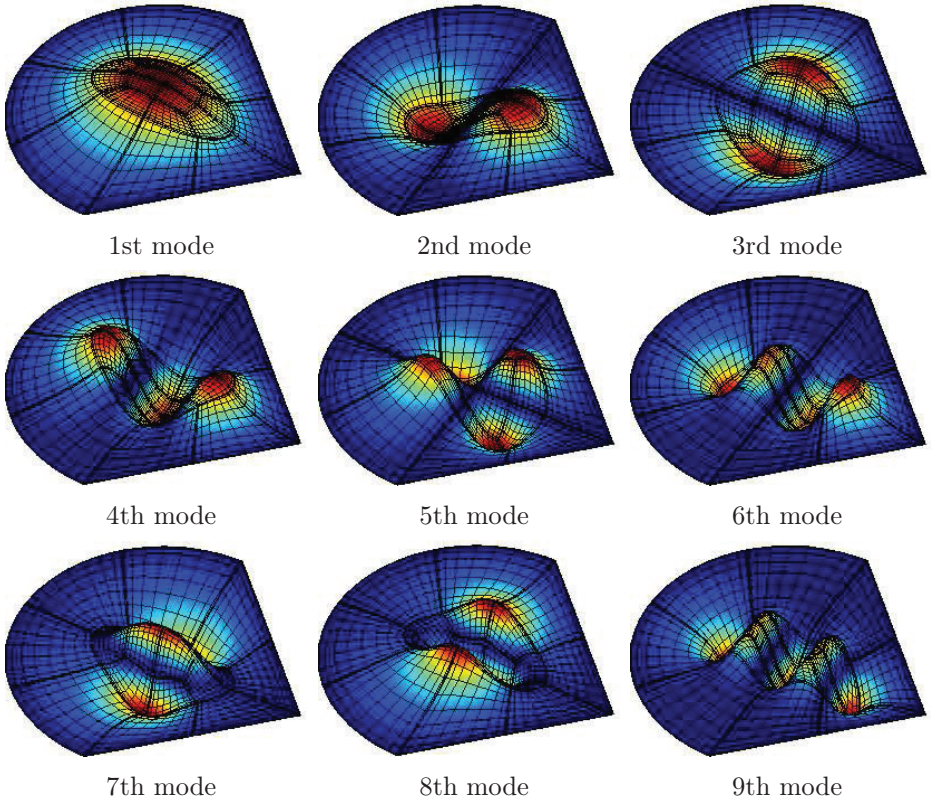

Figure 2.33: First 9 mode shapes for the arbitrarily shaped composite membrane for $\bar{\rho} = 100$.

f	GDQFEM								
	$\bar{\rho} = 0.01$	$\bar{\rho} = 0.5$	$\bar{\rho} = 1$	$\bar{\rho} = 2$	$\bar{\rho} = 5$	$\bar{\rho} = 10$	$\bar{\rho} = 20$	$\bar{\rho} = 50$	$\bar{\rho} = 100$
1	85.51755	12.0992	8.5555	6.04975	3.8261	2.7055	1.9131	1.2099	0.8556
2	145.1793	20.5398	14.5239	10.2700	6.4953	4.5929	3.2477	2.0540	1.4524
3	195.7015	27.6960	19.5841	13.8481	8.7583	6.1931	4.3792	2.7696	1.9584
4	208.3611	29.4776	20.8439	14.7389	9.3217	6.5914	4.6609	2.9478	2.0844
5	258.8820	36.6282	25.9002	18.3142	11.5830	8.1904	5.7915	3.6629	2.5900
6	273.3447	38.6698	27.3438	19.3350	12.2285	8.6469	6.1143	3.8670	2.7344
7	320.4384	45.3324	32.0550	22.6663	14.3355	10.1367	7.1677	4.5333	3.2055
8	327.0688	46.2894	32.7318	23.1450	14.6382	10.3508	7.3191	4.6290	3.2732
9	339.4402	48.0186	33.9544	24.0094	15.1849	10.7374	7.5925	4.8019	3.3955
10	382.0120	54.0395	38.2118	27.0199	17.0889	12.0837	8.5444	5.4040	3.8212

Table 2.22: First ten frequencies for an arbitrarily shape composite membrane $N = 11$.

Chapter 3

Composite Plane Structures with Discontinuities

Sommario

Il seguente capitolo fa riferimento ad una presentazione sommaria di un metodo generale per la soluzione di alcune classi di problemi piani. Il sistema differenziale in due equazioni riguardante la teoria dell'elasticità piana è risolto con la tecnica GDQFEM per studiare problemi di interesse pratico. Il problema viene caratterizzato matematicamente con il classico sistema di equazioni che è descritto in letteratura [1–3, 15, 16]. Successivamente, applicando la tecnica GDQ, il sistema è discretizzato e vengono risolti problemi di varia complessità con il metodo GDQFEM.

Nella parte introduttiva sono risassunte le principali equazioni governanti il problema piano (sia tensionale che deformativo). In particolare, viene illustrata la simbologia utilizzata per indicare spostamenti, tensioni e deformazioni. Successivamente la dualità del problema viene riassunta trattando un sistema in due equazioni e due incognite che sintetizza entrambi gli aspetti: dato che lo stato piano di tensione e deformazione differiscono soltanto per alcune costanti, dal punto di vista matematico, è possibile studiare un sistema facendo riferimento ad una certa nomenclatura che cambia di significato a seconda delle ipotesi iniziali.

In questo capitolo i primi esempi riportano strutture classiche in materiale omogeneo che permettono di valutare la convergenza e la stabilità della tecnica. Vengono, inoltre, proposti test ben noti (adottati anche per la validazione del metodo FE) come la trave sottile di MacNeal e la trave di Cook.

Infine, si riportano esempi di strutture in materiale composito, come travi laminate con nucleo soffice, travi curve composite e con fori, per i quali vengono risolti sia problemi di natura statica, con ricostruzione del profilo tensionale, sia che problemi di natura dinamica come le vibrazioni libere. Per ogni esempio i risultati ottenuti con la tecnica GDQFEM sono confrontati con quelli riportati in letteratura e con quelli derivanti dall'applicazione del metodo FE mostrando un ottimo accordo.

3.1 Introduction

This chapter is devoted to a concise presentation of one general method of solution of certain broad classes of two dimensional boundary value problems in elasticity [1–3]. The equations of the plane theory of elasticity are applied to two cases of equilibrium of elastic bodies which are of considerable interest in practice. The first is the case of a plain strain and the second one of the the deformation of a thin plate under forces applied to its boundary and acting in its plane. These two cases will be discussed in the following sections theoretically. After the characterization of the mathematical problem the main formulae are presented in order to apply the GDQFEM approach.

3.2 Preliminary remarks

A deformation or a tension state can be considered plane if the equations of motion can be defined by three stresses or strains components. If a thin plate is loaded by forces applied at the boundary, parallel to the plane of the plane and distributed uniformly over the thickness (Figure ...), the stress components $\sigma_z = \tau_{zx} = \tau_{zy} = 0$ are zero on both faces of the plate, and they may also assumed that they are zero within the plate. The state of stress is then specified by σ_x, σ_y, τ_{xy}. Furthermore, it can also be assumed that these components are independent of z, so any functional derivative $\partial/\partial z$ is equal to zero. As a result σ_x, σ_y, τ_{xy} do not vary through the thickness, and they are function of x and y only. In conclusion the stress tensor components for the plane stress analysis are

$$\begin{aligned} \sigma_x = \sigma_x(x,y), \quad \sigma_y = \sigma_y(x,y), \quad \sigma_z = 0 \\ \tau_{yz} = 0, \quad \tau_{xz} = 0, \quad \tau_{xy} = \tau_{xy}(x,y) \end{aligned} \tag{3.1}$$

An analogous simplification is possible at the other extreme when the dimension of the body in the z direction is very large. If a long prismatical body is loaded by forces which are perpendicular to the longitudinal elements and do not vary along the length, it may be assumed that all cross sections are in the same condition. The hypothesis of first and end section fixed, smooth and rigid can be considered, so that displacement in the axial direction is prevented. Since there is no axial displacement, by symmetric it can be assumed that the same holds at every cross section. There are many important problem of this kind in practical engineering applications. Given these hypotheses the following relations must be valid

$$w = 0, \quad \frac{\partial u}{\partial z} = 0, \quad \frac{\partial v}{\partial z} = 0 \tag{3.2}$$

where w is the axial displacement of the deformable solid, and u and v are the in plane displacements that do not vary with z because of the symmetry of the problem.

3.2.1 Equilibrium equations

Starting off the equilibrium equations valid for the three dimensional elasticity [1–3], the state plane hypotheses can be introduced. The derivatives respect to z and the out of plane stress are negligible. Thus, they can be written for a plane state as follows

$$\begin{aligned} \frac{\partial \sigma_x}{\partial x} + \frac{\partial \tau_{xy}}{\partial y} + f_x = 0 \\ \frac{\partial \tau_{xy}}{\partial x} + \frac{\partial \sigma_y}{\partial y} + f_y = 0 \end{aligned} \tag{3.3}$$

where the third equation is not reported due to the problem hypotheses, introduced above.

3.3 Plane strain state

Consider a prismatical solid in a plain strain state, parallel to the plane x-y, so the six deformation components, according to the hypotheses of a state plane, are

$$\begin{aligned} \varepsilon_x = \varepsilon_x(x,y), \quad \varepsilon_y = \varepsilon_y(x,y), \quad \varepsilon_z = 0 \\ \gamma_{yz} = 0, \quad \gamma_{xz} = 0, \quad \gamma_{xy} = \gamma_{xy}(x,y) \end{aligned} \tag{3.4}$$

From (3.4) the cubic dilation can be calculated. This quantity is equal to the first strain invariant $I_{1\varepsilon}$ that is

$$I_{1\varepsilon} = \varepsilon_x + \varepsilon_y \tag{3.5}$$

The congruence equations can be defined also

$$\varepsilon_x = \frac{\partial u}{\partial x}, \quad \varepsilon_y = \frac{\partial v}{\partial y}, \quad \gamma_{xy} = \frac{\partial u}{\partial y} + \frac{\partial v}{\partial x} \tag{3.6}$$

When the constitutive equations are introduced the stress components can be found as a function of the strain components

$$\sigma_x = 2G\varepsilon_x + \lambda I_{1\varepsilon}, \;\; \sigma_y = 2G\varepsilon_y + \lambda I_{1\varepsilon}, \;\; \sigma_z = \lambda I_{1\varepsilon}, \;\; \tau_{xy} = G\gamma_{xy} \tag{3.7}$$

which are called inverse Hooke's laws. It is noted that the third relation of (3.7) gives a normal stress along z that is not negligible. In fact when a state plain is considered it can not be assumed a plain stress also. Moreover in (3.7) G is the shear modulus and λ is the second Lamé constant. They can be both written as a function of the Young's modulus E and the Poisson's modulus ν

$$G = \frac{E}{2\,(1+\nu)}, \quad \lambda = \frac{\nu E}{(1+\nu)\,(1-2\nu)} \tag{3.8}$$

Introducing the congruence relations (3.6) into the constitutive equations (3.7) the inverse Hooke's laws can be written as a function of the displacements only.

$$\begin{aligned} \sigma_x = (\lambda + 2G)\,\frac{\partial u}{\partial x} + \lambda \frac{\partial v}{\partial y} \\ \sigma_y = (\lambda + 2G)\,\frac{\partial v}{\partial y} + \lambda \frac{\partial u}{\partial x} \\ \tau_{xy} = G\left(\frac{\partial u}{\partial y} + \frac{\partial v}{\partial x}\right) \end{aligned} \tag{3.9}$$

and using the constitutive equations in terms of displacements into the equilibrium equations for a general state plane the fundamental equations in terms of displacements can be found

$$\begin{aligned}(\lambda+2G)\frac{\partial^2 u}{\partial x^2}+G\frac{\partial^2 u}{\partial y^2}+(\lambda+G)\frac{\partial^2 v}{\partial x\partial y}+f_x=0\\(\lambda+2G)\frac{\partial^2 v}{\partial y^2}+G\frac{\partial^2 v}{\partial x^2}+(\lambda+G)\frac{\partial^2 u}{\partial x\partial y}+f_y=0\end{aligned}\tag{3.10}$$

the (3.10) is the static equilibrium equation system for the plain strain case. For the dynamic case the inertia forces can be added to (3.10) to obtain the equations of motion

$$\begin{aligned}(\lambda+2G)\frac{\partial^2 u}{\partial x^2}+G\frac{\partial^2 u}{\partial y^2}+(\lambda+G)\frac{\partial^2 v}{\partial x\partial y}+f_x=\rho\frac{\partial^2 u}{\partial x^2}\\(\lambda+2G)\frac{\partial^2 v}{\partial y^2}+G\frac{\partial^2 v}{\partial x^2}+(\lambda+G)\frac{\partial^2 u}{\partial x\partial y}+f_y=\rho\frac{\partial^2 y}{\partial y^2}\end{aligned}\tag{3.11}$$

where ρ is the material density. In the following only the static and the free vibration problem is solved. Thus for the free vibration case the equation of motion (3.11) are taken considering $f_x = f_y = 0$.

3.4 Plane stress state

Consider a thin plate in a plain stress state, the stress components are (3.9). As far as the strain components are concerned the Hooke's laws give

$$\varepsilon_x=\frac{\sigma_x-\nu\sigma_y}{E},\quad \varepsilon_y=\frac{\sigma_y-\nu\sigma_x}{E},\quad \varepsilon_z=-\frac{\nu\left(\sigma_x+\sigma_y\right)}{E},\quad \gamma_{xy}=\frac{\tau_{xy}}{G}\tag{3.12}$$

so it is clear that a plain stress case do not imply a plain strain one, because $\varepsilon_z \neq= 0$. The equilibrium equations are the same as the plain strain problem. Furthermore it can observed that substituting the congruence and the constitutive equations into the equilibrium equations the fundamental system in terms of displacements is formally equal to the plain strain case (3.10)

$$\begin{aligned}(\lambda^*+2G)\frac{\partial^2 u}{\partial x^2}+G\frac{\partial^2 u}{\partial y^2}+(\lambda^*+G)\frac{\partial^2 v}{\partial x\partial y}+f_x=0\\(\lambda^*+2G)\frac{\partial^2 v}{\partial y^2}+G\frac{\partial^2 v}{\partial x^2}+(\lambda^*+G)\frac{\partial^2 u}{\partial x\partial y}+f_y=0\end{aligned}\tag{3.13}$$

where the constant λ^* is related to the shear modulus G and the second Lamé constant

$$\lambda^*=\frac{2G\lambda}{2G+\lambda}\quad\text{or}\quad\lambda^*=\frac{E\nu}{1-\nu^2}\tag{3.14}$$

so the equation of motion for the plain stress case become

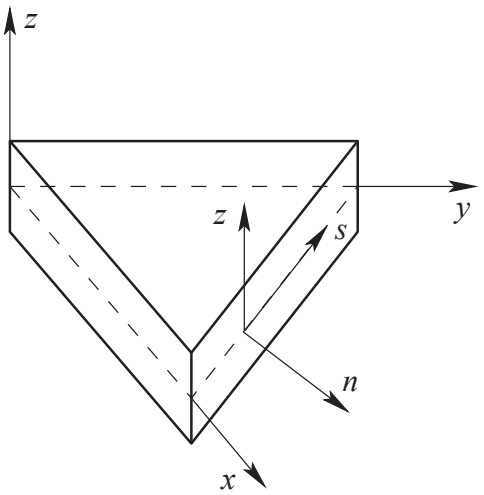

Figure 3.1: Local reference system of a generic side of normal **n**.

$$\begin{aligned}(\lambda^* + 2G)\frac{\partial^2 u}{\partial x^2} + G\frac{\partial^2 u}{\partial y^2} + (\lambda^* + G)\frac{\partial^2 v}{\partial x \partial y} + f_x &= \rho\frac{\partial^2 u}{\partial x^2} \\ (\lambda^* + 2G)\frac{\partial^2 v}{\partial y^2} + G\frac{\partial^2 v}{\partial x^2} + (\lambda^* + G)\frac{\partial^2 u}{\partial x \partial y} + f_y &= \rho\frac{\partial^2 y}{\partial y^2}\end{aligned} \tag{3.15}$$

It should be noted that both the plain states can be studied by the same set of fundamental equations. Formally the (3.11), (3.15) are the same, because the only difference is the definition of the parameter λ and λ^*. In the following only one set of differential equation is presented due to this symmetry between the two state plane cases.

3.5 Boundary conditions

The state plane problems described by (3.11) and (3.15) can be discretized by the GDQ method following the rules introduced in the first chapter. Once the static or the dynamic system is written in a discretized form, the boundary conditions and the inter-element boundary conditions must be defined (see section 1.7.3).

A triangular domain is considered in Figure 3.1, in which a generic reference system nsz is related to a Cartesian one xyz. According to the Theory of Elasticity [1–3] the normal and shear stresses of the local system nsz can be written as a function of the Cartesian system xyz

$$\begin{aligned}\sigma_n &= \sigma_x n_x^2 + \sigma_y n_y^2 + 2\tau_{xy} n_x n_y \\ \tau_{ns} &= (\sigma_y - \sigma_x)\, n_x n_y + \tau_{xy}\left(n_x^2 - n_y^2\right)\end{aligned} \tag{3.16}$$

where σ_x, σ_y are the normal stresses along the Cartesian axis x, y and τ_{xy} is the shear in-plane stress. Substituting (3.9) into (3.16) the stresses as a function of the Cartesian displacements are found.

$$\begin{aligned}
\sigma_n &= \left((\lambda + 2G)\, n_x^2 + \lambda n_y^2 \right) \frac{\partial u}{\partial x} + 2G n_x n_y \frac{\partial u}{\partial y} + \\
&+ 2G n_x n_y \frac{\partial v}{\partial x} + \left((\lambda + 2G)\, n_y^2 + \lambda n_x^2 \right) \frac{\partial v}{\partial y} \\
\tau_{ns} &= -2G n_x n_y \frac{\partial u}{\partial x} + G \left(n_x^2 - n_y^2 \right) \frac{\partial u}{\partial y} + \\
&+ G \left(n_x^2 - n_y^2 \right) \frac{\partial v}{\partial x} + 2G n_x n_y \frac{\partial v}{\partial y}
\end{aligned} \tag{3.17}$$

the relationships (3.17) can be directly mapped for an arbitrarily shaped domain using the extended derivative matrices introduced in section 1.4.1. The equations (3.17) are valid for any side. Either it is straight, with a constant normal vector along the side as depicted in Figure 3.1, or curved in which the normal vector changes node by node. It must be added that the geometric mapping plays a fundamental role in this aspect. It will be shown in the numerical examples that a 12-nodes elements works much better than an 8-nodes one, when there are several curved boundaries. In fact in order to capture a given curve generally more than one 8-nodes element is needed for the correct representation of the physical geometry.

3.6 State plane applications

Beyond the classic examples that are used for the introduction of states planes, such as thin uniform plates subjected to in plane loads or gravity walls in a plain strain condition. There are some more complex problems that can be studied by using simplified plain models.

The natural extension to the state plain problems is the study of composite materials. Today, these kinds of structures are widely used in several industries. Sandwich beams and plates which are categorized as composite structures with high values of strength to weight ratios. Another composite material application is the structural behaviour of structures with inclusions. In these cases, it is interested to know the stress distribution between two different kinds of materials. Another widely developed research branch is fracture mechanics, which is the study of cracks in a continuous media. For all these problems the classic GDQ technique is not sufficient due to the discontinuities that these problems have inherently. So in the following sections some numerical applications of the GDQFEM will be shown in order to study the accuracy of this advanced technique. As far as the numerical examples are concerned several cantilever elastic and composite beams will be studied in the following. In particular the free vibration case is firstly proposed. The natural frequencies of the given beam are reported as a function of the core elasticity, and geometric ratios. Secondly the static case of a cantilever composite beam is developed, where the stress recovery is reported in order to show the stress distribution along the beam thickness. Some inclusion and discontinuity problems follow the initial benchmarks of GDQFEM.

f [Hz]	Abaqus	MLPG Ref. [136]	NBNM Ref. [136]	EFG Ref. [136]	$n_e = 1$ $N = 41$	$n_e = 3$ $N = 21$
1	821.059	824.44	844.19	811.63	822.08	822.08
2	4925.76	5070.32	5051.21	4907.9	4931.61	4931.60
3	12823.2	12894.73	12827.6	12852	12823.20	12823.20
4	12975.4	13188.12	13258.2	13075	12989.85	12989.84
5	23581.1	24044.43	23992.8	24113	23605.51	23605.48
6	35964.9	36596.15	36432.2	37463	36000.21	36000.16
7	38440.5	38723.9	38436.4	38616	38441.64	38441.63
8	49516.7	50389.01	49937.2	51999	49564.38	49564.31
9	63831.7	64413.89	63901.2	64566	63894.24	63894.16
10	63965.6	64937.83	64085.9	68585	63970.67	63970.64

Table 3.1: First ten natural frequencies for a cantilever elastic beam.

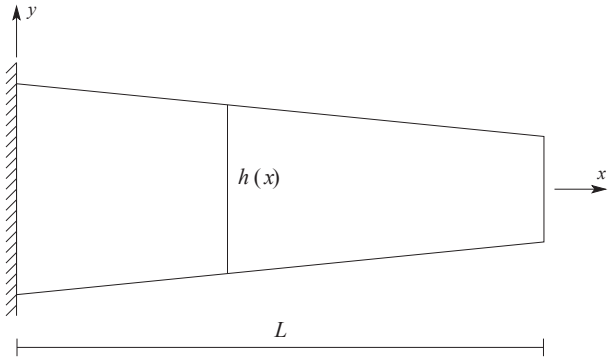

Figure 3.2: Geometry configuration of a tapered cantilever beam.

3.6.1 Free vibration analysis of a cantilever elastic beam

First of all for verification of the proposed method, a simple elastic cantilever beam is considered. As reported in [136] some other methods have been used in literature for the study of this problem. The properties of the beam are $E = 2.05939 \cdot 10^{11}$ N/m^2, $\nu = 0.3$, $\rho = 7845.32$ kg/m^3, where E is the Elastic modulus, ν the Poisson coefficient, ρ the material density. The geometric properties are $L = 0.10$ m, $D = 0.01$ m, where L is the beam length and D is the beam thickness.

In Table 3.1 the first ten natural frequencies f are reported. In the first column the FEM analysis is reported for the numerical comparison. A 200×20 element grid has been used for the FEM solution. The eigenfrequencies are obtained by various analysis methods also, such as "node by node method" (NBNM), Meshless Local Petrov-Galerkin (MLPG) and Element Free Galerkin (EFG). The GDQFEM is applied considering two simple cases. A single element with a grid of 41×41 points and a three element mesh in which a 21×21 points are used per element. All the results are in good agreement with the results proposed in literature and the one obtained by FEM.

3.6.2 Free vibration of a variable cross-section beam

In the following example the free vibration problem of a cantilever beam with variable cross-section is considered, as reported in [139]. The beam geometry is represented in

ω [rad/s]	MLPG Ref. [139]	FEM Ref. [139]	$n_e = 1$ $N = 13$	$n_e = 1$ $N = 21$	$n_e = 1$ $N = 31$	$n_e = 1$ $N = 41$
1	263.21	262.09	261.8031	261.6137	261.5746	261.5648
2	293.03	918.93	917.4574	917.5720	917.5941	917.5994
3	953.45	951.86	951.9089	951.9198	951.9247	951.9265
4	1855.14	1850.92	1852.2551	1852.2071	1852.1880	1852.1838
5	2589.78	2578.63	2584.4408	2584.3861	2584.3747	2584.3716
6	-	-	2736.5644	2736.5885	2736.5902	2736.5905
7	-	-	3286.4464	3286.4786	3286.4916	3286.4953
8	-	-	3701.2990	3701.8364	3701.8417	3701.8412
9	-	-	3853.8719	3853.9282	3853.9316	3853.9321
10	-	-	4155.5147	4155.4625	4155.4595	4155.4590

Table 3.2: Eigenvalues of a variable cross-section cantilever elastic beam.

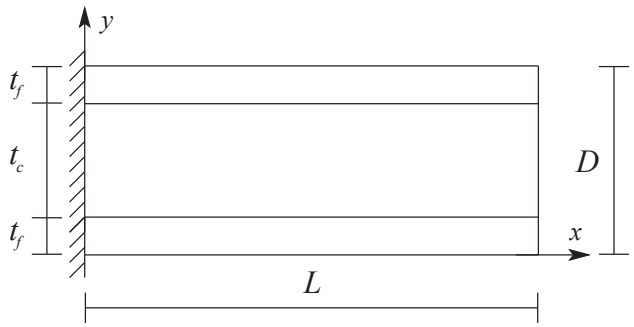

Figure 3.3: A fully clamped sandwich beam.

Figure 3.2 and the numerical parameters are: the length $L = 10$ m, the tapered height $h(x = 0) = 5$ m, $h(x = L) = 3$ m, the elastic modulus $E = 3 \cdot 10^7$ Pa and the Poisson's ratio $\nu = 0.3$.

The results in terms of eigenvalues ω are reported in Table 3.2. Moreover the results obtained by GDQFEM in the last column of the present table are compared with a reference solution as reported in [139] calculated by Meshless Local Petrov-Galerkin (MLPG) method and FE method (Abaqus). It has been shown that the present code with a single element and a sparse grid point distribution $N = M = 13$ can capture the solution with a small difference respect to the other solutions. Furthermore in Table 3.2 the convergence rate of GDQFEM can be seen in fact the solution does not oscillate increasing point numbers from $N = 13$ to $N = 41$.

3.6.3 Free vibration analysis of a cantilever sandwich beam

A cantilever sandwich beam is considered in the following. In Figure 3.3 a schematic diagram of the model is presented. In the case under study the beam has a flexible core which has an elastic modulus lower than the top and bottom face sheets. A partially clamped sandwich plate is considered also, where only the top and bottom sheets are fixed and the soft core is free instead.

The geometrical properties of the beams are $L = 1$ m, $D = 0.02$ m, where L is the beam length and D is the beam thickness as reported in Figure 3.3. In addition the core

f [Hz]	Abaqus	EFG [136]	$n_e = 3$ $N = 21$	$n_e = 3$ $N = 31$
1	21.5438	21.93	21.5620	21.5632
2	93.998	97.07	94.2283	94.2307
3	200.354	207.9	201.0721	201.0765
4	307.277	319.12	308.8174	308.8408
5	417.978	432.88	420.8502	420.8787
6	531.631	547.97	536.3943	536.4781
7	651.009	667.01	658.3320	658.4971
8	776.451	790.25	786.1107	787.3466
9	909.587	919.32	928.6953	924.6957
10	1050.72	1054.06	1136.3864	1070.8950

Table 3.3: First ten frequencies for a fully clamped sandwich cantilever beam.

f [Hz]	Abaqus	EFG [136]	$n_e = 3$ $N = 21$	$n_e = 3$ $N = 31$
1	21.5437	21.92	21.5643	21.6575
2	93.9951	96.81	94.2207	94.2002
3	200.346	207.24	201.0034	200.8917
4	307.264	318.1	308.7793	308.2736
5	417.961	431.49	420.6148	420.6976
6	531.609	546.14	536.3559	536.3396
7	650.981	664.67	658.6543	658.4117
8	776.418	787.28	779.5960	787.0041
9	909.547	915.61	904.8425	925.1526
10	1050.67	1049.9	1131.9594	1070.3390

Table 3.4: First ten frequencies for a partially clamped sandwich cantilever beam.

thickness is $t_c = 1.4 \cdot 10^{-2}$ m and the face sheet thickness $t_f = 3 \cdot 10^{-3}$ m. The material properties of the soft core are $E = 0.2$ GPa, $\nu = 0.27$, $\rho = 60$ kg/m^3 and the elastic properties of the sheets are $E = 200$ GPa, $\nu = 0.3$ and $\rho = 7800$ kg/m^3.

The first ten natural frequencies of the cantilever sandwich beam are extracted. The results of the present work and the FE analysis performed to check the solution are shown in Table 3.3. Furthermore the first ten eigenfrequencies of a partially clamped composited beam are written in Table 3.4. The numerical solutions show that the first ten frequencies of a cantilever sandwich beam with flexible core (Tables 3.3, 3.4) have good agreement with the results obtained in literature and the FE reference solution. The linear eigenvalue problem provides the modal shapes of the structure. So the first four modal shapes calculate with the GDQFEM code for the fully clamped beam are shown in Figure 3.4

To study the effect of flexibility of the core on the natural frequencies, the Young's modulus of the core is considered to be variable. The elastic modulus of the elastic core is $E_c = \chi E_f$, where the χ factor is reported in Table 3.5.The geometrical properties of the beam are the same, as given above. The first ten natural frequencies for fully clamped sandwich beam are given in Table 3.5. The results show that the natural frequencies of the sandwich beam increase when the Young's modulus of the core increases, which in

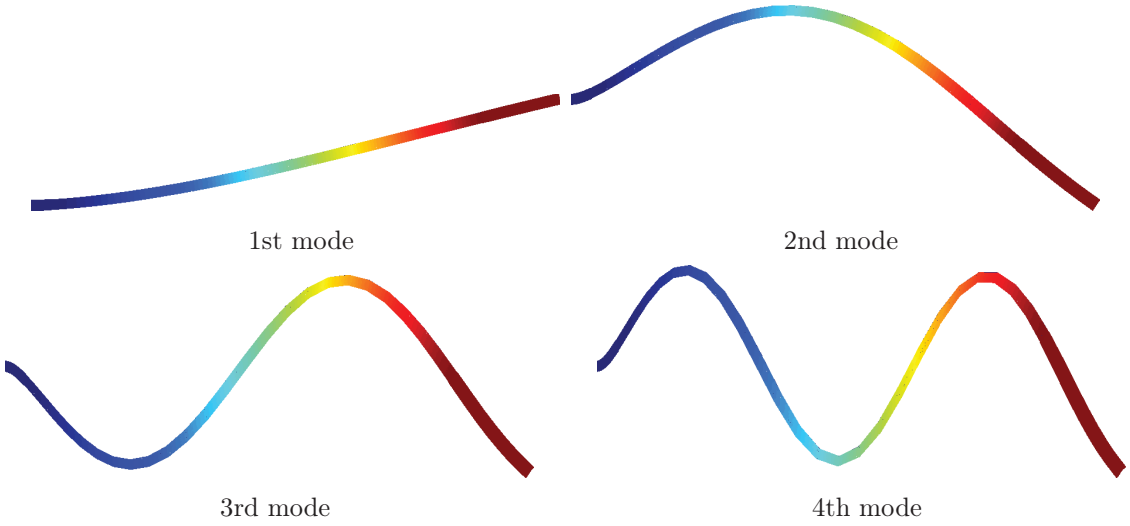

Figure 3.4: First four modal shapes of a cantilever sandwich beam.

turn is due to increasing the stiffness of the sandwich beam. Furthermore the difference between the the higher frequencies, keeping χ constant, is greater than the difference between the lower ones. Finally the first four modal shapes for the clamped composite cantilever beam are depicted in Figure 3.4.

χ	0.0001		0.001		0.01		0.1	
f [Hz]	EFG Ref. [136]	$n_e = 3$ $N = 31$	EFG Ref. [136]	$n_e = 3$ $N = 31$	EFG Ref. [136]	$n_e = 3$ $N = 31$	EFG Ref. [136]	$n_e = 3$ $N = 31$
1	13.744	13.40	21.93	21.56	24.085	23.77	25.08	24.58
2	45.235	44.70	97.07	94.23	141.64	139.30	155.82	152.70
3	85.857	86.77	207.9	201.08	364.23	356.48	430.59	421.75
4	129.63	135.08	319.12	308.84	645.17	628.03	828.52	810.72
5	181.01	194.44	432.88	420.88	960.92	930.75	1339.4	1308.72
6	240.41	265.12	547.97	536.48	1275.5	1249.23	1421	1393.58
7	309.26	348.60	667.01	658.50	1294.9	1269.31	1950	1901.87
8	388.13	444.90	790.25	787.35	1638.1	1575.31	2647.2	2576.28
9	477.52	554.53	919.32	924.70	1985.3	1904.92	3418.3	3318.73
10	577.98	677.41	1054.06	1070.90	2334.6	2236.38	4251.9	4117.36

Table 3.5: First ten natural frequencies of sandwich beams with various cores

3.6.4 Static analysis of a cantilever composite beam

In the following section a static analysis of the plain strain problem of composite beams is considered. A sandwich composite cantilever plate consisting of three layers of two materials, shown in Figure 3.3, is analyzed [11]. The composite beam is subjected to a uniform vertical load q. The upper and lower surface layers, are made of the same materials. The core layer is made of a material different from the surface sheets. For the surface sheets the Young's modulus $E = 1.67{\cdot}10^9 \mathrm{N/m^2}$ and for the core layer $E = 1.67{\cdot}10^8$ $\mathrm{N/m^2}$; the Poisson's ratio is $\nu = 0.3$ for both materials. The geometric parameters are $L = 4.8$ m, $D = 1.2$ m, where L is the beam length and D is the thickness of the beam,

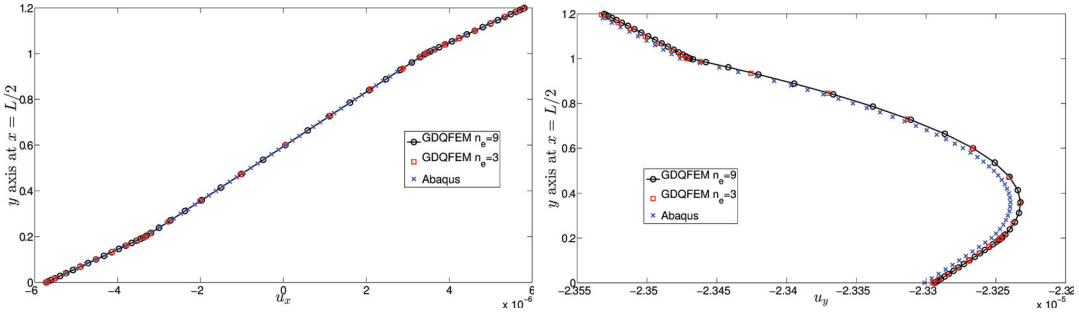

a) b)

Figure 3.5: Displacements of of sandwich cantilever beam at section $x = L/2$: a) Displacement along x axis; b) Displacement along y axis.

moreover $t_c = 0.8$ m, $t_f = 0.2$ m and $q = 100$ N/m. The solution is very well known in literature according to [11, 12, 38]. The solutions for the displacements and the stresses at the middle section $x = L/2$ are given in Figures 3.5-3.6. Displacements are continuous as required by the compatibility condition. It is noted that discontinuous finite jumps are observed at the material interfaces in σ_x and sharp turning point in shear stress τ_{xy}. The comparison is made with a FE analysis, performed with Abaqus.

In the case under study two GDQFEM meshes are considered: a three element mesh with a 21×11 grid points and a nine element mesh with a 21×21 grid. It is noted that three elements are not enough (with a uniform grid) to capture the numerical solution due to the highly stretched elements in the mesh. In fact $N \neq M$ has been used in order to have an accurate solution with three elements only. So, from Figures 3.5, 3.6 it is clear that the red lines that represents the three element mesh captures the axial displacement u_x, the vertical displacement u_y and the stresses σ_x and τ_{xy} especially at the top layer in which the loading q has been applied. This means that for the case under consideration three elements are enough to evaluate the composite beam stresses and displacements.

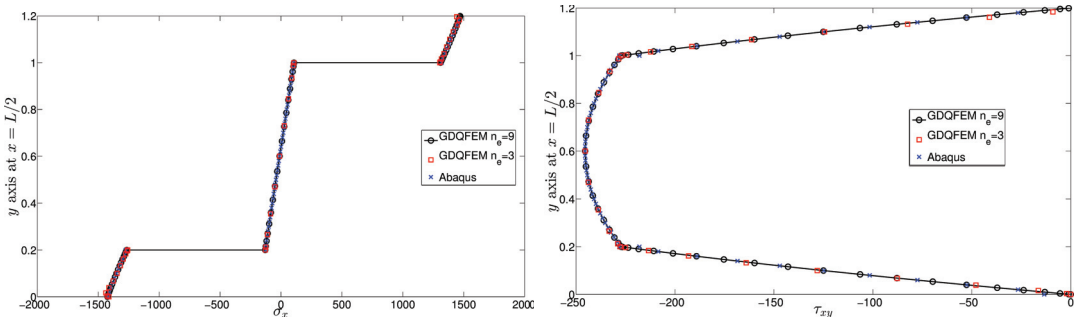

a) b)

Figure 3.6: Stress results of sandwich cantilever beam at section $x = L/2$: a) Normal stress σ_x; b) Tangential stress τ_{xy}.

3.6.5 MacNeal's thin cantilever beam

In the following example a standard benchmark used in several FE tests is performed [112]. It is worth noting that this kind of problem is a classic benchmark for measuring

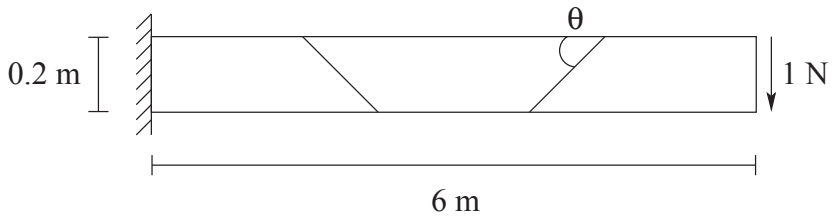

Figure 3.7: MacNeal's beam three elements mesh under shear force.

exact [124]	1.000 (0.1081 m)		
FEM [126]	Regular 0.993	Parallelelogram 0.985	Trapezoidal 0.988
GDQFEM	$n_e = 1$ 0.99882	$n_e = 3$, $\theta \approx \pi/6$ 0.99775	$n_e = 3$, $\theta \approx \pi/18$ 1.00031

Table 3.6: Normalized tip deflection of MacNeal's thin beam for different load cases and mesh geometries.

accuracy and testing the sensitivity to mesh distortion for plane elements, in fact some other researchers used this example in the past [113, 115, 116, 121, 123–126]. The given beam, represented in Fig. 3.7, is $L = 6$ m long and $H = 0.2$ m high. Since a state plane problem is under consideration the model has a constant thickness $h = 0.1$ m. The MacNeal's beam elastic modulus is $E = 10$ MPa and Poisson's ratio $\nu = 0.3$. An unit shear load $F = 1$ N is considered at the tip of the beam. The vertical displacement at the end of the beam is calculated in the following. The numerical solution obtained by GDQFEM has been compared to the exact solution $v = 0.1081$ and some other results found in literature. Furthermore for examining the accuracy and sensitivity of the present methodology regular and distorted meshes are considered as it has been already done by [126]. It should be underlined that GDQFEM does not need so many elements as FE because it is high-accuracy methodology. In fact from Table 3.6 it is clear that only one element is sufficient to capture the solution. Moreover some distorted meshes are attached for deeply underline the good accuracy that GDQFEM has. In particular the angle θ, reported in table 3.6 is graphically presented in Fig. 3.7, which is the angle between the horizontal axis and the shortest side of the elements used in the current mesh. In the present solution the considered grid distributions are Chebyshev-Gauss-Lobatto ones within $N = 41$ and $M = 21$ points. It is noted that more points are needed along x direction because a thin beam is under consideration. In table 3.6 the distortion angle θ is indicated. In order to visually see the mesh distortion Fig. 3.7 can be taken as a reference.

3.6.6 Cook's cantilever beam

In order to show the GDQFEM behaviour against the mesh distortion another popular benchmark, which is used to asses the efficiency of the plane elements, is the Cook's cantilever beam [117]. The reference geometry of a Cook's beam is graphically presented in Figure 3.8. The structure is subjected to a constant shear distributed load $P = 1$ N at the free edge. The beam is elastic and homogeneous within an elastic modulus $E = 1$ Pa and a Poisson's ratio $\nu = 1/3$. The numerical results obtained by means of GDQFEM

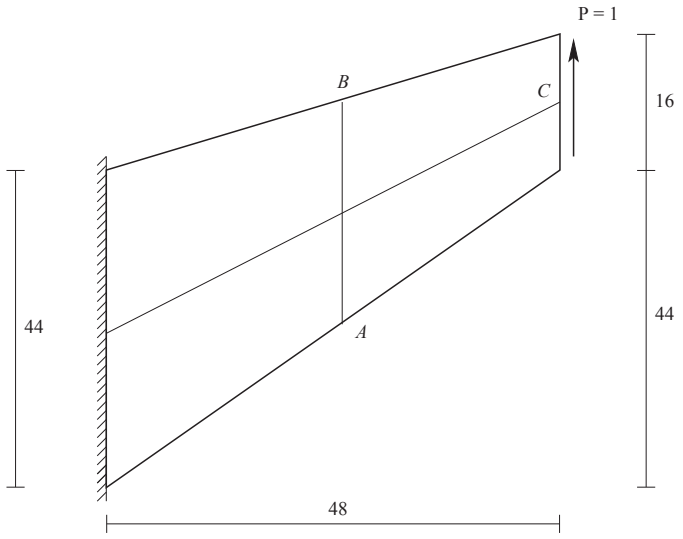

Figure 3.8: Cook's cantilever beam geometry.

methodology are compared with a FE analysis. In particular the maximum deflection at point C, the maximum principal stress at point A and the minimum principal stress at point B are considered in the comparison. The proposed example has been taken by other researchers' solution [126] and the present results are reported in Table 3.7. It must be added that this problem does not have an analytical solution, so a refined FE solution has been taken as a reference.

In order to calculate the principal stresses the following formulae will be used

$$\left.\begin{matrix}\sigma_1\\ \sigma_2\end{matrix}\right\} = \frac{\sigma_x + \sigma_y}{2} \pm \frac{1}{2}\sqrt{\left(\sigma_x - \sigma_y\right)^2 + 4\tau_{xy}^2} \tag{3.18}$$

where σ_1 is the maximum principal stress and σ_2 is the minimum principal stress. σ_x, σ_y and τ_{xy} are the stresses that are taken from the numerical solution written respect to the Cartesian Coordinate system.

The numerical solution obtained via GDQFEM is shown for several meshes and different levels of distortions. Moreover the number of grid points is variable to see the rate convergence number within each different mesh. In Table 3.7 four different meshes that are depicted in Figure 3.9 are presented for various grid point distributions, either uniform $N = M$ and not uniform $N \neq M$. It can be noticed that either with regular mesh or not regular mesh the results are in good agreement with literature [119, 126] and a FE solution obtained by ABAQUS.

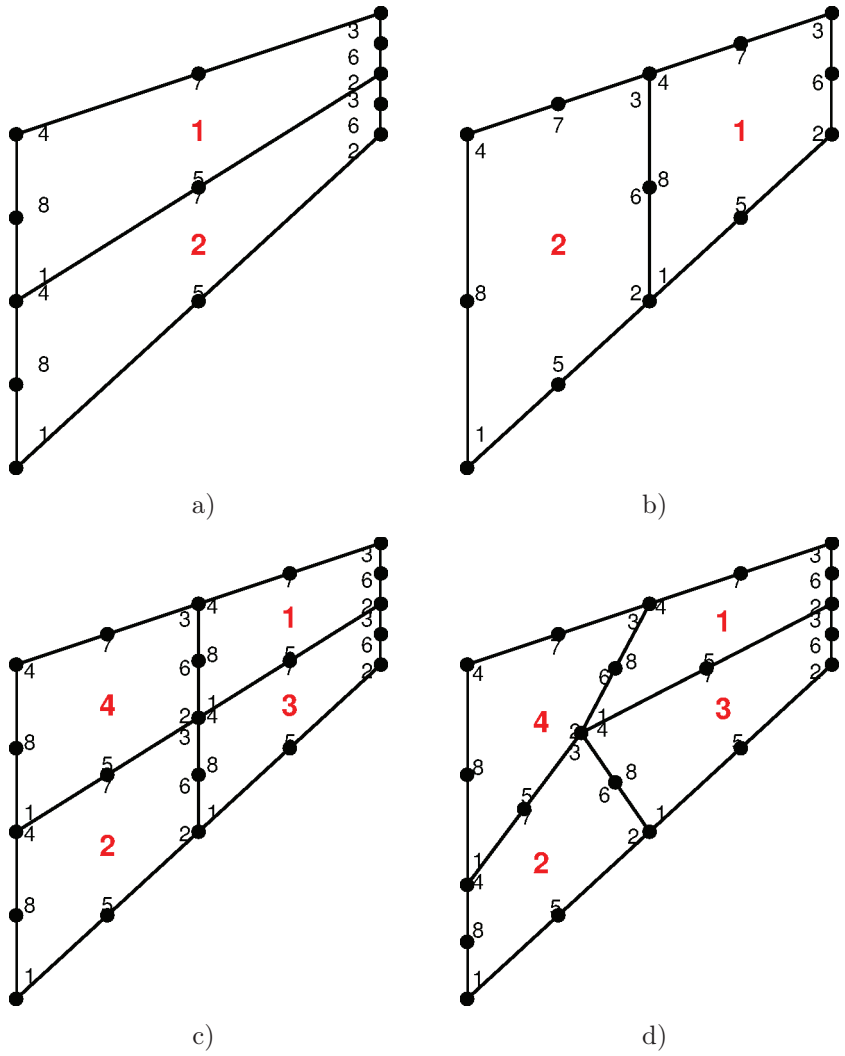

Figure 3.9: Cook's beam GDQFEM meshes: a) Two elements mesh after horizontal division; b) Two elements mesh after vertical division; c) Four elements mesh within regular division; d) Four elements distorted mesh.

	ABAQUS	Ref. [119]	Ref. [126]	GDQFEM $n_e = 1$		
				$N = 21$ $M = 21$	$N = 35$ $M = 27$	$N = 41$ $M = 31$
$\sigma_{A,max}$	0.2369	0.2362	0.2367	0.2374	0.2371	0.2367
$\sigma_{B,min}$	-0.2035	-0.2023	-0.2039	-0.2034	-0.2060	-0.2014
$u_{y,C}$	23.961	23.96	23.90	24.0627	23.9690	23.9677
	GDQFEM $n_e = 2$ (vertical)			GDQFEM $n_e = 2$ (horizontal)		
	$N = 21$ $M = 21$	$N = 31$ $M = 31$	$N = 41$ $M = 31$	$N = 21$ $M = 11$	$N = 31$ $M = 21$	$N = 41$ $M = 21$
$\sigma_{A,max}$	0.2379	0.2374	0.2383	0.2367	0.2371	0.2369
$\sigma_{B,min}$	-0.1970	-0.1992	-0.1943	-0.1967	-0.2050	-0.2009
$u_{y,C}$	23.9790	23.9717	23.9665	23.9644	23.9973	23.9680
	GDQFEM $n_e = 4$ (regular)			GDQFEM $n_e = 4$ (distorted)		
	$N = 21$ $M = 21$	$N = 23$ $M = 17$	$N = 31$ $M = 21$	$N = 21$ $M = 21$	$N = 23$ $M = 17$	$N = 31$ $M = 21$
$\sigma_{A,max}$	0.2371	0.2369	0.2369	0.2366	0.2368	0.2369
$\sigma_{B,min}$	-0.2032	-0.1982	-0.1980	-0.1962	-0.1773	-0.1726
$u_{y,C}$	24.0021	23.9756	23.9691	23.9431	23.9196	23.9386

Table 3.7: Numerical comparison for the Cook's beam.

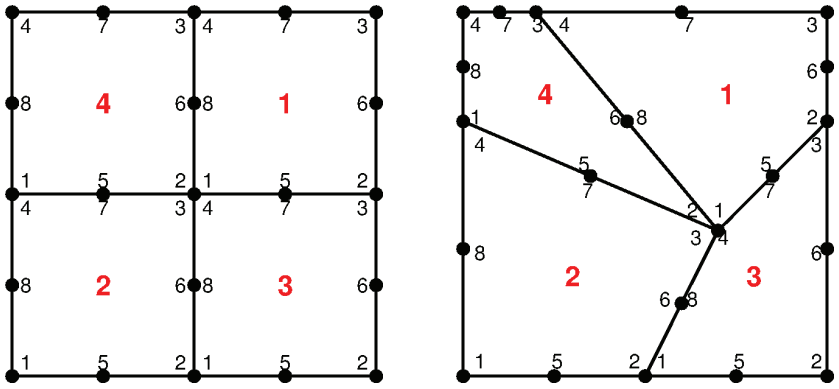

Figure 3.10: Cantilever wall GDQFEM meshes: a) Four elements regular mesh; b) Four elements highly distorted mesh.

3.6.7 Cantilever wall

In order to make further investigations into the accuracy of the GDQFEM technique, the in-plane vibration of a square cantilever plate, which can be viewed also as a deep beam under the plane stress condition. This problem can be considered as another standard benchmark due to the fact that it had been taken by several researchers under consideration [114, 120, 122]. In particular Gupta [114] studied this problem in great detail and provided a very fine mesh of plane stress elements that can be considered to be an exact solution.

This numerical solution had been taken as a reference for the accuracy tests of different alternatives for the same kind of problem by [114, 118, 120, 122]. As a result the in-plane vibration of a square cantilever plate under the plane stress condition can serve as a standard problem. The same parameters as in literature [114, 120, 122] have been used: the elastic modulus $E = 1$, the Poisson's ratio $\nu = 0.3$ and the density $\rho = 1$. The length and the width of the given cantilever wall are equal to $L = 10$. The numerical results in terms of frequencies obtained by GDQFEM and the results taken from literature are presented. Furthermore a FE numerical solution obtained by ABAQUS is added in the comparison. In Table 3.8 the first ten eigenfrequencies $\omega_i = 2\pi f_i$ are reported. Three different meshes have been used in the computation a single square element $n_e = 1$ is considered at first within several grid point numbers. A four regular and distorted meshes $n_e = 4$, graphically depicted in Figure 3.10, are used to show the accuracy and stability of GDQFEM methodology. It is noted that the four element distorted mesh has a high level of distortion (see Figure 3.10). For each numerical case a Chebyshev-Gauss-Lobatto grid points distribution have been used considering the same number of points along the master element coordinates $N = M$.

In addition some more detailed accuracy tests are presented in Figure 3.11. The logarithmic error is plotted as a function of the number of grid points $N = M$, considering the three meshes reported above. The convergence tests are based on the logarithm of the absolute error between the GDQFEM and FEM solution.

$$\log_{10}\left(\omega_{\text{GDQFEM}} - \omega_{\text{FEM}}\right) \tag{3.19}$$

It can be noticed that as the number of grid points increases the absolute error de-

ω [rad/s]	Ref. [120]	ABAQUS	GDQFEM $n_e = 1$			
			$N = 11$	$N = 21$	$N = 31$	$N = 41$
1	0.065853	0.065820	0.065917	0.065828	0.065819	0.065816
2	0.157951	0.157956	0.157948	0.157948	0.157950	0.157951
3	0.176908	0.177207	0.177197	0.177206	0.177206	0.177205
4	0.279651	0.281591	0.281572	0.281588	0.281590	0.281590
5	0.30337	0.303671	0.303475	0.303636	0.303652	0.303656
6	0.321367	0.322280	0.322276	0.322281	0.322280	0.322280
7	-	0.406225	0.406195	0.406225	0.406223	0.406223
8	-	0.427679	0.427694	0.427663	0.427662	0.427662
9	-	0.472234	0.472220	0.472235	0.472233	0.472233
10	-	0.475256	0.475288	0.475252	0.475249	0.475248
ω	GDQFEM $n_e = 4$ (Regular)			GDQFEM $n_e = 4$ (Distorted)		
[rad/s]	$N = 7$	$N = 11$	$N = 21$	$N = 7$	$N = 11$	$N = 21$
1	0.065952	0.065845	0.065818	0.065794	0.065826	0.065819
2	0.157974	0.157952	0.157951	0.158004	0.157952	0.157950
3	0.177241	0.177218	0.177208	0.177212	0.177217	0.177210
4	0.281638	0.281595	0.281591	0.281752	0.281601	0.281592
5	0.303666	0.303665	0.303661	0.303519	0.303671	0.303667
6	0.322306	0.322286	0.322281	0.322317	0.322287	0.322282
7	0.406221	0.406209	0.406222	0.406472	0.406213	0.406226
8	0.427720	0.427660	0.427665	0.427872	0.427694	0.427678
9	0.472557	0.472227	0.472232	0.472759	0.472242	0.472233
10	0.475375	0.475225	0.475243	0.475507	0.475209	0.475239

Table 3.8: First ten eigenfrequencies of a cantilever wall.

creases rapidly to the reference solution (ABAQUS). It should be noticed that as expected the GDQFEM solution using a four elements distorted mesh has a less rapid convergence respect to the regular mesh and the single element mesh. These kinds of results have been already reported for the membrane case in Chapter 2, in which the convergence rate is reported for a rectangular membrane compared to the analytical solution.

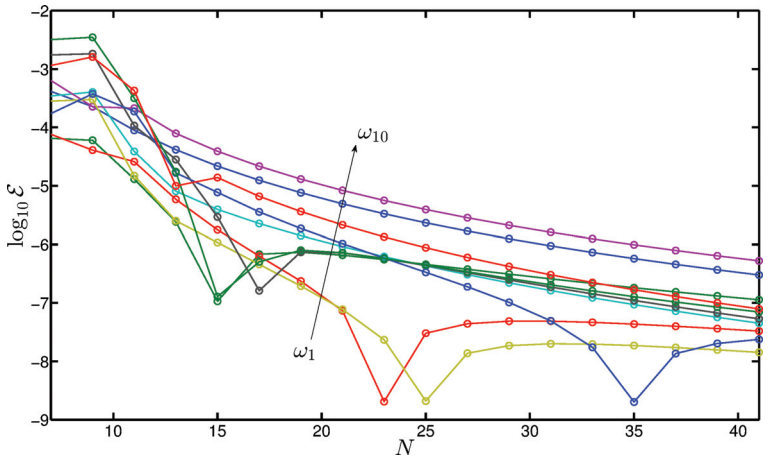

a)

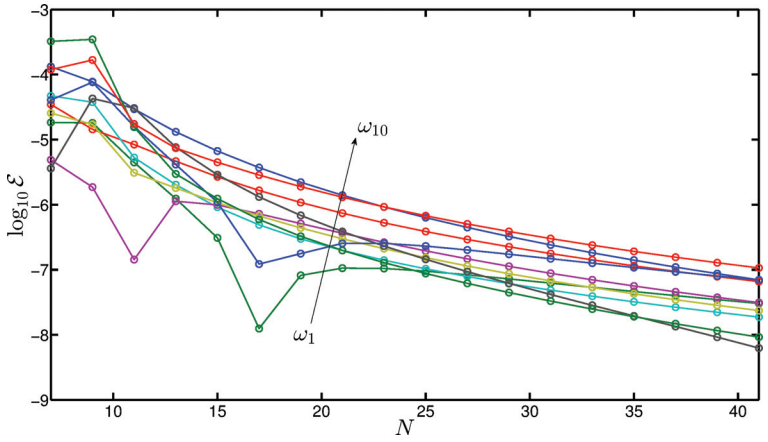

b)

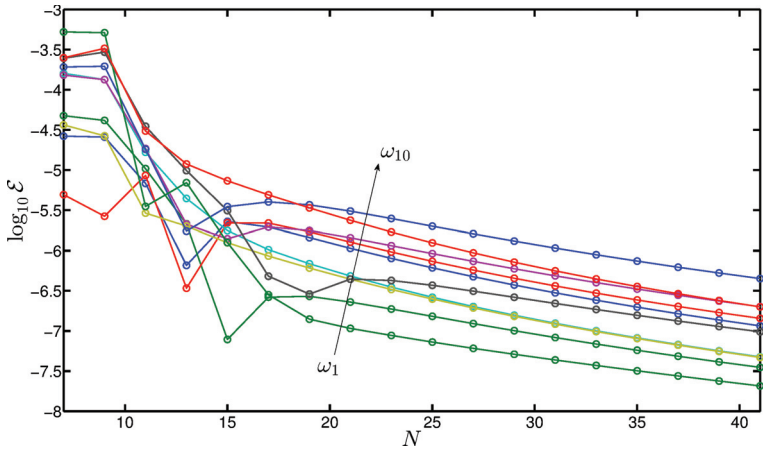

c)

Figure 3.11: Convergence tests for a cantilever wall: a) Single element; b) Four elements; c) Four elements within an highly distorted mesh.

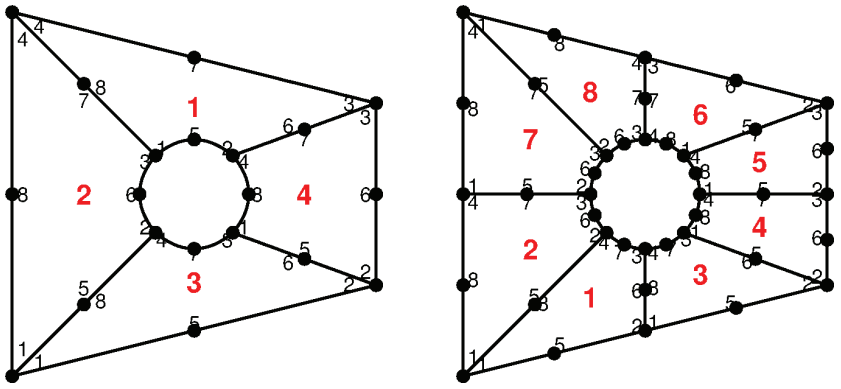

a) b)

Figure 3.12: Cantilever tapered plate with a circular centred hole: a) Four elements mesh; b) Eight elements mesh.

3.6.8 Tapered cantilever plate with a central circular hole

In the following example the vibration of a tapered cantilever plate with a central circular hole under plane stress conditions is considered. The side length is set to $L = 10$ and the radius of the inner circle is $R = 1.5$. Herein the main difficulty is given by the curved internal boundary. So more elements are needed in order to capture this particular shape.

ω [rad/s]	abaqus	GDQFEM $n_e = 4$			GDQFEM $n_e = 8$		
		$N = 11$	$N = 21$	$N = 41$	$N = 11$	$N = 21$	$N = 31$
1	0.0700	0.071226	0.070128	0.070120	0.069976	0.069978	0.069978
2	0.1558	0.155596	0.155998	0.155998	0.155851	0.155863	0.155864
3	0.1999	0.199411	0.199967	0.199962	0.199874	0.199880	0.199879
4	0.2620	0.262110	0.262643	0.262636	0.262028	0.262070	0.262071
5	0.2917	0.292303	0.292199	0.292197	0.291744	0.291732	0.291732
6	0.4192	0.419199	0.419846	0.419847	0.419260	0.419256	0.419259
7	0.4208	0.420896	0.420925	0.420918	0.420825	0.420818	0.420818
8	0.4678	0.468142	0.468025	0.468024	0.467834	0.467844	0.467845
9	0.4801	0.480427	0.480894	0.480894	0.480190	0.480122	0.480124
10	0.5281	0.525467	0.528197	0.528203	0.528079	0.528074	0.528076

Table 3.9: First ten eigenfrequencies of a tapered cantilever plate with a circular centered hole.

Once again this example is useful to examine the accuracy and applicability of the current methodology when irregular geometries are used in the analysis. As depicted in Figure 3.12 the tapered cantilever plate with a circular hole in its center is divided into eight irregular quadrilateral elements. This example had been studied by some researchers [120, 122], so the following material parameters are used in the analysis: elastic modulus $E = 1$, Poisson's ratio $\nu = 0.3$ and density $\rho = 1$. In this example the reference solution is obtained with the aid of ABAQUS. In Table 3.2 the first ten eigenfrequencies are reported $\omega_i = 2\pi f_i$ and several convergence tests are depicted in Figure 3.13 in which the logarithmic error is plotted as a function of the number of grid points $N = M$.

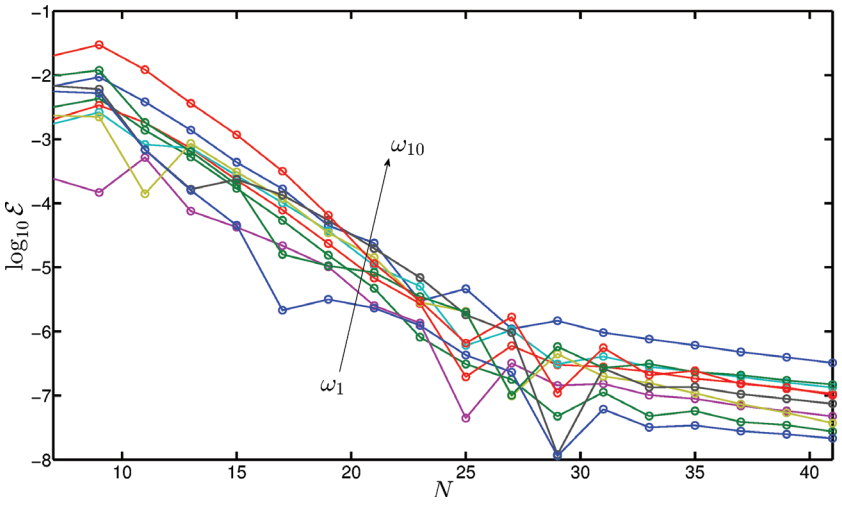

a)

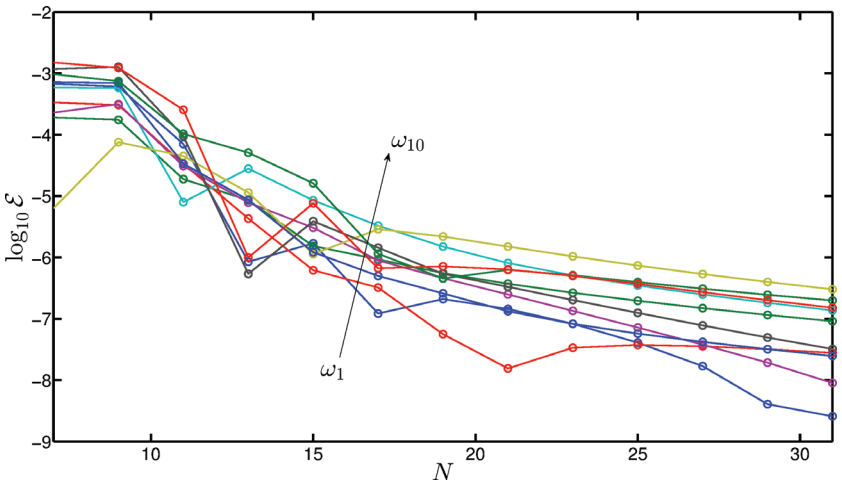

b)

Figure 3.13: Convergence tests for a tapered cantilever plate with a centred circular hole: a) Four elements mesh; b) Eight elements mesh.

Although few irregular elements have been used, the accuracy of the present solution is in very good agreement with the reference solution. It is clear that the solution within $n_e = 8$ is more accurate compared to $n_e = 4$ because the curved boundary is better approximated. For every computation a Chebyshev-Gauss-Lobatto grid distribution has been employed within various grid point number. It is underlined that the same number of points is used along the two sides of the element $N = M$.

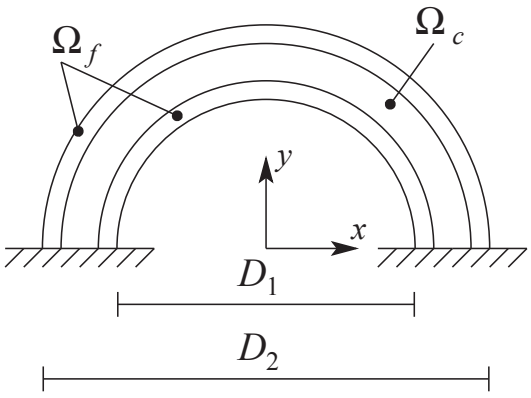

Figure 3.14: Geometry configuration of the sandwich circular arch.

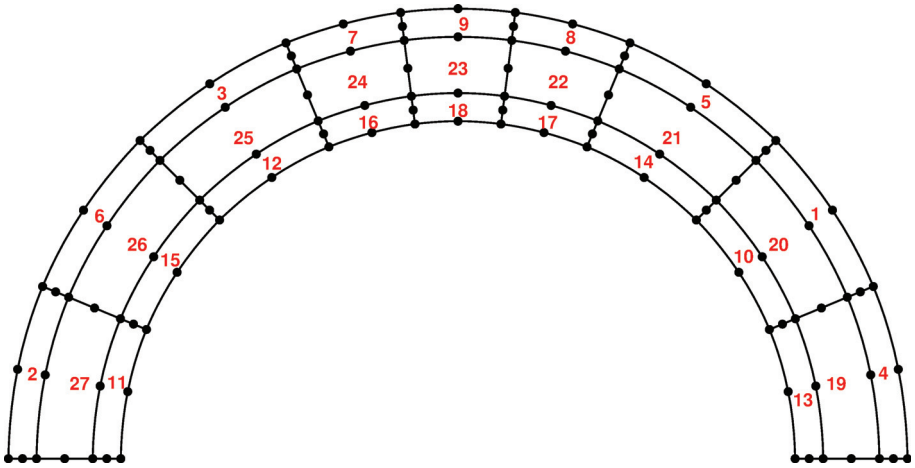

Figure 3.15: GDQFEM mesh of a sandwich circular arch.

3.6.9 Curved composite beam

In the following example the static and dynamic analyses of a composite circular plane arch are considered. The arch geometry is reported in figure 3.14, where the inner radius $D_1 = 6$ m and the outer radius $D_2 = 8$ m, as a result the arch thickness is $t = 1$ m. A sandwich circular arch is considered, in which the two face sheets at the top and the bottom of the arch are made of $E_f = 3 \cdot 10^7$ N/m^2 , $\nu_f = 0.3$ and density $\rho_f = 2000$ kg/m^3 with a thickness $t_f = 0.25$ m, in addition the core is made of a material that is softer than the top and bottom sheets with $E_c = 3 \cdot 10^4$ N/m^2, $\nu_c = 0.25$ and density $\rho_c = 100$ kg/m^3 with a thickness $t_c = 0.5$ m. It is noted that in this problem the elastic modulus of the core is 1000 times and the density is 20 times lower than the two face sheets.

Static analysis

Given the problem geometry depicted in Figure 3.14 an inner uniform pressure is applied to the structure $q = 100$ N/m. This kind of load simulate an internal pressure in the opposite direction of the conventional positive normal. A mesh composed of 27 elements has been used in which three elements are located along the thickness only, as reported in Figure 3.15). Moreover a 15×15 Chebyshev-Gauss-Lobatto grid point distribution is used in the computation per element. The comparison of displacements, strains and

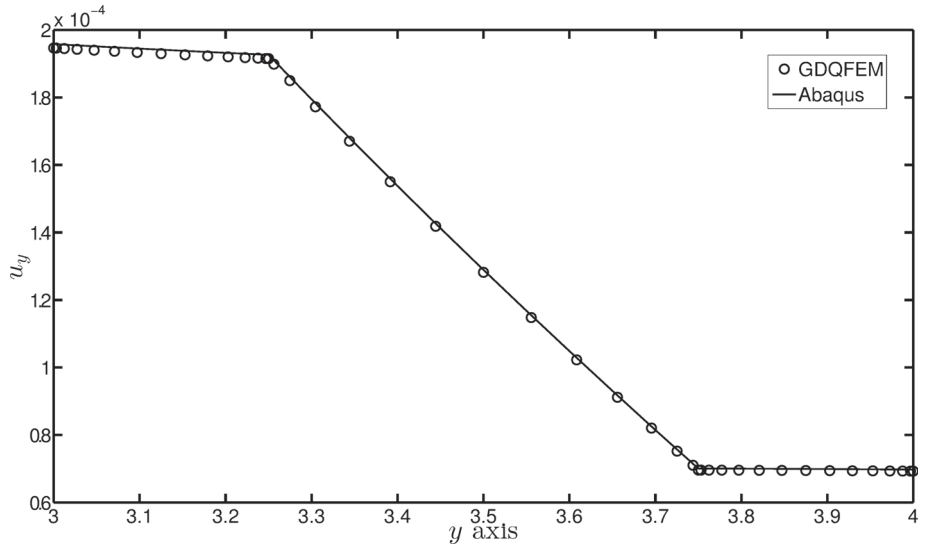

Figure 3.16: Displacement values along the arch thickness at section $x = 0$.

stresses have been done with Abaqus at the symmetry section of the arch, in other words all the Figures 3.16-3.17 are made along the y axis at $x = 0$.

In is obvious that the displacement in the x direction, u_x, is not represented due to the symmetry of the problem. It is also noted that the GDQFEM solution is in very good agreement with the solution obtained by Abaqus, either for the displacements and the stresses.

The GDQFEM, like the classic GDQ, solves the strong form of the fundamental governing system, so the static algebraic system gives the displacements of all the grid points of the current mesh. In order to obtain the strain and the stresses point by point no complex algorithm is needed. The strains are calculated deriving the displacements, computationally speaking multiplying the GDQ matrices to the obtained displacements and the stresses are computed using the constitutive equations of the theoretical problem.

Dynamic analysis

In this section the dynamic analysis of the composite circular arch represented in Figure 3.14 is presented. The first ten frequencies are reported in Table 3.10 for several mesh grids per element and compared with a FE solution. The eigenfrequencies are in good agreement with the ones of Abaqus and the solution converges when the number of points increases. It should be noted from Table 3.10 that not always the same number of grid points has been used. In fact an accurate solution can be found when $N \neq M$, in particular more points are considered along the circumference and less along the thickness obtaining almost the same accuracy of $N = M$. In Figure 3.18 the first four modal shapes are reported for the composite arch under study. It is underlined that the modal shapes involve the arch thickness due to the soft core of the curved beam.

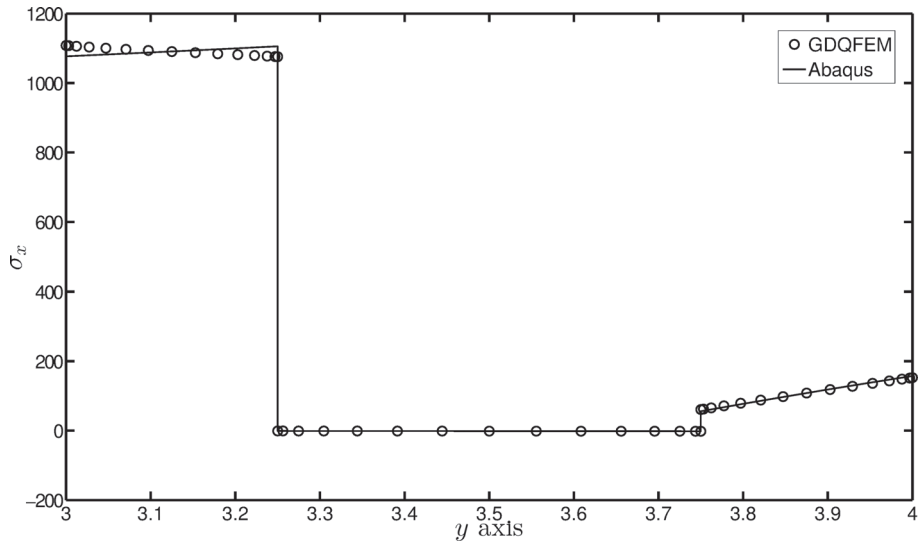

a)

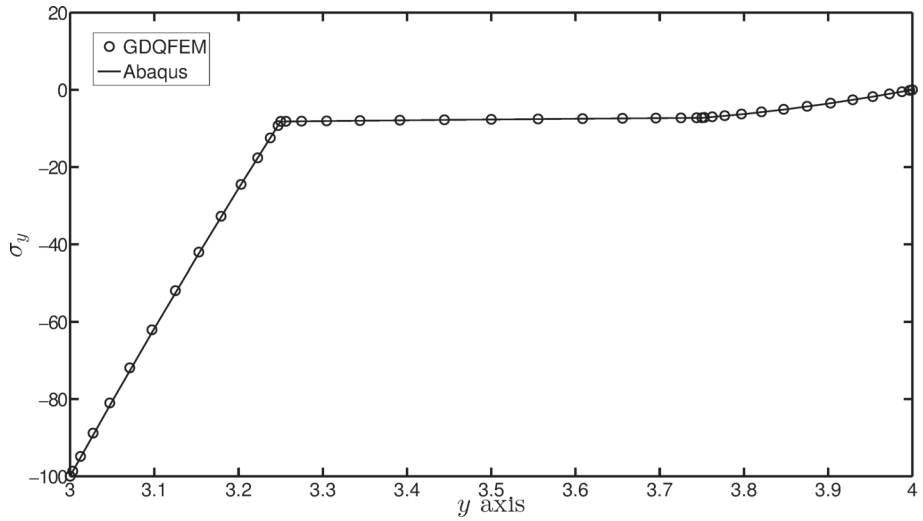

b)

Figure 3.17: Stress values along the arch thickness at section $x = 0$: a) Normal stress σ_x; b) Normal stress σ_y.

f [Hz]	Abaqus	$N=9$ $M=9$	$N=11$ $M=11$	$N=15$ $M=15$	$N=9$ $M=21$	$N=11$ $M=21$	$N=13$ $M=17$
1	0.5524	0.5531	0.5535	0.5531	0.5537	0.5531	0.5529
2	1.1561	1.1588	1.1584	1.1573	1.1580	1.1571	1.1570
3	1.9997	2.0027	2.0023	2.0008	2.0015	2.0004	2.0004
4	2.2463	2.2512	2.2497	2.2483	2.2479	2.2477	2.2479
5	2.6446	2.6459	2.6461	2.6456	2.6458	2.6454	2.6454
6	2.8359	2.8354	2.8354	2.8347	2.8356	2.8346	2.8345
7	3.2546	3.2557	3.2561	3.2554	3.2564	3.2554	3.2551
8	3.8607	3.8602	3.8605	3.8602	3.8612	3.8602	3.8600
9	4.1803	4.1815	4.1805	4.1789	4.1796	4.1786	4.1785
10	4.5884	4.5872	4.5868	4.5869	4.5870	4.5871	4.5870

Table 3.10: First ten frequencies for a circular composite arch for several grid points.

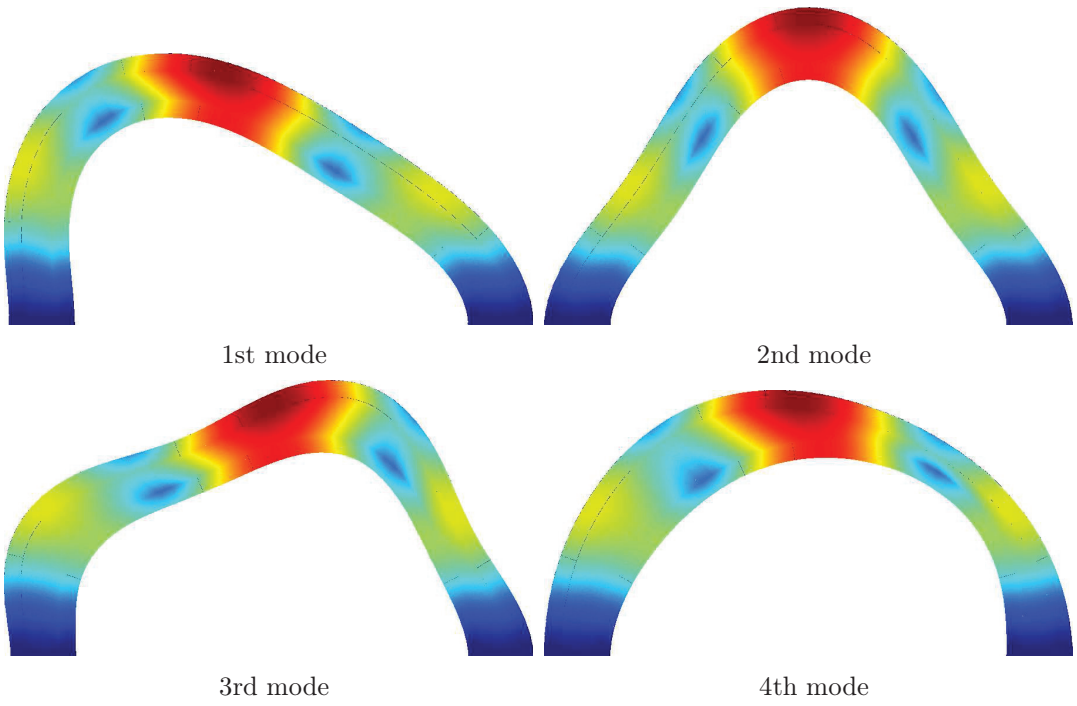

Figure 3.18: First four modal shapes of a composite circular arch.

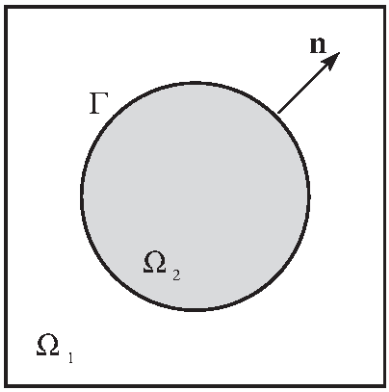

Figure 3.19: Graphical depiction for interface elasticity problem

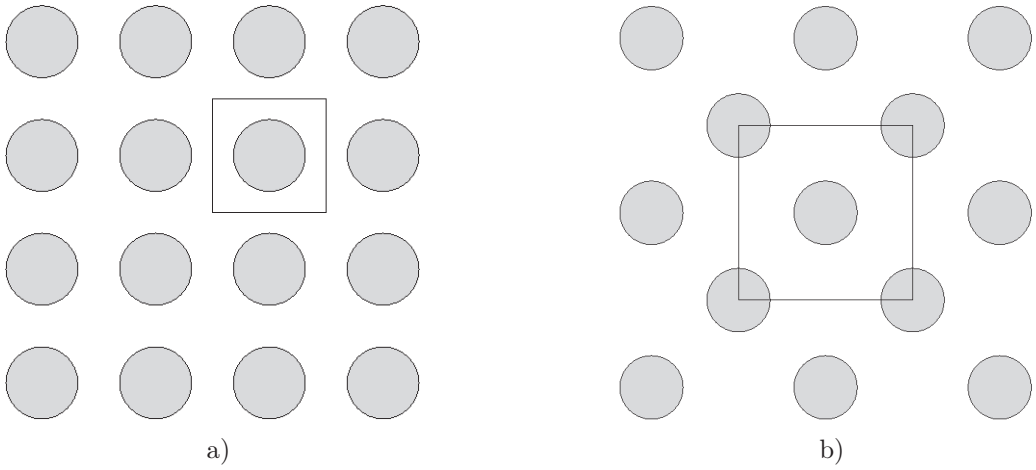

Figure 3.20: Generic RVE configurations: a) square packing; b) hexagonal packing.

3.6.10 Inclusion problem

The elasticity of composite solids such as particle and fibre-reinforced composites is a boundary value problem (BVP) that can be modelled in several ways according to [137]. These kinds of problems have discontinuous coefficients across the material interfaces in terms of displacements and stresses.

An elastic solid occupies a bounded and open domain as in Figure 3.19, that is composed of two perfectly bonded materials with zero-thickness interface Γ. The equilibrium configuration of the elastic body is characterized by the continuity of displacements and continuity of normal stresses across the material interface Γ. Typical inclusions of realistic morphology such as reinforced particles or fibres can be idealized as in Figure 3.19, in which the matrix is generally Ω_1 and the fibre is represented by Ω_2.

In a real unidirectional fibre-reinforced composite the fibres are arranged randomly. Since it is difficult to model random fibre arrangement, usually, the actual cross-section of the composite is idealized as a regular array of fibres, either in a square or hexagonal fibre array packing, as reported in [138]. In Figure 3.20 both square and hexagonal fibre packing are depicted.

One direct approach that comprehend the inclusion problem is the micro-mechanical analysis of heterogeneous materials. In particular it is of engineering interest the prediction of macroscopic moduli of heterogeneous materials given the moduli of the individual

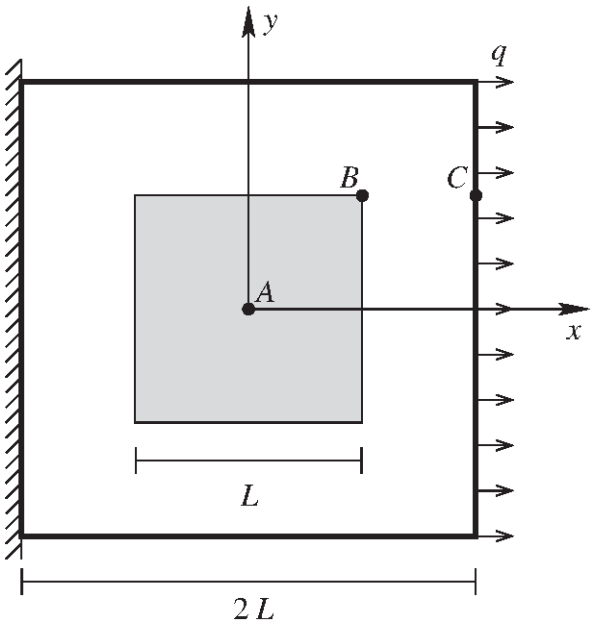

Figure 3.21: Square plate with a square inclusion.

phases and their geometric arrangement. Micro-mechanical analysis are typically conducted based on either the concept of a representative volume element (RVE), which characterizes heterogeneous materials with macroscopically or statistically heterogeneous micro-structures at an appropriate scale [106] or a repeating cell unit (RUC) which characterizes periodic heterogeneous materials . These two concepts are based on different geometric representations of heterogeneous micro-structures and require different boundary conditions in the micro-mechanical analysis of the smallest material sub-volume whose response is indistinguishable from that of the material-at-large. In particular, micro-mechanical analysis of an RVE is based on the equivalence of homogeneous traction and displacement boundary conditions, which in fact defines the RVE concept, while micro-mechanical analysis of an RUC is based on combined periodic displacement and traction boundary conditions [107].

The RVE and RUC concepts have been re-examined recently in greater deal by several investigators [108], [109], [110], [111]. It has been assumed in [138] that all effective characteristics and global behaviour of the composite are similar to those of the RVE. Hence, special care should be taken to select the correct RVE and to apply the correct boundary conditions to model the real loading conditions on the composite.

However in this PhD Thesis the problem of composite homogenization is not performed because the purpose of this work is to show that it is possible to obtain and compare some numerical application to inhomogeneous problems.

Static analysis of a square plate with a square inclusion

Considering the simple case of a square plate with a square inclusion at its center under uniform distributed forces at its right edge and clamped on the left side (see Figure 3.21). The plate and its inclusion posses different material properties, but the two parts are bonded firmly to each other.

According to the material and geometric discontinuity, the analysis domain can be

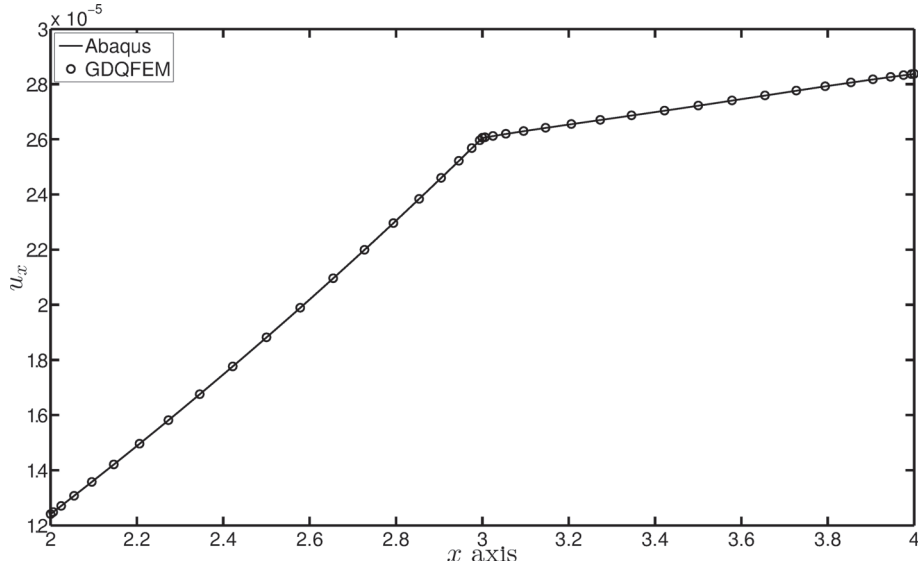

a)

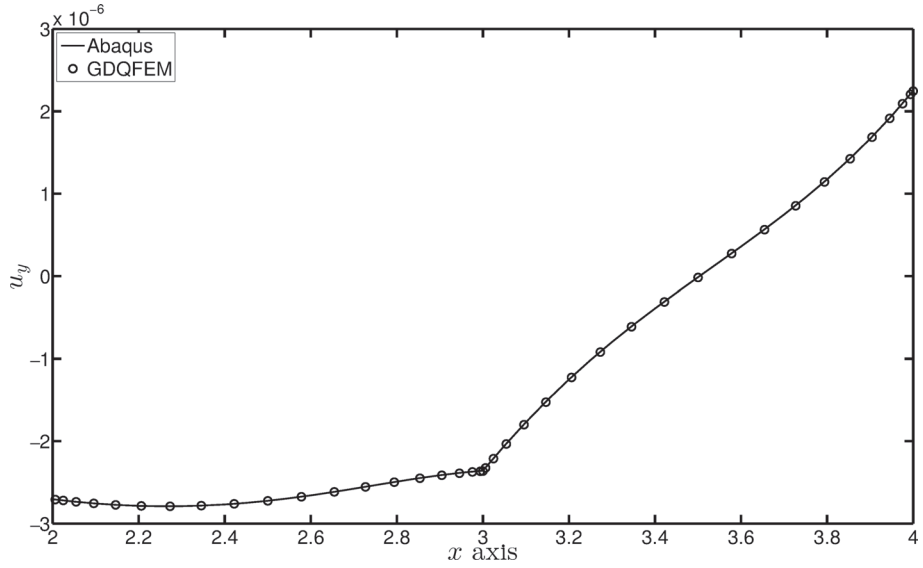

b)

Figure 3.22: Displacements on a square plate with a square inclusion at $y = L/2$: a) u_x. b) u_y.

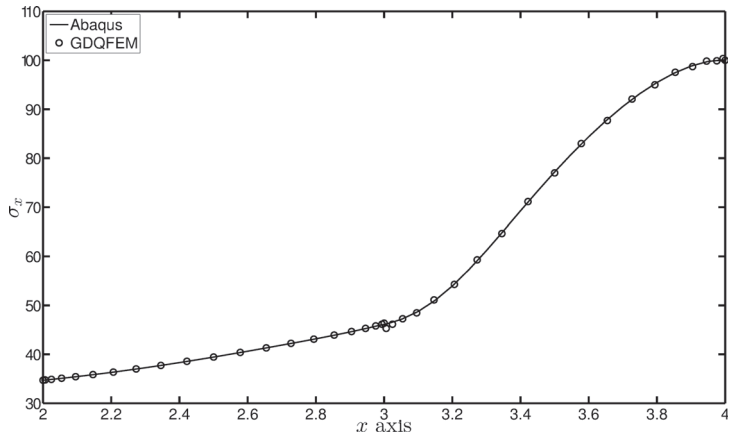

a)

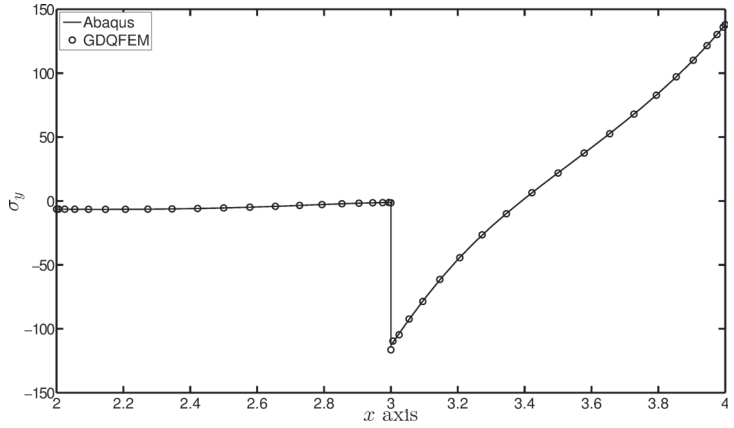

b)

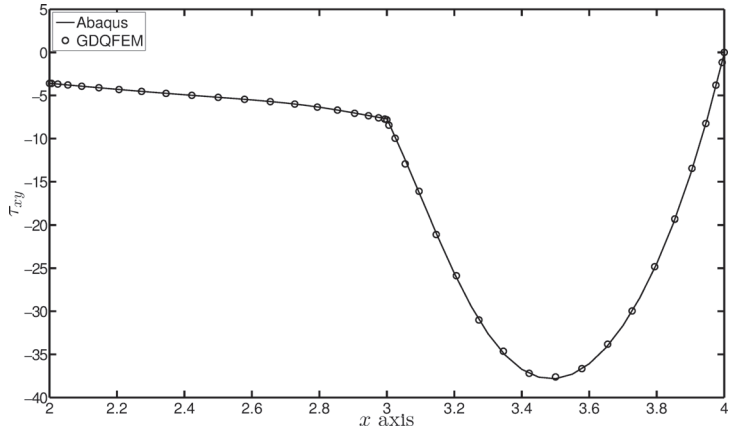

c)

Figure 3.23: Stresses on a square plate with a square inclusion at $y = L/2$: a) σ_x. b) σ_y. c) τ_{xy}.

N	σ_{xA}	σ_{yA}	$u_{xB} \cdot 10^6$	$u_{yB} \cdot 10^6$	σ_{xC}
7×7	38.5153	-6.9317	19.7554	-3.6159	100.0000
9×9	38.3985	-7.0648	19.7935	-3.6468	100.0000
11×11	38.3530	-7.1166	19.8141	-3.6722	100.0000
13×13	38.3300	-7.1423	19.8268	-3.6909	100.0000
15×15	38.3166	-7.1572	19.8353	-3.7049	100.0000
21×21	38.2980	-7.1775	19.8492	-3.7303	100.0000
Abaqus	38.2677	-7.2084	19.8945	-3.74357	99.8991

Table 3.11: Convergence of the GDQFEM results for the square plate with a square inclusion

divided into regular sub-domains. The material constants for the plate are $E_1 = 3 \cdot 10^7$ N/m^2, $\nu_1 = 0.3$, whereas for the inclusion $E_2 = 3 \cdot 10^6$ N/m^2, $\nu_2 = 0.25$. The problem has been solved for the plain stress case considering $L = 4$ m, $q = 100$ N. In order to transform the nine elements in the physical coordinates into the normalized natural coordinates - $1 \leq \xi, \eta \leq 1$ by 8-node quadratic sub-domain the mapping technique has been used. However the same problem could have been solved without coordinate transformation due to the fact that all the elements have a regular shape (rectangular), without achieving any computational error, as reported in [11]. Furthermore the numerical solution is compared to a finite element solution obtained with commercial FE program (Abaqus). For the analysis a 4×4 regular square element mesh has been used, within a 21×21 grid points per element.

In Figures 3.22-3.23 a horizontal section has been done at $y = L/2$ for displaying the stresses along the x axis. It is noted that the results in terms of stresses and displacements are in excellent agreement with those obtained by FE analysis. Moreover it is noted that the displacements are continuous but not smooth through the material interface. In fact a sharp turning point at the interface exists for the displacements, in other words the derivative of the displacements are not equal on the left and on the right side of the material discontinuity. On the other hand as illustrated in Figures 3.23 the normal stress σ_x and the shear stress τ_{xy} are continuous at the interface as compatibility conditions have enforced, whereas the normal stress σ_y clearly experiences a finite jump at the nodes upon the interface. It should be noted that the normal stress σ_y discontinuity can be clearly captured by GDQFEM, in fact the stress distribution around before and after the interface is smoother than the FE solution obtained by Abaqus. As a result the multi-domain DQ results to be first order accurate at the discontinuity due to the imposition of the compatibility conditions between adjacent elements.

For the sake of completeness and to further investigate the converge of the GDQFEM numerical solution, the results at some selected nodes are summarized in Table 3.11 with different grid sizes. The reference points A, B and C are shown in Figure 3.21. It is noted from Table 3.11 that the results have a very fast convergence as the grid number increases.

Static analysis of a square plate with a circular inclusion

A square plate with a circular inclusion subjected to uniform distributed forces at its upper edge is shown in Figure 3.24. According to the material and geometric discontinuity

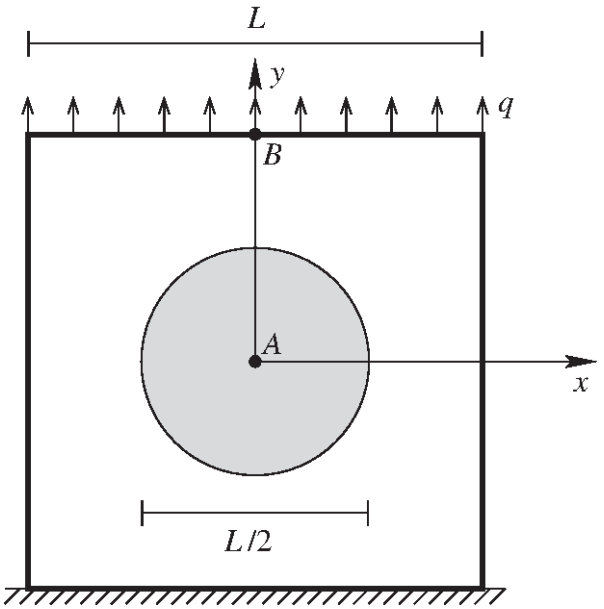

Figure 3.24: Square plate with a circular inclusion.

the physical problem is decomposed into twelve GDQFEM elements. All the material parameters are taken from the previous example, in which the material constant with the subscript 1 are given to the plate and the constants with the subscript 2 are related to the inclusion, nevertheless in this case $L = 5$ m. A plane stress simulation is performed also in this case.

It should be noted that, as it has been shown in the previous chapter, in order to capture an accurate solution in curved boundaries two ways can be chosen: on one hand a 12-node element can be used for the computation, on the other hand using an higher number of 8-node elements can be employed in the mesh in order to obtain the same numerical accuracy. For the sake of simplicity in this case four 8-node elements have been defined for modelling the inclusion.

A 21×21 grid point per element is used. The displacements u_x and u_y are reported in Figures 3.25,3.26, respectively. Figures 3.26 depict the stresses comparison with Abaqus. The two numerical solutions are very closed to each other, indicating the very good convergence rate that can be achieve with this methodology. In fact very few number of elements have been used compared to the FE solution. Once again Figures 3.25 show that a turning point occurs at the interface in the displacement plots and a finite jump is related to normal stresses σ_x and σ_y. Furthermore the tip stress is captured and smoother than the FE numerical results.

In Table 3.12 the numerical results at the points A and B are reported. The solution is given as a function of several grid points number, nevertheless an accurate solutions is reached with a few number of grid points.

Static analysis of a cantilever beam with elastic inclusion

A cantilever beam composed of two elastic materials is considered and depicted in Figure 3.27. The beam is composed of an elastic and homogeneous material of Young's modulus $E = 2 \cdot 10^7$ Pa and Poisson's ratio $\nu = 0.3$. The beam is $L = 4$ m long and $D = 1$ m high, clamped on the left edge and a vertical force of $P = 1$ kN is applied on the

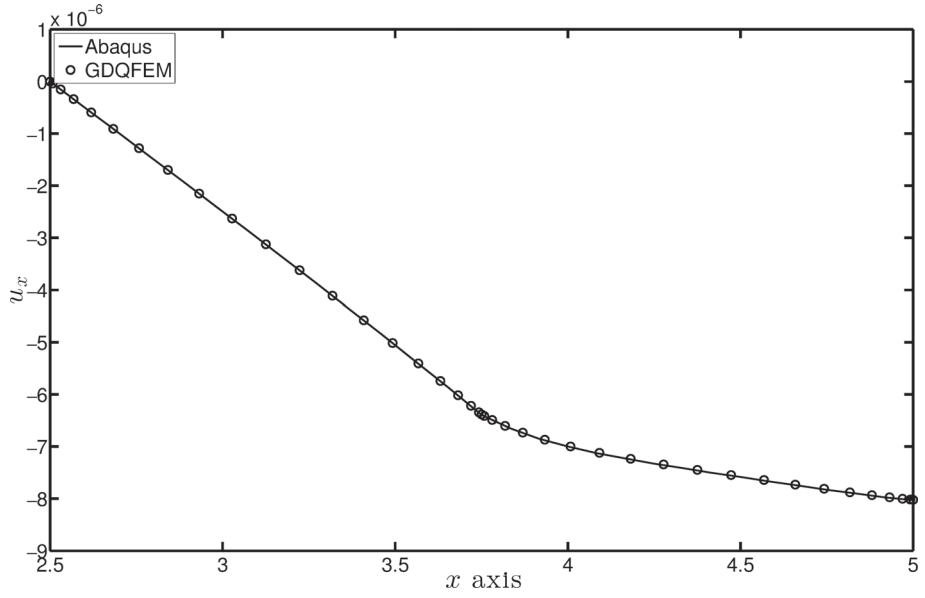

a)

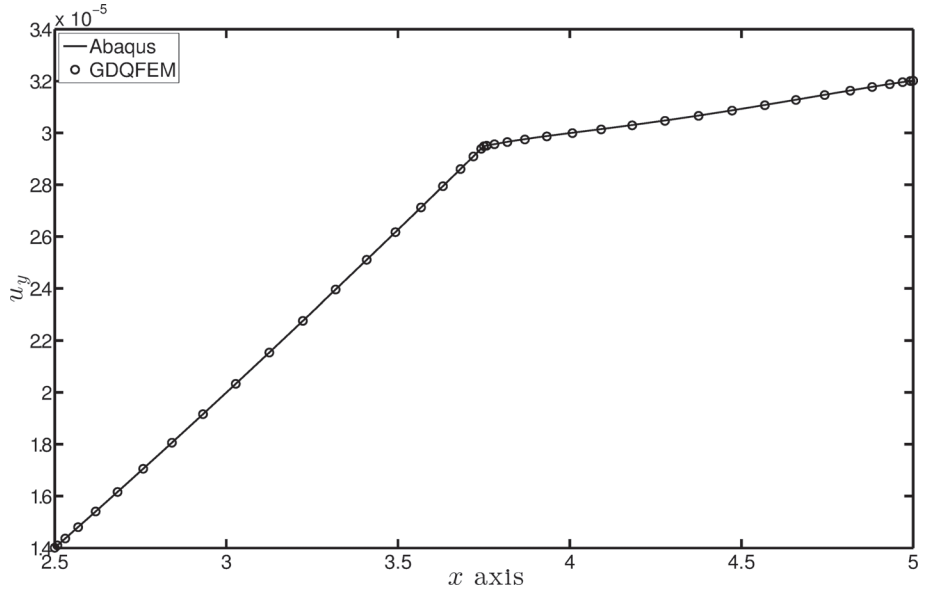

b)

Figure 3.25: Displacements on a square plate with a circular inclusion: a) u_x at x axis. b) u_y at y axis.

N	σ_{xA}	σ_{yA}	$u_{yB} \cdot 10^6$	σ_{yB}
7×7	-6.6406	33.3275	32.1107	100.0000
9×9	-6.5731	33.2575	32.0298	100.0000
11×11	-6.5719	33.2453	32.0189	100.0000
13×13	-6.5746	33.2422	32.0174	100.0000
15×15	-6.5771	33.2411	32.0174	100.0000
21×21	-6.5813	33.2403	32.0181	100.0000
Abaqus	-6.5856	33.2365	32.0232	99.6211

Table 3.12: Results of a square plate with a circular inclusion

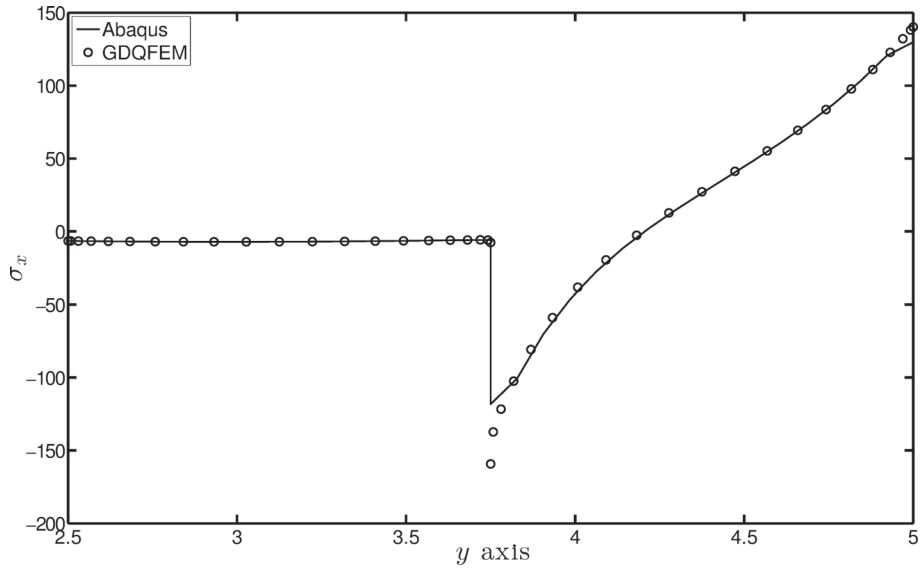

a)

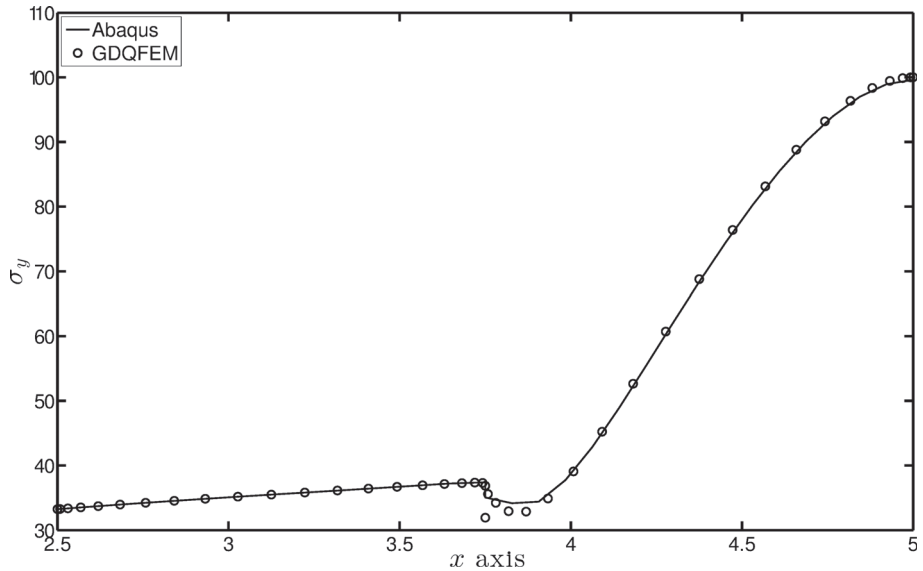

b)

Figure 3.26: Stresses on a square plate with a circular inclusion along y axis: a) σ_x. b) σ_y.

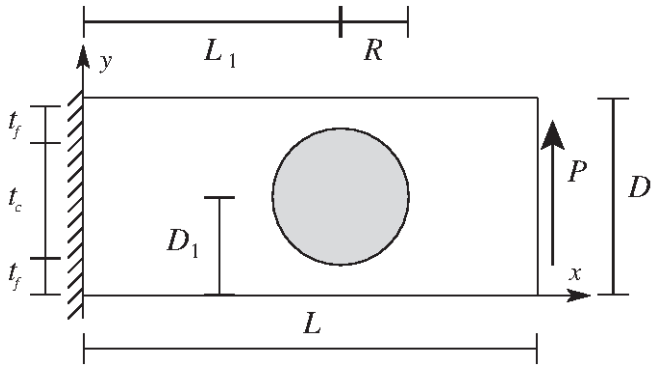

Figure 3.27: Cantilever beam problem: geometry and boundary conditions.

	ABAQUS	$n_e = 16$ $N = 11$	$n_e = 16$ $N = 21$
tip displ $\cdot 10^{-2}$	1.2272	1.2371	1.2364

Table 3.13: Maximum tip displacement comparison between GDQFEM solution and FE solution.

right edge. The inclusion is a circular elastic one, with radius $R = 0.4$ m, located at its center with $L_1 = 2.11$ m and $D_1 = 0.5$ m with an Elastic modulus of $E = 2 \cdot 10^{10}$ Pa and Poisson's ratio of $\nu = 0.3$. Since the exact solution is not available a FE reference solution has been calculated. The geometric description is taken from the work [137], in which several composite plane structures are studied. The tip displacement of the beam under consideration is reported in Table 3.13

The GDQFEM mesh used in the computation is composed of $n_e = 16$ with variable number of grid points per element. The mesh used in the computation is reported in Figure 3.28a. Moreover in order to underline the composite nature of this example the Von-Mises stress map is graphically presented in Figure 3.28b, in which a finite stress jump can be noticed between the beam and its inclusion.

In conclusion two stress recoveries along three different cross sections are depicted in Figures 3.29-3.30. The three sections are taken at $x = 1.71$ m, $x = 2.11$ m and $x = 2.51$ m, which are the section at immediate left hand of the inclusion, the sections that is at the middle of the inclusion and the last one is on the right hand of the inclusion, respectively. In the stress recovery the numerical GDQFEM solution is compared with a FE analysis obtained with Abaqus. It is noted from Figure 3.29b that there is an abrupt stress jump between the inclusion and the matrix due to the Young's Modulus difference between the two materials. In addition the same jump is related to a slope change of shear stress profile in Figure 3.30.

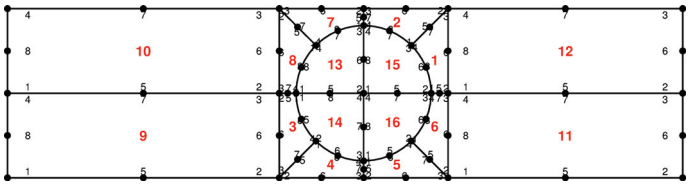

a)

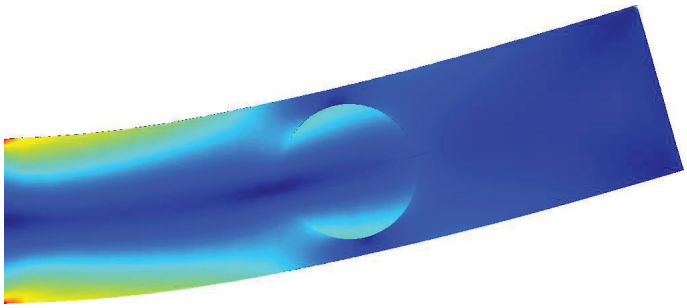

b)

Figure 3.28: Cantilever composite beam with elastic inclusion: a) GDQFEM mesh; b) Mises contour plot and deformed shape.

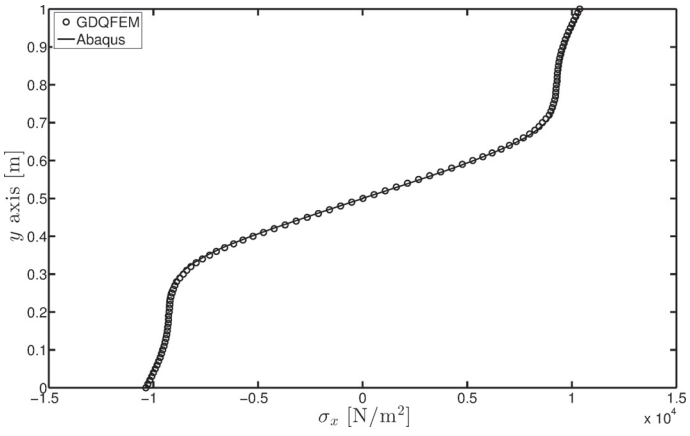

a)

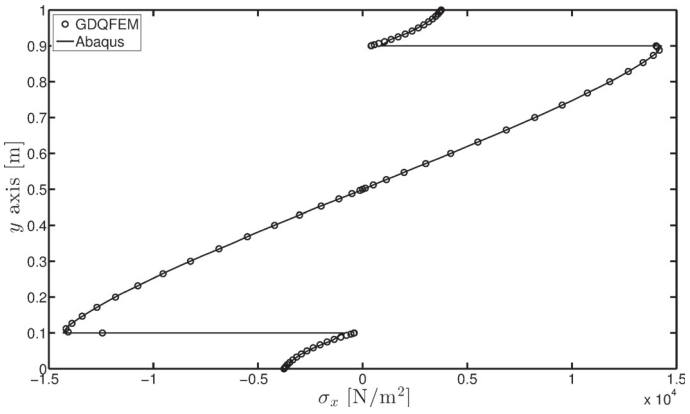

b)

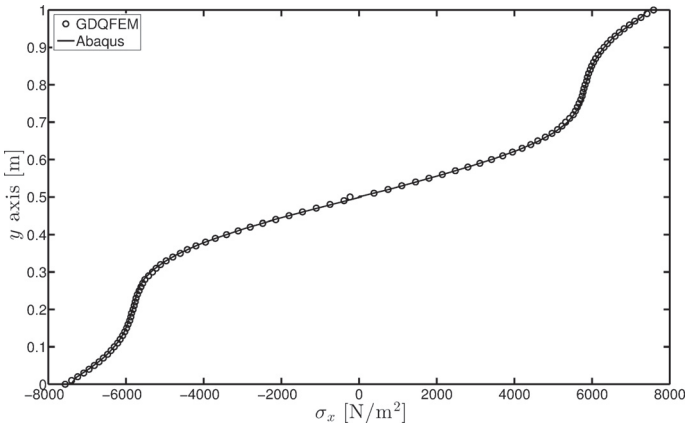

c)

Figure 3.29: Normal stress σ_x distribution though three sections along the beam length and compared with FE solution: a) $x = 1.71$ m; b) $x = 2.11$ m; c) $x = 2.51$ m.

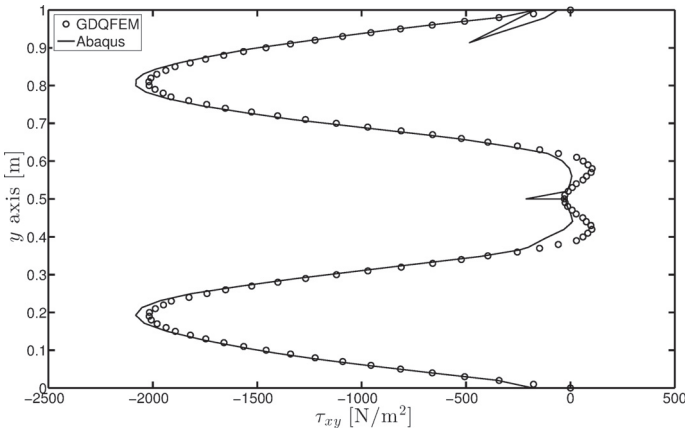

a)

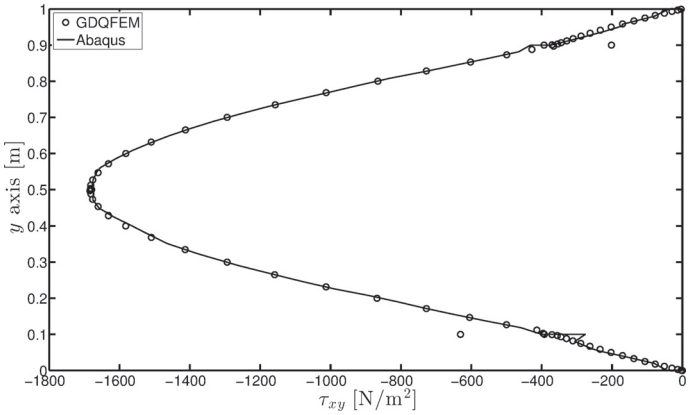

b)

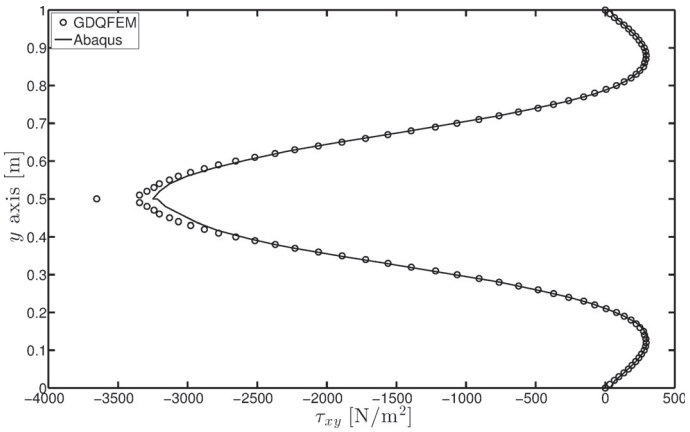

c)

Figure 3.30: Shear stress τ_{xy} distribution though three sections along the beam length and compared with FE solution: a) $x = 1.71$ m; b) $x = 2.11$ m; c) $x = 2.51$ m.

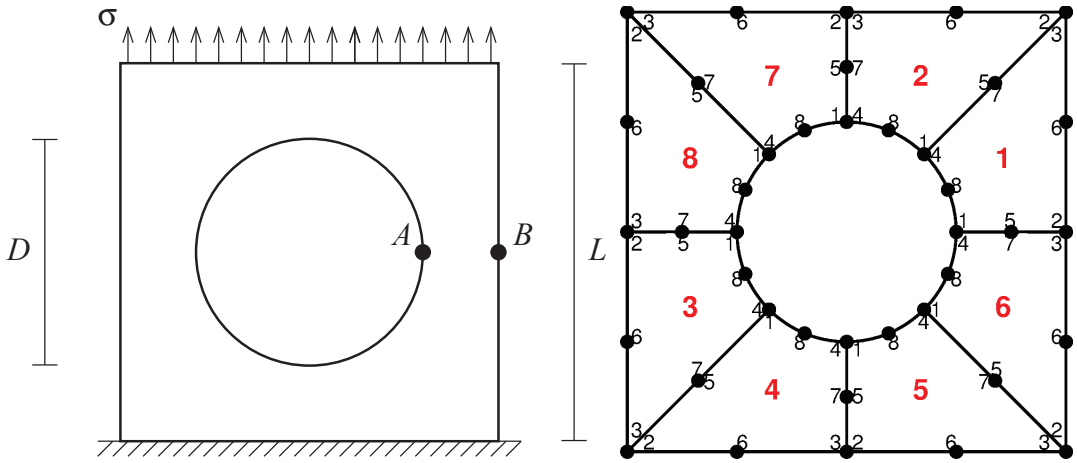

Figure 3.31: Square plate with a centred circular hole subjected to tension σ: a) Geometric representation; b) GDQFEM mesh.

3.6.11 Plate with circular hole

In the following section the classic example of a plate with a circular hole under tension is considered. In Figure 3.31a the geometry of the problem under consideration is depicted. The geometric parameters are the side of the plate $L = 5$ m, the diameter of the hole D that is variable and the tension $\sigma = 100$ Pa. The elastic constants of the material are Young's modulus $E = 3 \cdot 10^7$ Pa and Poisson's ratio $\nu = 0.3$. The numerical results obtained with this geometry are compared to a FE analysis performed with Abaqus for several ratios $\chi = D/L$. In Figure 3.32 four different solutions in term of the internal stress σ_y are represented. The solution in terms of stress captures well the tip stress for every ratio χ and the stress distribution is smooth all over the x axis even though for $\chi = 0.05$ and $\chi = 0.1$ two elements have been used in the computation. For the sake of completeness a GDQFEM mesh and a FE mesh is depicted in Figure 3.31b in order to show how simple the geometry mapping is respect to a FE analysis.

When the ratios $\chi = 0.5$ and $\chi = 0.25$ only eight elements have been used in the computation with a $N = M = 21$ grid points, otherwise for the other two cases sixteen elements have been used within $N = M = 15$ grid points. The grid point distribution for all the cases is a Chebyshev-Gauss-Lobatto one.

It can be notices, from Figure 3.32, that when the plate side is four times greater than the circle diameter the vertical stress σ_y tends to the value of the applied stress $\sigma = 100$ Pa. The x axis used in Figure 3.32 is indicated in Figure 3.31a within the two letters A and B.

3.6.12 Plate with hollow elastic inclusion

In the following example an hollow elastic inclusion is examined, in order to show how an elastic inclusion immersed into a softer matrix within a circular hole can be treated. The sample geometry is presented in Figure 3.33 where the side of the plate is $L = 5$ m, the outer radius $R_1 = 1.5625$ m and the inner radius $R_2 = 1.25$ m the external load is equal to the previous case $\sigma = 100$ Pa. The two material which constitute the plate are a soft

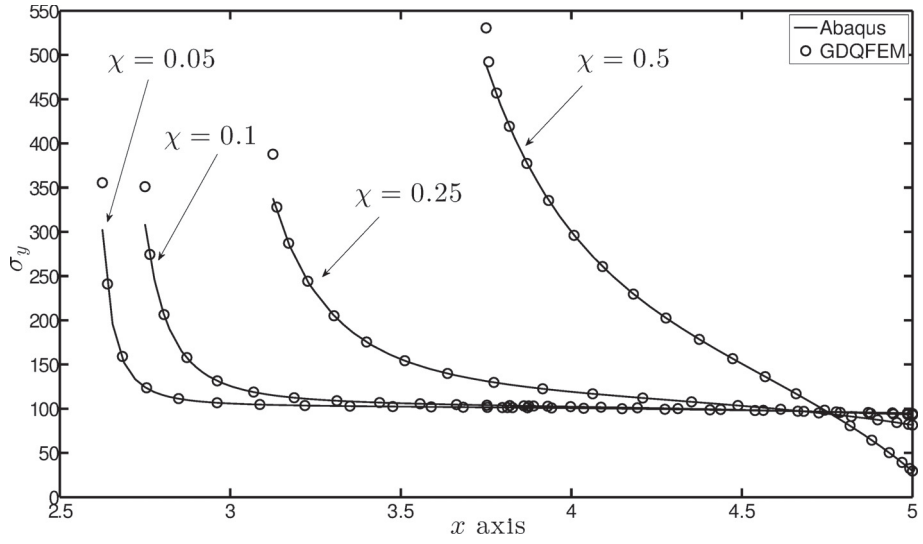

Figure 3.32: Stress profile of a square plate with a centred circular hole subjected to tension $\sigma = 100$ Pa.

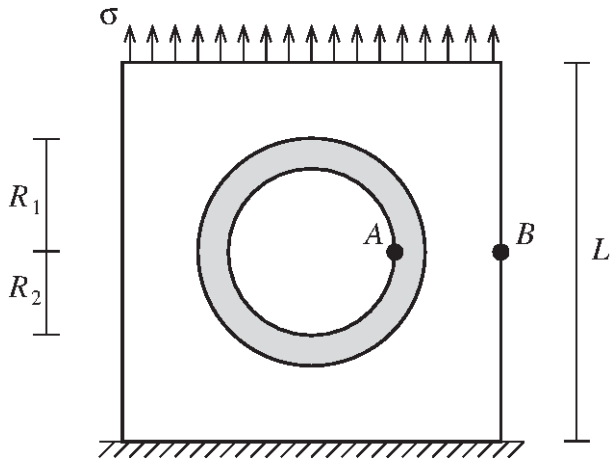

Figure 3.33: Square plate with a centred hollow inclusion subjected to tension σ.

matrix of $E_m = 3 \cdot 10^6$ Pa and a Poisson's ratio $\nu_m = 0.25$, whereas the fibre is made of a harder material with $E_i = 3 \cdot 10^7$ Pa and $\nu_i = 0.3$.

In Figure 3.34 the stress profile between the points A and B is depicted. It is noted that there is an abrupt jump at the material interface due to the difference in the elastic modulus. Figure 3.34 shows two groups of curves. The single dashed curve represents the homogeneous case in which only the matrix is present, and it is clear that there is a stress tip due to the circular hole but the stress profile is smooth from the tip A to the right edge of the plate B. Whereas the other two curves represent the matrix with the hollow inclusion obtained with a FE analysis and the GDQFEM. It is noted that even the bi-material case is in very good agreement respect to the homogeneous solution.

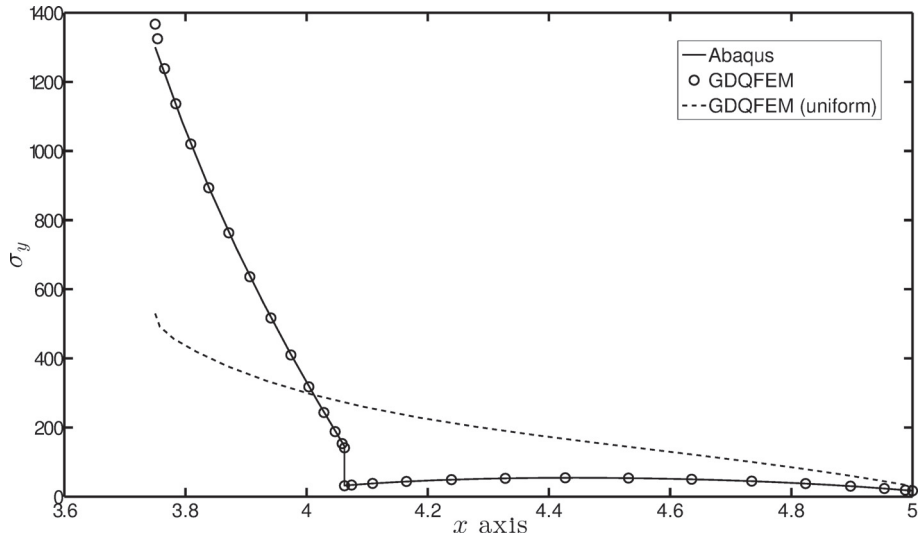

Figure 3.34: Stress profile of a square plate with a centred circular hollow inclusion subjected to tension $\sigma = 100$ Pa.

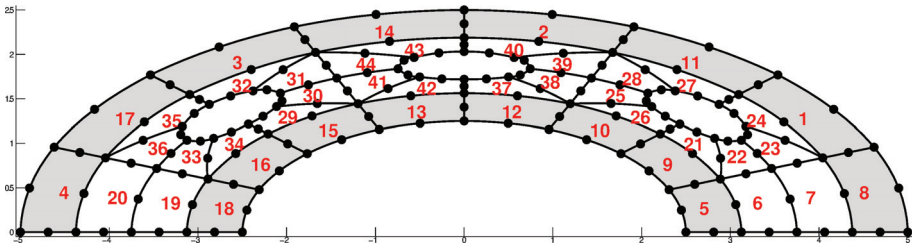

Figure 3.35: Geometric representation of an elliptic soft core arch with holes.

f [Hz]	Abaqus	$N = 9$	$N = 11$	$N = 13$
1	25.2318	25.2320	25.2691	25.2757
2	31.0079	31.8934	31.5975	31.4676
3	45.6878	45.9543	45.8373	45.8205
4	46.5109	47.9696	47.4468	47.1375
5	56.1484	57.5597	57.1569	56.8099
6	65.019	65.3243	65.2754	65.2259
7	70.9465	71.0756	70.9368	70.9230
8	74.8534	75.7430	75.4100	75.1430
9	87.995	88.2576	88.2303	88.2124
10	91.3028	91.5527	91.6743	91.6779

Table 3.14: First ten frequencies of an hollow soft core elliptic arch.

3.6.13 Free vibration of an elliptic soft core arch with holes

In this last section the free vibrations of a composite soft core elliptic arch with elliptic holes is considered. Due to the complexity of this geometry the geometry is graphically presented in Figure 3.35, where the top and bottom layers of a stronger material are indicated with a different colour respect to the soft core. The dimensions of the outer ellipse are $a_1 = 10$ m, $b_1 = 5$ m, whereas the inner ellipse is defined by $a_2 = 5$ m, $b_2 = 2.5$ m. The structure has a vertical symmetry where the inner and outer radii of curvature are not constant.

The mechanical properties of the top and bottom sheets are $E_s = 3 \cdot 10^9$ Pa and $\nu_s = 0.3$, whereas the soft core has an elastic modulus $E_c = 3 \cdot 10^7$ Pa and $\nu_c = 0.25$. Since a dynamic analysis is considered the density of the two materials are needed $\rho_s = 1000$ kg/m^3 and $\rho_c = 500$ kg/m^3.

It can be noticed that the frequencies are in very good agreement with the Abaqus solution as reported in Table 3.14. Furthermore the first four modal shapes of this complex structure are depicted in Figure 3.36. From Figure 3.36 is clear that the structure has a soft core because in any modal shape there is an independent movement of the core respect to the rest of the structure.

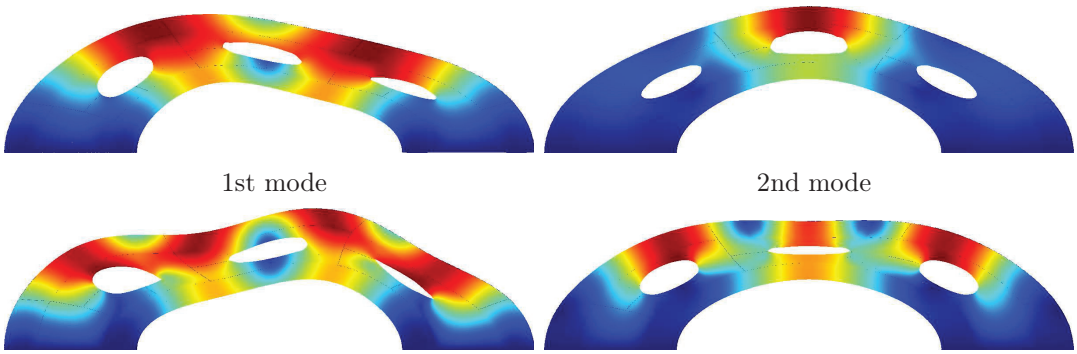

Figure 3.36: First four modal shapes for an elliptic soft core arch with holes.

Chapter 4

Arbitrarily Shaped Composite Cracked Plates

Sommario

Secondo la meccanica del continuo, le teorie delle piastre rappresentano la descrizione matematica della meccanica delle piastre piane. Le piastre sono strutture con uno spessore relativamente sottile rispetto alle dimensioni nel piano della struttura (ovvero strutture con rapporto tipico tra spessore e lato più corto pari a circa $h/L < 0.1$). Nel seguente capitolo la teoria classica del primo ordine delle piastre piane (FSDT) [10, 17, 41] è applicata utilizzando la tecnica GDQFEM a piastre composite e fessurate di forma generica.

Tutti gli esempi numerici sono incentrati sulle vibrazioni libere delle piastre suddette facendo uso di condizioni al contorno omogenee e non omogenee. Per quanto riguarda il materiale, si sono utilizzati materiali isotropi ma anche compositi laminati sfruttando la teoria del Singolo Strato Equivalente (ESL), riducendo cioè tutte le lamine ad una singola lamina equivalente in corrispondenza del piano medio della struttura. Tutti i risultati sono stati confrontati con una soluzione numerica ad FE e si è osservata un'ottima corrispondenza tra le due soluzioni, mostrando quindi la versatilità e la flessibilità della tecnica GDQFEM rispetto alle tecniche classiche ormai consolidate della letteratura.

Nei paragrafi seguenti, vengono inizialmente introdotte le equazioni governanti il problema, seguendo lo schema delle teorie fisiche. Quindi partendo dall'ipotesi cinematica si scrivono le caratterstiche di defomazione. Successivamente, tramite l'equilibrio del concio elementare, si ottengono le equazioni indefinite di equilibrio in regime statico che possono essere generalizzate al moto forzato aggiungendo le forze d'inerzia; in alternativa le equazioni del moto forzato possono ottenere tramite il principio di Hamilton. Dato che il materiale oggetto di studio è considerato omogeneo ed elastico, si introducono le leggi costitutive valide per i materiali laminati, composti da lamine isotrope o ortotrope nel loro piano. Infine sostituendo le equazioni di congruenza nel legame elastico e il risultato nelle equazioni del moto si ottengono le equazioni fondamentali in termini di spostamenti. In generale per una piastra laminata, con schema di laminazione generico, le equazioni sono cinque e si ha che gli spostamenti nel piano sono accoppiati a quelli fuori piano, grazie alla matrice di accoppiamento $\mathbf{B}$. Considerando invece un materiale composto da una singola lamina isotropa, il sistema fondamentale risulta disaccoppiato e quindi è possibile risolvere un sistema in tre equazioni e tre incognite, nel puro caso flessionale.

Infine si riportano le applicazioni numeriche relative a piastre isotrope, ortotrope e

fessurate con varie condizioni al contorno e con discontinuità di natura geometrica. Tutti i risultati numerici sono avvalorati da confronti con la letteratura e con modellazioni ad elementi finiti.

4.1 Introduction

In continuum mechanics, plate theories are mathematical descriptions of the mechanics of flat plates. Plates are defined as plane structural elements with a small thickness compared to the planar dimensions [4, 5]. The typical thickness to width ratio of a plate structure is less than $h/L < 0.1$. A plate theory takes advantage of this disparity in length scale to reduce the full three-dimensional solid mechanics problem to a two-dimensional problem. The aim of plate theory is to calculate the deformation and stresses in a plate subjected to in plane and out of plane loads. Of the numerous plate theories that have been developed since the late 19th century, two are widely accepted and used in engineering. These are the Kirchhoff-Love (KL) theory of plates, Classical Plate Theory (CPT) and the Reissner-Mindlin (RM) theory of plates, First-order Shear Deformation plate Theory (FSDT).

The RM theory of plates is an extension of KL plate theory that takes into account shear deformations through-the-thickness of a plate. The theory was proposed by Mindlin [141]. A similar, but not identical, theory had been proposed earlier by Reissner [140]. Both theories are intended for thick plates in which the normal to the mid-surface remains straight but not necessarily perpendicular to the mid-surface.

The form of RM plate theory that is most commonly used is actually due to Mindlin and is more properly called Mindlin plate theory [142]. The Reissner theory is slightly different. Both theories include in-plane shear strains and both are extensions of KL plate theory incorporating first-order shear effects. Mindlin's theory assumes that there is a linear variation of displacement across the plate thickness and but that the plate thickness does not change during deformation. This implies that the normal stress through the thickness is ignored; an assumption which is also called the plane stress condition. On the other hand, Reissner's theory assumes that the bending stress is linear while the shear stress is quadratic through the thickness of the plate. This leads to a situation where the displacement through-the-thickness is not necessarily linear and where the plate thickness may change during deformation. Therefore, Reissner's theory does not invoke the plane stress condition. The RM theory is often called the First-order Shear Deformation Theory (FSDT) of plates. Since a FSDT implies a linear displacement variation through the thickness, it is incompatible with Reissner's plate theory.

The Reissner-Mindlin rectangular plate problem is one of the most studied engineering problem over the last years 'citeTimWoi, Szilard, Reddypl, Leissa, Reis, Mind, WangLim-ReddyLee, Leissacrk1, Leissacrk2, Leissacrk3, Leissacrk4. In recent years the problem of composite rectangular plates has been widely investigated [4–6, 14, 140–146].

In this chapter the problem of Reissner-Mindlin (RM) flat plates is considered. As considered in the previous chapters, at first the flat plate formulation is presented for the general case. The generic thick plate is a composite anisotropic one in which the middle surface is the mathematical surface for the computation.

The Generalized Differential Quadrature Finite Element formulation will be shown in the following considering not only regular geometries but also complex plates with holes and arbitrary shape.

4.2 Theoretical equations

The shape of a plate is adequately defined by describing the geometry of its middle surface, which is a surface that bisects the plate thickness h at each point. The FSDT of plates was originally derived for isotropic plates using equilibrium considerations. A more general version of the theory based on energy considerations is discussed in [6]. In the following section the general framework of FSDT plates will be shown for FGM thick plates.

4.2.1 Displacement field

The RM hypothesis implies that the displacement field have the form

$$\begin{aligned} U(x,y,z) &= u_x(x,y) + z\beta_x(x,y) \\ V(x,y,z) &= u_y(x,y) + z\beta_y(x,y) \\ W(x,y,z) &= w(x,y) \end{aligned} \tag{4.1}$$

where x and y are the Cartesian coordinates on the mid-surface of the undeformed plate and z is the coordinate for the thickness direction, u, v are the in-plane displacements of the mid-surface, w is the displacement of the mid-surface in the z direction, β_1 and β_2 designate the angles which the normal to the mid-surface makes with the z axis. Unlike KL plate theory where are directly related to w, RM theory requires that $\beta_1 \neq \frac{\partial w}{\partial x}$ and $\beta_2 \neq \frac{\partial w}{\partial y}$.

As a result the theory under consideration has five degrees of freedom. It is noted that in literature can be found the RM theory within three displacement parameters only. Because some researchers prefer to uncouple the membrane deformation from the flexural ones, and that can be done if and only if in general the material is elastic homogeneous and isotropic or for some anisotropic cases. However in this PhD Thesis the general case of anisotropic Equivalent Single Layer (ESL) RM plate is considered, so all the parameters must be considered in the theoretical formulation.

4.2.2 Strain-displacement relations

The membrane and flexural strains are

$$\begin{aligned} &\varepsilon_x^0 = \frac{\partial u_x}{\partial x}, \quad \varepsilon_y^0 = \frac{\partial u_y}{\partial y}, \quad \gamma_{xy}^0 = \frac{\partial u_y}{\partial x} + \frac{\partial u_x}{\partial y} \\ &k_x = \frac{\partial \beta_x}{\partial x}, \quad k_y = \frac{\partial \beta_y}{\partial y}, \quad k_{xy} = \frac{\partial \beta_y}{\partial x} + \frac{\partial \beta_x}{\partial y} \\ &\gamma_{xz} = \beta_x + \frac{\partial w}{\partial x}, \quad \gamma_{yz} = \beta_y + \frac{\partial w}{\partial y} \end{aligned} \tag{4.2}$$

where ε_x^0, ε_y^0 and γ_{xy}^0 are the in plate deformation for normal and shear respectively, k_x, k_y and k_{xy} are the plate curvatures, finally γ_x and γ_y are the out of plane shear deformations of the plate.

4.2.3 Equilibrium equations

The equilibrium equations of a RM plate for small strains and small rotations have the form

$$\begin{aligned}
\frac{\partial N_x}{\partial x} + \frac{\partial N_{xy}}{\partial y} + p_x &= I_0 \ddot{u}_x + I_1 \ddot{\beta}_x \\
\frac{\partial N_{xy}}{\partial x} + \frac{\partial N_y}{\partial y} + p_y &= I_0 \ddot{u}_y + I_1 \ddot{\beta}_y \\
\frac{\partial T_x}{\partial x} + \frac{\partial T_y}{\partial y} + p_z &= I_0 \ddot{w} \\
\frac{\partial M_x}{\partial x} + \frac{\partial M_{xy}}{\partial y} - T_x + m_x &= I_1 \ddot{u}_x + I_2 \ddot{\beta}_x \\
\frac{\partial M_{xy}}{\partial x} + \frac{\partial M_y}{\partial y} - T_y + m_y &= I_1 \ddot{u}_y + I_2 \ddot{\beta}_y
\end{aligned} \tag{4.3}$$

where N_x, N_y and N_{xy} are the in plane stresses, T_x, T_y are the shear forces, M_x, M_y the bending moments and M_{xy} is the torque. Moreover p_x, p_y are the in plane loads, p_z is the out of plate load and finally m_x, m_y the distributed bending moments. Furthermore the inertias are indicated by I_0, I_1 and I_2.

It is noted that from (4.3) it is possible to study the static and dynamic case of flat RM plates. If the static analysis is considered the inertia forces are equal to zero $I_i = 0$ for $i = 0, 1, 2$, whereas if the free vibration of a plate has to be known so the domain loading are taken equal to zero $p_x = p_y = p_z = m_x = m_y = 0$.

In order to obtain the fundamental system of equations valid for the static and dynamic behaviour of RM flat plates the constitutive relations have to be introduced. In particular these are found starting from the 3D stress tensor valid under the RM plate hypotheses.

4.2.4 Constitutive equations

Beyond the classic RM hypotheses for the study of thick laminated plates some other statements have to be added. In fact these new hypotheses are related to the mechanical behaviour of laminated composites structures. They are called perfect bonding between layers also [4, 6, 10].

1. The bonding itself is infinitesimally small (there is no flaw or gap between layers).
2. The bonding is non-shear-deformable (no lamina can slip relative to another).
3. The strength of bonding is as strong as it needs to be (the laminate acts as a single lamina with special integrated properties).
4. The shear stresses at the top and the bottom of the plate are equal to the top and bottom shear load application.

The last hypothesis derives from the fact that the starting 3D problem becomes a plane model, defined upon the middle surface of the plate. Following the starting hypotheses of the FSDT the normal strain ε_n and the normal stress σ_n are negligible. So the Hooke's law can be written for a generic anisotropic lamina as follows

$$\begin{aligned}
\begin{bmatrix}\hat{\sigma}_x\\ \hat{\sigma}_y\\ \hat{\tau}_{xy}\end{bmatrix}^{(k)} &= \begin{bmatrix}C_{11} & C_{12} & C_{16}\\ C_{12} & C_{22} & C_{26}\\ C_{16} & C_{26} & C_{66}\end{bmatrix}^{(k)} \begin{bmatrix}\hat{\varepsilon}_x\\ \hat{\varepsilon}_y\\ \hat{\gamma}_{xy}\end{bmatrix}^{(k)}\\
\hat{\sigma}_n^{(k)} &= 0\\
\begin{bmatrix}\hat{\tau}_{xz}\\ \hat{\tau}_{yz}\end{bmatrix}^{(k)} &= \begin{bmatrix}C_{44} & C_{45}\\ C_{45} & C_{55}\end{bmatrix}^{(k)} \begin{bmatrix}\hat{\gamma}_{xz}\\ \hat{\gamma}_{yz}\end{bmatrix}^{(k)}
\end{aligned} \tag{4.4}$$

where σ_x, σ_y, σ_n are the three normal stresses along the three dimensional material reference system, the corresponding strains are ε_x, ε_y, ε_z. Whereas the shear stresses are τ_{xy}, τ_{xz}, τ_{yz} and the corresponding strains are γ_{xy}, γ_{xz} and γ_{yz}. The hat symbol $\hat{}$ represents the fact that all the stresses of equation (4.4) are written in the material reference system that in general has a generic angle θ with the geometric reference system. When the generic lamina is orthotropic the relations (4.4) become

$$\begin{aligned}
\begin{bmatrix}\hat{\sigma}_x\\ \hat{\sigma}_y\\ \hat{\tau}_{xy}\end{bmatrix}^{(k)} &= \begin{bmatrix}Q_{11} & Q_{12} & 0\\ Q_{12} & Q_{22} & 0\\ 0 & 0 & Q_{66}\end{bmatrix}^{(k)} \begin{bmatrix}\hat{\varepsilon}_x\\ \hat{\varepsilon}_y\\ \hat{\gamma}_{xy}\end{bmatrix}^{(k)}\\
\hat{\sigma}_n^{(k)} &= 0\\
\begin{bmatrix}\hat{\tau}_{xz}\\ \hat{\tau}_{yz}\end{bmatrix}^{(k)} &= \begin{bmatrix}Q_{44} & Q_{45}\\ Q_{45} & Q_{55}\end{bmatrix}^{(k)} \begin{bmatrix}\hat{\gamma}_{xz}\\ \hat{\gamma}_{yz}\end{bmatrix}^{(k)}
\end{aligned} \tag{4.5}$$

where $Q_{ij}^{(k)}$ are the generic lamina material constants that are defined as follows

$$\begin{aligned}
&Q_{11}^{(k)} = \frac{E_1^{(k)}}{1-\nu_{12}^{(k)}\nu_{21}^{(k)}}, \quad Q_{22}^{(k)} = \frac{E_2^{(k)}}{1-\nu_{12}^{(k)}\nu_{21}^{(k)}}, \quad Q_{12}^{(k)} = \frac{\nu_{12}^{(k)}E_2^{(k)}}{1-\nu_{12}^{(k)}\nu_{21}^{(k)}}\\
&Q_{66}^{(k)} = G_{12}^{(k)}, \quad Q_{44}^{(k)} = G_{13}^{(k)}, \quad Q_{55}^{(k)} = G_{23}^{(k)}
\end{aligned} \tag{4.6}$$

Since each lamina of the stacking sequence can have its orientation θ. The constitutive equations for each lamina must be transformed into problem coordinate system. For the generic lamina k the stress components are

$$\begin{aligned}
\begin{bmatrix}\sigma_x\\ \sigma_y\\ \tau_{xy}\end{bmatrix}^{(k)} &= \begin{bmatrix}\bar{Q}_{11} & \bar{Q}_{12} & \bar{Q}_{16}\\ \bar{Q}_{12} & \bar{Q}_{22} & \bar{Q}_{26}\\ \bar{Q}_{16} & \bar{Q}_{26} & \bar{Q}_{66}\end{bmatrix}^{(k)} \begin{bmatrix}\varepsilon_x\\ \varepsilon_y\\ \gamma_{xy}\end{bmatrix}^{(k)}\\
\sigma_n^{(k)} &= 0\\
\begin{bmatrix}\tau_{xz}\\ \tau_{yz}\end{bmatrix}^{(k)} &= \begin{bmatrix}\bar{Q}_{44} & \bar{Q}_{45}\\ \bar{Q}_{45} & \bar{Q}_{55}\end{bmatrix}^{(k)} \begin{bmatrix}\gamma_{xz}\\ \gamma_{yz}\end{bmatrix}^{(k)}
\end{aligned} \tag{4.7}$$

in order to obtain the stresses in the global coordinate system (4.7) the $\bar{Q}_{ij}^{(k)}$ transformations are needed [10].

In case the generic lamina is isotropic or inhomogeneous along the thickness (functionally graded lamina) the stiffness constants are

$$Q_{11}^{(k)} = Q_{22}^{(k)} = \frac{E^{(k)}}{1-\left(\nu^{(k)}\right)^2}, \quad Q_{12}^{(k)} = \frac{\nu^{(k)}E^{(k)}}{1-\left(\nu^{(k)}\right)^2}, \quad Q_{66}^{(k)} = Q_{44}^{(k)} = Q_{55}^{(k)} = G^{(k)} \tag{4.8}$$

4.2.5 Internal stresses

The internal stress characteristics acting on the generic plate element are function of x, y since they represent the integration along the thickness of the stress components. In this way the original 3D problem is highly simplified because the unknown displacements are function of x and y only. The stress components can be recovered afterwards once the solution in terms of displacements is found from the fundamental system of equations. The recovery procedure can be done most of the times by using numerical procedures because of the complexity of the 3D stress equilibrium equations.

As far as the internal stresses are concerned several integrations along the thickness must be performed. For the present case the stress components can be written as a function of the strain on the middle surface as

$$\begin{aligned}
\sigma_x^{(k)} &= \bar{Q}_{11}^{(k)}\left(\varepsilon_x^0 + \zeta\chi_x\right) + \bar{Q}_{12}^{(k)}\left(\varepsilon_y^0 + \zeta\chi_y\right) + \bar{Q}_{16}^{(k)}\left(\gamma_{xy}^0 + \zeta\chi_{xy}\right) \\
\sigma_y^{(k)} &= \bar{Q}_{12}^{(k)}\left(\varepsilon_x^0 + \zeta\chi_x\right) + \bar{Q}_{22}^{(k)}\left(\varepsilon_y^0 + \zeta\chi_y\right) + \bar{Q}_{26}^{(k)}\left(\gamma_{xy}^0 + \zeta\chi_{xy}\right) \\
\sigma_n^{(k)} &= 0 \\
\tau_{xy}^{(k)} &= \bar{Q}_{16}^{(k)}\left(\varepsilon_x^0 + \zeta\chi_x\right) + \bar{Q}_{26}^{(k)}\left(\varepsilon_y^0 + \zeta\chi_y\right) + \bar{Q}_{66}^{(k)}\left(\gamma_{xy}^0 + \zeta\chi_{xy}\right) \\
\tau_{xz}^{(k)} &= \kappa\left(\bar{Q}_{44}^{(k)}\gamma_{xz} + \bar{Q}_{45}^{(k)}\gamma_{yz}\right) \\
\tau_{yz}^{(k)} &= \kappa\left(\bar{Q}_{45}^{(k)}\gamma_{xz} + \bar{Q}_{55}^{(k)}\gamma_{yz}\right)
\end{aligned} \tag{4.9}$$

It must be noted that the shear stresses τ_{xz}, τ_{yz} associated to the two sliding strains γ_{xz}, γ_{yz} are defined with a shear correction factor κ, due to the RM original hypotheses. The shear correction factor takes into account the fact that the shear stresses are not constant along the thickness but they have a parabolic shape distribution. For thick shells the shear correction factor is assumed to be equal to $\kappa = 5/6$.

The stress resultants introduced in the equilibrium equations (4.3) are defined as the integral of the stress components along the plate thickness. Since a generic flat plate can be composed of several laminae l, the stress resultants are defined as

$$N_x(x,y) = \sum_{k=1}^{l}\int_{\zeta_k}^{\zeta_{k+1}} \sigma_x(x,y,\zeta)d\zeta \tag{4.10}$$

$$N_y(x,y) = \sum_{k=1}^{l}\int_{\zeta_k}^{\zeta_{k+1}} \sigma_y(x,y,\zeta)d\zeta \tag{4.11}$$

$$N_{xy}(x,y) = \sum_{k=1}^{l}\int_{\zeta_k}^{\zeta_{k+1}} \tau_{xy}(x,y,\zeta)d\zeta \tag{4.12}$$

$$M_x(x,y) = \sum_{k=1}^{l}\int_{\zeta_k}^{\zeta_{k+1}} \zeta\sigma_x(x,y,\zeta)d\zeta \tag{4.13}$$

$$M_y(x,y) = \sum_{k=1}^{l} \int_{\zeta_k}^{\zeta_{k+1}} \zeta \sigma_y(x,y,\zeta) d\zeta \tag{4.14}$$

$$M_{xy}(x,y) = \sum_{k=1}^{l} \int_{\zeta_k}^{\zeta_{k+1}} \zeta \tau_{xy}(x,y,\zeta) d\zeta \tag{4.15}$$

$$T_x(x,y) = \sum_{k=1}^{l} \int_{\zeta_k}^{\zeta_{k+1}} \tau_{xz}(x,y,\zeta) d\zeta \tag{4.16}$$

$$T_y(x,y) = \sum_{k=1}^{l} \int_{\zeta_k}^{\zeta_{k+1}} \tau_{yz}(x,y,\zeta) d\zeta \tag{4.17}$$

Substituting the stress components into the internal stresses

$$\begin{aligned}
\begin{bmatrix} N_x \\ N_y \\ N_{xy} \end{bmatrix} &= \sum_{k=1}^{l} \int_{\zeta_k}^{\zeta_{k+1}} \begin{bmatrix} \bar{Q}_{11}^{(k)} & \bar{Q}_{12}^{(k)} & \bar{Q}_{16}^{(k)} \\ \bar{Q}_{12}^{(k)} & \bar{Q}_{22}^{(k)} & \bar{Q}_{26}^{(k)} \\ \bar{Q}_{16}^{(k)} & \bar{Q}_{26}^{(k)} & \bar{Q}_{66}^{(k)} \end{bmatrix} \begin{bmatrix} \varepsilon_x^0 + \zeta\chi_x \\ \varepsilon_y^0 + \zeta\chi_y \\ \gamma_{xy}^0 + \zeta\chi_{xy} \end{bmatrix} d\zeta \\
\begin{bmatrix} M_x \\ M_y \\ M_{xy} \end{bmatrix} &= \sum_{k=1}^{l} \int_{\zeta_k}^{\zeta_{k+1}} \begin{bmatrix} \bar{Q}_{11}^{(k)} & \bar{Q}_{12}^{(k)} & \bar{Q}_{16}^{(k)} \\ \bar{Q}_{12}^{(k)} & \bar{Q}_{22}^{(k)} & \bar{Q}_{26}^{(k)} \\ \bar{Q}_{16}^{(k)} & \bar{Q}_{26}^{(k)} & \bar{Q}_{66}^{(k)} \end{bmatrix} \begin{bmatrix} \varepsilon_x^0 + \zeta\chi_x \\ \varepsilon_y^0 + \zeta\chi_y \\ \gamma_{xy}^0 + \zeta\chi_{xy} \end{bmatrix} \zeta d\zeta \\
\begin{bmatrix} T_x \\ T_y \end{bmatrix} &= \kappa \sum_{k=1}^{l} \int_{\zeta_k}^{\zeta_{k+1}} \begin{bmatrix} \bar{Q}_{44}^{(k)} & \bar{Q}_{45}^{(k)} \\ \bar{Q}_{45}^{(k)} & \bar{Q}_{55}^{(k)} \end{bmatrix} \begin{bmatrix} \gamma_{xz} \\ \gamma_{yz} \end{bmatrix} d\zeta
\end{aligned} \tag{4.18}$$

Introducing the matrices **A**, **B**, **D** usually indicated in literature as membrane stiffness matrix, mixed stiffness matrix and flexural stiffness matrix. So the (4.18) can be written in matrix form as

$$\begin{bmatrix} N_x \\ N_y \\ N_{xy} \\ M_x \\ M_y \\ M_{xy} \\ T_x \\ T_y \end{bmatrix} = \begin{bmatrix} A_{11} & A_{12} & A_{16} & B_{11} & B_{12} & B_{16} & 0 & 0 \\ A_{12} & A_{22} & A_{26} & B_{12} & B_{22} & B_{26} & 0 & 0 \\ A_{16} & A_{26} & A_{66} & B_{16} & B_{26} & B_{66} & 0 & 0 \\ B_{11} & B_{12} & B_{16} & D_{11} & D_{12} & D_{16} & 0 & 0 \\ B_{12} & B_{22} & B_{26} & D_{12} & D_{22} & D_{26} & 0 & 0 \\ B_{16} & B_{26} & B_{66} & D_{16} & D_{26} & D_{66} & 0 & 0 \\ 0 & 0 & 0 & 0 & 0 & 0 & \kappa A_{44} & \kappa A_{45} \\ 0 & 0 & 0 & 0 & 0 & 0 & \kappa A_{45} & \kappa A_{55} \end{bmatrix} \begin{bmatrix} \varepsilon_x^0 \\ \varepsilon_y^0 \\ \gamma_{xy}^0 \\ \chi_x \\ \chi_y \\ \chi_{xy} \\ \gamma_{xz} \\ \gamma_{yz} \end{bmatrix} \tag{4.19}$$

It must be underlined that the mixed stiffness matrix **B** couples the in-plane membrane stresses with the flexural bending moments. So if $\mathbf{B} = \mathbf{0}$ the in-plane equations are uncoupled with the bending equations and the fundamental system of equations can be split into two independent set of equations. In addition the stiffness matrices components depend on the elastic coefficients $\bar{Q}_{ij}^{(k)}$ and they are defined as

$$A_{ij} = \sum_{k=1}^{l} \int_{\zeta_k}^{\zeta_{k+1}} \bar{Q}_{ij}^{(k)} d\zeta, \quad B_{ij} = \sum_{k=1}^{l} \int_{\zeta_k}^{\zeta_{k+1}} \bar{Q}_{ij}^{(k)} \zeta d\zeta, \quad D_{ij} = \sum_{k=1}^{l} \int_{\zeta_k}^{\zeta_{k+1}} \bar{Q}_{ij}^{(k)} \zeta^2 d\zeta \tag{4.20}$$

4.2.6 Fundamental equations

Using all the previous relationships from the kinematic and static definitions for RM flat plates the fundamental system of equations can be found

First fundamental equation

$$\begin{aligned}&\left(A_{11}\frac{\partial^2}{\partial x^2}+A_{66}\frac{\partial^2}{\partial y^2}+2A_{16}\frac{\partial^2}{\partial x\partial y}\right)u_x+\\&+\left(A_{16}\frac{\partial^2}{\partial x^2}+A_{26}\frac{\partial^2}{\partial y^2}+(A_{12}+A_{66})\frac{\partial^2}{\partial x\partial y}\right)u_y+\\&+\left(B_{11}\frac{\partial^2}{\partial x^2}+B_{66}\frac{\partial^2}{\partial y^2}+2B_{16}\frac{\partial^2}{\partial x\partial y}\right)\beta_x+\\&+\left(B_{16}\frac{\partial^2}{\partial x^2}+B_{26}\frac{\partial^2}{\partial y^2}+(B_{12}+B_{66})\frac{\partial^2}{\partial x\partial y}\right)\beta_y+p_x=I_0\ddot{u}_x+I_1\ddot{\beta}_x\end{aligned}\tag{4.21}$$

Second fundamental equation

$$\begin{aligned}&\left(A_{16}\frac{\partial^2}{\partial x^2}+A_{26}\frac{\partial^2}{\partial y^2}+(A_{12}+A_{66})\frac{\partial^2}{\partial x\partial y}\right)u_x+\\&+\left(A_{66}\frac{\partial^2}{\partial x^2}+A_{22}\frac{\partial^2}{\partial y^2}+2A_{26}\frac{\partial^2}{\partial x\partial y}\right)u_y+\\&+\left(B_{16}\frac{\partial^2}{\partial x^2}+B_{26}\frac{\partial^2}{\partial y^2}+(B_{12}+B_{66})\frac{\partial^2}{\partial x\partial y}\right)\beta_x+\\&+\left(B_{66}\frac{\partial^2}{\partial x^2}+B_{22}\frac{\partial^2}{\partial y^2}+2B_{26}\frac{\partial^2}{\partial x\partial y}\right)\beta_y+p_y=I_0\ddot{u}_y+I_1\ddot{\beta}_y\end{aligned}\tag{4.22}$$

Third fundamental equation

$$\begin{aligned}&\left(\kappa A_{44}\frac{\partial^2}{\partial x^2}+\kappa A_{55}\frac{\partial^2}{\partial y^2}+2\kappa A_{45}\frac{\partial^2}{\partial x\partial y}\right)w+\\&+\left(\kappa A_{44}\frac{\partial}{\partial x}+\kappa A_{45}\frac{\partial}{\partial y}\right)\beta_x+\left(\kappa A_{45}\frac{\partial}{\partial x}+\kappa A_{55}\frac{\partial}{\partial y}\right)\beta_y+p_n=I_0\ddot{w}\end{aligned}\tag{4.23}$$

Fourth fundamental equation

$$\begin{aligned}&\left(B_{11}\frac{\partial^2}{\partial x^2}+B_{66}\frac{\partial^2}{\partial y^2}+2B_{16}\frac{\partial^2}{\partial x\partial y}\right)u_x+\\&+\left(B_{16}\frac{\partial^2}{\partial x^2}+B_{26}\frac{\partial^2}{\partial y^2}+(B_{12}+B_{66})\frac{\partial^2}{\partial x\partial y}\right)u_y+\\&-\left(\kappa A_{44}\frac{\partial}{\partial x}+\kappa A_{45}\frac{\partial}{\partial y}\right)w+\\&+\left(D_{11}\frac{\partial^2}{\partial x^2}+D_{66}\frac{\partial^2}{\partial y^2}+2D_{16}\frac{\partial^2}{\partial x\partial y}-\kappa A_{44}\right)\beta_x+\\&+\left(D_{16}\frac{\partial^2}{\partial x^2}+D_{26}\frac{\partial^2}{\partial y^2}+(D_{12}+D_{66})\frac{\partial^2}{\partial x\partial y}-\kappa A_{45}\right)\beta_y+m_x=I_1\ddot{u}_x+I_2\ddot{\beta}_x\end{aligned}\tag{4.24}$$

Fifth fundamental equation

$$\begin{aligned}
&\left(B_{16}\frac{\partial^2}{\partial x^2}+B_{26}\frac{\partial^2}{\partial y^2}+\left(B_{12}+B_{66}\right)\frac{\partial^2}{\partial x\partial y}\right)u_x+\\
&+\left(B_{66}\frac{\partial^2}{\partial x^2}+B_{22}\frac{\partial^2}{\partial y^2}+2B_{26}\frac{\partial^2}{\partial x\partial y}\right)u_y+\\
&-\left(\kappa A_{45}\frac{\partial}{\partial x}+\kappa A_{55}\frac{\partial}{\partial y}\right)w+\\
&+\left(D_{16}\frac{\partial^2}{\partial x^2}+D_{26}\frac{\partial^2}{\partial y^2}+\left(D_{12}+D_{66}\right)\frac{\partial^2}{\partial x\partial y}-\kappa A_{45}\right)\beta_x+\\
&+\left(D_{66}\frac{\partial^2}{\partial x^2}+D_{22}\frac{\partial^2}{\partial y^2}+2D_{26}\frac{\partial^2}{\partial x\partial y}-\kappa A_{55}\right)\beta_y+m_y=I_1\ddot{u}_y+I_2\ddot{\beta}_y
\end{aligned}\tag{4.25}$$

the five equations written above represent the fundamental system of equations for a RM rectangular plate composed of a generic anisotropic material for the static and dynamic case.

4.3 Isotropic case

In case of isotropic rectangular plates the five fundamental equations can be separated into the membrane problem and the flexural one. In particular the first two equations represent the in plane displacements u_x and u_y of the plate and the other set of three equations give the vertical displacement w and the two rotations β_x and β_y of the plate. Furthermore some elastic coefficients can be neglected for the present case. In particular

$$\begin{aligned}
&A_{11}=A_{22}=\frac{Eh}{1-\nu^2},\quad A_{12}=\nu A_{11},\quad A_{44}=A_{55}=A_{66}=\frac{1-\nu}{2}A_{11}\\
&D_{11}=D_{22}=\frac{Eh^3}{12(1-\nu^2)},\quad D_{12}=\nu D_{11},\quad D_{44}=D_{55}=D_{66}=\frac{1-\nu}{2}D_{11}\\
&A_{16}=A_{26}=A_{45}=0,\quad D_{16}=D_{26}=D_{45}=0,\quad B_{ij}=0
\end{aligned}\tag{4.26}$$

in the following the three flexural fundamental equations for the flat plates are presented

First flexural fundamental equation

$$\left(\kappa A_{44}\frac{\partial^2}{\partial x^2}+\kappa A_{55}\frac{\partial^2}{\partial y^2}\right)w+\left(\kappa A_{44}\frac{\partial}{\partial x}\right)\beta_x+\left(\kappa A_{55}\frac{\partial}{\partial y}\right)\beta_y+p_n=I_0\ddot{w}\tag{4.27}$$

Second flexural fundamental equation

$$\begin{aligned}
&-\left(\kappa A_{44}\frac{\partial}{\partial x}\right)w+\left(D_{11}\frac{\partial^2}{\partial x^2}+D_{66}\frac{\partial^2}{\partial y^2}-\kappa A_{44}\right)\beta_x+\\
&+\left(\left(D_{12}+D_{66}\right)\frac{\partial^2}{\partial x\partial y}\right)\beta_y+m_x=I_1\ddot{u}_x+I_2\ddot{\beta}_x
\end{aligned}\tag{4.28}$$

Third flexural fundamental equation

$$\begin{aligned} &-\left(\kappa A_{55}\frac{\partial}{\partial y}\right)w+\left(\left(D_{12}+D_{66}\right)\frac{\partial^2}{\partial x\partial y}\right)\beta_x+\\ &+\left(D_{66}\frac{\partial^2}{\partial x^2}+D_{22}\frac{\partial^2}{\partial y^2}-\kappa A_{55}\right)\beta_y+m_y=I_1\ddot{u}_y+I_2\ddot{\beta}_y \end{aligned} \tag{4.29}$$

4.4 Boundary conditions

In order to solve the static or the dynamic problem for a RM plate the boundary conditions must be imposed. However, as it has already shown for the state plane case and the membrane problem, the boundary conditions implementation for the RM plate are different considering the outward normal of the given boundary. In particular two kinds of boundary conditions have to be considered: the first kind is the external boundary condition and the second kind is the inter-element compatibility condition or the internal boundary condition. Firstly the external boundary conditions for a single element GDQ will be considered in the following. Secondly these conditions are extended for the GDQFEM case using the composition of the normal and shear stresses given by the 3D elasticity.

Starting off the internal stresses matrix form presented in (4.19), the same forces and moments in terms of displacements can be written as

$$\begin{aligned} N_x=&\left(A_{11}\frac{\partial}{\partial x}+A_{16}\frac{\partial}{\partial y}\right)u_x+\left(A_{16}\frac{\partial}{\partial x}+A_{12}\frac{\partial}{\partial y}\right)u_y+\\ &+\left(B_{11}\frac{\partial}{\partial x}+B_{16}\frac{\partial}{\partial y}\right)\beta_x+\left(B_{16}\frac{\partial}{\partial x}+B_{12}\frac{\partial}{\partial y}\right)\beta_y \end{aligned} \tag{4.30}$$

$$\begin{aligned} N_y=&\left(A_{12}\frac{\partial}{\partial x}+A_{26}\frac{\partial}{\partial y}\right)u_x+\left(A_{26}\frac{\partial}{\partial x}+A_{22}\frac{\partial}{\partial y}\right)u_y+\\ &+\left(B_{12}\frac{\partial}{\partial x}+B_{26}\frac{\partial}{\partial y}\right)\beta_x+\left(B_{26}\frac{\partial}{\partial x}+B_{22}\frac{\partial}{\partial y}\right)\beta_y \end{aligned} \tag{4.31}$$

$$\begin{aligned} N_{xy}=N_{yx}=&\left(A_{16}\frac{\partial}{\partial x}+A_{66}\frac{\partial}{\partial y}\right)u_x+\left(A_{66}\frac{\partial}{\partial x}+A_{26}\frac{\partial}{\partial y}\right)u_y+\\ &+\left(B_{16}\frac{\partial}{\partial x}+B_{66}\frac{\partial}{\partial y}\right)\beta_x+\left(B_{66}\frac{\partial}{\partial x}+B_{26}\frac{\partial}{\partial y}\right)\beta_y \end{aligned} \tag{4.32}$$

$$\begin{aligned} M_x=&\left(B_{11}\frac{\partial}{\partial x}+B_{16}\frac{\partial}{\partial y}\right)u_x+\left(B_{16}\frac{\partial}{\partial x}+B_{12}\frac{\partial}{\partial y}\right)u_y+\\ &+\left(D_{11}\frac{\partial}{\partial x}+D_{16}\frac{\partial}{\partial y}\right)\beta_x+\left(D_{16}\frac{\partial}{\partial x}+D_{12}\frac{\partial}{\partial y}\right)\beta_y \end{aligned} \tag{4.33}$$

$$\begin{aligned} M_y=&\left(B_{12}\frac{\partial}{\partial x}+B_{26}\frac{\partial}{\partial y}\right)u_x+\left(B_{26}\frac{\partial}{\partial x}+B_{22}\frac{\partial}{\partial y}\right)u_y+\\ &+\left(D_{12}\frac{\partial}{\partial x}+D_{26}\frac{\partial}{\partial y}\right)\beta_x+\left(D_{26}\frac{\partial}{\partial x}+D_{22}\frac{\partial}{\partial y}\right)\beta_y \end{aligned} \tag{4.34}$$

$$M_{xy} = M_{yx} = \left(B_{16}\frac{\partial}{\partial x} + B_{66}\frac{\partial}{\partial y} \right) u_x + \left(B_{66}\frac{\partial}{\partial x} + B_{26}\frac{\partial}{\partial y} \right) u_y + \\ + \left(D_{16}\frac{\partial}{\partial x} + D_{66}\frac{\partial}{\partial y} \right) \beta_x + \left(D_{66}\frac{\partial}{\partial x} + D_{26}\frac{\partial}{\partial y} \right) \beta_y \tag{4.35}$$

$$T_x = \kappa \left(A_{44}\frac{\partial}{\partial x} + A_{45}\frac{\partial}{\partial y} \right) w + \kappa A_{44}\beta_x + \kappa A_{45}\beta_y \tag{4.36}$$

$$T_y = \kappa \left(A_{45}\frac{\partial}{\partial x} + A_{55}\frac{\partial}{\partial y} \right) w + \kappa A_{45}\beta_x + \kappa A_{55}\beta_y \tag{4.37}$$

It must be noted that the external loadings of the rectangular element follow the positive rule of the external forces (the sum of all the external forces must equilibrate the infinitesimal element), whereas the external forces which are on the generic side of normal **n** follow the direction of the n, s and z axis. The transformed stresses are defined on the generic normal **n** as

$$\begin{aligned} N_n &= N_x n_x^2 + N_y n_y^2 + 2N_{xy} n_x n_y \\ N_{ns} &= (N_y - N_x)\, n_x n_y + N_{xy}\left(n_x^2 - n_y^2\right) \\ T_n &= T_x n_x + T_y n_y \\ M_n &= M_x n_x^2 + M_y n_y^2 + 2M_{xy} n_x n_y \\ M_{ns} &= (M_y - M_x)\, n_x n_y + M_{xy}\left(n_x^2 - n_y^2\right) \end{aligned} \tag{4.38}$$

It must be noted that (4.38) are valid for external boundary conditions only. If the inter-element compatibility conditions in terms of stresses have to be written the relationships are quite different. For the sake of completeness they are reported in the following

$$\begin{aligned} N_n &= N_x n_x^2 + N_y n_y^2 + 2N_{xy} n_x n_y \\ N_{ns} &= (N_y - N_x)\, n_x n_y + N_{xy}\left(n_x^2 - n_y^2\right) \\ T_n &= T_x\left(n_x - n_y\right)^2 + T_y\left(n_x + n_y\right)^2 \\ M_n &= M_x n_x^2 + M_y n_y^2 + 2M_{xy} n_x n_y \\ M_{ns} &= (M_y - M_x)\, n_x n_y + M_{xy}\left(n_x^2 - n_y^2\right) \end{aligned} \tag{4.39}$$

comparing (4.39) to (4.38) only the shear forces relation is different, in fact changes the projection of the shear force of one element respect to given outward normal.

In the following the external and internal boundary conditions (4.39), (4.38) are reported in extended form as a function of the plate degrees of freedom. The membrane stresses are

$$
\begin{aligned}
N_n = &\left(A_{11}\frac{\partial u_x}{\partial x} + A_{16}\frac{\partial u_x}{\partial y}\right) n_x^2 + \left(A_{12}\frac{\partial u_x}{\partial x} + A_{26}\frac{\partial u_x}{\partial y}\right) n_y^2 + 2\left(A_{16}\frac{\partial u_x}{\partial x} + A_{66}\frac{\partial u_x}{\partial y}\right) n_x n_y + \\
&+ \left(A_{16}\frac{\partial u_y}{\partial x} + A_{12}\frac{\partial u_y}{\partial y}\right) n_x^2 + \left(A_{26}\frac{\partial u_y}{\partial x} + A_{22}\frac{\partial u_y}{\partial y}\right) n_y^2 + 2\left(A_{66}\frac{\partial u_y}{\partial x} + A_{26}\frac{\partial u_y}{\partial y}\right) n_x n_y + \\
&+ \left(B_{11}\frac{\partial \beta_x}{\partial x} + B_{16}\frac{\partial \beta_x}{\partial y}\right) n_x^2 + \left(B_{12}\frac{\partial \beta_x}{\partial x} + B_{26}\frac{\partial \beta_x}{\partial y}\right) n_y^2 + 2\left(B_{16}\frac{\partial \beta_x}{\partial x} + B_{66}\frac{\partial \beta_x}{\partial y}\right) n_x n_y + \\
&+ \left(B_{16}\frac{\partial \beta_y}{\partial x} + B_{12}\frac{\partial \beta_y}{\partial y}\right) n_x^2 + \left(B_{26}\frac{\partial \beta_y}{\partial x} + B_{22}\frac{\partial \beta_y}{\partial y}\right) n_y^2 + 2\left(B_{66}\frac{\partial \beta_y}{\partial x} + B_{26}\frac{\partial \beta_y}{\partial y}\right) n_x n_y
\end{aligned}
\tag{4.40}
$$

$$
\begin{aligned}
N_{ns} = &\left((A_{12} - A_{11})\frac{\partial u_x}{\partial x} + (A_{26} - A_{16})\frac{\partial u_x}{\partial y}\right) n_x n_y + \left(A_{16}\frac{\partial u_x}{\partial x} + A_{66}\frac{\partial u_x}{\partial y}\right)(n_x^2 - n_y^2) + \\
&+ \left((A_{26} - A_{16})\frac{\partial u_y}{\partial x} + (A_{22} - A_{12})\frac{\partial u_y}{\partial y}\right) n_x n_y + \left(A_{66}\frac{\partial u_y}{\partial x} + A_{26}\frac{\partial u_y}{\partial y}\right)(n_x^2 - n_y^2) + \\
&+ \left((B_{12} - B_{11})\frac{\partial \beta_x}{\partial x} + (B_{26} - B_{16})\frac{\partial \beta_x}{\partial y}\right) n_x n_y + \left(B_{16}\frac{\partial \beta_x}{\partial x} + B_{66}\frac{\partial \beta_x}{\partial y}\right)(n_x^2 - n_y^2) + \\
&+ \left((B_{26} - B_{16})\frac{\partial \beta_y}{\partial x} + (B_{22} - B_{12})\frac{\partial \beta_y}{\partial y}\right) n_x n_y + \left(B_{66}\frac{\partial \beta_y}{\partial x} + B_{26}\frac{\partial \beta_y}{\partial y}\right)(n_x^2 - n_y^2)
\end{aligned}
\tag{4.41}
$$

The shear force valid for an external boundary condition

$$
\begin{aligned}
T_n = &\kappa\left(\left(A_{44}n_x + A_{45}n_y\right)\frac{\partial}{\partial x} + \left(A_{45}n_x + A_{55}n_y\right)\frac{\partial}{\partial y}\right) w + \\
&+ \kappa\left(A_{44}n_x + A_{45}n_y\right)\beta_x + \kappa\left(A_{45}n_x + A_{55}n_y\right)\beta_y
\end{aligned}
\tag{4.42}
$$

The shear force valid for an internal boundary condition

$$
\begin{aligned}
T_n = &\kappa\left(\left(A_{44}\left(n_x - n_y\right)^2 + A_{45}\left(n_x + n_y\right)^2\right)\frac{\partial}{\partial x} + \right. \\
&\left. + \left(A_{45}\left(n_x - n_y\right)^2 + A_{55}\left(n_x + n_y\right)^2\right)\frac{\partial}{\partial y}\right) w + \\
&+ \kappa\left(A_{44}\left(n_x - n_y\right)^2 + A_{45}\left(n_x + n_y\right)^2\right)\beta_x + \\
&+ \kappa\left(A_{45}\left(n_x - n_y\right)^2 + A_{55}\left(n_x + n_y\right)^2\right)\beta_y
\end{aligned}
\tag{4.43}
$$

In conclusion the bending moments are reported in the following

$$M_n = \left(B_{11}\frac{\partial u_x}{\partial x} + B_{16}\frac{\partial u_x}{\partial y}\right) n_x^2 + \left(B_{12}\frac{\partial u_x}{\partial x} + B_{26}\frac{\partial u_x}{\partial y}\right) n_y^2 + 2\left(B_{16}\frac{\partial u_x}{\partial x} + B_{66}\frac{\partial u_x}{\partial y}\right) n_x n_y +$$
$$+ \left(B_{16}\frac{\partial u_y}{\partial x} + B_{12}\frac{\partial u_y}{\partial y}\right) n_x^2 + \left(B_{26}\frac{\partial u_y}{\partial x} + B_{22}\frac{\partial u_y}{\partial y}\right) n_y^2 + 2\left(B_{66}\frac{\partial u_y}{\partial x} + B_{26}\frac{\partial u_y}{\partial y}\right) n_x n_y +$$
$$+ \left(D_{11}\frac{\partial \beta_x}{\partial x} + D_{16}\frac{\partial \beta_x}{\partial y}\right) n_x^2 + \left(D_{12}\frac{\partial \beta_x}{\partial x} + D_{26}\frac{\partial \beta_x}{\partial y}\right) n_y^2 + 2\left(D_{16}\frac{\partial \beta_x}{\partial x} + D_{66}\frac{\partial \beta_x}{\partial y}\right) n_x n_y +$$
$$+ \left(D_{16}\frac{\partial \beta_y}{\partial x} + D_{12}\frac{\partial \beta_y}{\partial y}\right) n_x^2 + \left(D_{26}\frac{\partial \beta_y}{\partial x} + D_{22}\frac{\partial \beta_y}{\partial y}\right) n_y^2 + 2\left(D_{66}\frac{\partial \beta_y}{\partial x} + D_{26}\frac{\partial \beta_y}{\partial y}\right) n_x n_y \tag{4.44}$$

$$M_{ns} = \left((B_{12} - B_{11})\frac{\partial u_x}{\partial x} + (B_{26} - B_{16})\frac{\partial u_x}{\partial y}\right) n_x n_y + \left(B_{16}\frac{\partial u_x}{\partial x} + B_{66}\frac{\partial u_x}{\partial y}\right)(n_x^2 - n_y^2) +$$
$$+ \left((B_{26} - B_{16})\frac{\partial u_y}{\partial x} + (B_{22} - B_{12})\frac{\partial u_y}{\partial y}\right) n_x n_y + \left(B_{66}\frac{\partial u_y}{\partial x} + B_{26}\frac{\partial u_y}{\partial y}\right)(n_x^2 - n_y^2) +$$
$$+ \left((D_{12} - D_{11})\frac{\partial \beta_x}{\partial x} + (D_{26} - D_{16})\frac{\partial \beta_x}{\partial y}\right) n_x n_y + \left(D_{16}\frac{\partial \beta_x}{\partial x} + D_{66}\frac{\partial \beta_x}{\partial y}\right)(n_x^2 - n_y^2) +$$
$$+ \left((D_{26} - D_{16})\frac{\partial \beta_y}{\partial x} + (D_{22} - D_{12})\frac{\partial \beta_y}{\partial y}\right) n_x n_y + \left(D_{66}\frac{\partial \beta_y}{\partial x} + D_{26}\frac{\partial \beta_y}{\partial y}\right)(n_x^2 - n_y^2) \tag{4.45}$$

For the boundary conditions implementations the same rules, introduced in the previous chapters, are introduced for RM flat plates. It must be noted that two different kinds of boundary conditions are implemented in order to distinguish the external and the internal boundary conditions.

4.5 Numerical applications

In this section several static and dynamic numerical applications will be shown in order to demonstrate the accuracy and stability of GDQFEM applied to RM flat plates.

4.5.1 Free vibrations of a rectangular plate

As it has already been demonstrated in chapter 2, the free vibrations of a thin membrane give the same results of a thin plate simply supported on all the edges. In the following section it is shown that given the same geometry the same results can be reached. For the sake of clarity the rectangular plate has got two sides of length $a = 1.2$ m, $b = 0.9$ m. Since an isotropic plate must be considered for the literature comparison only the flexural RM problem is applied. This choice brings two computational advantages, firstly the flexural modal shapes are separated from the membrane motions and secondly the computational effort of the problem is highly reduced, because the system goes from five differential equations to three only. Computationally speaking if $N \times M$ grid points per element are considered the total algebraic system effort is $N \cdot M \cdot n_e \cdot 3$, where n_e is the total number of element of the problem under consideration.

f [Hz]	Exact	FEM	GDQFEM				
			$N = 13$	$N = 15$	$N = 21$	$N = 31$	$N = 41$
1	47.58	47.56	47.56	47.56	47.56	47.56	47.56
2	98.96	98.89	98.89	98.89	98.89	98.89	98.89
3	138.93	138.79	138.79	138.79	138.79	138.79	138.79
4	184.60	184.35	184.35	184.35	184.35	184.35	184.35
5	190.31	190.05	190.05	190.05	190.05	190.05	190.05
6	275.95	275.39	275.39	275.39	275.39	275.39	275.39
7	291.18	290.55	290.56	290.55	290.55	290.55	290.55
8	304.50	303.82	303.61	303.83	303.82	303.82	303.82
9	342.56	341.70	341.70	341.70	341.70	341.70	341.70
10	395.85	394.70	394.53	394.71	394.70	394.70	394.70

Table 4.1: First ten eigenfrequencies of a rectangular simply supported RM plate considering the flexural problem only.

In the present example a steel plate is considered with an elastic modulus $E = 2.1 \cdot 10^{11}$ Pa and a Poisson ratio $\nu = 0.3$, the material density is $\rho = 7800$ kg/m^3 and the uniform plate thickness is equal to $h = 0.01$ m. So the slenderness ratio of the plate under consideration is almost 1/100. In table 4.1 the first ten frequencies of a rectangular plate considering only three degrees of freedom is reported. Furthermore the numerical results are compared with the exact solution and a numerical solution obtain with a commercial FE program. The GDQFEM numerical solutions are obtain within a C-G-L grid distribution of grid points considering $N = M$ so equal number of points along x and y.

For the computational point of view it can be interested seen if the algorithm is stable considering an irregular geometry. In the following example several distorted geometries are shown in order to see the stability and accuracy of GDQFEM methodology. The same example has been already performed for the membrane case, so the same geometric sample is used. It can be seen from table 4.2 that if the mesh is distorted more points per element are needed. In fact increasing the distortion, e.g. $c < 0.5$, the error increases for higher natural frequencies. The error decreases passing from $N = 13$ to $N = 21$. For the flexural problem of thin membranes presented in chapter 2 degenerate quadrilateral element could be considered ($c = 0.0$), in the flexural RM plate can not be considered instead because numerical issues occur. So the minimum value of the distortion parameter is $c = 0.1$.

4.5.2 Free vibrations of a V-notched plate

In the present section the same geometry used in the membrane problems (Chapter 2) is used for the FSDT computation. However in the present case mixed boundary conditions are taken into account. In particular the v-notched part is let free and the other external boundaries are once clamped and once simply supported. In Table 4.3 the first ten natural frequencies obtained by GDQFEM are compared to FE solution. Furthermore the first nine modal shapes are graphically presented for the simply supported case in Figure 4.1.

f [Hz]	Exact	GDQFEM $N = 13$				
		0.5	0.4	0.3	0.2	0.1
1	47.58	47.85	49.04	50.84	51.27	49.79
2	98.96	98.89	98.82	98.61	98.32	98.41
3	138.93	138.71	138.53	138.36	138.26	138.33
4	184.60	184.38	184.35	184.65	185.01	184.86
5	190.31	190.14	191.52	195.80	197.55	193.46
6	275.95	275.36	275.39	275.24	274.52	274.92
7	291.18	290.97	292.79	295.97	296.49	293.56
8	304.50	303.82	303.79	303.82	303.71	303.77
9	342.56	341.70	341.50	340.91	340.23	340.62
10	395.85	394.81	395.19	394.69	397.71	400.46
f [Hz]	Exact	GDQFEM $N = 21$				
		0.5	0.4	0.3	0.2	0.1
1	47.58	47.60	47.69	47.76	47.86	47.88
2	98.96	98.89	98.88	98.78	98.56	98.57
3	138.93	138.79	138.74	138.62	138.47	138.56
4	184.60	184.36	184.35	184.41	184.57	184.58
5	190.31	190.06	190.19	190.47	190.90	190.96
6	275.95	275.39	275.39	275.34	274.83	274.57
7	291.18	290.61	290.74	290.85	291.00	291.02
8	304.50	303.82	303.81	303.82	303.73	303.53
9	342.56	341.71	341.68	341.42	340.87	340.89
10	395.85	394.72	394.75	394.70	395.02	395.18

Table 4.2: First ten frequencies for a distorted 2 element plate for two grid points selection.

4.5.3 Arbitrarily Shaped Plate with elliptic hole

In the following section arbitrarily shaped composite plates are considered within the dynamic case. The plate under consideration is a three layer composite of two sheets of Graphite-Epoxy and a core of Glass-Epoxy with the following mechanical properties. The Graphite-Epoxy is defined by $E_1 = 137.9$ GPa, $E_2 = 8.96$ GPa, $G_{12} = G_{13} = 7.1$ GPa, $G_{23} = 6.21$ GPa, $\nu_{12} = \nu_{13} = 0.3$, $\nu_{23} = 0.49$ and $\rho = 1450$ kg/m^3. The Glass-Epoxy is $E_1 = 53.78$ GPa, $E_2 = 17.93$ GPa, $G_{12} = G_{13} = 8.96$ GPa, $G_{23} = 3.45$ GPa, $\nu_{12} = \nu_{13} = 0.25$, $\nu_{23} = 0.34$ and $\rho = 1900$ kg/m^3. The two sheets have a constant thickness of $h_s = 0.03$ m and the core thickness is equal to $h_c = 0.04$ m. The three laminae have different orientations $\theta_1 = 30$ for the first lamina, $\theta_2 = 65$ for the core and $\theta_3 = 45$ for the top sheet. The first example considers an arbitrarily shaped plate, with a shape of half of a circle and a triangle ad and inner elliptic hole. The external boundaries are clamped and the inner elliptic hole is free instead. The results in terms of natural frequencies are reported in Table 4.4 within the first nine modal shapes depicted in Figure 4.2. It is noted that the reference solution is obtained with a 3D FE analysis and the GDQFEM solution is an ESL solution, so it has much less computational effort on the machine.

In the second example the same geometry and lamination scheme is considered but fixing all the edges, instead. Compared to the previous case the frequencies are expected

f [Hz]	Clamped edges				Simply supported edges			
	ABAQUS	GDQFEM			ABAQUS	GDQFEM		
		$N = 15$	$N = 19$	$N = 23$		$N = 15$	$N = 19$	$N = 23$
1	83.598	83.611	83.571	83.573	45.764	44.819	45.514	45.920
2	141.453	141.628	141.410	141.332	92.146	92.671	92.482	92.401
3	201.464	201.126	201.341	201.411	136.853	136.605	136.948	137.076
4	233.511	232.811	232.903	232.955	166.040	165.895	166.105	166.193
5	234.049	234.339	234.034	233.928	174.109	175.148	174.733	174.586
6	321.943	321.731	321.478	321.380	250.309	251.154	250.902	250.812
7	350.397	350.514	350.450	350.413	271.291	272.575	272.506	272.479
8	382.438	382.356	382.384	382.379	289.007	289.295	289.386	289.354
9	411.891	411.340	411.676	411.793	322.755	322.817	323.132	323.253
10	447.395	447.248	447.174	447.158	353.763	354.761	354.748	354.744

Table 4.3: First ten natural frequencies of a partially clamped and simply supported v-notched free plate.

f [Hz]	ABAQUS 3D	GDQFEM			
		$N = 9$	$N = 11$	$N = 15$	$N = 21$
1	342.338	343.1773	343.3080	343.3374	343.3375
2	403.947	405.5717	405.7801	405.7815	405.7803
3	580.529	584.2223	584.1184	584.1061	584.1063
4	675.803	680.2441	680.2718	680.2600	680.2613
5	779.553	784.9928	784.9080	784.9043	784.9047
6	905.879	908.5571	908.6854	908.6918	908.6909
7	976.738	984.9963	984.7488	984.7125	984.7134
8	1033.360	1039.0524	1039.3920	1039.4444	1039.4438
9	1154.610	1158.6843	1158.6069	1158.6693	1158.6688
10	1219.100	1231.1261	1231.1231	1231.1331	1231.1351

Table 4.4: First ten frequencies for an arbitrarily shaped plate with elliptic hole free and lamination scheme 30/65/45.

to be greater due to the stronger boundary conditions. In Table 4.5 the first ten natural frequencies are presented and compared with 3D ABAQUS model. Very good agreement is observed. The solution in terms of modal shapes is graphically shown in Figure 4.3.

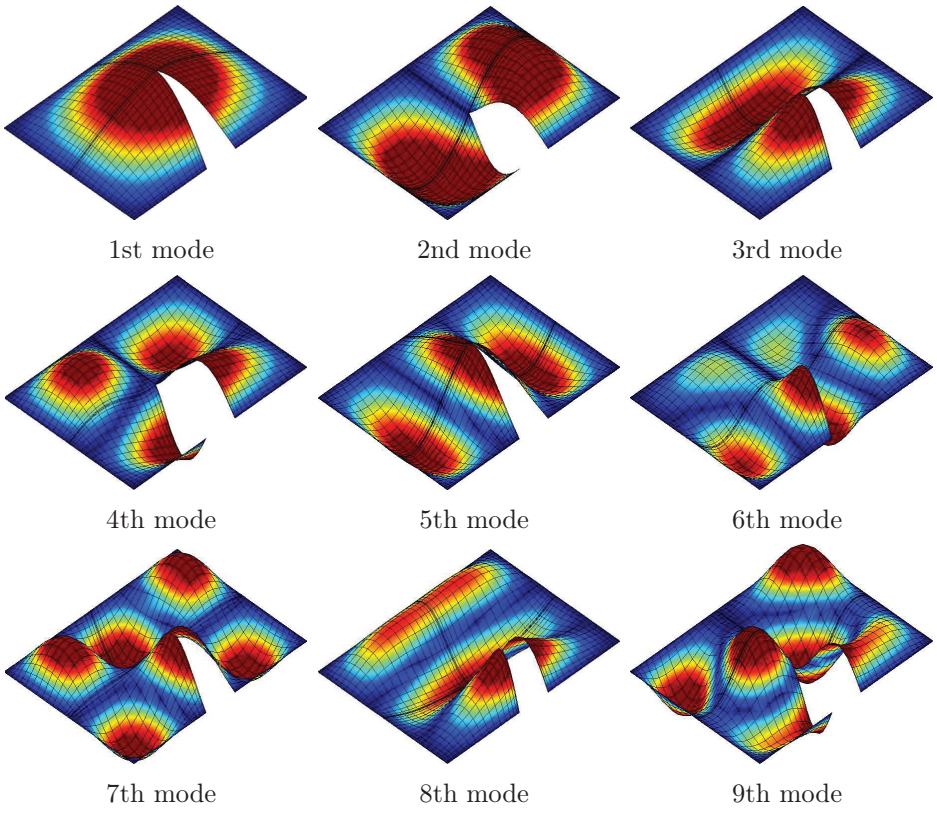

Figure 4.1: First 9 mode shapes for the V-notched Simply supported plate.

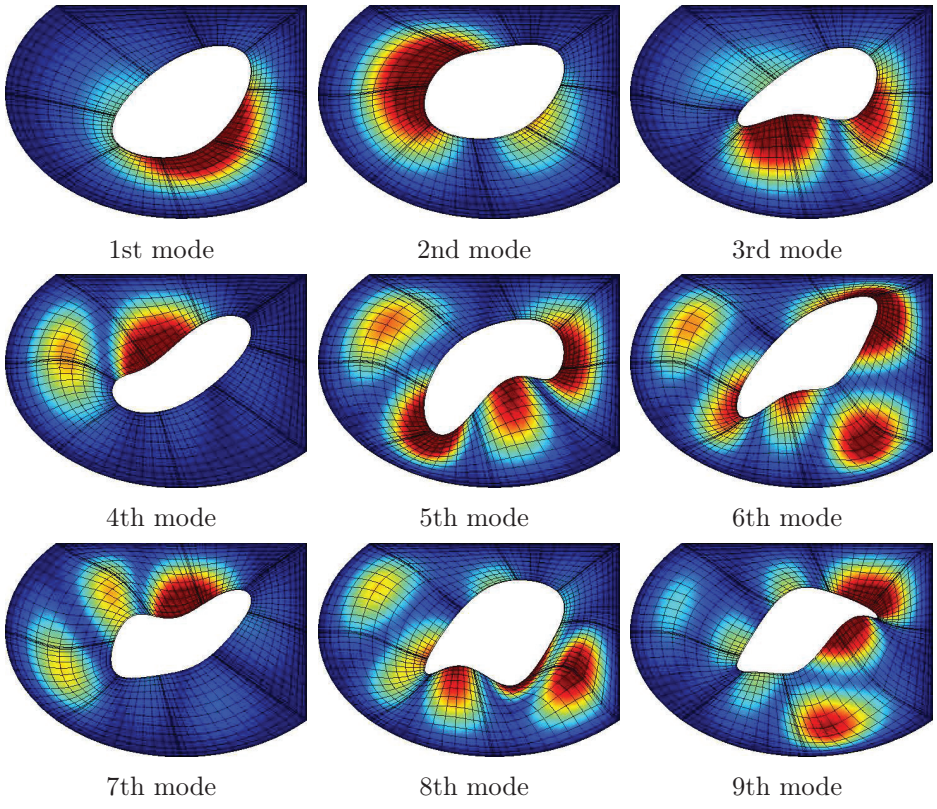

Figure 4.2: First 9 mode shapes for an arbitrarily shaped composite plate.

f [Hz]	ABAQUS 3D	GDQFEM			
		$N = 9$	$N = 11$	$N = 15$	$N = 21$
1	705.635	708.2110	708.2110	708.2103	708.2102
2	885.299	880.5386	880.5386	880.5419	880.5420
3	1087.090	1095.0781	1095.0781	1095.0781	1095.0781
4	1192.900	1190.2398	1190.2398	1190.2417	1190.2416
5	1299.990	1306.3506	1306.3506	1306.3502	1306.3500
6	1429.970	1430.0371	1430.0371	1430.0381	1430.0381
7	1519.500	1525.4432	1525.4432	1525.4455	1525.4456
8	1612.750	1620.9464	1620.9464	1620.9511	1620.9512
9	1644.720	1652.4347	1652.4347	1652.4291	1652.4291
10	1761.310	1769.9693	1769.9693	1769.9765	1769.9770

Table 4.5: First ten frequencies for an arbitrarily shaped plate completely clamped with a lamination scheme 30/65/45.

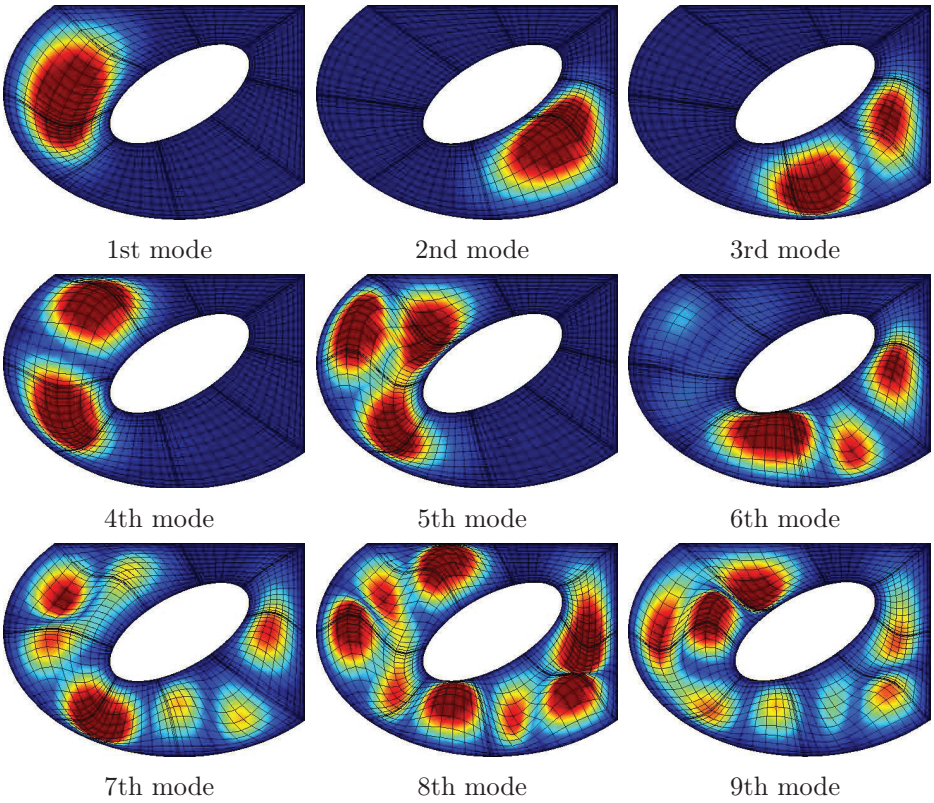

Figure 4.3: First 9 mode shapes for an arbitrarily shaped composite plate.

f [Hz]	ABAQUS 3D	GDQFEM			
		$N = 9$	$N = 11$	$N = 15$	$N = 21$
1	208.147	204.1345	205.8710	206.8864	207.2350
2	294.469	294.7771	294.9040	294.9505	294.9638
3	362.795	363.7379	363.6722	363.5987	363.6076
4	401.596	402.2692	402.3907	402.4663	402.5144
5	559.412	552.5122	555.1034	557.4070	558.5249
6	598.087	600.4364	600.6977	600.9066	601.0051
7	660.154	664.1406	663.8556	663.7433	663.7312
8	757.921	757.7512	757.9036	758.0472	758.1167
9	765.747	766.7499	767.3330	767.3254	767.3737
10	800.982	804.1498	804.0763	804.1637	804.2068

Table 4.6: First ten frequencies for an arbitrarily shaped plate with mixed boundary conditions with a lamination scheme 30/65/45.

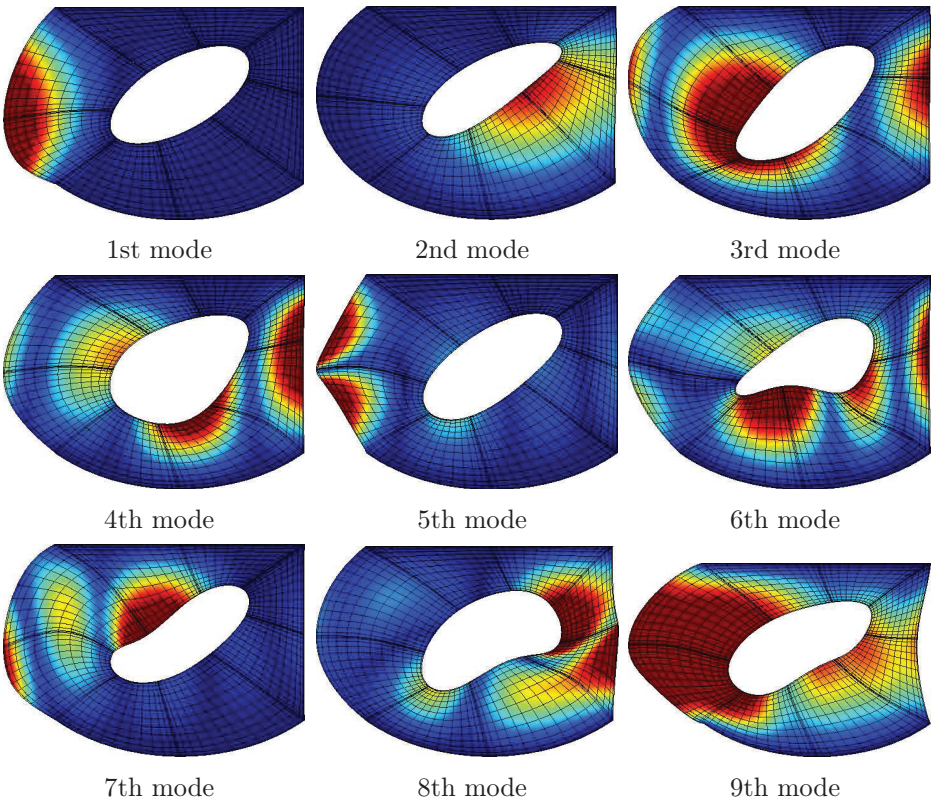

Figure 4.4: First 9 mode shapes for an arbitrarily shaped composite plate.

f [Hz]	ABAQUS 3D	GDQFEM			
		$N = 9$	$N = 11$	$N = 15$	$N = 21$
1	399.734	397.5259	397.4676	397.4302	397.4265
2	430.049	428.3228	428.4792	428.4647	428.4611
3	669.013	666.0062	665.5853	665.4911	665.4902
4	770.025	766.0478	765.5949	765.5113	765.5091
5	792.164	792.2105	792.5574	792.6193	792.6199
6	843.403	837.8935	837.3440	837.1955	837.1920
7	991.892	989.6197	989.8877	989.8844	989.8874
8	1081.220	1075.4533	1075.5904	1075.6027	1075.6055
9	1228.200	1226.2621	1226.2535	1226.2428	1226.2399
10	1232.880	1229.0524	1229.0333	1228.9714	1228.9697

Table 4.7: First ten frequencies for a composite arbitrarily shaped plate with 0/0/0 lamination scheme.

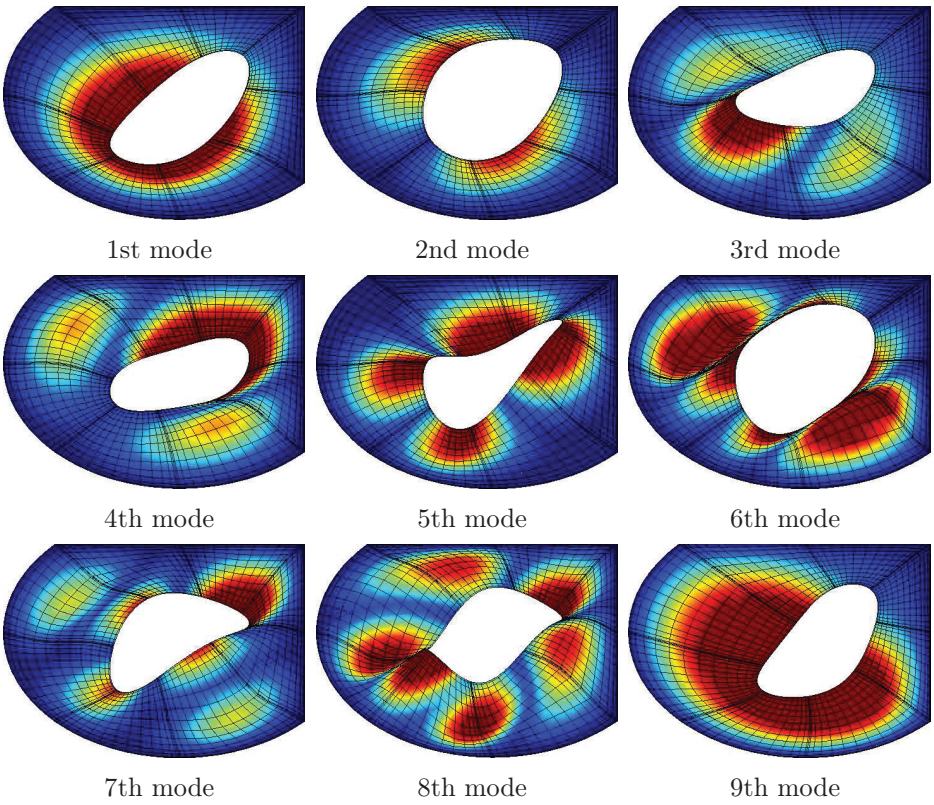

Figure 4.5: First 9 mode shapes for an arbitrarily shaped composite plate.

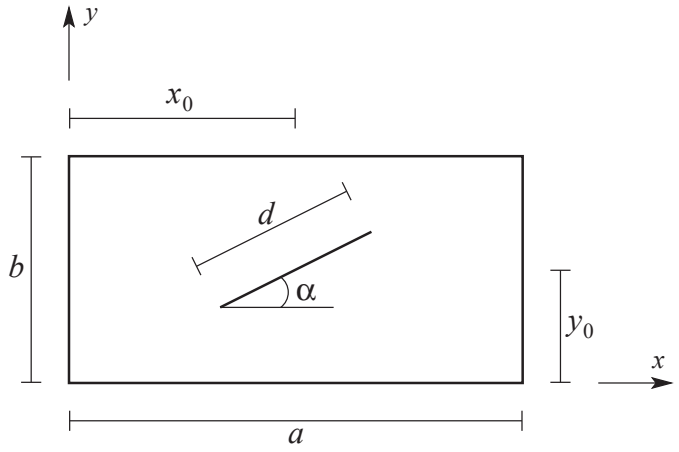

Figure 4.6: Dimensions and coordinates for a rectangular plate with an internal crack (x_0 and y_0 locate the center of the crack)

4.5.4 Cracked plates with central and side cracks

In the following section some numerical results are compared with literature for several isotropic cases of cracked plates [143–146]. In the given reference papers this kind of problem is solved by using the Ritz method. In [143] rectangular plates with internal cracks or slits had been studied. The geometry of this kind of problem is depicted in Figure 4.6. Since crackes square plates with simple support boundary conditions were often studied in the published literature, convergence studies were carried out for such plates with different crack lengths to verify the correctness of the solutions and demonstrate the effects of the number of grid points on the solutions. All the numerical results are presented for the first ten non-dimensional frequency parameters $\Lambda = \omega a^2\sqrt{\rho h/D}$, which are commonly used in the plate vibration literature. In the following different crack lengths $d/a = 0.2$, $d/a = 0.5$, $d/a = 0.8$ and inclination angle α are shown below. The plate under consideration has got a side $a = 2$ m and thickness $h = 0.01$ m. The material is an homogeneous, isotropic and elastic one with Young's modulus of $E = 210$ GPa and Poisson's ratio $\nu = 0.3$. In Table 4.8 the first ten natural frequencies of a square plate with a centred crack of $d/a = 0.2$ are reported. Moreover the numerical solution by FE analysis is presented in the first column. A very good agreement is shown among the three different methodologies. In addition the first nine modal shapes are graphically presented in Figure 4.7. For a crack length equal to $d/a = 0.5$ the numerical results are reported in Table 4.9. In this case also good agreement is observed. The first nine eigenvectors are graphically presented in Figure fig:square-hor-05. The last example for a square plate with a linear crack is presented in Table 4.10 in which the crack length is $d/a = 0.8$. It is noted that in this case, due to the strong discontinuity, a lot of nodes per elements are needed to obtain a correct solution, respect to the previous cases. Finally the first nine modal shapes for the cracked plate under consideration is shown in Figure 4.9.

It is noted that all the results given for the current examples are in good agreement with the results obtained with ABAQUS 2D shell solution and the solution given by Huang *et al.* [143]. In these particular cases the plate is isotropic and so only three equations of the complete set can be considered for the flexural vibration case of FSDT plates.

In the first part of this section a internal crack has been considered. Using the work by Huang *et al.* [144] as a reference, some examples about plates with side cracks are con-

Λ	ABAQUS	Ref. [143]	GDQFEM				
			$N = 13$	$N = 15$	$N = 17$	$N = 19$	$N = 21$
1	19.300	19.32	19.371	19.362	19.360	19.362	19.366
2	49.163	49.18	49.132	49.138	49.142	49.145	49.147
3	49.314	49.32	49.216	49.237	49.258	49.276	49.293
4	78.912	78.95	78.827	78.848	78.862	78.870	78.877
5	93.818	94.11	94.128	94.033	93.952	93.885	93.831
6	98.657	-	98.611	98.621	98.628	98.633	98.637
7	127.506	-	127.350	127.378	127.399	127.415	127.426
8	128.036	-	127.801	127.840	127.873	127.901	127.923
9	165.485	-	164.954	165.035	165.101	165.154	165.195
10	167.510	-	167.304	167.334	167.362	167.385	167.403

Table 4.8: Convergence of frequency parameter Λ for a simply supported square plate with a horizontal center crack ($x_0/a = y_0/b = 0.5$, $d/a = 0.2$, $\alpha = 0$).

Λ	ABAQUS	Ref. [143]	GDQFEM				
			$N = 13$	$N = 15$	$N = 17$	$N = 19$	$N = 21$
1	17.698	17.72	5.928	13.086	15.483	16.574	17.111
2	42.969	43.06	43.966	43.438	43.138	42.965	42.864
3	48.668	48.69	46.728	48.301	49.001	49.288	49.376
4	77.658	77.72	77.917	77.714	77.634	77.602	77.589
5	82.034	82.17	86.759	84.953	83.971	83.415	83.073
6	95.070	-	95.680	94.906	94.679	94.643	94.670
7	98.349	-	105.120	102.460	101.193	100.441	99.937
8	122.768	-	129.553	127.032	125.654	124.811	124.252
9	134.881	-	134.813	134.562	134.527	134.552	134.591
10	166.253	-	166.216	166.216	166.218	166.221	166.222

Table 4.9: Convergence of frequency parameter Λ for a simply supported square plate with a horizontal center crack ($x_0/a = y_0/b = 0.5$, $d/a = 0.5$, $\alpha = 0$).

sidered in the following. The parametric representation is graphically reported in Figure 4.10. Convergence studies are carried out, as in the previous case, for simply supported rectangular plates with different crack lengths to verify the correctness of the solutions and demonstrate the effect of the number of grid points per element. The material is once again an isotropic and homogeneous one, so only the three flexural equations are considered in the computation. In Table 4.11 the first ten frequencies of a simply supported rectangular plate compared with FE analysis and literature results are shown. Moreover the first nine modal shapes for the current plate are depicted in Figure 4.11.

In the last example taken from [144] a square plate with a not-centred crack $c/b = 0.75$ with a length $d/a = 0.3$ and an inclination $\alpha = \pi/6$ is considered. The first ten frequency parameters Λ are reported in Table 4.13 and the first nine modal shapes are graphically presented in Figure 4.13.

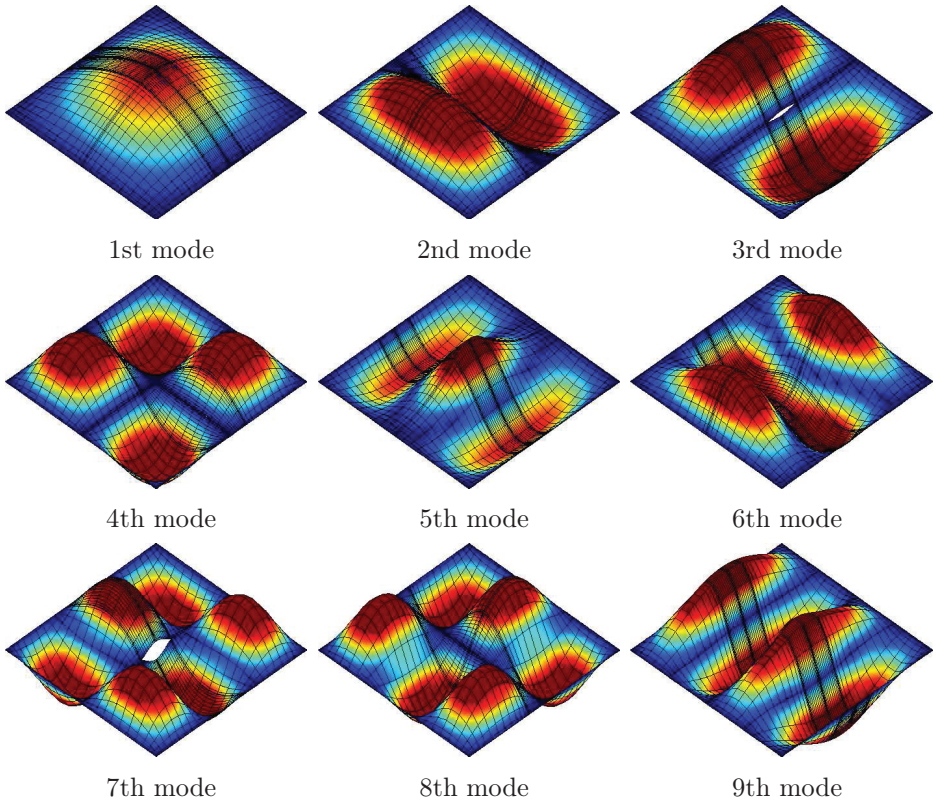

Figure 4.7: First 9 mode shapes for a cracked square plate with a centred crack and $d/a = 0.2$.

Λ	ABAQUS	Ref. [143]	GDQFEM				
			$N = 15$	$N = 21$	$N = 23$	$N = 25$	$N = 27$
1	16.397	16.41	16.676	16.557	16.534	16.515	16.500
2	27.703	27.77	27.419	27.545	27.583	27.615	27.640
3	47.179	47.21	47.234	47.213	47.209	47.206	47.203
4	65.642	65.76	65.399	65.421	65.431	65.440	65.448
5	76.297	76.37	76.391	76.322	76.299	76.279	76.260
6	78.308	-	78.153	78.203	78.212	78.217	78.221
7	96.702	-	96.600	96.653	96.668	96.681	96.692
8	113.338	-	113.024	113.122	113.135	113.144	113.148
9	121.207	-	120.824	120.889	120.908	120.923	120.936
10	125.768	-	125.388	125.410	125.418	125.423	125.427

Table 4.10: Convergence of frequency parameter Λ for a simply supported square plate with a horizontal center crack ($x_0/a = y_0/b = 0.5$, $d/a = 0.8$, $\alpha = 0$).

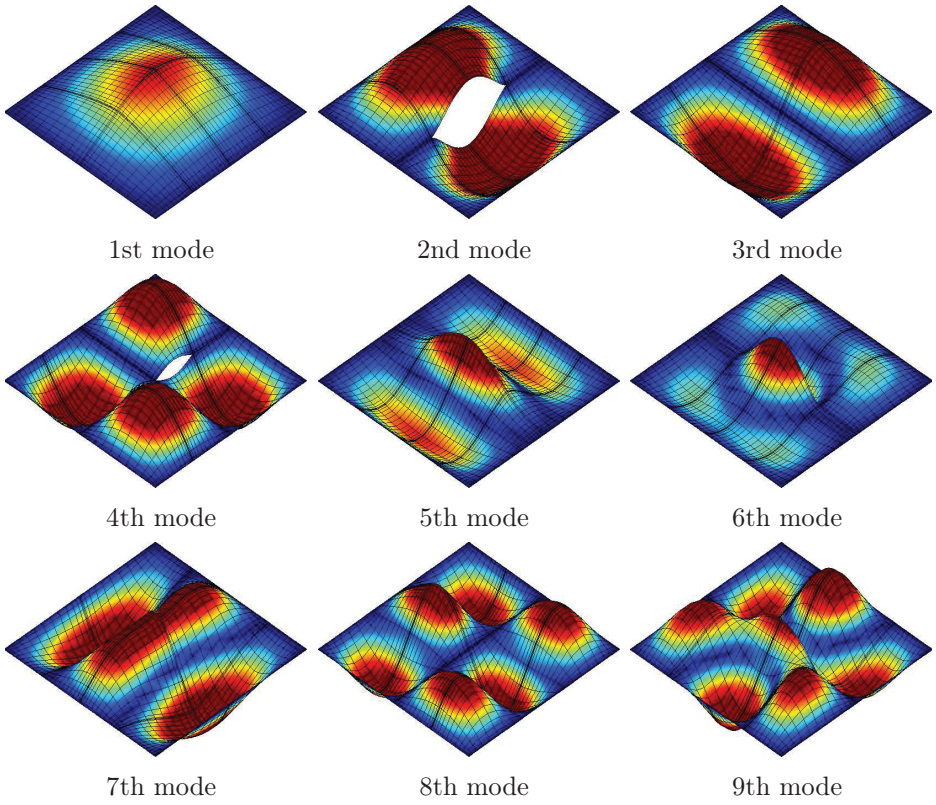

Figure 4.8: First 9 mode shapes for a cracked square plate with a centred crack and $d/a = 0.5$.

Λ	ABAQUS	Ref. [144]	GDQFEM			
			$N = 21$	$N = 23$	$N = 25$	$N = 27$
1	48.948	48.98	49.027	49.060	49.082	49.096
2	77.802	77.89	77.918	77.976	78.015	78.039
3	126.430	126.6	126.518	126.571	126.608	126.631
4	166.926	167.1	166.844	166.854	166.860	166.865
5	193.664	194.2	193.388	193.430	193.459	193.478
6	194.969	-	194.998	195.018	195.030	195.038
7	237.292	-	236.766	236.853	236.913	236.955
8	283.318	-	283.290	283.286	283.283	283.281
9	298.406	-	297.669	297.789	297.875	297.937
10	357.819	-	357.195	357.273	357.330	357.372

Table 4.11: Convergence of frequency parameters Λ for a simply supported rectangular plate having a central ($c/b = 0.5$) side crack with $d/a = 0.2$.

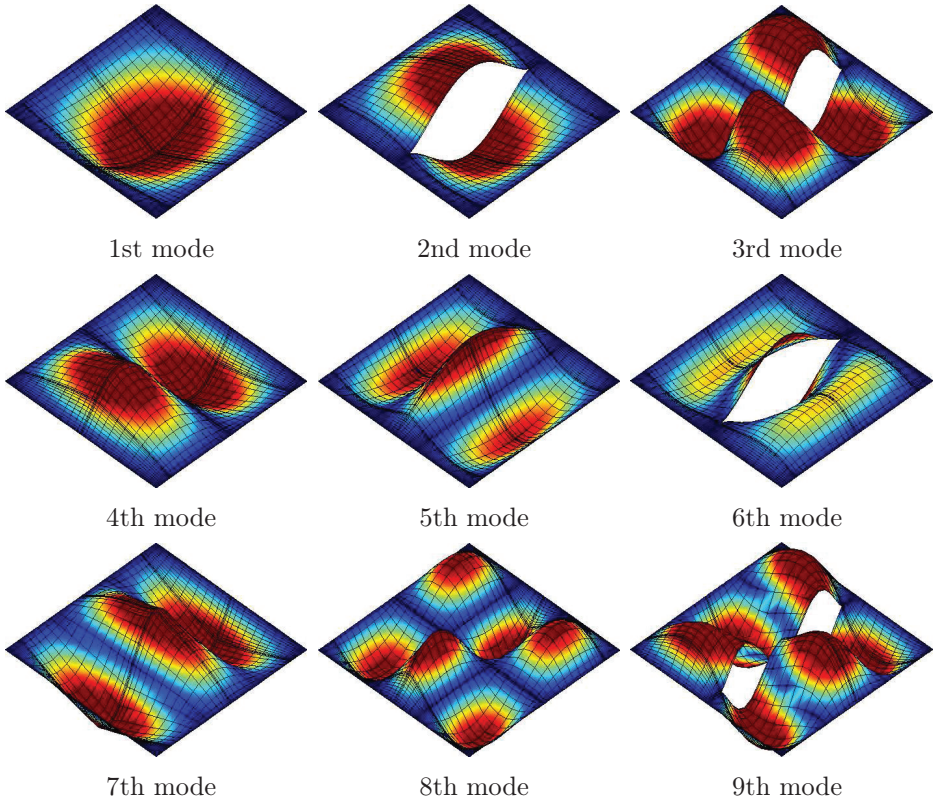

Figure 4.9: First 9 mode shapes for a cracked square plate with a centred crack and $d/a = 0.8$.

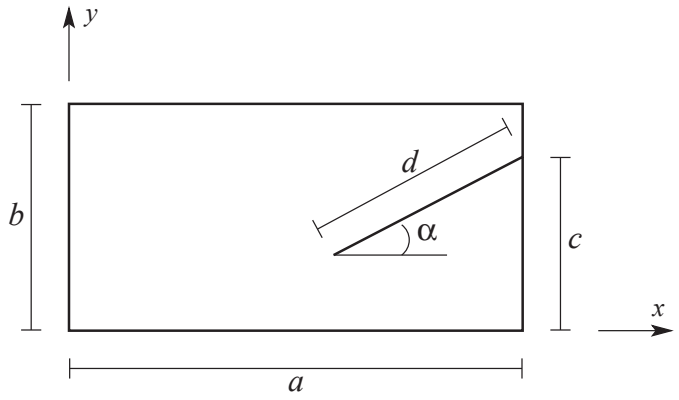

Figure 4.10: Dimensions and coordinates for a side-cracked plate.

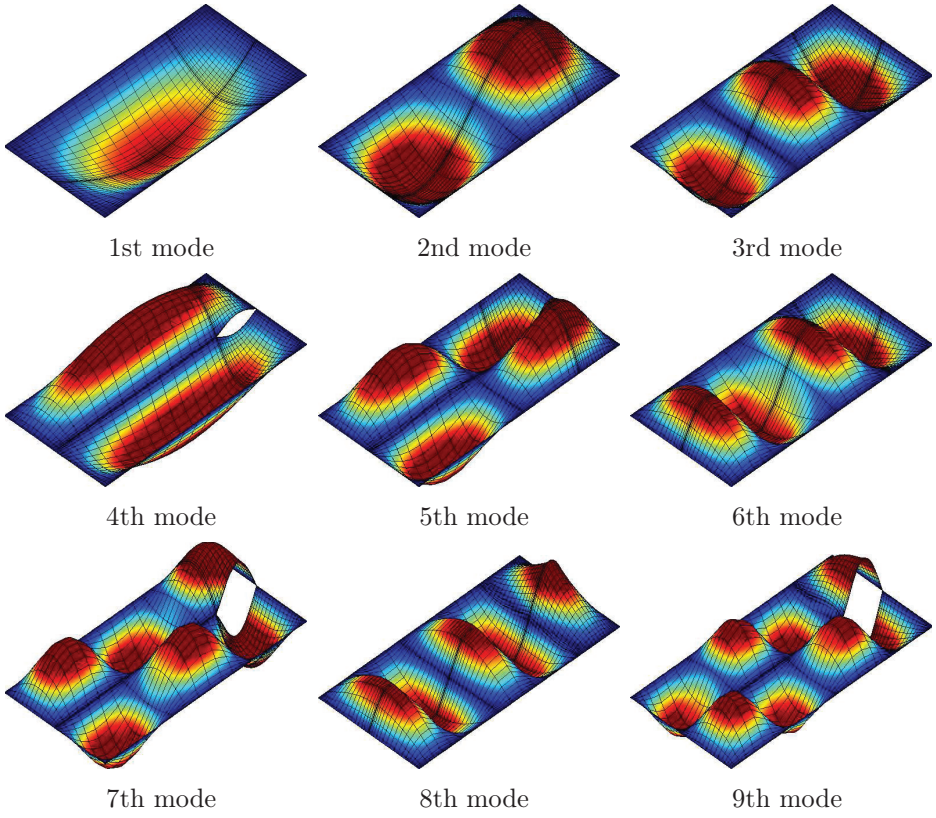

Figure 4.11: First 9 mode shapes for a rectangular side-cracked plate with a centred crack $c/b = 0.5$ and $d/a = 0.2$.

Λ	ABAQUS	Ref. [144]	GDQFEM			
			$N = 21$	$N = 23$	$N = 25$	$N = 27$
1	40.224	40.42	40.388	40.442	40.489	40.529
2	72.728	72.82	72.740	72.725	72.715	72.707
3	73.290	75.63	73.103	73.114	73.122	73.129
4	123.289	123.5	123.145	123.104	123.073	123.050
5	168.461	169.3	168.215	168.233	168.245	168.255
6	191.723	-	191.772	191.752	191.739	191.730
7	197.712	-	197.446	197.470	197.488	197.501
8	256.068	-	255.979	255.977	255.977	255.977
9	280.218	-	280.287	280.277	280.272	280.271
10	288.093	-	287.734	287.763	287.786	287.806

Table 4.12: Convergence of frequency parameters Λ for a simply supported rectangular plate having a central ($c/b = 0.5$) side crack with $d/a = 0.5$.

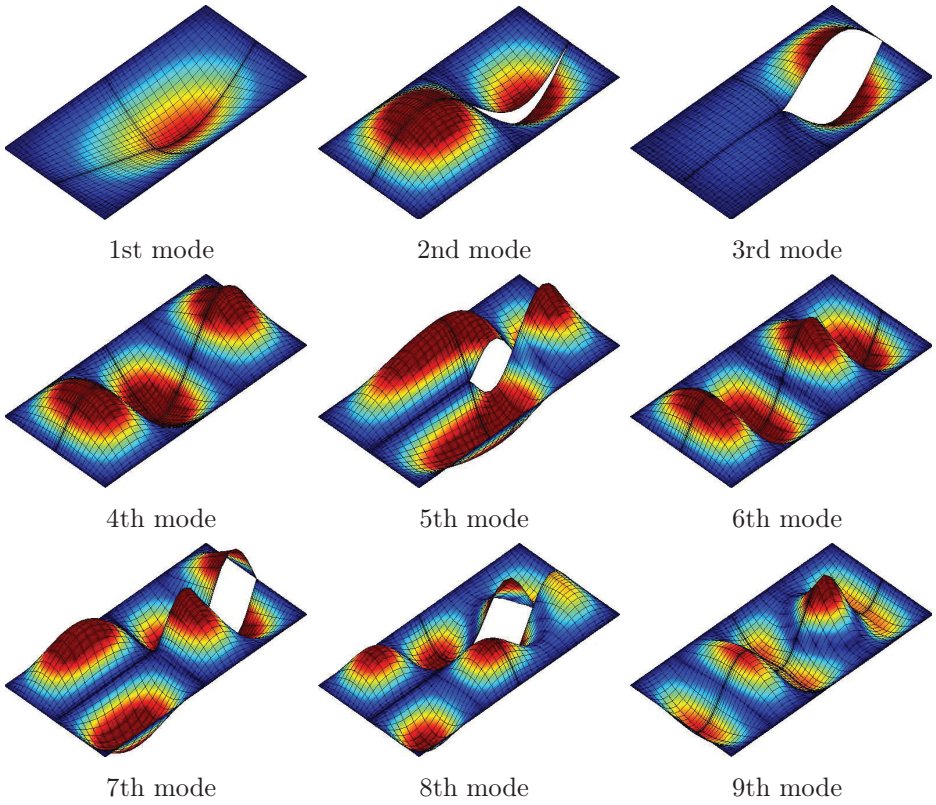

Figure 4.12: First 9 mode shapes for a rectangular side-cracked plate with a centred crack $c/b = 0.5$ and $d/a = 0.5$.

Λ	ABAQUS	Ref. [144]	GDQFEM			
			$N = 21$	$N = 23$	$N = 25$	$N = 27$
1	19.434	19.44	16.592	17.554	18.102	18.445
2	48.292	48.33	48.320	48.326	48.335	48.333
3	49.287	49.3	49.310	49.352	49.343	49.324
4	77.725	77.78	77.151	77.344	77.458	77.532
5	96.024	96.12	92.032	93.227	93.943	94.391
6	98.085	-	97.969	97.965	97.963	97.964
7	122.634	-	121.251	121.767	122.099	122.321
8	125.669	-	125.573	125.601	125.608	125.601
9	157.826	-	156.896	157.723	158.265	158.624
10	167.255	-	167.191	167.194	167.198	167.202

Table 4.13: Frequency parameters Λ for simply supported square plates with side cracks at orientation $\alpha = \pi/6$, location $c/b = 0.75$ and length $d/a = 0.3$.

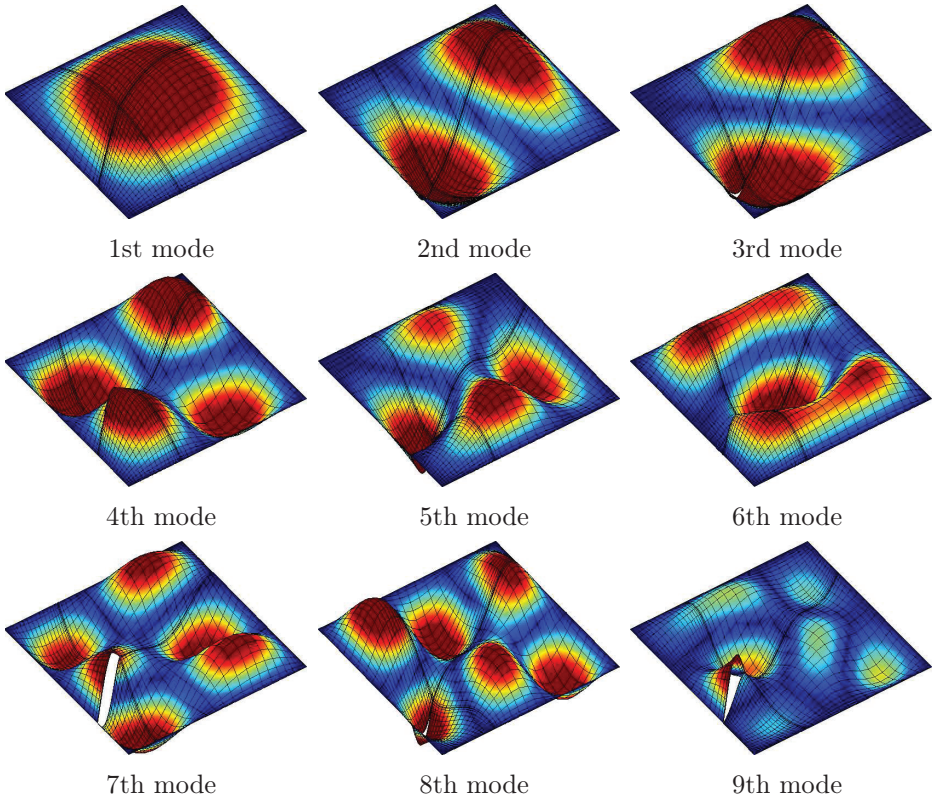

Figure 4.13: First 9 mode shapes for a rectangular side-cracked plate with a centred crack $c/b = 0.5$ and $d/a = 0.5$.

Bibliography

[1] S. Timoshenko, J.N. Goodier, Theory of elasticity, McGraw Hill (1951).

[2] N.I. Muskhelishvili, Some basic problems of the mathematical theory of elasticity, Groningen, P. Noordhoff, (1953)

[3] I.S. Sokolnikoff, Mathematical theory of elasticity, McGraw Hill (1956).

[4] S. Timoshenko, S. Woinowsky-Krieger, Theory of plates and shells. McGraw Hill (1959).

[5] R. Szilard, Theory and analysis of plates classical and numerical methods, Prentice Hall (1974).

[6] J.N. Reddy, Theory and analysis of elastic plates, Taylor and Francis (1999).

[7] R.E. Bellman, J. Casti, Differential quadrature and long-term integration, J. Math. Anal. Appl. 3 (1971) 235-238.

[8] R.E. Bellman, B.G. Kashef, J. Casti, Differential quadrature: a technique for the rapid solution of nonlinear partial differential equations, J. Comput. Phys 10 (1972) 40-52.

[9] C. Shu, Differential quadrature and its application in engineering, Springer (2000).

[10] F. Tornabene, Meccanica delle strutture a guscio in materiale composito, Esculapio (2012).

[11] Z. Zong, Y. Zhang, Advanced differential quadrature methods, CRC Press (2009).

[12] G.R. Liu, Mesh Free Methods, Moving beyond the Finite Element Method, CRC Press, Boca Raton (FL) (2002).

[13] G. Chen, J. Zhou, Boundary element methods, Academic Press (1992).

[14] A.W. Leissa, Vibration of plates, Acoustical Society of America, (1993).

[15] E. Viola, Scienza delle costruzioni. Vol. 1: Teoria dell'Elasticità, Pitagora Editrice Bologna (1990) (In Italian).

[16] E. Viola, Teoria delle strutture. Vol. 1: Stati tensionali e piastre, Pitagora Editrice Bologna (2010) (In Italian).

[17] E. Viola, Teoria delle strutture Vol. 2: Gusci di rivoluzione, Pitagora Editrice Bologna (2010) (In Italian).

[18] J.R. Quan, C.T. Chang, New insights in solving distributed system equations by the quadrature methods, I. Comput. Chem. Engrg. 13 (1989) 779-788.

[19] J.R. Quan, C.T. Chang, New insights in solving distributed system equations by the quadrature methods, II. Comput. Chem. Engrg. 13 (1989) 1017-1024.

[20] C. Shu, Generalized differential-integral quadrature and application to the simulation of incompressible viscous flows including parallel computation, PhD Thesis, Univ. of Glasgow (1991).

[21] C. Shu, B.E. Richards, Parallel simulation of incompressible viscous flows by generalized differential quadrature, Comput. Syst. Eng. 3 (1992) 271-281.

[22] H.Z. Zhong, Y.H. He, Solution of Poisson and Laplace equations by quadrilateral quadrature element, Int. J. Solids Struct. 35 (1998) 2805-2819.

[23] C.N. Chen, The two-dimensional frame model of the differential quadrature element method, Comput. Struct. 62 (1997) 555-571.

[24] C.N. Chen, Solution of beam on elastic foundation by DQEM, Eng. Mech-Asce 124 (1998) 1381-1384.

[25] C.N. Chen, The warping torsion bar model of the differential quadrature element method, Comput. Struct. 66 (1998) 249-257.

[26] C.-N. Chen, A generalized differential quadrature element method, Comput. Methods Appl. Mech. Engrg. 188 (2000) 553-566.

[27] C.-N. Chen, DQEM and DQFDM for the analysis of composite two-dimensional elasticity problems, Compos. Struct. 59 (2003) 3-13.

[28] C.N. Chen, The development of irregular elements for differential quadrature element method: steady-state heat conduction analysis, Comput. Method Appl. Mech. Eng. 170 (1999) 1-14.

[29] C.-N. Chen, The differential quadrature element method irregular element torsion analysis model, Appl. Math. Model. 23 (1999) 309-328.

[30] F.L. Liu, K.M. Liew, Static analysis of Reissner-Mindlin plates by differential quadrature element method, J. Appl. Mech. 65 (1998) 705-710.

[31] F.L. Liu, K.M. Liew, Vibration analysis of discontinuous Mindlin plates by differential quadrature element method, J. Vib. Acoust. 121 (1999) 204-208.

[32] A.G. Striz, W.L. Chen, C.W. Bert, Static analysis of structures by the quadrature element method (QEM), Int. J. Solids Struct. 31 (1994) 2807-2818.

[33] A.G. Striz, W.L. Chen, C.W. Bert, Free vibration of plates by the high accuracy quadrature element method, J. Sound Vib. 202 (1997) 689-702.

[34] X.W. Wang, H.Z. Gu, Static analysis of frame structures by the differential quadrature element method, Int. J. Numer. Meth. Eng. 40 (1997) 759-772.

[35] X.W. Wang, Y.L. Wang, R.B. Chen, Static and free vibrational analysis of rectangular plates by the differential quadrature element method, Commun. Numer. Meth. En. 14 (1998) 1133-1141.

[36] C.N. Chen, DQEM and DQFDM for the analysis of composite two-dimensional elasticity problems, Compos. Struct. 59 (2003) 3-13.

[37] C.-N. Chen, A generalized differential quadrature element method, Comput. Methods Appl. Mech. Engrg. 188 (2000) 553-566.

[38] Z. Zong, K.Y. Lam, Y.Y. Zhang, A multidomain differential quadrature approach to plane elastic problems with material discontinuity, Math. Comput. Model. 41 (2005) 539-553.

[39] E. Viola, F. Tornabene, Vibration analysis of damaged circular arches with varying cross-section, Struct. Integr. Durab. (SID-SDHM) 1 (2005) 155-169.

[40] E. Viola, F. Tornabene, Vibration analysis of conical shell structures using GDQ method, Far East J. Appl. Math. 25 (2006) 23-39.

[41] F. Tornabene, Modellazione e Soluzione di Strutture a Guscio in Materiale Anisotropo, PhD Thesis, University of Bologna - DISTART Department, 2007.

[42] F. Tornabene, E. Viola, Vibration analysis of spherical structural elements using the GDQ method, Comput. Math. Appl. 53 (2007) 1538-1560.

[43] E. Viola, M. Dilena, F. Tornabene, Analytical and numerical results for vibration analysis of multi-stepped and multi-damaged circular arches, J. Sound Vib. 299 (2007) 143-163.

[44] A. Marzani, F. Tornabene, E. Viola, Nonconservative stability problems via generalized differential quadrature method, J. Sound Vib. 315 (2008) 176-196.

[45] F. Tornabene, E. Viola, 2-D solution for free vibrations of parabolic shells using generalized differential quadrature method, Eur. J. Mech. A-Solid 27 (2008) 1001-1025.

[46] F. Tornabene, Vibration analysis of functionally graded conical, cylindrical and annular shell structures with a four-parameter power-law distribution, Comput. Methods Appl. Mech. Engrg. 198 (2009) 2911-2935.

[47] F. Tornabene, E. Viola, Free vibrations of four-parameter functionally graded parabolic panels and shell of revolution, Eur. J. Mech. A-Solid 28 (2009) 991-1013.

[48] F. Tornabene, E. Viola, Free vibration analysis of functionally graded panels and shells of revolution, Meccanica 44 (2009) 255-281.

[49] F. Tornabene, E. Viola, D.J. Inman, 2-D differential quadrature solution for vibration analysis of functionally graded conical, cylindrical and annular shell structures, J. Sound Vib. 328 (2009) 259-290.

[50] E. Viola, F. Tornabene, Free vibrations of three parameter functionally graded parabolic panels of revolution, Mech. Res. Commun. 36 (2009) 587-594.

[51] F. Tornabene, A. Marzani, E. Viola, I. Elishakoff, Critical flow speeds of pipes conveying fluid by the generalized differential quadrature method, Adv. Theor. Appl. Mech. 3 (2010) 121-138.

[52] F. Tornabene, Free Vibrations of laminated composite doubly-curved shells and panels of revolution via the GDQ method, Comput. Methods Appl. Mech. Engrg. 200 (2011) 931-952.

[53] F. Tornabene, 2-D GDQ solution for free vibrations of anisotropic doubly-curved shells and panels of revolution, Compos. Struct. 93 (2011) 1854-1876.

[54] F. Tornabene, Free vibrations of anisotropic doubly-curved shells and panels of revolution with a free-form meridian resting on Winkler-Pasternak elastic foundations, Compos. Struct. 94 (2011) 186-206.

[55] F. Tornabene, A. Liverani, G. Caligiana, FGM and laminated doubly-curved shells and panels of revolution with a free-form meridian: a 2-D GDQ solution for free vibrations, Int. J. Mech. Sci. 53 (2011) 446-470.

[56] F. Tornabene, A. Liverani, G. Caligiana, Laminated composite rectangular and annular plates: a GDQ solution for static analysis with a posteriori shear and normal stress recovery, Compos. Part B-Eng. 43 (2012) 1847-1872.

[57] F. Tornabene, A. Liverani, G. Caligiana, Static analysis of laminated composite curved shells and panels of revolution with a posteriori shear and normal stress recovery using Generalized Differential Quadrature Method, Int. J. Mech. Sci. 61 (2012) 71-87.

[58] F. Tornabene, A. Liverani, G. Caligiana, General anisotropic doubly-curved shell theory: a Differential Quadrature Solution for free vibrations of shells and panels of revolution with a free-form meridian, J. Sound Vib. 331 (2012) 4848-4869.

[59] E. Viola, L. Rossetti, N. Fantuzzi, Numerical investigation of functionally graded cylindrical shells and panels using the generalized unconstrained third order theory coupled with the stress recovery, Compos. Struct. (2012) 3736-3758.

[60] E. Viola, F. Tornabene, N. Fantuzzi, General higher-order shear deformation theories for the free vibration analysis of completely doubly-curved laminated shells and panels, Compos. Struct. 95 (2013) 639-666.

[61] F. Tornabene, E. Viola, Static analysis of functionally graded doubly-curved shells and panels of revolution, Meccanica. (2012) Accepted Manuscript.

[62] Ö. Civalek, M. Gurses, Free vibration of curvilinear membranes by eight-noded discrete singular convolution, Int. J. Sci. Tech. 3 (2008) 165-171.

[63] B.C. Bhadra, Symmetrical vibration of a composite circular membrane fastened at the circumference, J. pure appl. Math. 10 (1979) 223-229.

[64] G.R. Buchanan, Jr. J. Peddieson, Vibraion of circular and annular membranes with variable density, J. Sound Vib. 226 (1999) 379-382.

[65] G.R. Buchanan, Vibration of circular membranes with linearly varying density along a diameter, J. Sound Vib. 280 (2005) 407-414.

[66] P.A.A. Laura, R.E. Rossi, R.H. Gutierrez, The fundamental frequency of non-homogeneous rectangular membranes, J. Sound Vib. 204 (1997) 373-376.

[67] P.A.A. Laura, D.V. Bambill, R.H. Gutierrez, A note on transverse vibrations of circular, annular, composite membranes, J. Sound Vib. 205 (1997) 692-697.

[68] Ö. Civalek, Eigenvalues of membranes having skew and rhombic geometry using discrete singular convolution algorithm, Commun. Nonlinear Sci. Numer. Simulat. 14 (2009) 4003-4009.

[69] H. Ersoy, Ö. Civalek, L. Özpolat, Free vibration analysis of rectangular membranes with variable density using the descrete singular convolution approach, Asian J. Civil Engrg. 11 (2010) 83-94.

[70] J.T. Chen, J.H. Lin, S.R. Kuo, S.W. Chyuan, Boundary element analysis for the Helmholtz eigenvalue problems with a multiply connected domain, Proceedings Royal Society A 457 (2001) 2521-2546.

[71] S.Y. Reutskiy, The methods of external excitation for analysis of arbitrary-shaped hollow conducting waveguides, Prog. Electromagn. Res. 82 (2008) 203-226.

[72] P. Amore, D. Chowell, Collocation approach to the Helmholtz eigenvalue problem on multiply connected domains, J. Sound Vib. 329 (2010) 1362-1375.

[73] C. Shu, H. Xue, Solution of Helmholtz by differential quadrature method, Comput. Methods Appl. Mech. Engrg. 175 (1999) 203-212.

[74] C. Shu, Y.T. Chew, Fourier expansion-based differential quadrature and its application to Helmholtz eigenvalue problems, Commun. Numer. Methods Engrg. 13 (1997) 643-653.

[75] C. Shu, Y.T. Chew, Application of multi-domain GDQ method to analysis of waveguides with rectangular boundaries, Prog. Electromagn. Res. 21 (1999) 1-19.

[76] Z. Ding, Vibration of arbitrarily shaped membranes with elastical supports at points, Appl. Math. Mech. 10 (1989) 1171-1177.

[77] S.W. Kang, J.M. Lee, Y.J. Kang, Vibration analysis of arbitrarily shaped membranes using non-dimensional dynamic influence function, J. Sound Vib. 221 (1999) 117-132.

[78] S.W. Kang, J.M. Lee, Eigenmode analysis of arbitrarily shaped two-dimensional cavities by the method of point-matching, J. Acoustical Society America 107 (2000) 1153-1160.

[79] S.W. Kang, J.M. Lee, Application of free vibration analysis of membranes using the non-dimensional dynamic influence function, J. Sound Vib. 234 (2000) 455-470.

[80] S.W. Kang, J.M. Lee, Free vibration analysis of arbitrarily shaped plates with clamped edges using wave-type functions, J. Sound Vib. 242 (2002) 9-26.

[81] S.W. Kang, J.M. Lee, Free vibration analysis of an unsymmetric trapezoidal membrane, J. Sound Vib. 272 (2004) 450-460.

[82] S.W. Kang, J.M. Lee, Free vibration analysis of composite rectangular membranes with an oblique interface, J. Sound Vib. 251 (2002) 505-517.

[83] S.W. Kang, S.H. Kim, Free vibration analysis of free plates with smoothly varying boundary shapes using non-dimensional dynamic influence functions, J. Vib. Acoustics 130 (2008) 1-8.

[84] W.X. Wu, C. Shu, C.M. Wang, Vibration analysis of arbitrarily shaped membranes using local radial basis function-based differential quadrature method, J. Sound Vib. 306 (2007) 252-270.

[85] S.W. Kang, S.N. Atluri, Free vibration analysis of arbitrarly shaped polygonal plates with simply supported edges using a sub-domain method, J. Sound Vib. 327 (2009) 271-284.

[86] M.G. Milsted, J.R. Hutchinson, Use of trigonometric terms in the finite element with application to vibrating membranes, J. Sound Vib. 32 (1974) 327-346.

[87] H.D. Conway, K.A. Farnham, The free flexural vibrations of triangular, rhombic and parallelogram plates and some analogies, Int. J. Mech. Sci. 7 (1965) 811-816.

[88] S. Durvasula, Natural frequencies and modes of skew membranes, J. Acoustic Society America 44 (1968) 1636-1646.

[89] L. Bauer, E.L. Reiss, Free vibrations of rhombic plates and membranes, J. Acoustic Society America 54 (1973) 1373-1375.

[90] T. Irie, G. Yamada, K. Umesato, Free vibration of regular polygonal plates with simply supported edges, J. Acoustic Society America 69 (1981) 1330-1336.

[91] T. Irie, G. Yamada, M. Tsujino, Natural frequencies of concavely shaped polygonal plates with simply supported edges, J. Acoustic Society America 69 (1981) 1507-1509.

[92] C.Y. Wang, C.M. Wang, Exact solutions for vibrating rectangular membranes placed in a vertical plane, Int. J. Appl. Mech. 3 (2011) 625-631.

[93] J.A. Cottrell, A. Reali, Y. Bazilevs, T.J.R. Hughes, Isogeometric analysis of structural vibrations, Comput. Methods Appl. Engrg. 195 (2006) 5257-5296.

[94] T.J.R. Hughes, A. Reali, G. Sangalli, Efficient quadrature for NURBS-based isogeometric analysis, Comput. Methods Appl. Mech. Engrg. 199 (2010) 301-313.

[95] A.J. Burton, G.F. Miller, The application of integral equation methods to the numerical solution of some exterior boundary-value problems, Proc. R. Soc. Lond. A 323 201-210.

[96] C. Bert, M. Malik, Differential quadrature method in computational mechanics, Appl. Mech. Rev. 49 (1996) 1-27.

[97] F.L. Liu, K.M. Liew, Differential quadrature element method: a new approach for free vibration of polar Mindlin plates having discontinuities, Comput. Methods Appl. Mech. Engrg. 179 (1999) 407-423.

[98] K.M. Liew, F.-L. Liu, Differential quadrature method for vibration analysis of shear deformable annular sector plates, J. Sound Vib. 230 (2000) 335-356.

[99] G.R. Liu, T.Y. Wu, Vibration analysis of beams using the generalized differential quadrature rule and domain decomposition, J Sound Vib. 246 (2001) 461-481.

[100] G. Karami, P. Malekzadeh, An efficient differential quadrature methodology for free vibration analysis of arbitrary straight-sided quadrilateral thin plates, J. Sound Vib. 263 (2003) 415-442.

[101] G. Karami, P. Malekzadeh, In-plane free vibration analysis of circular arches with varying cross-sections using differential quadrature method, J. Sound Vib. 274 (2004) 777-799.

[102] J.-J. Li, C.-J. Cheng, Differential quadrature method for nonlinear vibration of orthotropic plates with finite deformation and transverse shear effect, J. Sound Vib. 281 (2005) 295-309.

[103] Y.-J. Shin, K.-M. Kwon, J.-H. Yun, Vibration analysis of a circular arch with variable cross-section using differential transformation and generalized differential quadrature, J. Sound Vib. 309 (2008) 9-19.

[104] S.C. Pradhan, T. Murmu, Thermo-mechanical vibration of FGM sandwich beam under variable elastic foundations using differential quadrature method, J. Sound Vib. 321 (2009) 342-362.

[105] H. Zhong, C. Pan, H. Yu, Buckling analysis of shear deformable plates using the quadrature element method, Appl. Math. Model. 35 (2011) 5059-5074.

[106] R. Hill, Elastic properties of reinforced solids: some theoretical principals, J. Mech. Phys Solids 11 (1963) 357-372.

[107] A. Drago, M.J. Pindera, Micro-mechanical analysis of heterogeneous materials: macroscopically homogeneous vs periodic microstructures, Compos. Sci. Tech. 67 (2007) 1243-1263.

[108] S. Hazanov, M. Amieur, On overall properties of elastic heterogeneous bodies smaller than the representative volume element, Int. J. Eng. Sci. 33 (1995) 1289-1301.

[109] S. Hazanov, C. Huet, Order relationships for boundary conditions effect in heterogeneous bodies smaller than the representative volume, J. Mech. Phys. Solids 42 (1994) 1995-2011.

[110] S.J. Hollister, N. Kikuchi, A comparison of homogenization and standard mechanics analyses for periodic porous composites, Comput. Mech. 10 (1992) 73-95.

[111] C. Huet, Application of variational concepts to size effects in elastic heterogeneous bodies, J. Mech. Phys. Solids 38 (1990) 813-841.

[112] R.H. MacNeal, R.L. Harder, A proposed standard set of problems to test finite element accuracy, Finite Elem. Anal. Design, 1 (1985) 3-20.

[113] R.L. Taylor, P.J. Beresford, E.L. Wilson, A non-conforming element for stress analysis, Int. J. Num. Meth. Eng., 10 (1976) 1211-1219.

[114] K.K. Gupta, Development of a finite dynamic element for free vibration analysis of two-dimensional structures, Int. J. Numer. Methods Eng., 12 (1978) 1311-1327.

[115] T.H.H. Pian, K. Sumihara, Rational approach for assumed stress finite elements, Int. J. Num. Meth. Eng., 20 (1984) 1685-1695.

[116] D.J. Allman, A quadrilateral finite element including vertex rotations for plane elasticity analysis, Int. J. Num. Meth. Eng., 26 (1988) 717-730.

[117] R.D. Cook, D.S. Malkus, M.E. Plesha, Concepts and applications of finite element analysis, John Wiley & Sons (1989).

[118] R.D. Cook, J. Avrashi, Error estimation and adaptive meshing for vibration problems, Comput. Struct., 44 (1992) 619-626.

[119] Y.Q. Long, Y. Xu, Generalized conforming triangular membrane element with vertex rigid rotational freedom, Finite Elem. Anal. Design, 17 (1994) 259-271.

[120] C. Zhao, G.P. Steven, Asymptotic solutions for predicted natural frequencies of two-dimensional elastic solid vibration problems in finite element analysis, Int. J. Numer. Methods Eng., 39 (1996) 2821-2835.

[121] N. Choi, Y.S. Choo, B.C. Lee, A hybrid Trefftz plane elasticity element with drilling degrees of freedom, Comput. Methods Appl. Mech. Engrg., 195 (2006) 4095-4105.

[122] S. de Miranda, L. Molari, F. Ubertini, A consistent approach for mixed stress finite element formulations in linear elastodynamics, Comput. Methods Appl. Engrg., 197 (2008) 1376-1388.

[123] S. Cen, M.J. Zhou, X.R. Fu, A 4-node hybrid stress-function (HS-F) plane element with drilling degrees of freedom less sensitive to severe mesh distortions, Comput. & Struct., 89 (2011) 517-528.

[124] S. Cen, X.M. Chen, C.F. Li, X.R. Fu, Qradrilateral membrane elements with analytical element stiffness matrices formulated by the new quadrilateral area coordinate method (QACM-II), Int. J. Num. Meth. Eng., 77 (2009) 1172-1200.

[125] A. Madeo, G. Zagari, R. Casciaro, An isostatic quadrilateral membrane finite element with drilling rotations and no spurious modes, Finite Elem. Anal. Design, 50 (2012) 21-32.

[126] M. Rezaiee-Pajand, M. Karkon, An effective membrane element based on analytical solution, Europ. J. Mech. A/Solids (2013), doi:10.1016/j.euromechsol.2012.12.004.

[127] C. Shu, Y.T. Chew, B.C. Khoo, K.S. Yeo, Application of GDQ scheme to simulate incompressible viscous flows around complex geometries, Mech. Res. Commun. 95 (1995) 319-325.

[128] K.M. Kiew, J.-B. Han, A four-node differential quadrature method for straight-sided quadrilateral Reissner/Mindlin plates, Commun. Numer. Methods Eng. 13 (1997) 73-81.

[129] J.-B. Han, K.M. Liew, An eight-node curvilinear differential quadrature formulation for Reissner/Mindlin plates, Comput. Methods Appl. Mech. Engrg. 141 (1997) 265-280.

[130] F.-L. Liu, Differential quadrature element method for static analysis of shear deformable cross-ply laminates, Int. J. Numer. Meth. Engng. 46 (1999) 1203-1219.

[131] F.-L. Liu, Static analysis of thick rectangular laminated plates: three-dimensional elasticity solutions via differential quadrature element method, Int. J. Solids Struct. 37 (2000) 7671-7688.

[132] H. Zhong, Y. He, A note on incorporation of domain decomposition into the differential quadrature method, Commun. Numer. Methods Eng. 19 (2003) 297-306.

[133] Y. Wang, X. Wang, Y. Zhou, Static and free vibration analyses of rectangular plates by the new version of the differential quadrature element method, Int. J. Numer. Methods Eng. 59 (2004) 1207-1226.

[134] Y. Xing, B. Liu, High-accuracy differential quadrature finite element method and its application to free vibrations of thin plate with curvilinear domain, Int. J. Numer. Meth. Engrg. 80 (2009) 1718-1742.

[135] Y. Xing, B. Liu, G. Liu, A differential quadrature finite element method, Int. J. Appl. Mech. 2 (2010) 1-20.

[136] M. Chehel Amirani, S.M.R. Khalili, N. Nemati, Free vibration analysis of sandwich beam with FG core using the element free Galerkin method, Compos. Struct. 90 (2009) 373-379.

[137] C.T. Wu, Y. Guo, E. Askari, Numerical modeling of composite solids using an immersed meshfree Galerkin method, Compos. Part B 45 (2013) 1397-1413.

[138] M. Bayat, M.M. Aghdam, A micromechanics-based analysis of effects of square and hexagonal fiber arrays in fibrous composites using DQEM, Europ. J. Mech. A/Solids 32 (2012) 32-40.

[139] Y.T. Gu, G.R. Liu, A meshless local Petrov-Galerkin (MLPG) method for free and forced vibration analyses for solids, Comput. Mech. 27 (2001) 188-198.

[140] E. Reissner, The effect of transverse shear deformation on the bending of elastic plates, ASME J. Applied Mech. 12 (1945) A68-77.

[141] R.D. Mindlin, Influence of rotatory inertia and shear on flexural motions of isotropic, elastic plates, ASME J. Applied Mech. 18 (1951) 31-38.

[142] C.M. Wang, G.T. Lim, J.N. Reddy, K.H. Lee, Relationships between bending solutions of Reissner and Mindlin plate theories, Eng. Struct. 23 (2001) 838-849.

[143] C.S. Huang, A.W. Leissa, C.W. Chan, Vibrations of rectangular plates with internal cracks or slits, Int. J. Mech. Sciences 53 (2011) 436-445.

[144] C.S. Huang, A.W. Leissa, VIbration analysis of rectangular plates with side cracks via the Ritz method, J. Sound Vib. 323 (2009) 974-988.

[145] C.S. Huang, A.W. Leissa, R.S. Li, Accurate vibration analysis of thick, cracked rectangular plates, J. Sound Vib. 330 (2011) 2079-2093.

[146] C.S. Huang, A.W. Leissa, S.C. Liao, Vibration analysis of rectangular plates with edge V-notches, Int. J. Mech. Sciences 50 (2008) 1255-1262.

DiQuMASPAB

http://software.dicam.unibo.it/diqumaspab-project

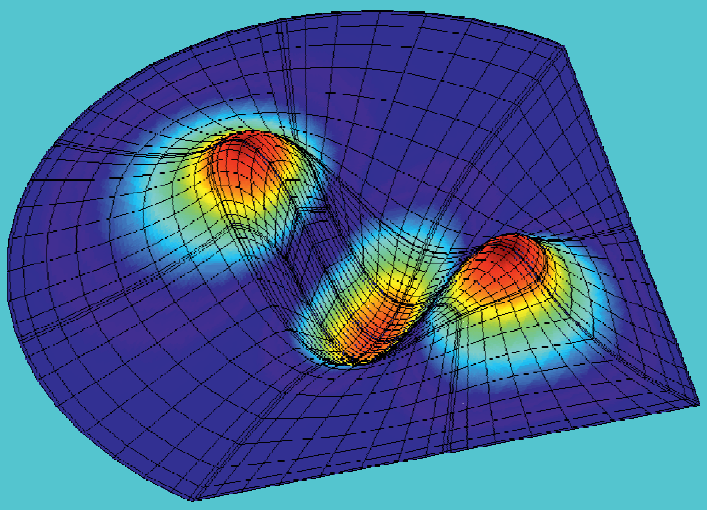

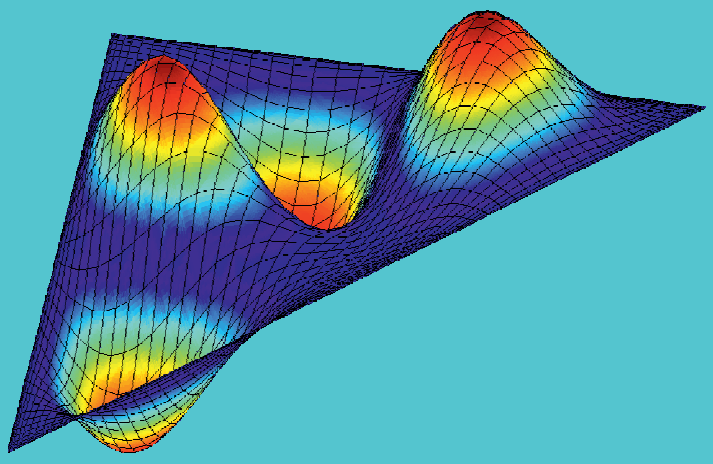

Over the years Generalized Differential Quadrature (GDQ) method has distinguished due to its high accuracy, straightforward implementation and general application to several engineering problems.

However, the applicability of GDQ in its original form is still limited. In fact, it fails with strong material discontinuities and geometric irregularities. On the other hand these issues can be overcome subdividing the physical domain into regular or irregular sub-domains as well as in the Finite Element Method (FEM). Furthermore, through the mapping technique it is possible to describe any irregular geometry into a regular one, where the classic GDQ can be applied. This methodology is indicated as Generalized Differential Quadrature Finite Element Method (GDQFEM).

Starting from the theoretical framework of the GDQ method, the main aim of this PhD Thesis is to show the applicability and the implementation of the GDQFEM, which goes beyond any GDQ drawback.

In order to show the accuracy, stability and flexibility of the current methodology several numerical applications are shown. The static and dynamic behavior of advanced engineering structures are compared to literature and other numerical solutions. Very good agreement has been observed.

Department of Civil, Chemical, Environmental and Material Engineering

University of Bologna